

## Passive seismic multiscale subsurface imaging and characterization by utilizing natural quakes

Nishitsuji, Yohei

**DOI**

[10.4233/uuid:d85dec82-72dd-4b06-b6a0-2751c0ee6049](https://doi.org/10.4233/uuid:d85dec82-72dd-4b06-b6a0-2751c0ee6049)

**Publication date**

2017

**Document Version**

Final published version

**Citation (APA)**

Nishitsuji, Y. (2017). *Passive seismic multiscale subsurface imaging and characterization by utilizing natural quakes*. [Dissertation (TU Delft), Delft University of Technology]. <https://doi.org/10.4233/uuid:d85dec82-72dd-4b06-b6a0-2751c0ee6049>

**Important note**

To cite this publication, please use the final published version (if applicable). Please check the document version above.

**Copyright**

Other than for strictly personal use, it is not permitted to download, forward or distribute the text or part of it, without the consent of the author(s) and/or copyright holder(s), unless the work is under an open content license such as Creative Commons.

**Takedown policy**

Please contact us and provide details if you believe this document breaches copyrights. We will remove access to the work immediately and investigate your claim.

**PASSIVE SEISMIC MULTISCALE SUBSURFACE  
IMAGING AND CHARACTERIZATION BY  
UTILIZING NATURAL QUAKES**



# **PASSIVE SEISMIC MULTISCALE SUBSURFACE IMAGING AND CHARACTERIZATION BY UTILIZING NATURAL QUAKES**

## **Proefschrift**

ter verkrijging van de graad van doctor  
aan de Technische Universiteit Delft,  
op gezag van de Rector Magnificus prof. ir. K.C.A.M. Luyben,  
voorzitter van het College voor Promoties,  
in het openbaar te verdedigen op woensdag 25 januari 2017 om 10:00 uur

door

**Yohei NISHITSUJI**

Master of Science,  
Kyoto University, Kyoto, Japan,  
geboren te Hokkaido, Japan.

Dit proefschrift is goedgekeurd door de promotor:

Prof. dr. ir. C.P.A. Wapenaar

Copromotor:

Dr. ir. D.S. Draganov

Samenstelling promotiecommissie:

Rector Magnificus,	voorzitter
Prof. dr. ir. C.P.A. Wapenaar,	Technische Universiteit Delft, promotor
Dr. ir. D.S. Draganov,	Technische Universiteit Delft, copromotor

*Onafhankelijke leden:*

Prof. dr. D.F. Bruhn,	Technische Universiteit Delft
Prof. dr. L.G. Evers,	Technische Universiteit Delft
Prof. dr. J.O.A. Robertsson,	Eidgenössische Technische Hochschule Zürich
Prof. dr. J.A. Trampert,	Universiteit Utrecht
drs. A.R. Verdel,	Nederlandse Organisatie voor Toegepast Natuurwetenschappelijk Onderzoek



*Printed by:* Gildeprint

*Front:* K. Nishitsuji, *Tsukibito (Man on the Moon)*, Exhibited at Masters of Modern Japanese Art 88th KOKUTEN, Tokyo, Japan, May 2014.

Copyright © 2016 by Y. Nishitsuji

ISBN 978-94-6186-769-8

An electronic version of this dissertation is available at

<http://repository.tudelft.nl/>.

*Dedicated to my parents, ancestors, and family.*

*I learned from my mother  
"I am odd (she always told me so)."*

*I learned from my father  
"Challenge the status quo when only it is stable."*

*I learned from my ancestors  
"Think outside the box to make a success of business in Russia."*

*I learned from my sons  
"I am a perfectly imperfect human."*

*I learned from my wife  
"I am really odd (she emphasizes so)."*

Yohei Nishitsuji



# CONTENTS

<b>Summary</b>	<b>ix</b>
<b>Samenvatting</b>	<b>xi</b>
<b>1 Introduction</b>	<b>1</b>
1.1 Natural quakes	1
1.2 Passive seismic methods	1
1.3 Cost-effective explorations for hydrocarbons and renewables	3
1.4 Objectives and thesis outline	4
References	6
<b>2 Basin-scale seismic imaging and characterization</b>	<b>9</b>
2.1 Global-phase H/V spectral ratio	11
2.1.1 Introduction	11
2.1.2 MalARRgue	12
2.1.3 Malargüe basin	14
2.1.4 Global phases	14
2.1.5 Global-phase H/V spectral ratio	16
2.1.6 Results and discussion	19
2.2 Sp-wave phase and $Q_S/Q_P$	24
2.2.1 Introduction	24
2.2.2 Data set and study area	25
2.2.3 Sp-wave analysis	25
2.2.4 Frequency-dependent $Q$	32
2.2.5 Discussion	33
2.2.6 Appendix A: System of equations for Sp-waves analysis	36
References	36
<b>3 Crustal-scale seismic imaging</b>	<b>41</b>
3.1 Local earthquake P-wave coda seismic interferometry	42
3.1.1 Introduction	42
3.1.2 Study area and data	44
3.1.3 Local-earthquake P-wave coda seismic interferometry	47
3.1.4 Data processing	52
3.1.5 Results and interpretation	64
3.1.6 Appendix B: Approximated multidimensional deconvolution	69
3.1.7 Appendix C: Truncated singular-value decomposition	71
References	71



<b>4</b>	<b>Lithospheric-scale seismic imaging and characterization</b>	<b>79</b>
4.1	On the Earth: Global-phase seismic interferometry . . . . .	81
4.1.1	Introduction . . . . .	81
4.1.2	Global-phase seismic interferometry . . . . .	82
4.1.3	Data . . . . .	84
4.1.4	Data processing . . . . .	88
4.1.5	Results interpretation and discussion . . . . .	96
4.2	On the Earth: Radiation efficiency of intermediate-depth earthquakes . . . . .	99
4.2.1	Introduction . . . . .	99
4.2.2	Data . . . . .	99
4.2.3	Method . . . . .	102
4.2.4	Results . . . . .	107
4.2.5	Discussion . . . . .	113
4.3	On the Moon: Deep-moonquake seismic interferometry . . . . .	115
4.3.1	Introduction . . . . .	115
4.3.2	Study area and data . . . . .	116
4.3.3	Deep-moonquake seismic interferometry . . . . .	121
4.3.4	Data processing . . . . .	124
4.3.5	Numerical wavefield modeling. . . . .	132
4.3.6	Results and discussion . . . . .	136
	References . . . . .	138
<b>5</b>	<b>General conclusions</b>	<b>151</b>
5.1	Conclusions. . . . .	151
	References . . . . .	153
	<b>Acknowledgements</b>	<b>155</b>
	<b>Curriculum Vitae</b>	<b>159</b>
	<b>List of Publications</b>	<b>161</b>

# SUMMARY

**I**N seismic exploration, passive seismic methods are those that do not use active seismic sources for imaging and characterization of the subsurface. Passive seismic methods make use of induced and natural quakes, the latter can also include noise. One major advantage of employing these methods is the financial reason connected to the shooting cost when using active sources for the active seismic methods. Another major advantage of the passive seismic methods with natural quakes is related to environment and social acceptances, especially in the hydrocarbon and renewable-energy industries. Still, compared to active seismic methods, the number of field applications of passive seismic methods with natural quakes in the exploration/production industry is low. The main reason for this is the lack of control over natural passive sources.

The main motivation in this thesis is to investigate the potential usage of passive seismic methods with natural quakes as cost-effective and environmentally responsible applications for multiscale subsurface imaging and characterization. I am looking not only at applications for the natural-resource industries, but also for the scientific community. For this purpose, I develop various methods that utilize natural quakes and apply those to various targets. In particular, I focus on the technique of seismic interferometry (SI), which provides pseudo-reflection imaging of subsurface structures.

I investigate the application of the passive seismic methods with natural quakes to targets at three major scales: basin scale, crustal scale, and lithospheric scale. For the basin-scale seismic investigation, I develop a technique to delineate the basin depth (top of a basement) using horizontal- and vertical-components (H/V) spectral ratio. For this application I use exclusively global phases of distant earthquakes to calculate the H/V spectral ratio. In another investigation, I integrate the Sp-wave method and an analysis of the frequency-dependent quality factor to characterize subsurface heterogeneities at the basin scale. Both results show good agreement with active-seismic profiles acquired in the past in the two investigation regions.

I also develop an SI method that could be used for crustal-scale seismic imaging. This method uses the P-wave coda of natural earthquakes. I apply this method to data from the Neuquén basin in Argentina. From the results, I conclude that utilization of multidimensional deconvolution, based on the truncated singular-value decomposition scheme, for the retrieval of virtual responses allows better structural imaging than do the conventional crosscorrelation, crosscoherence, and also multidimensional deconvolution based on the damped least-squares scheme. I suggest that this method could be useful, for example, as a prescreening-exploration tool for deep geothermal applications whose targets can be as deep as 10 km.

I also develop SI methods for lithospheric-scale seismic investigations of the Earth and the Moon. I apply SI with global phases to shed light on one of the challenging topics in lithospheric imaging, which is to obtain detailed images of aseismic parts of subduction slabs. I use data recorded in the Neuquén basin above the Nazca slab. In this region,

no seismicity has been recorded deeper than 200 km, where the slab is expected to be in this area. Although the interpretation of the imaging results of the aseismic parts is not unambiguous, the results confirm that the method I apply is useful for imaging aseismic parts of slabs. From the imaging, I interpret that an aseismic spot could correspond to a deformation in the slab at that place; I also interpret that the deeper aseismic part of the slab is not detaching.

At the lithospheric scale, I also determine the radiation efficiency of the intermediate-depth earthquakes to understand the difference of the focal mechanisms between shallow and deep earthquakes. From this investigation, I find that the radiation efficiency tends to decrease as a function of source depth, which suggests that the deeper the earthquakes, the more ductile the earthquake's characteristics. This implies that one of the reasons for the slabs to be aseismic at certain depths might be related to the domination of the ductile property.

As a final lithospheric-scale seismic investigation, I apply SI to deep moonquakes on the Moon. With this application, I perform reflection imaging of the lunar subsurface. I succeed in interpreting the possible lunar Moho – it resides around 50 km depth. My interpretation might contribute to the evolution study of the Moon.

Based on my results from applications at different scales, I conclude that the passive seismic methods with natural quakes have excellent potential usage in both the resource industry and academia. To help the decision on the future choice and usage of a passive seismic method for a specific result and target scale, I conclude the thesis by indicating the applicability of the various methods as a function of target scale.

# SAMENVATTING

**P**assieve seismische methodes zijn methodes in het onderzoeksveld van seismische exploratie die geen gebruik maken van actieve seismische bronnen voor het afbeelden en karakteriseren van de ondergrond. Passieve seismische methodes maken zowel gebruik van geïnduceerde bronnen als van natuurlijke aardbevingsbronnen. In het laatste geval kan de bron ook ruis bevatten. Een groot voordeel van deze passieve methodes is dat de kosten die gepaard gaan met het gebruik van een actieve bron worden vermeden. Een ander groot voordeel van het gebruik van natuurlijke bevingen is gerelateerd aan het milieu en de maatschappelijke omstandigheden, met name voor de olie- en gas industrie en de duurzame-energie industrie. Er is echter maar een beperkt aantal situaties waarop de passieve methodes met natuurlijke bevingen kan worden toegepast in de exploratie- en productie industrie. De belangrijkste reden hiervoor is het ontbreken van controle over deze passieve natuurlijke bronnen.

De belangrijkste motivatie voor dit proefschrift komt voort uit de vraag of het mogelijk is om passieve seismiek met natuurlijke bevingen te gebruiken als een efficiënte, goedkope en milieubewuste methode voor verschillende toepassingen voor het afbeelden en karakteriseren van de ondergrond. Ik onderzoek niet alleen toepassingen voor de olie- en gas industrie, maar ook toepassingen die voor de wetenschappelijke gemeenschap van nut kunnen zijn. Ik ontwikkel verschillende methodes die gebruik maken van natuurlijke bevingen voor verschillende doeleinden. Ik richt daarbij mijn aandacht voornamelijk op de methode van de Seismische Interferometrie (SI), welke met behulp van pseudo-reflectiemetingen de ondergrond in beeld brengt.

Ik onderzoek de toepassing van de passieve seismische methodes met natuurlijke bevingen, met doelen op drie verschillende schalen van grootte: namelijk de schaal van sedimentaire bekkens, van de korst en van de lithosfeer. Voor het seismische onderzoek op de sedimentaire-bekken schaal ontwikkel ik een methode die de diepte en het profiel van de top van het sedimentaire bekken kan bepalen, met behulp van de zogenaamde horizontale- en verticale-componenten (H/V) spectrale ratio. Voor deze toepassing maak ik specifiek alleen gebruik van de globale fases van aardbevingen op grote afstand om de H/V spectrale ratio te bepalen. In een ander onderzoek combineer ik de Sp-golf methode met een analyse van de frequentie-afhankelijke kwaliteitsfactor om de heterogeniteiten in de ondergrond te bepalen op bekkenschaal. Beide resultaten vertonen een sterke overeenkomst met profielen die in twee eerdere onderzoeken in dezelfde gebieden zijn verkregen met behulp van actieve seismische bronnen.

Ik ontwikkel ook een SI methode die gebruikt kan worden voor het afbeelden van doelen op de schaal van de korst. Deze methode maakt gebruik van de P-golf coda van natuurlijke aardbevingen. Ik pas deze methode toe op data van het Neuquén bekken in Argentinië. Uit de resultaten concludeer ik dat het gebruik van een multidimensionale deconvolutie, gebaseerd op getrunceerde singuliere-waarde decompositie, betere resultaten oplevert voor het afbeelden van de ondergrond dan het gebruik van conventionele

kruis-correlatie, kruis-coherentie en multidimensionale deconvolutie gebaseerd op een gedempte kleinste-kwadraten methode. Ik stel deze methode voor als een preselectie methode voor geothermische exploratie tot dieptes van 10 kilometer.

Ik ontwikkel ook SI methodes voor seismisch onderzoek op lithosferische schaal van zowel de aarde als de maan. Met behulp van globale fases pas ik SI toe om licht te werpen op één van de meest uitdagende onderwerpen van het afbeelden van de lithosfeer, namelijk het verkrijgen van gedetailleerde beelden van aseismische delen van subductie platen. Hiervoor maak ik gebruik van data die is verkregen in het Neuquén bekken boven de Nazca plaat. In deze regio is geen seismische activiteit waargenomen dieper dan 200 km, de diepte waarop de Nazca plaat zich vermoedelijk bevindt. Hoewel de interpretatie van de resultaten een zekere mate van ambiguïteit bevat, bevestigen de resultaten dat de methode die ik toepas van nut is voor het afbeelden van de aseismische delen van de platen. Uit de verkregen resultaten interpreteer ik dat een aseismische locatie kan overeenkomen met de locatie van deformatie in de plaat. Ik interpreteer ook dat de diepere aseismische delen van de plaat niet loslaten van de rest van de plaat.

Op lithosferische schaal bepaal ik ook de stralingsefficiëntie van aardbevingen op middelgrote dieptes om het verschil van de focale mechanismes tussen ondiepe en diepe aardbevingen te begrijpen. Uit dit onderzoek leid ik af dat de stralingsefficiëntie afneemt naarmate de diepte van de bron groter wordt, hetgeen suggereert dat diepere aardbevingen gerelateerd zijn aan grotere buigzaamheid. Dit suggereert dat buigzaamheid één van de redenen is dat de plaat aseismisch is op grotere diepte.

Als laatste lithosferisch onderzoek pas ik SI toe op maanbevingen op de Maan. Met behulp van deze toepassing pas ik reflectie-beeldvorming toe en breng ik de ondergrond van de maan in beeld. Ik slaag erin de mogelijke Moho van de Maan te interpreteren op een diepte van rond de 50 kilometer. Mijn interpretatie kan bijdragen aan het bestuderen van de ontwikkeling van de maan.

Op basis van de resultaten van mijn toepassingen op verschillende grootte-schalen concludeer ik dat passieve seismische methodes met natuurlijke bevingen veel potentie hebben om zowel door de industrie als de academische wereld gebruikt te worden. Om te bepalen welke passieve seismische methode het best kan worden gebruikt voor een bepaald doel, sluit ik mijn proefschrift af met een overzicht van alle voor- en nadelen van de verschillende methodes.

# 1

## INTRODUCTION

*Anxiety is the dizziness of freedom.*

Søren Kierkegaard

### 1.1. NATURAL QUAKES

Natural quakes are phenomena that occur when the surface/subsurface of Earth, the Moon, the Sun, planets, or stars shake due to a natural reason (Figure 1.1). The quakes can be seen as the consequence of a sudden release of energy. Natural quakes can be distinguished from artificial quakes (e.g. vibroseis) and induced quakes (e.g. due to nuclear exploration, due to hydrocarbon production) from the standpoint of their nature. Among the natural quakes, an earthquake (quake occurring on Earth) is the most known one in our societies. Historically speaking, earthquakes have been recognized as unfavorable phenomena due to them causing ground shakings, tsunamis, volcanoes, or landslides, and connected with them the material and non-material damages to the societies. Therefore, earthquake prediction is one of the ultimate goals among scientists who investigate earthquakes. In parallel, with the seismic-wave analysis, macroscopic imaging of the Earth's interior has also been intensively investigated with partial connection to earthquake prediction.

### 1.2. PASSIVE SEISMIC METHODS

Passive seismic methods are methods that use the natural quakes to investigate the interior of a celestial body. The quakes are often called passive sources. This is because we record the quakes passively by seismic stations (arrays). The origin of the passive seismic methods can be traced back to the work of Mohorovičić [1]. He discovered the first Moho discontinuity in Yugoslavia using travelttime analysis.

Today, in addition to travelttime analysis, several other approaches have also been developed as passive seismic methods. Such methods are, for example, seismic tomography [e.g. 2, 3], receiver-function analysis [4], horizontal- and vertical-components (H/V)

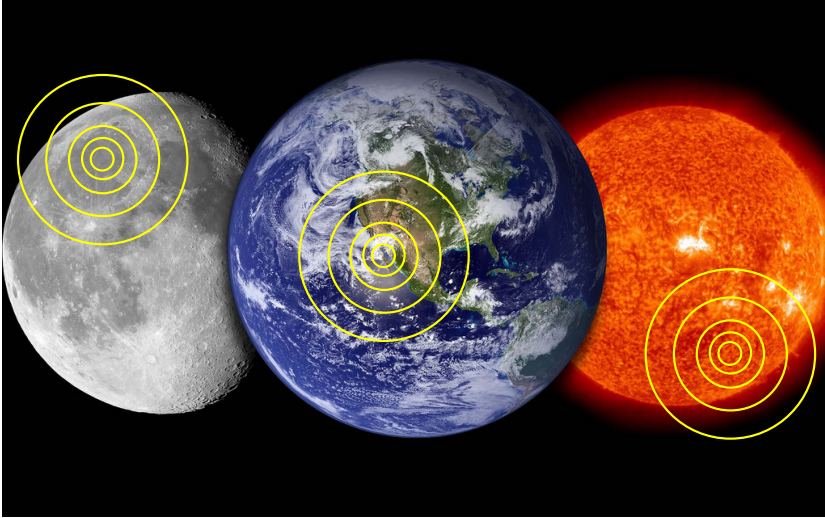


Figure 1.1: Cartoon illustrating natural quakes on the Moon, Earth and Sun, respectively. This image was modified from [www.glogster.com](http://www.glogster.com).

spectral-ratio method [5], Sp-wave method [6] and seismic interferometry (SI) [e.g. 7–11]. While seismic tomography maps velocity perturbations of the medium, the receiver-function and the Sp-wave methods map structural heterogeneities as structural discontinuities. On the other hand, the H/V spectral-ratio method has been heavily used in the construction industry to evaluate site effects of the subsurface for building foundations.

SI is a method that can generate new seismic responses from the existing seismic records. Currently, the most commonly used application of SI relates to retrieval and utilization of surface waves [e.g. 10, 12]. This approach most often uses ambient noise. For example, Gerstoft *et al.* [13] demonstrated how to extract the surface waves (Rayleigh waves) from ambient noise and invert them to estimate group velocities. On the other hand, however, the number of SI works that involve body waves is much less than the ones by the surface-wave SI. This is because, even though the first application with body waves was proven in 1968 [8], good understanding and robust field examples were missing. However, after Wapenaar [14] proved that SI can be used for an arbitrary inhomogeneous (acoustic or elastic) medium, practical applications [e.g. 15–20] including further theoretical developments [e.g. 11, 21] have followed. In particular, because SI with body waves (passive reflection method) can provide structural imaging of the medium without actual shootings [e.g. 22], this method is now drawing attention as a cost-effective reflection method to save the upfront costs in the industry for renewable energy.

Although surface-wave SI seems to be richer in connection to data availability, the reflection approach by body-wave SI has the potential to provide higher structural resolution when we have the same frequency bandwidth. Because of this, in this thesis we investigate body-wave SI for the retrieval of reflections. Furthermore, we are more interested in the reflection structures (impedance contrasts) than in the velocity pertur-

bations.

### 1.3. COST-EFFECTIVE EXPLORATIONS FOR HYDROCARBONS AND RENEWABLES

In the oil and gas industry, decisions for seismic surveys are very important financial steps. Because of that, the decisions are mainly subject to their commercial justifications. More specifically, in frontier regions where the existing seismic data are insufficient, such decisions will be a highly sensitive matter due to higher technical (discovery) risks. On top of these financial and technical aspects, environmental and societal aspects are also important practical concerns that need to be addressed with sincerity.

The environmental concerns are extremely delicate subjects in the industry of renewable energy, such as deep geothermal energy including enhanced geothermal systems (EGS) (hot dry rock). The deep geothermal energy is one of the most notable energy concepts in the renewables (Figure 1.2). The International Energy Agency (IEA) foresees that the share in global electricity generation supplied by all geothermal plays will reach at least 3.5 % in 2050. The deep geothermal energy obtained from EGS will be then dominant with a share of 50 % of the total amount of all the geothermal plays (Figure 1.3).

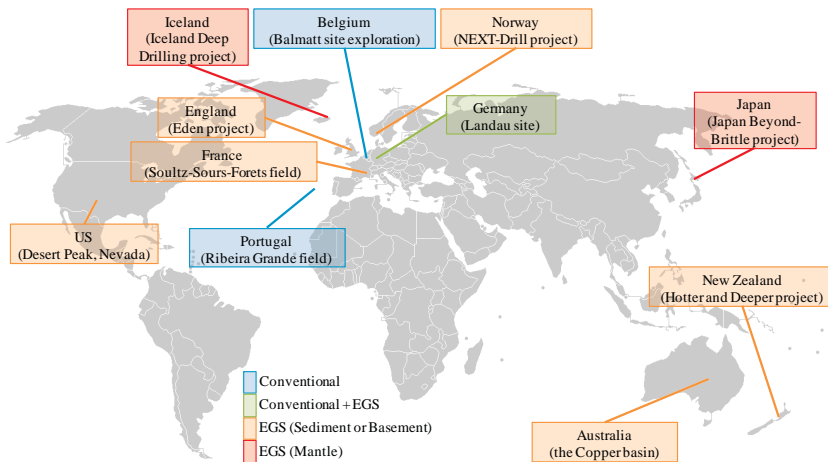


Figure 1.2: World map with indicated examples of deep geothermal industry and research projects including enhanced geothermal systems.

To sum up, although the conventional seismic surveys using active sources (e.g. dynamite) are still the most powerful and useful tool, their practical execution is not always desirable or even (financially) possible. This tendency might be even stronger for surveys in frontier regions or in the renewable-energy domain.

Following the above arguments, it is logical to tackle a business strategy by including the passive seismic methods due to their financial, environmental, and social aspects. However, the passive seismic methods themselves are inherently limited in terms of the



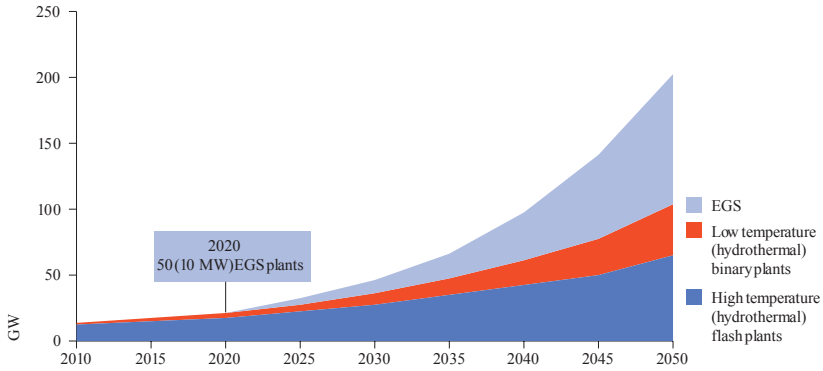


Figure 1.3: Predicted growth of geothermal power capacities by technology type according to the International Energy Agency. EGS stands for enhanced geothermal system (one type of deep geothermal energy). The vertical and horizontal axes indicate gigawatt electricity and year, respectively. The commercial justification of EGS is expected in 2030.

obtainable resolution due to the lack of control over the sources. The methods could be practically utilized if they would provide information at least about the major features (e.g. major heterogeneities, major faults, major structural horizons) as a first-screening tool, for example. Table 1.1 shows a comparison of several exploration methods for the deep geothermal energy in terms of their advantages and disadvantages. Note that from the passive seismic methods, only the passive reflection method is included as it is one of the main topics of this thesis.

## 1.4. OBJECTIVES AND THESIS OUTLINE

The main objective of this thesis is to investigate the potential usage of several passive seismic methods that make use of body waves, and more specifically the passive reflection method, as cost-effective applications for multiscale subsurface imaging and characterization. The passive methods and applications in the following three chapters are categorized by the target scale – from the basin to the lithosphere (Figure 1.4).

In Chapter 2, we look at basin-scale investigations. In the first subchapter, we apply the H/V spectral-ratio method to delineate a part of the Neuquén basin in Argentina. This method is applied exclusively to global phases of earthquakes. In the subsequent subchapter, we apply the Sp-wave method to image subsurface heterogeneity for exploration and production acreage in Japan. This is the application for a basin-scale target. With this method, we also derive the frequency-dependent quality factor  $Q_S/Q_P$  and use it as a proxy method of characterizing physical properties of the subsurface structures.

In Chapter 3, we look at crustal-scale investigations. We apply SI using P-wave coda of local earthquakes in order to obtain the pseudo reflection image of the subsurface structures. This method is applied for structures beneath the Neuquén basin whose depth is independently investigated in Chapter 2. This application shows the potential of the passive seismic method as a prescreening exploration tool for, e.g., deep geother-

Table 1.1: Comparison of several exploration methods used for deep geothermal energy

Method	Pros	Cons
✓ Active seismic reflection (Airgun, Dynamite)	<ul style="list-style-type: none"> <li>✓ Could provide high resolution</li> <li>✓ Control over the sources</li> <li>✓ Structural imaging</li> </ul>	<ul style="list-style-type: none"> <li>✓ Relatively high cost</li> <li>✓ Not environmentally and socially friendly</li> <li>✓ Lack of lower frequencies needed for deeper imaging</li> </ul>
✓ Magnetotelluric	<ul style="list-style-type: none"> <li>✓ Low cost</li> <li>✓ Indicator of the heat flow</li> <li>✓ Environmentally and socially friendly</li> </ul>	<ul style="list-style-type: none"> <li>✓ Low resolution</li> </ul>
✓ Gravity	<ul style="list-style-type: none"> <li>✓ Low cost</li> <li>✓ Environmentally and socially friendly</li> </ul>	<ul style="list-style-type: none"> <li>✓ Low resolution</li> </ul>
✓ Subsurface temperature	<ul style="list-style-type: none"> <li>✓ Indicator for the heat flow</li> </ul>	<ul style="list-style-type: none"> <li>✓ Depending on the place of existing wells</li> <li>✓ Extrapolation and interpolation needed</li> <li>✓ Higher uncertainty for sections deeper than the existing wells</li> </ul>
✓ Passive seismic reflection (Earthquake, Noise)	<ul style="list-style-type: none"> <li>✓ Low cost</li> <li>✓ Structural imaging</li> <li>✓ Lower frequencies, needed for deeper imaging</li> <li>✓ Environmentally and socially friendly</li> </ul>	<ul style="list-style-type: none"> <li>✓ Could provide only low resolution</li> <li>✓ Further R&amp;D is needed</li> </ul>

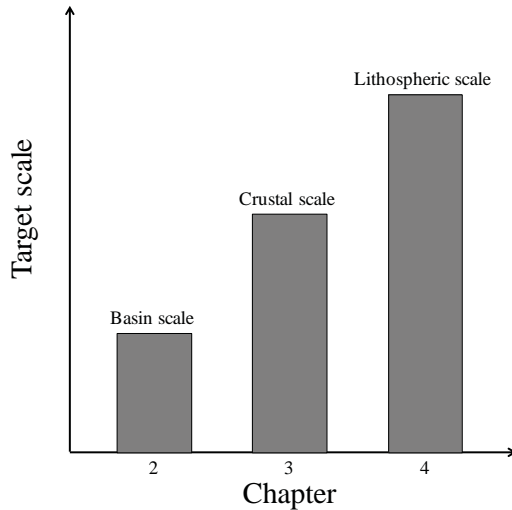


Figure 1.4: Schematic diagram of the various scales of the targets considered in this thesis.

mal reservoirs.

In Chapter 4, we look at lithospheric-scale investigations. In the first subchapter, we apply SI using global phases of earthquakes to image structures around the Moho and the Nazca aseismic zones beneath the Neuquén basin. Our results show the reflection images delineating the aseismic zone and a deformed part of the Nazca slab. In the subsequent subchapter, we estimate the radiation efficiency of the intermediate-depth earthquakes in Japan to understand the difference in the physical property of the oceanic slab at shallow and deeper depths (thus the source-mechanism difference between seismic and aseismic zones). This investigation exclusively estimates the source parameters of the intermediate-depth earthquakes. In the last subchapter, we apply SI using deep moonquakes to obtain a lithospheric image of the Moon. This application shows a reflection image of the structures around the lunar Moho.

In Chapter 5, we give general conclusions.

Note that in Chapters 2 to 4, some information may overlap, as the material in these chapters was independently published as peer-reviewed journal articles.

## REFERENCES

- [1] A. Mohorovičić, *Epcenters of earthquakes in Croatia and Slavonia (Epicentra potresa u Hrvatskoj i Slavoniji)*, in *Yearly report of the Zagreb meteorological observatory for the year 1909* (1910).
- [2] K. Aki and W. H. K. Lee, *Determination of three-dimensional velocity anomalies under a seismic array using first P arrival times from local earthquakes: 1. A homogeneous initial model*, *Journal of Geophysical Research* **81** (1976).
- [3] A. M. Dziewonski, B. H. Hager, and R. J. O'Connell, *Large-scale heterogeneities in the lower mantle*, *Journal of Geophysical Research* **82** (1977), [10.1029/JB082i002p00239](https://doi.org/10.1029/JB082i002p00239).
- [4] C. A. Langston, *Structure under Mount Rainier, Washington, inferred from teleseismic body waves*, *Journal of Geophysical Research: Solid Earth* **84** (1979), [10.1029/JB084iB09p04749](https://doi.org/10.1029/JB084iB09p04749).
- [5] Y. Nakamura, *A method for dynamic characteristics estimation of subsurface using microtremor on the ground surface*, in *Quarterly Report of RTRI* (1989).
- [6] I. Doi and H. Kawakata, *High resolution spatial distribution of the velocity discontinuities in and around the swarm region beneath the Wakayama district, southwest Japan*, *Bulletin of the Seismological Society of America* **103** (2013), [10.1785/0120120316](https://doi.org/10.1785/0120120316).
- [7] K. Aki, *Space and time spectra of stationary stochastic waves, with special reference to microtremors*, *Bulletin of the Earthquake Research Institute* **35** (1957).
- [8] J. F. Claerbout, *Synthesis of a layered medium from its acoustic transmission response*, *Geophysics* **33** (1968), [10.1190/1.1439927](https://doi.org/10.1190/1.1439927).

- [9] K. Wapenaar, *Synthesis of an inhomogeneous medium from its acoustic transmission response*, *Geophysics* **68** (2003), [10.1190/1.1620649](https://doi.org/10.1190/1.1620649).
- [10] N. M. Shapiro and M. Campillo, *Emergence of broadband Rayleigh waves from correlations of the ambient seismic noise*, *Geophysical Research Letters* **31** (2004), [10.1029/2004GL019491](https://doi.org/10.1029/2004GL019491).
- [11] R. Snieder and E. Şafak, *Extracting the Building Response Using Seismic Interferometry: Theory and Application to the Millikan Library in Pasadena, California*, *Bulletin of the Seismological Society of America* **96** (2006), [10.1785/0120050109](https://doi.org/10.1785/0120050109).
- [12] D. Halliday and A. Curtis, *Seismic interferometry, surface waves and source distribution*, *Geophysical Journal International* **175** (2008), [10.1111/j.1365-246X.2008.03918.x](https://doi.org/10.1111/j.1365-246X.2008.03918.x).
- [13] P. Gerstoft, K. G. Sabra, P. Roux, W. A. Kuperman, and M. C. Fehler, *Green's functions extraction and surface-wave tomography from microseisms in southern California*, *Geophysics* **71** (2006), [10.1190/1.2210607](https://doi.org/10.1190/1.2210607).
- [14] K. Wapenaar, *Retrieving the elastodynamic Green's function of an arbitrary inhomogeneous medium by cross correlation*, *Physical Review Letters* **93** (2004), [10.1103/PhysRevLett.93.254301](https://doi.org/10.1103/PhysRevLett.93.254301).
- [15] P. Roux, K. G. Sabra, P. Gerstoft, and W. A. Kuperman, *P-waves from cross-correlation of seismic noise*, *Geophysical Research Letters* **32** (2005), [10.1029/2005GL023803](https://doi.org/10.1029/2005GL023803).
- [16] D. Draganov, K. Wapenaar, and J. Thorbecke, *Seismic interferometry: Reconstructing the earth's reflection response*, *Geophysics* **71** (2006), [10.1190/1.2209947](https://doi.org/10.1190/1.2209947).
- [17] D. Draganov, X. Campman, J. Thorbecke, A. Verdel, and K. Wapenaar, *Reflection images from ambient seismic noise*, *Geophysics* **74** (2009), [10.1190/1.3193529](https://doi.org/10.1190/1.3193529).
- [18] N. Nakata, R. Snieder, T. Tsuji, K. Larner, and T. Matsuoka, *Shear wave imaging from traffic noise using seismic interferometry by cross-coherence*, *Geophysics* **76** (2011), [10.1190/geo2010-0188.1](https://doi.org/10.1190/geo2010-0188.1).
- [19] Z. Xu, C. Juhlin, O. Gudmundsson, F. Zhang, C. Yang, A. Kashubin, and L. Stefan, *Reconstruction of subsurface structure from ambient seismic noise: An example from Ketzin, Germany*, *Geophysical Journal International* **189** (2012), [10.1111/j.1365-246X.2012.05411.x](https://doi.org/10.1111/j.1365-246X.2012.05411.x).
- [20] Z. Zhan, S. Ni, D. V. Helmberger, and R. W. Clayton, *Retrieval of Moho-reflected shear wave arrivals from ambient seismic noise*, *Geophysical Journal International* **182** (2010), [10.1111/j.1365-246X.2010.04625.x](https://doi.org/10.1111/j.1365-246X.2010.04625.x).
- [21] K. Wapenaar, J. van der Neut, E. Ruigrok, D. Draganov, J. Hunziker, E. Slob, J. Thorbecke, and R. Snieder, *Seismic interferometry by cross-correlation and by multidimensional deconvolution: A systematic comparison*, *Geophysical Journal International* **185** (2011), [10.1111/j.1365-246X.2011.05007.x](https://doi.org/10.1111/j.1365-246X.2011.05007.x).

- [22] D. Draganov, K. Wapenaar, W. Mulder, J. Singer, and A. Verdel, *Retrieval of reflections from seismic background-noise measurements*, [Geophysical Research Letters](#) **34** (2007), [10.1029/2006GL028735](#).

# 2

## BASIN-SCALE SEISMIC IMAGING AND CHARACTERIZATION

**Yohei NISHITSUJI, Elmer RUIGROK, Martín GOMEZ,  
Issei DOI, Deyan DRAGANOV**

*People understand me so poorly that  
they don't even understand my complaint about them not understanding me.*

Søren Kierkegaard

### **Summary**

*In the first subchapter, we propose to use phases from distant earthquakes, such as SKS, SKKS, SKKKS, PKP, and PKPPcP, for the H/V spectral ratio method to identify the fundamental resonance frequencies of receiver-side structure. We demonstrate this method using data recorded in the Malargüe region, Mendoza, Argentina. We show that the method is largely sensitive to the mix of phases that is used as an input. Both with time windows with merely P-wave phases (and converted energy on the horizontal component) and with time windows with mixed phases, the same resonance frequencies are found. However, the H/V spectral ratio has to be stacked over many (>10) earthquakes to suppress source-side resonances and phase cross terms. From the extracted fundamental resonance frequencies, we delineate the bottom of part of the Malargüe basin. Comparison with an active-source*

---

The first subchapter has been published in Seismological Research Letters **85**, 5 (2014) [1].

The second subchapter has been published in Geophysics **79**, 6 (2014) [2].

Parts of the appendix has been presented at 82nd SEG Annual Meeting (2012) [3].

Note that minor changes have been introduced to make the text consistent with the other chapters of this thesis.

*seismic profile, recorded in the past close to our study region, and with the Bouguer gravity anomaly of the region, shows a very good agreement with the delineated structure. This suggests reliable applicability of our method.*

## 2

*In the second subchapter, we present a method to estimate seismic heterogeneity on the basin scale with  $S_p$ -waves and frequency-dependent quality-factor analysis using local earthquakes. We image horizontal velocity discontinuities using  $S_p$ -waves originating in the southeast of Hokkaido, Japan. Our interpretation is supported by results of an active source survey carried out nearby. We combine the results of the  $S_p$ -waves with results for a distribution of the  $Q_S/Q_P$  ratio below the same area. This allows us to identify a zone in the south, characterized by a relatively constant  $Q_S/Q_P$  ratio and clearer velocity discontinuities; we also identify a zone in the north, characterized by a relatively larger variation in the  $Q_S/Q_P$  ratio (with several high values) and less clear velocity discontinuities. The latter might be interpreted as a fractured zone, for example. Although it fully relies on the positions of the earthquakes, receivers, and the area of interest, the proposed method could be used as a first screening tool to investigate frontier exploration areas in which limited previous active-source seismic data are available. The regions in which natural earthquakes occur could have favourable conditions to apply the method we present here.*

## 2.1. GLOBAL-PHASE H/V SPECTRAL RATIO

### 2.1.1. INTRODUCTION

Structural estimation of unconsolidated sediments and basins is of fundamental importance for resources exploration, geohazard assessments, and other geophysical aspects. The estimation contributes not only to the understanding of the tectonic settings, but also to the choice of parameters for possible further seismic processing, for example, predictive deconvolution, the result of which could be used for imaging the subsurface structures below the basin.

Within a number of conventional passive-seismic methodologies, the Nakamura technique [4], initially proposed for the purpose of eliminating the effect of Rayleigh waves from noise records, is widely applied. This technique can be used to estimate the resonance frequencies of the subsurface of a region of interest by taking the amplitude spectral ratio between the horizontal and vertical components (H/V) of ambient-noise records. In addition to the investigation of local site effects, if the velocity model is known, this resonance frequency can also be interpreted as the thickness of the geophysical and/or geologic layer, characterized by relatively high-impedance contrasts on either side [5]. The top boundary of this layer is often the Earth's surface, whereas the lower boundary could be the interface between basement and basin. The H/V spectral ratio has been applied to estimate the depth of sedimentary boundaries and basins [e.g. 6–10].

The H/V spectral ratio has been widely applied with ambient noise [e.g. 11–13], as well as with arrivals from earthquake records [e.g. 10, 12–15], because of its stability and its relatively simple application procedure. Lermo and Chávez-García [13] and Field and Jacob [12], for example, have applied the H/V spectral ratio to S waves from local-earthquake records and the resonant frequencies have been successfully identified. With P waves from local earthquakes, Ni *et al.* [16] lately succeeded in estimating the shear-wave velocity. In a recent work, Ruigrok *et al.* [10] extended the epicentral distance of earthquakes using a single teleseismic earthquake, and several resonance frequencies were clearly identified. Ferretti *et al.* [14] used a wide range of epicentral distances from 41° to 185° by selecting 18 earthquakes. To this date, studies have not applied the H/V spectral ratio exclusively to recordings of global phases. Global phases are the arrivals from distant earthquakes (epicentral distance  $\geq 120^\circ$ ) that traverse the core before reaching the receivers; their ray parameters are smaller than 0.04 s/km for P-wave phases. The amplitude spectra derived from the H/V spectral ratio are commonly interpreted as the resonance spectra for vertically propagating body waves [e.g. 12]. Global phases have a near vertical incidence. Hence, the resonance spectra derived from global phases could straightforwardly be interpreted.

In the following, we apply the global phase H/V spectral ratio, which hereafter is abbreviated as GloPHV, to data recorded by the Malargüe seismic array (MalARRgüe; [17]) in the Malargüe region, Mendoza, Argentina, to delineate a part of the local structure of the Malargüe basin.



### 2.1.2. MALARRGUE

MalARRgue recorded continuous seismic waveforms from January 2012 to January 2013. It was located between longitudes 68.25°W and 70.50°W and latitudes 34.75°S and 35.50°S, about 250 km east of the Maule Region in Chile (Figure 2.1), infamous because of the Maule earthquake (27 February 2010  $M_W$  8.8). The array contained two areal subarrays: PV-array (black squares in Figure 2.1), situated on the eastern flank of the Peteroa Volcano; and T-array, situated on a high plateau east of the Andes. The T-array itself was composed of two linear subarrays: the TN-array (white triangles in Figure 2.1) had 19 stations labeled TN02 to TN20 deployed every 2 km in the south-southeast–north-northwest direction with TN02 the southernmost station. The TE-array (black triangles in Figure 2.1) had 13 stations labeled TE01 to TE13 deployed at about 4 km spacing in the west-southwest–east-northeast direction with TE01 the westernmost station. All stations recorded three orthogonal components of particle velocity (vertical, north, and east). MalARRgue used mainly 2 Hz sensors (Sercel L-22) borrowed from the Incorporated Research Institutions for Seismology–Program for Array Seismic Studies of the Continental Lithosphere (IRIS-PASSCAL). In the current study, we use the data from the T-array.

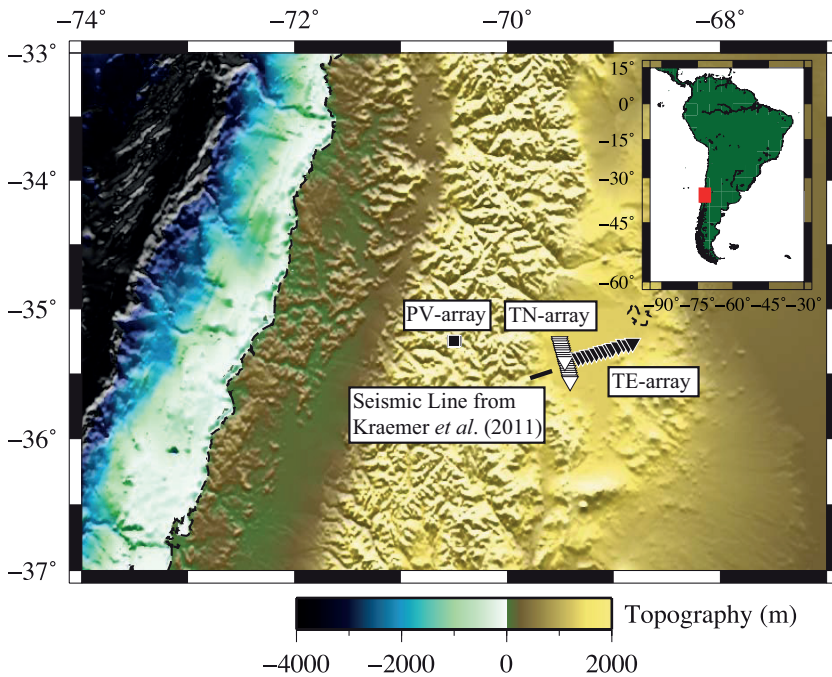


Figure 2.1: Topography map of the study region. The topography data is adapted from Becker *et al.* [18]. The white and black triangles depict the locations of the seismic stations of the TN and TE-subarrays of the Malargüe seismic array. The black squares show the location of the PV-array stations. The black line indicates the location at which an active-source seismic section is obtained in Kraemer *et al.* [19]

The two lines of the T-array recorded arrivals with a wide range of epicentral distances starting from local and regional seismicity (because of their proximity to the Nazca subduction zone) and going to teleseismic and global phases (related to their alignment with large transects of the Ring of Fire). The illumination characteristics of the linear subarrays for structural imaging, but also other details about MalARRgue, can be found in Ruigrok *et al.* [17], for example, Figure 3 in their article.

Strollo *et al.* [20] previously evaluated the suitability of a 2 Hz (L-22), 1 Hz, and other short-period sensors for the H/V spectral ratio using ambient-noise records as input data. The authors concluded that the 2 Hz and 1 Hz sensors could be used at least down to 0.3 and 0.2 Hz, respectively. The reliability lower than these frequencies would depend on the magnitude (amplitude) level of the input data. MalARRgue also contained one 0.033 Hz (Güralp 40T) reference sensor, named TN99, which was collocated with station TN11, which had a 2 Hz (L-22) sensor. Comparing GloPHV from earthquakes with  $M_W \geq 5.5$ , which show clearly higher amplitudes than the ambient noise, calculated for TN11 and TN99 (Figure 2.2), we see that the ratios are similar in shape, but not in amplitude down to 1 Hz. The peaks and troughs remain at the same frequencies down to around 0.2 Hz. For values lower than that frequency, the tendencies of the ratios start to differ, see, for example, the black arrows in Figure 2.2. Therefore, we limit our analysis to frequencies down to 0.15 Hz, with the notion that only the very large features may be interpreted at the lower end of this band.

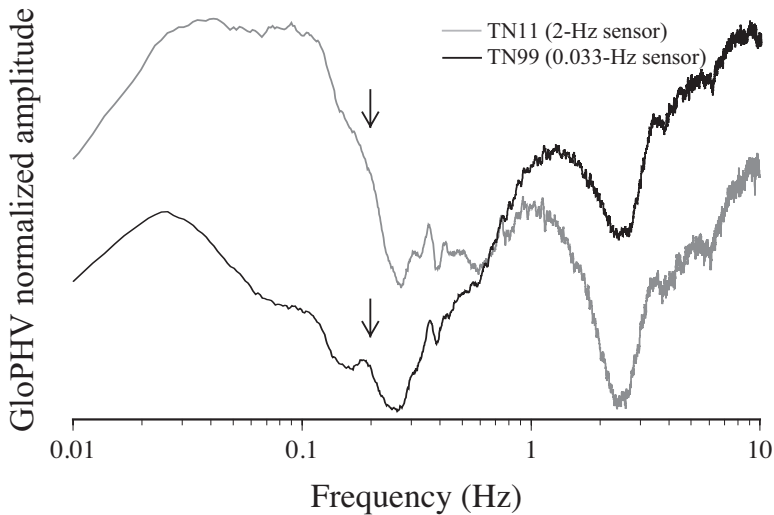


Figure 2.2: Comparison of GloPHV between the TN11 station (with a 2 Hz sensor) and the TN99 (with a 0.033 Hz sensor) reference station. The black arrows indicate the frequency of 0.2 Hz, below which the two ratios start exhibiting differing trends.

Because we are targeting to delineate the Malargüe basin using the fundamental resonance frequency, we limit our band for interpretations to a maximum frequency of 2.5 Hz.

## 2

### 2.1.3. MALARGÜE BASIN

The Malargüe basin is Permo-Triassic age and is quasisedimentary. It is a subbasin in the Neuquén basin [e.g. 21]. It has been producing about 44 % of the Argentinian oil and has a promising potential of unconventional resources (e.g. shale gas). It is located in the eastern part of the Andes, between 35°S and 37°S latitude, forming an elongated structure in the north–south direction at the eastern side of the Malargüe anticline. Witte and Periale [21] reported that the Neuquén basin is thinning to the east. Because of this, the Malargüe basin is likely to be thinning toward the east. Kraemer *et al.* [19] studied the geometry and evolution of the Andean fold and thrust belt in the location situated to the southwest from MalARRgüe. Their results show that the depth of the depocenter and the western part of the Malargüe basin, widely being covered by more than 2 km of Tertiary sediments, would be around 5.5 to 6.0 km from the acquisition (Earth) surface. Their imaged seismic section, obtained from recordings from active sources (location shown in Figure 2.1 with the black line), with the stratigraphic interpretations in their article shows that the basin becomes shallower toward the east, that is, toward the location of the T-array from MalARRgüe. Because the active seismic section does not pass through our study region, the depth of the Malargüe basin under the T-array is not known.

### 2.1.4. GLOBAL PHASES

For the purpose of obtaining GloPHV, we extract from the recordings windows with length of 600 s, starting 5 s before the first P-wave phase (PKiKP) or S-wave phase arrival, from earthquakes with epicentral distances larger than 120° (see Figure 2.3). In the following, we refer to the aforementioned window as the P window or S window, respectively. We extract these windows using Java version of Windows Extracted from Event Data (JWEED) from IRIS. Based on the earthquake catalog from the U.S. Geological Survey (USGS; last accessed December 2013), we select 69 global earthquakes for the TN-array (shown as circles in Figure 2.3) and 79 global earthquakes for the TE-array (shown as stars in Figure 2.3) with  $M_W \geq 5.5$ . A complete listing of the used earthquakes is given in Table 2.1.4. Because of the 600 s window duration, the recordings from each earthquake will contain several global phases and a few teleseismic phases, such as PPP. The time window for each of the earthquakes is individually determined using a function of JWEED and a ray-tracing model [22] based on iasp91 [23]. The P window is dominated by P-wave phases, such as PKP, PKiKP, and PKIKP. Similarly, the S window is dominated by S-wave phases, such as SKS, SKKS, and SKKKS, but also has a few P-wave phase arrivals, such as PKPPcP and PPP. The predominant ray parameters, often called horizontal slowness as well, for the P-wave phases and the S-wave phases would be smaller than 0.04 and 0.076 s/km, respectively.

Table 2.1: Global-phase seismic used in this study

Date (month/d/yr)	Time (hr:min:s)	Lat. (°N)	Lon. (°E)	Dep. (km)	$M_W$	ArrayID
----------------------	--------------------	--------------	--------------	--------------	-------	---------

01/18/12	12:50:21	-0.877	126.829	19.1	5.7	TE
02/04/12	13:09:23	11.872	125.754	12.0	5.8	TN/TE
02/06/12	03:49:13	9.999	123.206	11.0	6.7	TE
02/06/12	04:20:00	10.092	123.227	10.0	5.6	TE
02/06/12	10:10:20	9.885	123.095	9.0	6.0	TN/TE
02/06/12	11:33:37	9.821	123.080	15.0	5.9	TN/TE
02/14/12	06:22:01	36.214	141.386	28.0	5.8	TN/TE
02/26/12	02:46:21	-24.477	-177.500	10.0	5.5	TE
02/26/12	06:17:20	51.708	95.991	12.0	6.6	TN/TE
02/29/12	14:32:48	35.200	141.001	26.2	5.7	TE
03/08/12	22:50:08	39.383	81.307	38.0	5.9	TE
03/12/12	06:06:41	36.741	73.152	11.0	5.7	TN/TE
03/12/12	12:32:46	45.239	147.609	110.4	5.6	TE
03/14/12	09:08:35	40.887	144.944	12.0	6.9	TN/TE
03/14/12	10:49:25	40.781	144.761	10.0	6.1	TN/TE
03/14/12	12:05:05	35.687	140.695	10.0	6.0	TN/TE
03/16/12	07:58:02	10.037	125.633	18.0	5.8	TN/TE
03/22/12	00:21:37	3.513	125.859	116.9	5.6	TE
03/27/12	11:00:45	39.859	142.017	15.0	6.0	TN/TE
04/01/12	14:04:25	37.116	140.957	48.0	5.7	TN/TE
04/11/12	08:38:37	2.327	93.063	20.0	8.6	TN/TE
04/11/12	10:43:11	0.802	92.463	25.1	8.2	TN/TE
04/13/12	10:10:01	36.988	141.152	11.0	5.7	TN/TE
04/14/12	15:13:14	49.380	155.651	90.3	5.6	TE
04/15/12	05:57:40	2.581	90.269	25.0	6.3	TN
04/20/12	22:19:47	3.256	93.853	24.6	5.8	TE
04/20/12	22:28:59	3.269	93.821	21.9	5.9	TN/TE
04/20/12	23:14:31	2.158	93.360	28.0	5.9	TN/TE
04/21/12	01:16:53	-1.617	134.276	16.0	6.7	TN/TE
04/23/12	21:21:45	0.374	125.293	48.0	5.7	TE
04/23/12	22:40:22	48.397	154.739	31.0	5.7	TN/TE
04/24/12	14:57:10	8.868	93.949	14.1	5.6	TN/TE
04/25/12	07:42:23	9.011	93.945	9.0	5.9	TN/TE
04/29/12	08:09:04	2.704	94.509	14.1	5.8	TN/TE
04/29/12	10:28:52	35.596	140.349	44.0	5.8	TN/TE
05/12/12	23:28:44	38.612	70.354	10.0	5.7	TN/TE
05/23/12	15:02:25	41.335	142.082	46.0	6.0	TN/TE
06/05/12	19:31:34	34.943	141.132	15.0	6.1	TN/TE
06/09/12	14:23:20	48.851	154.852	48.6	5.5	TE
06/09/12	21:00:18	24.572	122.248	70.0	5.9	TN/TE
06/11/12	05:29:12	36.023	69.351	16.0	5.7	TE
06/14/12	20:17:25	1.293	126.828	61.4	5.5	TE
06/15/12	01:14:08	5.719	126.354	41.4	5.7	TN/TE
06/16/12	22:18:47	15.593	119.563	28.0	5.9	TN/TE
06/17/12	20:32:21	38.919	141.831	36.0	6.3	TN/TE
06/23/12	04:34:53	3.009	97.896	95.0	6.1	TN/TE
06/29/12	21:07:34	43.433	84.700	18.0	6.3	TN/TE
07/08/12	11:33:03	45.497	151.288	20.0	6.0	TE
07/11/12	02:31:17	45.401	151.424	10.0	5.7	TN/TE
07/12/12	12:51:59	45.452	151.665	12.0	5.7	TE
07/12/12	14:00:34	36.527	70.906	198.0	5.8	TN/TE
07/19/12	07:36:35	37.248	71.375	98.4	5.6	TN/TE
07/20/12	03:40:12	49.506	155.599	14.8	5.5	TE
07/20/12	06:10:25	49.407	155.907	19.0	6.0	TN/TE
07/20/12	06:32:56	49.354	156.132	10.0	5.9	TN
07/25/12	00:27:45	2.707	96.045	22.0	6.4	TN
08/11/12	12:34:36	38.389	46.745	12.0	6.3	TE
08/12/12	10:47:06	35.661	82.518	13.0	6.2	TN/TE
08/14/12	02:59:38	49.800	145.064	583.2	7.7	TN/TE
08/18/12	09:41:52	-1.315	120.096	10.0	6.3	TN/TE
08/18/12	15:31:40	2.645	128.697	10.0	5.8	TE
08/25/12	14:16:17	42.419	142.913	54.5	5.9	TN/TE
08/26/12	15:05:37	2.190	126.837	91.1	6.6	TN/TE
08/29/12	19:05:11	38.425	141.814	47.4	5.5	TN/TE
08/31/12	12:47:33	10.811	126.638	28.0	7.6	TN/TE
08/31/12	23:37:58	10.388	126.719	40.3	5.6	TN/TE
09/03/12	06:49:50	6.610	123.875	12.0	5.9	TN/TE
09/03/12	18:23:05	-10.708	113.931	14.0	6.3	TN
09/03/12	19:44:22	7.905	125.044	10.0	5.7	TN
09/08/12	06:54:19	21.527	145.923	5.0	5.6	TE
09/08/12	10:51:44	-3.177	135.109	21.0	6.1	TN
09/09/12	05:39:37	49.247	155.750	31.0	5.9	TE
09/11/12	01:28:19	45.335	151.111	14.0	5.5	TN/TE
09/11/12	16:36:50	11.838	143.218	8.0	5.9	TE
09/14/12	04:51:47	-3.319	100.594	19.0	6.3	TN
10/01/12	22:21:46	39.808	143.099	15.0	6.0	TN
10/08/12	11:43:31	-4.472	129.129	10.0	6.2	TN
10/12/12	00:31:28	-4.892	134.030	13.0	6.6	TN
10/14/12	09:41:59	48.308	154.428	35.0	5.8	TN
10/16/12	12:41:26	49.618	156.438	81.0	5.6	TN
10/17/12	04:42:30	4.232	124.520	326.0	6.0	TN
11/01/12	23:37:18	1.229	122.105	35.0	5.5	TE
11/02/12	18:17:33	9.219	126.161	37.0	6.1	TN/TE
11/05/12	04:30:27	37.791	143.610	19.1	5.6	TN/TE
11/06/12	01:42:26	1.357	122.167	35.0	5.6	TE
11/11/12	01:12:39	23.005	95.885	13.7	6.8	TN/TE
11/14/12	05:21:42	9.982	122.472	40.9	5.7	TN/TE
11/16/12	18:12:40	49.280	155.425	29.0	6.5	TN/TE
11/27/12	02:59:07	-2.952	129.219	11.2	5.7	TE

12/07/12	08:18:23	37.890	143.949	31.0	7.3	TN/TE
12/09/12	21:45:35	6.703	126.166	63.2	5.5	TN/TE
12/10/12	16:53:09	-6.533	129.825	155.0	7.1	TN
12/11/12	06:18:27	0.533	126.231	30.0	6.0	TN
12/17/12	09:16:31	-0.649	123.807	44.2	6.1	TN/TE

We visually inspect the chosen windows to make sure that they contain global phases only from a single earthquake. Recordings with high pre-event noise levels, due to the microseism, anthropogenic noise, but also due to regional and/or local seismicity, were not used (Figure 2.3 shows only the earthquakes that were actually used).

### 2.1.5. GLOBAL-PHASE H/V SPECTRAL RATIO

We assume the global phases are nearly vertically incident at the receivers and have no predominant resonance frequency within our frequency band of interest, prior to interaction with the crust below the receivers. Moreover, we assume that the illuminating wavefront contains only P-wave phases for the P window. In this case, the observed amplitude spectra for vertical and horizontal components can be written as [e.g. 10, 12]

$$|\hat{O}^V(\mathbf{X}_R)| = |\hat{E}\hat{G}^P(\mathbf{X}_B, \mathbf{x}_S)\hat{L}^P(\mathbf{X}_R, \mathbf{x}_B)\hat{I}(\mathbf{X}_R)| \quad (2.1)$$

and

$$|\hat{O}^H(\mathbf{X}_R)| = |\hat{E}\hat{G}^P(\mathbf{X}_B, \mathbf{x}_S)\hat{L}^S(\mathbf{X}_R, \mathbf{x}_B)\hat{I}(\mathbf{X}_R)|, \quad (2.2)$$

in which  $\hat{O}$  is the observed amplitude spectrum;  $\hat{E}$  is the spectrum of the source function of the global phases;  $\hat{G}(\mathbf{X}_B, \mathbf{x}_S)$  is the Green's function (path effect) between the source  $\mathbf{x}_S$  and the top of the basement  $\mathbf{X}_B$ ;  $\hat{L}(\mathbf{X}_R, \mathbf{x}_B)$  is the local site effect between the top of the basement and the receiver  $\mathbf{X}_R$ . The expression  $\hat{I}(\mathbf{X}_R)$  is the instrument response; the hats indicate that the quantities are in the frequency domain; superscripts  $V$  and  $H$  denote the vertical and the horizontal component, respectively; and superscripts  $P$  and  $S$  denote P and S waves, respectively. The time window does not contain S-wave phases. Hence, we assume that the horizontal-component recording (equation 2.2) contains primarily P-to-S converted waves. Because we select to use data from earthquakes with large epicentral distances ( $\geq 120^\circ$ ), the wave front at the stations is practically planar. For most distances, the corresponding ray parameters are still sufficiently large for converted waves to occur. GloPHV is obtained by the spectral division from equations 2.1 and 2.2:

$$GloPHV = |\hat{O}^H(\mathbf{X}_R)| / |\hat{O}^V(\mathbf{X}_R)| \approx |\hat{L}^S(\mathbf{X}_R, \mathbf{x}_B)| / |\hat{L}^P(\mathbf{X}_R, \mathbf{x}_B)|. \quad (2.3)$$

On the other hand, for the S window, we assume that the observed amplitude spectra for vertical and horizontal components are dominant by P-wave phases (e.g. PPP) and S-wave phases (e.g. SKS), respectively. Then, the observed amplitude spectra for vertical and horizontal components can be written as

$$|\hat{O}^V(\mathbf{X}_R)| = |\hat{E}\hat{G}^P(\mathbf{X}_B, \mathbf{x}_S)\hat{L}^P(\mathbf{X}_R, \mathbf{x}_B)\hat{I}(\mathbf{X}_R)| \quad (2.4)$$

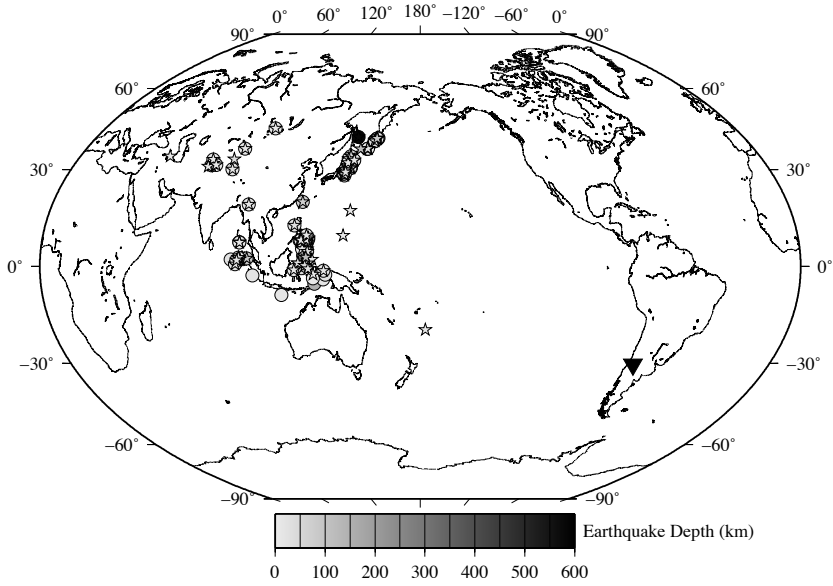


Figure 2.3: Distribution map of the global earthquakes (epicentral distance  $\geq 120^\circ$ ) with  $M_W \geq 5.5$  used in our study. The 69 circles and 79 stars show the location of the earthquakes used for the TN- and TE-array, respectively, gray scaled as a function of their focal depth. The location of the Malargüe seismic array is indicated by the black triangle.

and

$$|\hat{O}^H(\mathbf{X}_R)| = |\hat{E}\hat{G}^S(\mathbf{X}_B, \mathbf{x}_S)\hat{L}^S(\mathbf{X}_R, \mathbf{x}_B)\hat{I}(\mathbf{X}_R)|. \quad (2.5)$$

Clearly, the paths effects for P-wave phases are very different from S-wave phases and hence  $G^P \neq G^S$ . However, possible resonance frequencies in  $|\hat{G}^P|$  and  $|\hat{G}^S|$ , such as the one from the D-double-prime layer, should result in much lower frequency than our band of interest (0.15–2.5 Hz). Hence, we assume that, in the frequency band of interest,  $|\hat{G}^P| = a|\hat{G}^S|$ , in which  $a$  is a frequency independent scaling factor. Dividing equation 2.5 by equation 2.4, using the above assumption and assuming that for a distant earthquake  $\hat{E}$  is the same for the P- and S-wave phases (or they are related by a frequency independent scaling factor), we find a scaled version of equation 2.3. Besides resonances from the crustal layers below the receivers, computing equation 2.3 for a single earthquake might result in resonances from the layers near the source. For this reason, only after averaging GloPHV over multiple earthquakes, the incoherent source-side resonances are suppressed, which allows interpretation of the averaged GloPHV for the receiver-side structure. Each of the time windows we use for implementing equation 2.3 contains multiple phases in practice. Overlapping reverberations from different phases can lead to spurious resonances. The delay times between the phases vary with earthquake (distance). Hence the spurious phase cross terms are also suppressed by averaging GloPHV over multiple earthquakes.

Equation 2.3 allows isolating the resonance spectra of the basin from the observed waveforms. The resonance frequencies for P or S waves  $\hat{L}^P(\mathbf{X}_R, \mathbf{x}_B)$  or  $\hat{L}^S(\mathbf{X}_R, \mathbf{x}_B)$ , lead to troughs or peaks because they are in the denominator or numerator in equation 2.3, respectively. We take the root mean square of the north and east components to obtain the value of the horizontal component [e.g. 8, 14]. According to Tsai [5] and Ibs-von Seht and Wohlenberg [24], for example, the fundamental resonance frequency, a part of  $\hat{L}(\mathbf{X}_R, \mathbf{x}_B)$ , can be written as

$$f_0^{P,S} = 1/T_0^{P,S} = V^{P,S}/4Z, \quad (2.6)$$

in which  $f_0^{P,S}$  is the resonance frequency for a P- or S wave,  $T_0^{P,S}$  is the resonance period,  $V^{P,S}$  is the velocity of a P- or S wave, and  $Z$  is the thickness of a layer. This equation can be used to estimate the depth to a seismic boundary from the resonance frequency. The resonance frequency  $f_0^P$  of the P wave should be higher than the resonance frequency  $f_0^S$  of the S wave, when the two are a resonance from the same structure.

The data processing procedure is as follows. First, using JWEED, we extract the 600 s windows for each of the three components for all chosen earthquakes. For each of the windows, we remove the mean level. Then, running absolute-mean normalization is applied with a 10 s running window to make the different global phases of the same order and to boost the amplitudes of the P- and S-wave reverberations with respect to the otherwise dominating direct arrivals. Subsequently, using 10 per cent tapering, a fast Fourier transform was applied. Then, we obtain GloPHV for each station of the TN- and the TE-arrays from the chosen 69 and 79 global earthquakes, respectively. Finally, for each station we take the mean GloPHV from all global phases at that station. As a post processing step, we apply a moving average (low-pass filtering) to ease the identification

of the dominant resonance frequencies and subsequently we normalize the amplitudes. An example of the mean GloPHV after the moving average for the station TE01 from the TE-array is shown in Figure 2.4 in black; the 79 individual contributions to the mean result are shown in gray in the figure.

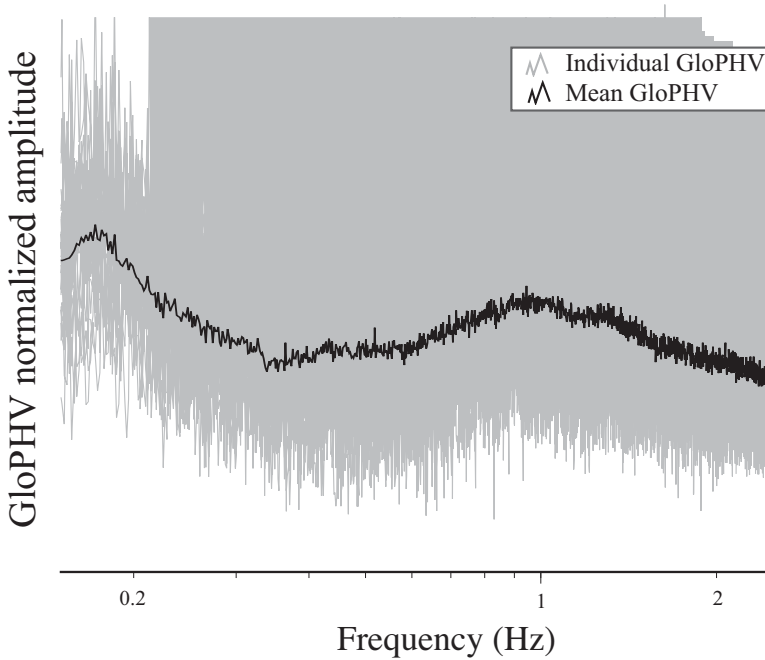


Figure 2.4: Example of the 79 individual GloPHVs (gray) and the mean GloPHV (black) for station TE01, the westernmost station of the TE-array. The mean GloPHV is shown before application of the moving average from the postprocessing.

### 2.1.6. RESULTS AND DISCUSSION

The mean and amplitude-normalized GloPHVs for each station from the TN-array of MalARRgue from the P and S windows are shown in Figure 2.5a and 2.5b, respectively. The analogous results for the TE-array are shown in Figure 2.5c,d with filled peaks for ease of interpretation. Although there are small differences in the particulars for each mean GloPHV, the features of the fundamental resonance frequency show very good similarity between Figure 2.5a and 2.5b, and between Figure 2.5c and 2.5d. Because the fundamental resonance frequencies using the S window show somewhat clearer results (e.g. TN04, TN05, TE07, and TE08), hereafter we use the results shown in Figure 2.5b,d.

Looking at the fundamental resonance frequency for the TN-array in Figure 2.5b, we see that it is difficult to identify the related peaks (corresponding to the S-wave reso-



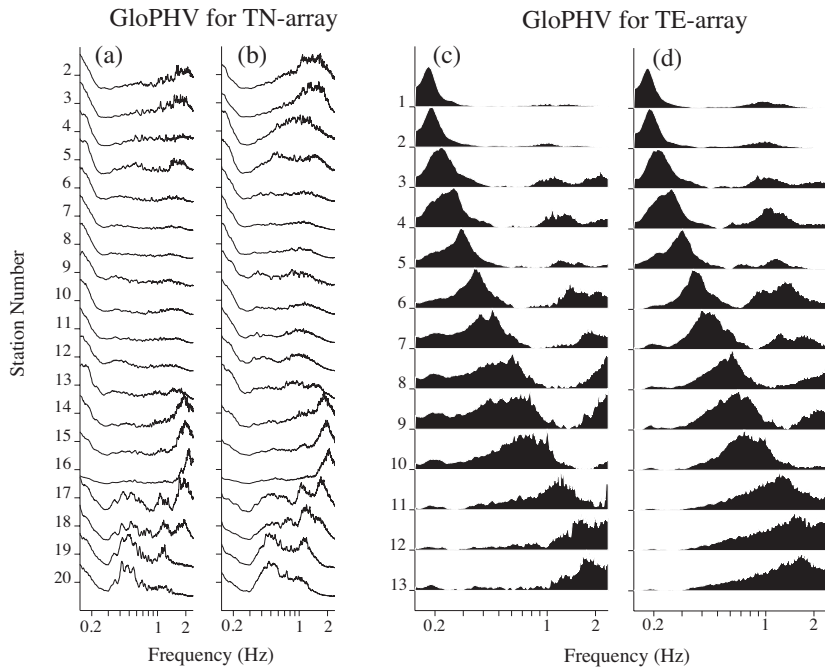


Figure 2.5: GloPHV results for: TN-array from (a) the P window; (b) the S window; and TE-array from (c) the P window; (d) the S window. The individual spectra are sorted as a function of the station number. The peaks for TE-array are filled in black.

nances) around 0.15 Hz probably due to our choice of using 0.15 Hz as a low frequency limit. On the other hand, the troughs (corresponding to the P-wave resonances) are fairly easily identifiable around 0.25 Hz. For the TE-array results in Figure 2.5d, we can see that fundamental peaks can be clearly identified (e.g. the peak around 0.2 Hz for TE02). These peaks can be identified for all of the TE-array stations and appear to be shifting toward higher frequency with increasing station number (from the TE01 to TE13). The troughs for the TE-array are also identifiable, but generally less clearly.

In Figure 2.6a,b, we show the fundamental resonance periods (1/Hz) at each station as a function of distance from the station with the lowest station number for each sub-array obtained using the troughs for the TN-array and the peaks for the TE-array. For clarity, above each period in Figure 2.6a,b we also show GloPHV of the corresponding station with the fundamental troughs or peaks between 0.15 and 2.5 Hz indicated by dashed or solid arrows, respectively.

Following the work of Farías *et al.* [25] for central Chile, we assume average values of the P- and S-wave velocity through the basin of 5.2 and 2.9 km/s, respectively. Thereby, we convert the periods from Figure 2.6a,b to the estimated depth of the bottom of the Malargüe basin using only the average P- and only the average S-wave velocity, respectively. We show the respective results in Figure 2.7a,b. Below the TN-array, the basin's bottom (basement's top) is at about 5 km depth. We can also see that there is a shallowing trend of the basin's bottom in the north-northwest direction. Under the TE-array, the basin's bottom shows clear shallowing trend from west to east going from a depth of 4 km to a depth of 0.5 km.

MalARRgue's T-array is about 10 km to the east from the arrays Kraemer *et al.* [19] used to obtain their active-source seismic section. In their seismic section, the depocenter (the basin's center) is at depth of about 5.5 to 6 km and there is a clear shallowing trend in the east direction. Extrapolation of their results to the T-array would mean a good agreement with the depths we obtain from GloPHV taking into account the possible variations of the depths due to uncertainties in the assumed velocities.

There are also other peaks and troughs in GloPHV results at frequencies higher than the fundamental resonance frequency, which could be related to the depths to sedimentary boundaries inside the basin. Because our interest is determining the depth to the bottom of the basin, we do not interpret sedimentary boundaries in this study.

To further evaluate the accuracy of the estimated depth to the top of the basement we obtained from GloPHV, we compare our results to a Bouguer-anomaly map. The Bouguer gravitational anomaly is often used in petroleum exploration to estimate the location of basins. In Figure 2.8, we show the Bouguer anomaly map around MalARRgue, which we took from the Bureau Gravimétrique International (BGI; last accessed October 2013). On the anomaly, we overlay the T-array (the triangles) with the estimated depths depicted by the gray-scale circles around each station. Lower values for the Bouguer anomaly indicate thickening of the basin, whereas higher values indicate thinning of the basin. Very good agreement exists between the basin's bottom structure we obtain and the gravity anomalies, implying that GloPHV is effective to estimate the depth of the basin using the fundamental resonance frequencies.

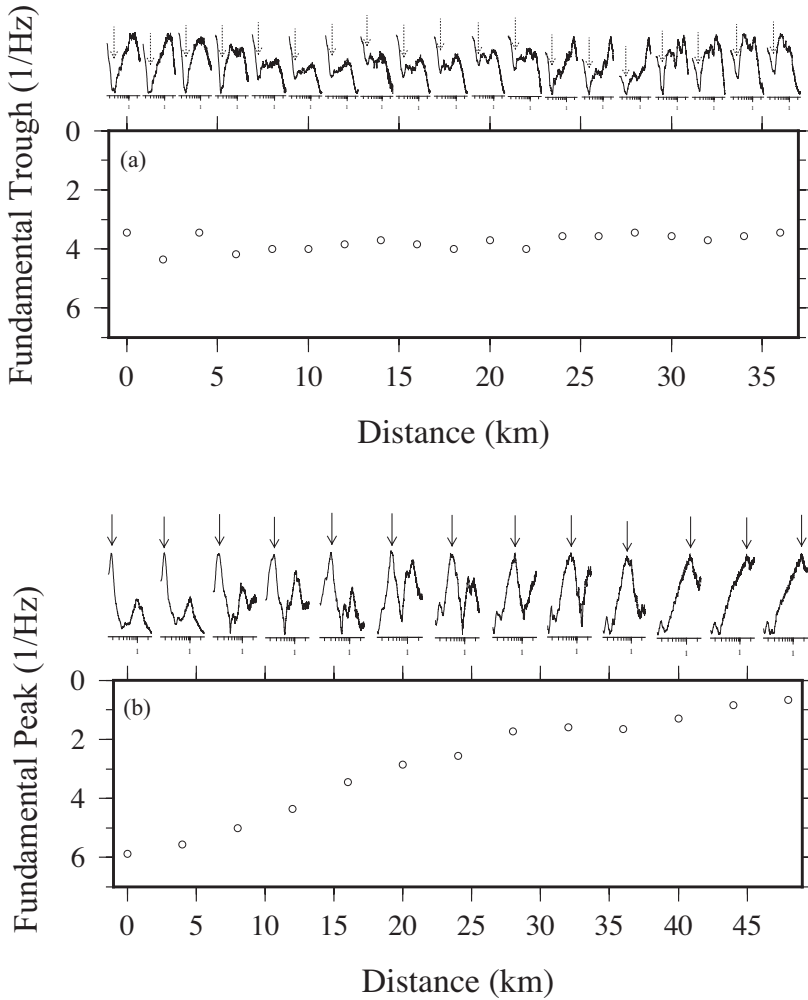


Figure 2.6: Fundamental resonant periods obtained from GloPHV for: (a) TN-array results in Figure 2.5b as a function of the distance from station TN02 (south-southeast–north-northwest); (b) TE-array results in Figure 2.5d as a function of distance from station TE01 (west-southwest–east-northeast). Above each station position is shown the station's spectrum from Figure 2.5 with the used trough or peak.

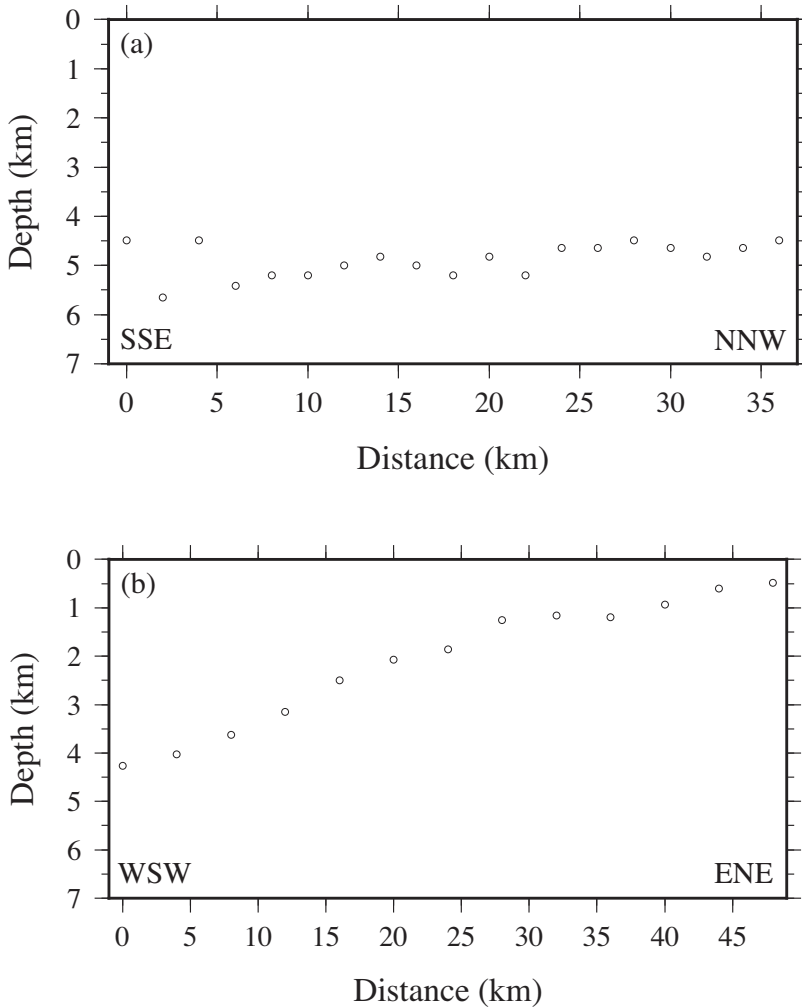


Figure 2.7: Estimated depth of the bottom of the Malargüe basin derived from the fundamental periods from Figure 2.6: (a) below the TN-array as a function of the distance from station TN02 using an average P-wave velocity of 5.2 km/s; (b) below the TE-array as a function of the distance from station TE01 using an average S-wave velocity of 2.9 km/s.

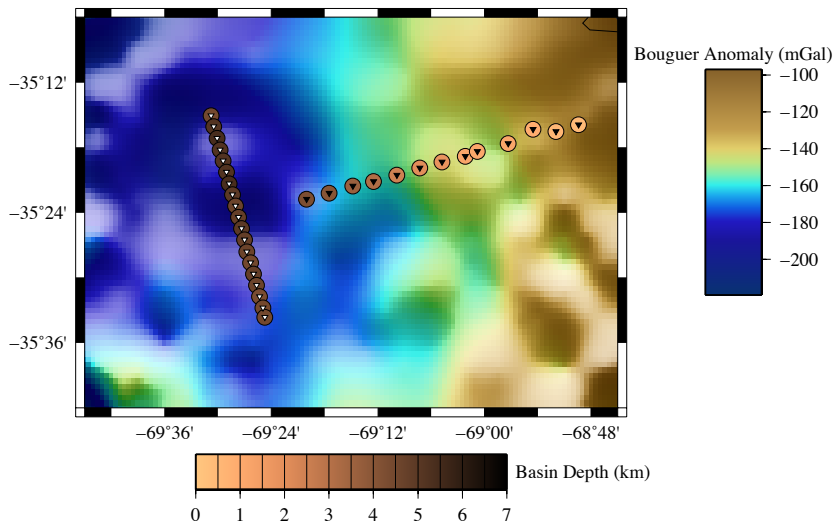


Figure 2.8: Map of the Bouguer gravity anomaly, obtained from the Bureau Gravimétrique International (BGI), around the T-array. The white and black triangles indicate the positions of the seismic stations as in Figure 2.1. The estimated depth of the bottom of the basin is depicted by the gray-scale circles.

## 2.2. SP-WAVE PHASE AND $Q_S/Q_P$

### 2.2.1. INTRODUCTION

Imaging heterogeneities in the subsurface is a crucial topic in hydrocarbon exploration as well as academia. However, acquiring these images using conventional active sources (e.g. explosives, vibroseis, and airgun) is not always easily achievable because of costs, environmental concerns, and other practical issues. Therefore, the use of passive seismic methods, such as microseism reflection imaging [e.g. 26–28] and seismic interferometry with ambient noise [e.g. 10, 29–31], has recently become more attractive. In this sense, despite the fact that earthquakes are usually seen as abhorrent phenomena in human communities (due to the risks they pose), it is natural to also view weaker earthquakes as attractive natural resources if one can use their information in appropriate analyses. In this study, we propose a new passive imaging technique with spatial resolution higher than the one normally achieved with already established passive seismic techniques using naturally occurring earthquakes. Our technique could be used as a first screening tool for frontier exploration areas with limited available seismic surveys and before a decision is made for acquisition with conventional surveys with active sources.

There are several methods for using earthquakes to image velocity discontinuities in the subsurface, such as reflection [e.g. 32] and receiver-function [e.g. 33] analyses. However, reflection analysis can image only the parts of the subsurface deeper than the focal depths. The receiver-function method uses waves coming from the deeper part to the surface, which enables one to obtain information of the shallower subsurface structure. This method, however, uses teleseismic events with large magnitudes. As a result, high

spatial resolution may not be expected from this method because the expected frequencies at the receivers would be relatively lower than the frequencies recorded from local earthquakes. Because of this, it is important to have a method to image the shallower parts of the subsurface with higher spatial resolution in areas where natural resources (e.g. hydrocarbons) are found and produced.

Doi and Kawakata [34] propose a new method to image subsurface velocity discontinuities with relatively higher resolution using a different type of seismic phase Sp-waves. Advantages of this method are that one could avoid having to treat the possible strong amplitudes of the S-waves and that one expects to have higher resolution because local, weaker earthquakes can be used (which thus have signals with higher frequency content).

However, having only an image of the discontinuities might not be sufficient to estimate the physical properties of the subsurface structures because the amplitudes of the converted or reflected waves depend on the densities as well as P- and S-wave velocities below and above the discontinuities. The quality factor  $Q$ , characteristic of the attenuation, could provide one with additional information to estimate the condition of the medium. For seismic exploration, Klimentos [35] suggests that the  $Q_S/Q_P$  ratio estimated from well-log data could be used as a tool for distinguishing gas and condensate from oil and water, and Zarean *et al.* [36] report that a high value of the  $Q_S/Q_P$  ratio, obtained from the spectra of earthquake coda, could be related to strong heterogeneity, such as a highly fractured area.

Thus, integrated analysis of Sp-waves and the  $Q_S/Q_P$  ratio could be a useful tool to characterize heterogeneous structures in the shallower part of the crust. In the following, we show how to apply such analysis to field waveform data.

### 2.2.2. DATA SET AND STUDY AREA

We analyzed 40 waveforms from 28 earthquakes, which occurred from 28 September 2002 to 4 April 2011 offshore, southeast of Hokkaido, Japan. The earthquakes were recorded by two nearby seismic stations: ONBETS, operated by the Japan Meteorological Agency (JMA), and N.SNSH, operated by the National Research Institute for Earth Science and Disaster (NIED). The locations of the epicenters and the seismic stations are shown in Figure 2.9. The magnitudes of the earthquakes we used were in the range of  $M_j$  (the local magnitude defined and calculated by JMA) 2.0 to 4.2. We excluded larger events from our analysis because these may have a relatively longer source-time duration, which would cause difficulties in imaging with Sp-waves and in the spectral analysis. We have access to an active-source seismic profile (see the black solid line in Figure 2.9), which was shot close to our study area [37]. The seismic section (GH76-2) was acquired in 1976 by the Geological Survey of Japan (currently the National Institute of Advanced Industrial Science and Technology) under a contract from Japan's Ministry of International Trade and Industry (currently Japan's Ministry of Economy, Trade, and Industry).

### 2.2.3. SP-WAVE ANALYSIS

#### METHOD

Following the pioneering work of Doi and Kawakata [34], we briefly show what Sp-waves are and how they could be analysed. An S-wave incident with an angle on a velocity dis-

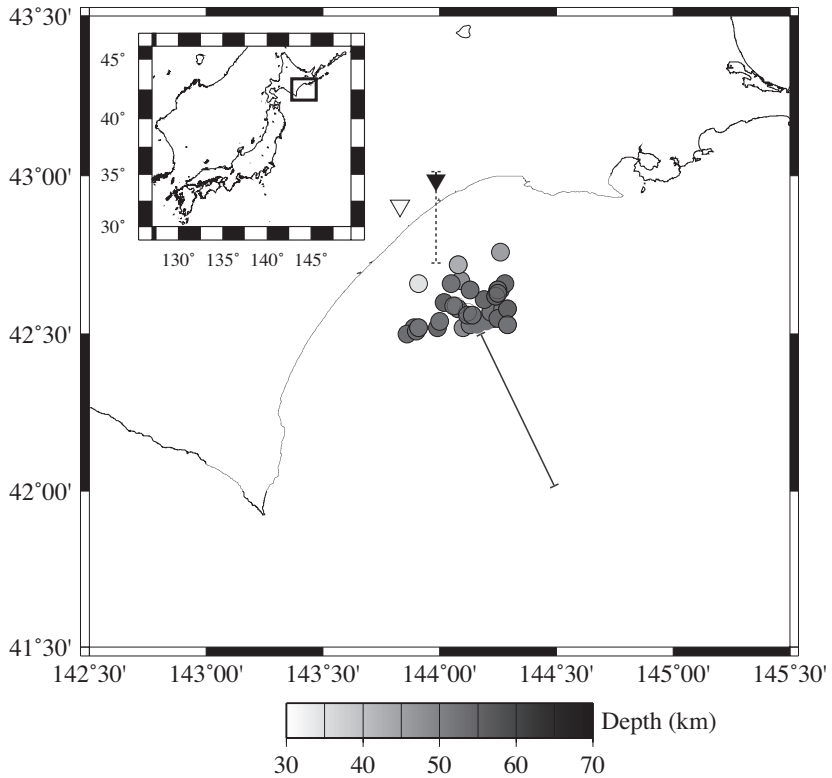


Figure 2.9: Map of the study area showing the position of the two stations (N.SNSH, black triangle; ONBETS, white triangle) and the hypocenter distribution of the 28 earthquakes (circles) used in this work provided by NIED and JMA. The grayscale of the circles indicates the event depth. The dashed and solid lines indicate the profile lines where the seismic images are obtained in this study and in Honza [37], respectively.

continuity from a source (in our case, a local earthquake) splits in its upward propagation into P- and S-waves. The converted P-waves (Sp-waves) arrive at the station earlier than the direct S-waves (Figure 2.10). The Sp-waves have lower amplitudes than do the direct S-waves. Figure 2.11 shows the vertical and transverse components of the recorded displacement waveforms for events with depths between 50 and 60 km after application of a band-pass filter between 2 and 5 Hz. The vertical locations of the traces are proportional to the P-wave traveltimes. To estimate the slownesses of the phases needed here, one would normally plot the waveforms in terms of epicentral distances. However, we use the P-wave traveltimes, which are approximately proportional to the hypocentral distance, because the focal depths of the earthquakes are different. The horizontal axis is reduced such that the S-phases are aligned almost vertically. The Sp-waves may contain frequencies higher than 5 Hz. Still, the range of our band-pass filtering was chosen so that any influence from local scattering is suppressed. A similar result could be obtained by using frequencies lower than 2 Hz; however, in our case, such a filter does not result in a better identification. To minimize the effect of P-wave coda during the use of the Sp-waves, we use the time window starting 3.5 s after the onset of the P-waves and finishing at the onset of the S-waves.

In Figure 2.11, we observe three coherent Sp-phases as indicated by the dashed-dotted and dotted lines. To confirm that those phases are indeed Sp-phases, we analyze their particle motion. Figure 2.12 shows three particle-motion plots, which are sampled from the vertical- and transverse-component waveforms highlighted with bold black in Figure 2.11. The three time windows correspond to the times indicated in Figure 2.11 as possibly containing Sp-phases. The particle-motion plots reveal what is also expected as a typical feature of the Sp-waves — predominant vertical motion because the recorded waves are converted P-waves.

We calculate  $h$  by trial and error using ray tracing. In this study, we use a simple homogeneous background velocity model ( $V_P = 6.4$  km/s and  $V_S = 3.7$  km/s) taken from Miyamachi *et al.* [38] who estimate the crustal velocity structure in northern Japan using traveltome tomography. When desired, one could consider a depth-dependent velocity structure. However, calculation using several possible models showed that the expected bending had a smaller effect on the results compared with the spatial resolution (2.5 km in the horizontal direction) expected in our study. Equations to calculate  $h$  are given in Appendix A.

Wilson *et al.* [39] report that there is a constraint for the receiver function to use Sp-waves because other teleseismic phases (e.g. pPPP and SKSp) arrive simultaneously with the Sp-phases. Because we use local earthquakes, the expected Sp-waves on the records must be completely free of the mentioned contaminating phases.

## RESULTS

In Figure 2.13, we show the averaged amplitude of the envelopes, which are calculated for waveform traces whose conversion points at the same depths for Sp-waves are very close to each other. The averaged amplitudes are ordered as a function of the distance from N.SNSH to the positions of the conversion points at a depth of 4 km. Thus, the averaged amplitudes given at another depth only indicate a model with a possible conversion point at that depth, but not the exact horizontal location of the trace. The blank



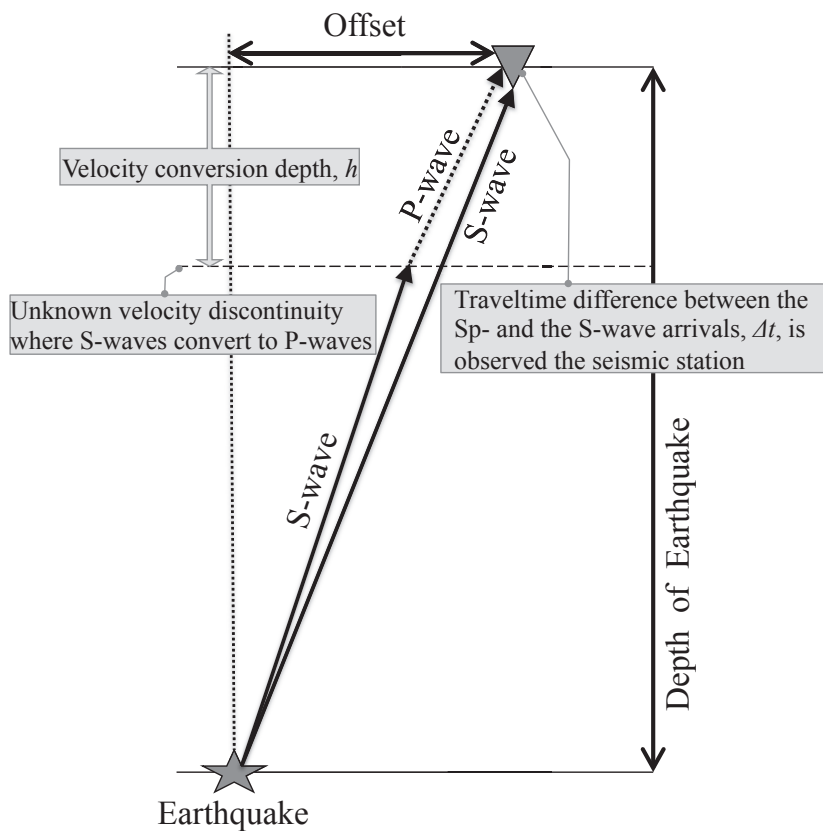


Figure 2.10:  $S_p$ - and S-wave are recorded at the seismic station. The vertical and horizontal distances are 25 and 60 km, respectively, which is in the same scale as the geometry in this study.

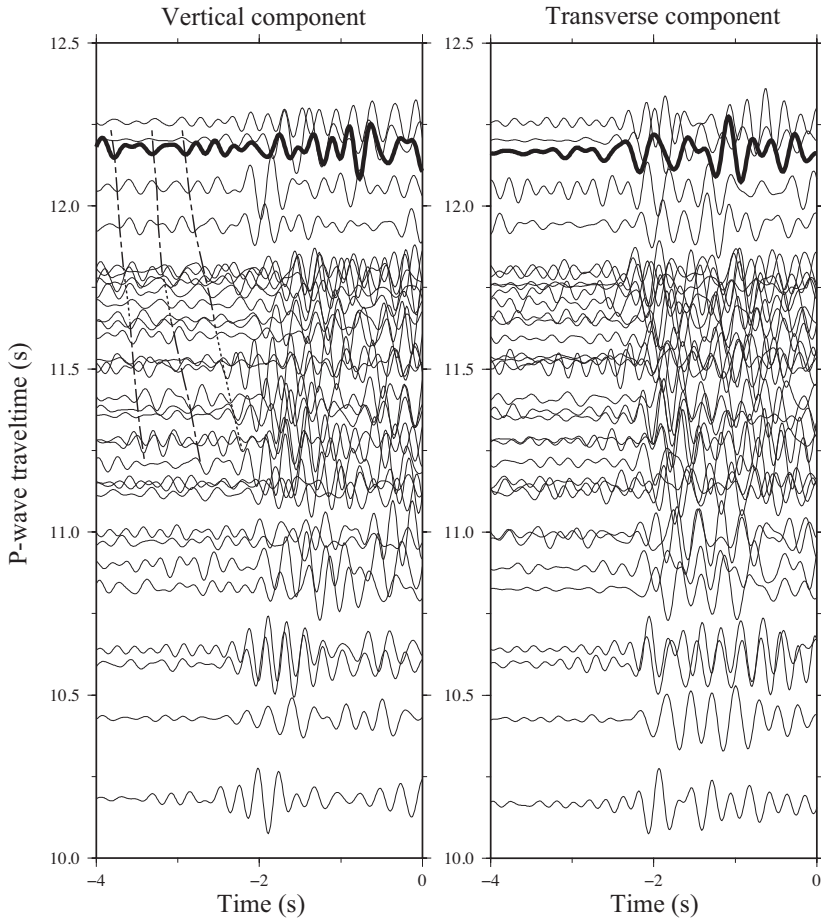


Figure 2.11: Sorted seismograms (depth between 50 and 60 km) from the vertical and transverse components as a function of the traveltimes of the P-wave. The horizontal axis is reduced such that the S-waves align vertically. The trace highlighted in bold indicates the example waveform for the particle-motion analysis shown in Figure 2.12. The dashed-dotted and dashed lines indicate the Sp-wave candidates with and without clear visual coherency among neighboring traces, respectively.

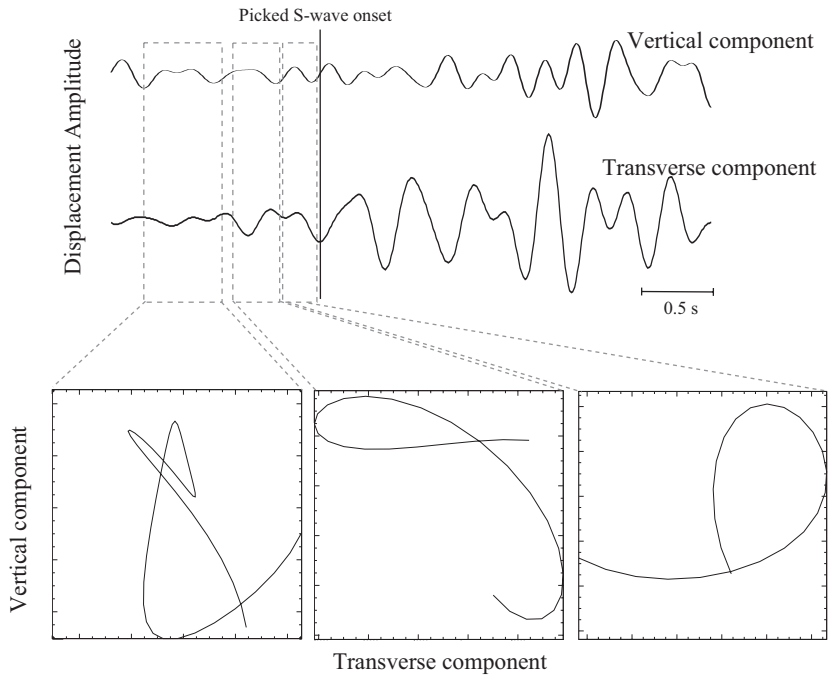


Figure 2.12: Examples of the particle motions. The three time windows are taken around the  $S_p$ -phase arrival times as indicated in Figure 2.11. The scale of the vertical axes is the same in the two upper panels (seismograms); the scales of the horizontal and vertical axes of the particle motions are also the same. The seismogram was recorded by N.SNSH with the origin time at 00:22:42 on 3 October 2003.

(gap) areas in Figure 2.13 represent areas where the available earthquakes cannot cause a conversion at a depth of 4 km. In Figure 2.13, we have indicated three laterally coherent phases, highlighted by red (1.0 to 2.5 km), blue (3.0 to 4.5 km), and green (6.5 to 7.0 km) dots. Because these phases are coherent and dominant in the vertical component (see Figure 2.12), we interpret these phases as resulting from the presence of velocity discontinuities that cause S-to-P conversions at those depths.

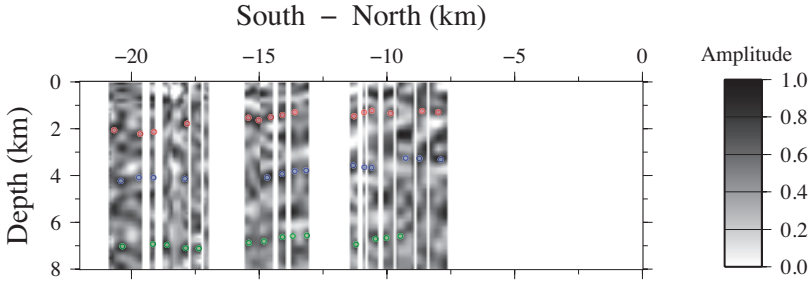


Figure 2.13: Averaged amplitude of envelopes for Sp-waves as a function of the horizontal distance from N.SNSH for points at a conversion depth of 4 km. The northern origin location at  $43.0^\circ$  in latitude and  $144.0^\circ$  in longitude is set as 0 km in the horizontal axis. Red, blue, and green dots represent phases of large amplitudes with lateral coherency.

To check and possibly confirm the interpretation from Figure 2.13, and also to understand the distributions of the velocity discontinuities in three dimensions, we spatially stack the amplitudes of the envelopes of the Sp-waves. The stacking procedure is as follows: The origin of the offset is set at  $43.0^\circ$  in latitude and  $144.0^\circ$  in longitude, which is near station N.SNSH. We set a projection plane together with the x- and y-axes, which are parallel and perpendicular to it, respectively. We discretize the 3D model to consist of bins defined by 2.5 (x-offset), 2.5 (y-offset), and 0.5 km (depth). The conversion points are computed by ray tracing for every possible Sp-wave arriving at the stations with 0.01 s intervals. The amplitudes of the waveforms that fall in the same bin are summed. Finally, we average the summed amplitudes by the number of the traces that fall in that bin.

The summed amplitudes along the north–south cross section with a back azimuth of  $350^\circ$  are shown in Figure 2.14. In the cross section, we can see parts with relatively strong continuous amplitudes at depths of 1.0–2.0 km (shown with red arrows), 3.0–4.5 km (shown with blue arrows), and 7.0–7.5 km (shown with green arrows) in the southern section. Although it is not as distinct, we also detect two continuous amplitudes in the northern section (shown with dotted arrows). Note that the three coherent phases in Figure 2.13 mainly contribute to the blocks with large amplitudes in Figure 2.14. For example, the strong-amplitude blocks between  $-22.5$  and  $-15$  km lateral direction and at a depth of around 7.0 km in Figure 2.14 are attributed to the phases with green dots in Figure 2.13.

The image in Figure 2.14 gives us confidence in our interpretation in Figure 2.13 because randomly distributed phases with high amplitudes would not provide any similar-

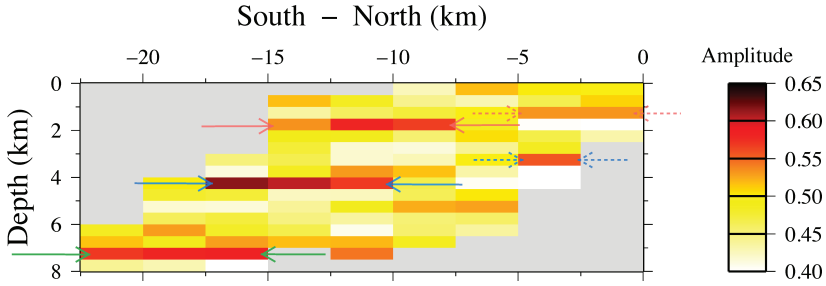


Figure 2.14: Stacked seismic section of the Sp-waves envelopes. The color indicates the stacked amplitude. The horizontal axis is identical to the one in Figure 2.13. The solid and dashed arrows indicate locations where relatively strong and moderate amplitudes (higher than 0.5), respectively, are interpreted as laterally continuous features.

ity between our interpretations (Figure 2.13) and the amplitude continuity (Figure 2.14).

The spatial distribution of the velocity discontinuities along two more cross sections is shown in Figure 2.15. The stacked images are projected from the northern origin point described above to 22.5 km south with back azimuth of 340° and 360°. Because of the spatial distribution of the earthquakes and the position of the stations, as well as the spatial resolution (bin size), the imaging nearby the northern origin point shows a similar or identical result along the different projection planes. The interpreted features along the projection plane with the 350° azimuth (Figure 2.14 and the green frame in Figure 2.15) are continuous (and can be interpreted) in the eastern and western directions.

#### 2.2.4. FREQUENCY-DEPENDENT $Q$

##### METHOD

We estimate  $Q$  for P- and S-waves using a frequency-dependent model to investigate a possible relationship with the detected velocity discontinuities by Sp-waves. Abercrombie [40] estimates corner frequency and  $Q$  by using a single corner frequency source model of the far-field displacement spectrum with frequency-independent  $Q$ . We modify the author's method, assuming  $Q$  to be proportional to frequency to the power of a constant. With a reference to the standard source model of Brune [41], which assumes a point-source model keeping constant radiated energy ratio between P- and S-waves for different sizes of magnitudes, the corner frequency of the far-field term is derived based on the so-called  $\omega^{-2}$  model from Aki [42]. We extract a window of 3-s length around each identified P- and S-wave arrival from the recorded seismic waveforms. The windows are transformed to the temporal frequency domain using a fast Fourier transform with a 10 % taper. We estimate  $Q_P$  and  $Q_S$  as a function of frequency and the corner frequency with a grid-search method, so as to fit the observed P- and S-wave spectrum in the frequency band of 1–20 Hz. We use this frequency band because it has high signal-to-noise ratios. An example of the fitting for the  $Q_P$ - and  $Q_S$ - values is shown in Figure 2.16. Subsequently, we calculate the value of the  $Q_S/Q_P$  ratio for every waveform trace recorded at the sta-

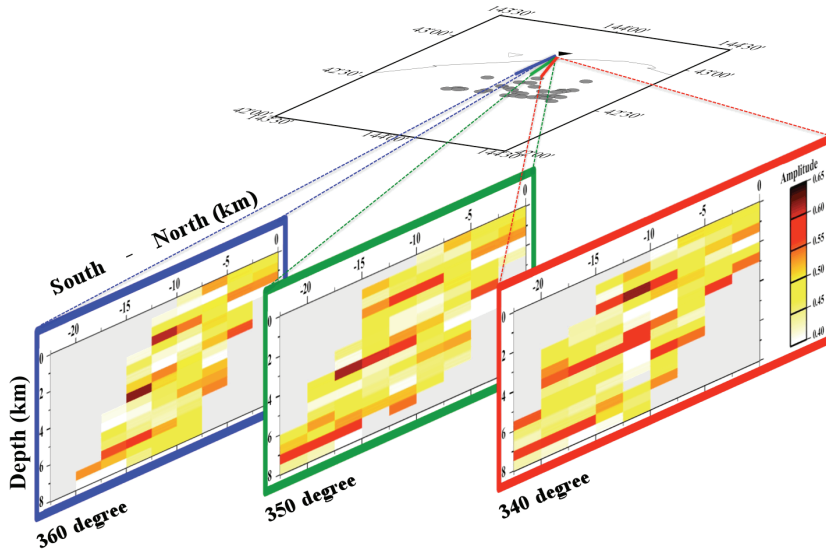


Figure 2.15: Stacked sections, as the one in Figure 2.14, shown as a function of back azimuth. The green-framed section in the middle corresponds to the section of Figure 2.14. The red and blue-framed sections have  $10^\circ$  back-azimuth differences with respect to the middle stacked section.

tion. The effect of focal mechanisms is not considered because we did not estimate the seismic moment in this study.

## RESULTS

In Figure 2.17, we show the estimated values of the  $Q_S/Q_P$  ratio at 3.5 Hz, which is inside the range of the band-pass filter we apply for the use of Sp-waves. Each dot represents the  $Q_S/Q_P$  ratio of each trace, which passes through the shown lateral distance for the conversion depth of 4 km. For the northern part (lateral distance between  $-7.5$  and  $-11$  km), we see that the  $Q_S/Q_P$  ratios show large variations including several values higher than 1.5. In contrast, the  $Q_S/Q_P$  ratios exhibit less scatter in the southern part.

### 2.2.5. DISCUSSION

Honza [37] presents results from subsurface imaging obtained using conventional active sources (airguns) along a seismic line a few tens of kilometers away toward the southeast direction from the area of our study. The author interpreted three major geologic horizons: top Quaternary, top Pliocene, and top of lower Miocene. These geologic horizons are interpreted in Honza [37] as slightly inclined in the north-northwest direction. The depths and trends of these three horizons correspond to the velocity discontinuities found in our study (e.g. Figure 2.14).

Aki [43] argues that the scattering waves with conversions from P- to S-waves would be more commonly generated than the scattering with conversion from S- to P-waves.

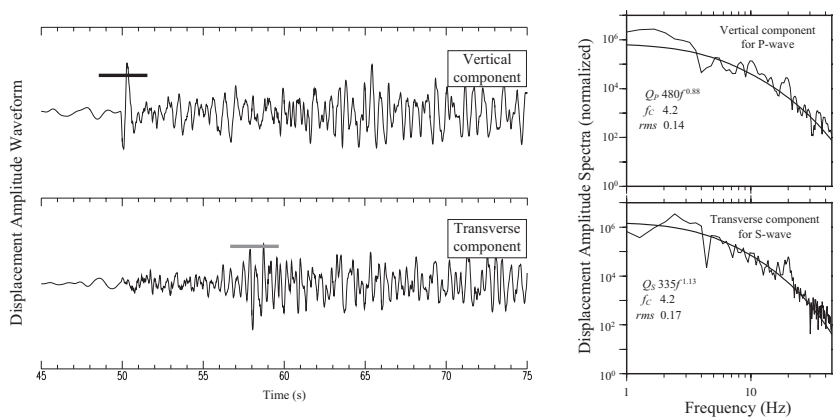


Figure 2.16: Example of spectral fitting of the data. The seismogram was recorded by N.SNSH with origin time at 01:49:38 on 6 May 2009. The black and gray bars above the vertical and horizontal component of the seismogram indicate the time windows used for  $Q_P$  and  $Q_S$  estimation, respectively. The black curved lines in the spectra show the best-fit results of the grid searching.

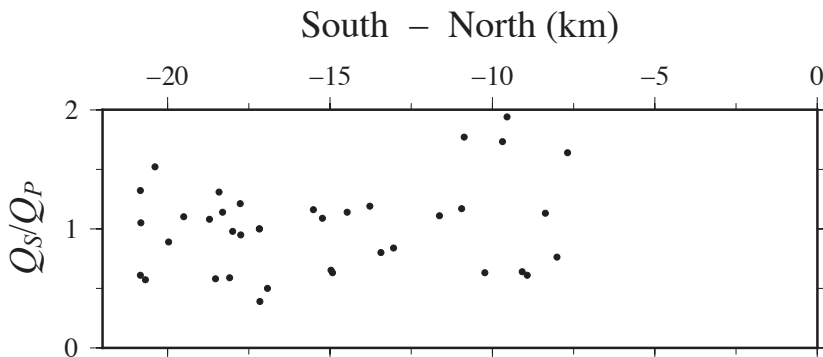


Figure 2.17: The  $Q_S/Q_P$  ratios as a function of the horizontal distance from N.SNSH. The horizontal axis is identical to those in Figures 2.13 and 2.14.

This could be interpreted as the P-waves being attenuated more than the S-waves. In our study, coherent Sp-waves are mainly found in the southern part in Figure 2.14, for which we can observe in Figure 2.17 a relatively smaller variation of the  $Q_S/Q_P$  ratios. On the other hand, we could detect less coherent phases in the northern part, for which we observe the relatively larger variation of the  $Q_S/Q_P$  ratios (with several high values of  $> 1.5$ ). It is possible that the geologic layers of the Quaternary, Pliocene, and Miocene periods generate the coherent converted waves in the southern part, whereas strong heterogeneity disturbs the wavefield in the northern part.

Using well-log data, Klimentos [35] demonstrates that a high value of the  $Q_S/Q_P$  ratio would indicate the presence of gas, and Zarean *et al.* [36] report that a high value of the  $Q_S/Q_P$  ratio, obtained using records of natural earthquakes, could be related to highly fractured areas. This means that a possible interpretation of our result for the northern part of the study area, which exhibits relatively higher  $Q_S/Q_P$  ratios, may be attributed to well-developed fractures and/or the presence of gas.

Integrating the information of converted-wave amplitudes and relative  $Q_S/Q_P$  ratios can be used to interpret the physical properties of certain layers. However, the resolution of the images is dependent on how densely the raypaths are distributed in the area of interest; in other words, it fully relies on the positions of the earthquakes (passive sources) and receivers. For example, the  $Q$ -values estimated here are interpreted as representative for the complete raypaths. When more earthquakes or stations are available, identifying the depth of most attenuated locations could be done with a higher spatial resolution due to the available variety of crossing raypaths.

Another possibility is to try to use the method proposed recently by Draganov *et al.* [44, 45] for estimation of a layer-specific  $Q$ -value. In this method, the authors propose to use nonphysical (ghost) arrivals retrieved from seismic interferometry applied to records at the surface from subsurface sources. The ghost arrivals are retrieved from cross-correlation (or autocorrelation) and summation of specific arrivals from the subsurface sources and represent reflected energy that would have been measured from the bottom of a specific layer as if with a source and receiver placed directly on top of that layer. The retrieval of such ghost arrivals is directly dependent on the  $Q$ -value of the overburden above the layer that causes a ghost. If the method were applied by autocorrelation to each of the two stations from the example we showed, then it would be sufficient to have recordings from earthquakes below the stations. Separate estimation of the  $Q_S$ - and  $Q_P$ -value of the top layer could be done from separate S- and P-wave arrivals, respectively. The application of this method would require P- and S-wave arrivals with near-vertical incidence. This means that we would require other earthquakes than those we used for the interpretation of Sp-wave conversion points. This is so because for a conversion to take place, earthquakes away from the stations were needed. Having more stations would also be helpful to facilitate the overlap between the Sp-wave stacked sections and the information about  $Q_S/Q_P$  ratios extracted from ghost reflections.

Further investigation in different locations with hydrocarbons where natural earthquakes occur often (e.g. the west coast of North America, Chile, and Argentina) would help further verify the method we propose.



### 2.2.6. APPENDIX A: SYSTEM OF EQUATIONS FOR SP-WAVES ANALYSIS

The depth of conversion points of Sp-waves are estimated through following equations. First, the equation of Shell's law is described as

$$\frac{\sin\theta_2}{\sin\theta_1} = \frac{V_P}{V_S}, \quad (\text{A-1})$$

where  $\theta_1$  is the incident angle where S-waves are converted to P-waves due to the presence of velocity discontinuity and  $\theta_2$  is the take-off angle of Sp-wave formed from a perpendicular axis to the subsurface, respectively. When we consider the traveltimes of the Sp-waves and the direct S-waves, the following equation can be written;

$$\Delta t = \frac{\sqrt{H^2 + L^2}}{V_S} - \left( \frac{H-h}{V_S \cos\theta_1} + \frac{h}{V_P \cos\theta_2} \right), \quad (\text{A-2})$$

where  $\Delta t$  is the traveltime difference between the Sp-waves and the direct S-waves,  $H$  is a depth of an earthquake,  $h$  is a depth of the velocity discontinuity (Figure 2.10), and  $L$  is the epicentral distance. Calculating equations A-1 and A-2 as being satisfied as the system of equations, the depth of the velocity discontinuity  $h$  is calculated from  $\Delta t$  in equation A-2.

## REFERENCES

- [1] Y. Nishitsuji, E. Ruigrok, M. Gomez, and D. Draganov, *Global-phase H/V spectral ratio for delineating the basin in the Malargue region, Argentina*, *Seismological Research Letters* **85** (2014), 10.1785/0220140054.
- [2] Y. Nishitsuji, I. Doi, and D. Draganov, *The potential of imaging subsurface heterogeneities by natural local earthquakes*, *Geophysics* **79** (2014), 10.1190/geo2013-0391.1.
- [3] Y. Nishitsuji and I. Doi, *A method to estimate seismic heterogeneity through Sp-waves and frequency dependent quality factor Q analyses: A case study in southeastern offshore of Hokkaido, Japan*, in *SEG Technical Program Expanded Abstracts 2012* (2012).
- [4] Y. Nakamura, *A method for dynamic characteristics estimation of subsurface using microtremor on the ground surface*, in *Quarterly Report of RTRI* (1989).
- [5] N. C. Tsai, *A note on the steady-state response of an elastic half-space*, *Bulletin of the Seismological Society of America* **60** (1970).
- [6] J. Delgado, P. Alfaro, J. Galindo-Zaldivar, A. Jabaloy, A. C. López Garrido, and C. Sanz de Galdeano, *Structure of the Padul-Nigüelas basin (S Spain) from H/V ratios of ambient noise: Application of the method to study peat and coarse sediments*, *Pure and Applied Geophysics* **159** (2002), 10.1007/s00024-002-8756-1.
- [7] G. De Luca, S. Marcucci, G. Milana, and T. Sanò, *Evidence of low-frequency amplification in the city of L'Aquila, central Italy, through a multidisciplinary approach including strong- and weak-motion data, ambient noise, and numerical modelling*, *Bulletin of the Seismological Society of America* **95** (2005), 10.1785/0120030253.

- [8] J. W. Lane, E. A. White, G. V. Steele, and J. C. Cannia, *Estimation of bedrock depth using the horizontal-to-vertical (H/V) ambient-noise seismic method*, in *Symposium on the Application of Geophysics to Engineering and Environmental Problems* (2008).
- [9] D. Bindi, S. Marzorati, S. Parolai, A. Strollo, and K. H. Jäkel, *Empirical spectral ratios estimated in two deep sedimentary basins using microseisms recorded by short-period seismometers*, *Geophysical Journal International* **176** (2009), [10.1111/j.1365-246X.2008.03958.x](https://doi.org/10.1111/j.1365-246X.2008.03958.x).
- [10] E. Ruigrok, X. Campman, and K. Wapenaar, *Basin delineation with a 40-hour passive seismic record*, *Bulletin of the Seismological Society of America* **102** (2012), [10.1785/0120110242](https://doi.org/10.1785/0120110242).
- [11] T. Ohmachi, Y. Nakamura, and T. Toshinawa, *Ground motion characteristics in the San Francisco bay area detected by microtremor measurements*, in *International Conferences on Recent Advances in Geotechnical Earthquake Engineering and Soil Dynamics* (1991).
- [12] E. H. Field and K. H. Jacob, *A comparison and test of various site-response estimation techniques, including three that are not reference-site dependent*, *Bulletin of the Seismological Society of America* **85** (1995).
- [13] J. Lermo and F. J. Chávez-García, *Site effect evaluation using spectral ratios with only one station*, *Bulletin of the Seismological Society of America* **83** (1993).
- [14] G. Ferretti, M. Massa, L. Isella, and C. Eva, *Site-amplification effects based on teleseismic wave analysis: The case of the Pellice Valley, Piedmont, Italy*, *Bulletin of the Seismological Society of America* **97** (2007), [10.1785/0120060064](https://doi.org/10.1785/0120060064).
- [15] B. Grecu, V. Raileanu, A. Bala, and D. Tataru, *Estimation of site effects in the eastern part of Romania on the basis of H/V ratios of S and coda waves generated by Vrancea intermediate-depth earthquakes*, *Romanian Journal of Physics* **56** (2011).
- [16] S. Ni, Z. Li, and P. Somerville, *Estimating subsurface shear velocity with radial to vertical ratio of local P waves*, *Seismological Research Letters* **85** (2014), [10.1785/0220130128](https://doi.org/10.1785/0220130128).
- [17] E. Ruigrok, D. Draganov, M. Gómez, J. Ruzzante, D. Torres, I. López Pumarega, N. Barbero, A. Ramires, A. R. Castaño Gañan, K. van Wijk, and K. Wapenaar, *Malargüe seismic array: Design and deployment of the temporary array*, *The European Physical Journal Plus* **127** (2012), [10.1140/epjp/i2012-12126-7](https://doi.org/10.1140/epjp/i2012-12126-7).
- [18] J. J. Becker, D. T. Sandwell, W. H. F. Smith, J. Braud, B. Binder, J. Depner, D. Fabre, J. Factor, S. Ingalls, S.-H. Kim, R. Ladner, K. Marks, S. Nelson, A. Pharaoh, R. Trimmer, J. Von Rosenberg, G. Wallace, and P. Weatherall, *Global bathymetry and elevation data at 30 arc seconds resolution: SRTM30\_PLUS*, *Marine Geodesy* **32** (2009), [10.1080/01490410903297766](https://doi.org/10.1080/01490410903297766).

- [19] P. Kraemer, J. Silvestro, F. Achilli, and W. Brinkworth, *Kinematics of a hybrid thick-thin-skinned fold and thrust belt recorded in Neogene syntectonic wedge-top basins, southern central Andes between 35° and 36° S, Malargüe, Argentina*, *AAPG Memoir* **94** (2011), [10.1306/13251340M943099](https://doi.org/10.1306/13251340M943099).
- [20] A. Strollo, S. Parolai, K.-H. Jackel, S. Marzorati, and D. Bindi, *Suitability of short-period sensors for retrieving reliable H/V peaks for frequencies less than 1 Hz*, *Bulletin of the Seismological Society of America* **98** (2008), [10.1785/0120070055](https://doi.org/10.1785/0120070055).
- [21] J. Witte and S. L. Periale, *New aspects on Tertiary thick-skinned thrust geometries related to inherited Permo-Triassic extensional faults in the Bardas Blancas area, Neuquén Basin*, in *VII Congreso de Exploración y Desarrollo de Hidrocarburos* (2008).
- [22] M. Knapmeyer, *TTBox: A MATLAB toolbox for the computation of 1D teleseismic travel times*, *Seismological Research Letters* **75** (2004), [10.1785/gssrl.75.6.726](https://doi.org/10.1785/gssrl.75.6.726).
- [23] B. L. N. Kennett and E. R. Engdahl, *Traveltimes for global earthquake location and phase identification*, *Geophysical Journal International* **105** (1991), [10.1111/j.1365-246X.1991.tb06724.x](https://doi.org/10.1111/j.1365-246X.1991.tb06724.x).
- [24] M. Ibs-von Seht and J. Wohlenberg, *Microtremor measurements used to map thickness of soft sediments*, *Bulletin of the Seismological Society of America* **89** (1999).
- [25] M. Farías, D. Comte, R. Charrier, J. Martinod, C. David, A. Tassara, F. Tapia, and A. Fock, *Crustal-scale structural architecture in central Chile based on seismicity and surface geology: Implications for Andean mountain building*, *Tectonics* **29** (2010), [10.1029/2009TC002480](https://doi.org/10.1029/2009TC002480).
- [26] M. N. Toksöz, *Microseisms and an attempted application to exploration*, *Geophysics* **29** (1964), [10.1190/1.1439344](https://doi.org/10.1190/1.1439344).
- [27] K. Tamakawa, H. Asanuma, H. Niitsuma, and N. Soma, *Reflection imaging using microseismic multiplets as a source*, in *SEG Technical Program Expanded Abstracts 2010* (2010).
- [28] A. Reshetnikov, J. Kummerow, S. A. Shapiro, H. Asanuma, and M. Häring, *Multi-source multi-receiver microseismic reflection imaging: Case study Basel*, in *SEG Technical Program Expanded Abstracts 2012* (2012).
- [29] D. Draganov, X. Campman, J. Thorbecke, A. Verdel, and K. Wapenaar, *Reflection images from ambient seismic noise*, *Geophysics* **74** (2009), [10.1190/1.3193529](https://doi.org/10.1190/1.3193529).
- [30] E. Ruigrok, X. Campman, and K. Wapenaar, *Extraction of P-wave reflections from microseisms*, *Comptes Rendus Geoscience* **343** (2011), [10.1016/j.crte.2011.02.006](https://doi.org/10.1016/j.crte.2011.02.006).
- [31] V. Grechka and Y. Zhao, *Microseismic interferometry*, *The Leading Edge* **31** (2012), [10.1190/tle31121478.1](https://doi.org/10.1190/tle31121478.1).
- [32] D. E. James and M. K. Savage, *A search for seismic reflections from the top of the oceanic crust beneath Hawaii*, *Bulletin of the Seismological Society of America* **80** (1990).

- [33] C. A. Langston, *Structure under Mount Rainier, Washington, inferred from teleseismic body waves*, *Journal of Geophysical Research: Solid Earth* **84** (1979), [10.1029/JB084iB09p04749](https://doi.org/10.1029/JB084iB09p04749).
- [34] I. Doi and H. Kawakata, *High resolution spatial distribution of the velocity discontinuities in and around the swarm region beneath the Wakayama district, southwest Japan*, *Bulletin of the Seismological Society of America* **103** (2013), [10.1785/0120120316](https://doi.org/10.1785/0120120316).
- [35] T. Klimentos, *Attenuation of P- and S-waves as a method of distinguishing gas and condensate from oil and water*, *Geophysics* **60** (1995), [10.1190/1.1443782](https://doi.org/10.1190/1.1443782).
- [36] A. Zarean, M. Farrokhi, and S. Chaychizadeh, *Attenuation of High frequency P and S Waves in Qeshm Island, Iran*, in *The 14th World Conference on Earthquake Engineering* (2008).
- [37] E. Honza, *Evolution of sedimentary basins in the northern and southern Hokkaido offshore area since the late Miocene*, *Chishitsu News* **542** (1999).
- [38] H. Miyamachi, M. Kasahara, S. Suzuki, K. Tanaka, and A. Hasegawa, *Seismic velocity structure in the crust and upper mantle beneath northern Japan*, *Journal of Physics of the Earth* **42** (1994), [10.4294/jpe1952.42.269](https://doi.org/10.4294/jpe1952.42.269).
- [39] D. C. Wilson, D. A. Angus, J. F. Ni, and S. P. Grand, *Constraints on the interpretation of S-to-P receiver functions*, *Geophysical Journal International* **165** (2006), [10.1111/j.1365-246X.2006.02981.x](https://doi.org/10.1111/j.1365-246X.2006.02981.x).
- [40] R. E. Abercrombie, *Earthquake source scaling relationships from -1 to 5 ML using seismograms recorded at 2.5-km depth*, *Journal of Geophysical Research: Solid Earth* **100** (1995), [10.1029/95JB02397](https://doi.org/10.1029/95JB02397).
- [41] J. N. Brune, *Tectonic stress and the spectra of seismic shear waves from earthquakes*, *Journal of Geophysical Research* **75** (1970), [10.1029/JB075i026p04997](https://doi.org/10.1029/JB075i026p04997).
- [42] K. Aki, *Scaling law of seismic spectrum*, *Journal of Geophysical Research* **72** (1967).
- [43] K. Aki, *Scattering conversions P to S versus S to P*, *Bulletin of the Seismological Society of America* **82** (1992).
- [44] D. Draganov, R. Ghose, E. Ruigrok, J. Thorbecke, and K. Wapenaar, *Seismic interferometry, intrinsic losses and Q-estimation*, *Geophysical Prospecting* **58** (2010), [10.1111/j.1365-2478.2009.00828.x](https://doi.org/10.1111/j.1365-2478.2009.00828.x).
- [45] D. Draganov, R. Ghose, K. Heller, and E. Ruigrok, *Monitoring changes in velocity and Q using non-physical arrivals in seismic interferometry*, *Geophysical Journal International* **192** (2013), [10.1093/gji/ggs037](https://doi.org/10.1093/gji/ggs037).



# 3

## CRUSTAL-SCALE SEISMIC IMAGING

**Yohei NISHITSUJI, Shohei MINATO, Boris BOULLENGER,  
Martín GOMEZ, Kees WAPENAAR, Deyan DRAGANOV**

*There are two ways to be fooled. One is to believe what isn't true;  
the other is to refuse to believe what is true.*

Søren Kierkegaard

### **Summary**

*We present seismic interferometry for P-wave coda from local earthquakes (LEPC SI) in order to obtain crustal-scale reflection imaging without active sources. We apply LEPC SI with a linear array in the Malargüe region, Argentina, where a part of the Neuquén basin exists underneath. We compare SI by crosscorrelation, crosscoherence, and MDD, each followed by standard seismic processing from exploration seismology. For the MDD method, we find that the truncated SVD scheme gives a more stable solution of the matrix inversion than the one by damped least-squares. This MDD result provides us slightly better structural imaging at our scale of interest among all LEPC SI approaches we investigate. We also interpret not only the deep thrust fault but also possible melting zones that are previously suggested by active-seismic (including exploration well) as well as magnetotelluric surveys. Depending on the frequency-bandwidth, the availability of the local earthquakes, and the spatial sampling of receivers, LEPC SI has a potential to reveal not only the crustal-scale structure but also lithospheric-scale or basin-scale structures.*

---

This chapter has been published in Interpretation 4, 3 (2016) [1].

Note that minor changes have been introduced to make the text consistent with the other chapters of this thesis.

### 3.1. LOCAL EARTHQUAKE P-WAVE CODA SEISMIC INTERFEROMETRY

#### 3.1.1. INTRODUCTION

Crustal imaging is vitally relevant for understanding processes like earthquake mechanisms, magmatism, and basin tectonics. It can also contribute to resource exploration, e.g., exploration for deep geothermal energy. In order to obtain an image of the crust, both active sources (e.g. vibroseis and airguns) and passive sources (e.g. ambient noise and earthquakes) have been used. For the former, the reflection method [e.g. 2] and refraction method [e.g. 3] are well known, whereas for the latter, travelttime tomography [4], full waveform tomography [5], receiver function [6], and the Sp-waves method [7] have been applied.

A very attractive passive seismic method is seismic interferometry (SI) [e.g. 8–12], which retrieves virtual seismic records from existing seismic records. In this study, we focus on body-wave SI. Although the imaging resolution achieved by passive SI might not be easily compatible with the one achieved by the active-source reflection method, it has a potential to contain low-frequency information, i.e.,  $< 5$  Hz, which enables us to interpret deeper structures, such as in the lower crust and lithosphere. Moreover, as an economically attractive aspect, the shooting cost of the passive seismic method is zero. For reflection retrieval by passive SI, several applications have been already reported, both for ambient noise [e.g. 13–17] and local earthquakes [e.g. 18, 19].

There are five ways SI can be applied: using correlation [8, 9, 20]; coherence [8]; trace deconvolution [21–23]; convolution [24]; and multidimensional deconvolution (MDD; [25]). Nakata *et al.* [18] compared the common midpoint (CMP) stacks obtained from SI by crosscorrelation, trace deconvolution, and crosscoherence using traffic noise. The authors suggested that the selection of a proper SI method depends on the data set at hand. In addition to the synthetic comparison of the results obtained from crosscorrelation and MDD by Wapenaar *et al.* [26], Nakata *et al.* [19] compared SI results obtained using trace deconvolution, crosscoherence, and MDD results (after applying wavefield decomposition), applied to data representing local earthquakes in order to retrieve reflected plane waves. They concluded that MDD provides gathers that have the best signal-to-noise ratio (SNR) among the compared SI methods.

In this chapter, we propose a seismic imaging technique that applies passive SI (two-way travelttime  $\leq 20$  s) to P-wave coda due to local earthquakes ( $2^\circ \leq$  epicentral distances  $\leq 6^\circ$ ). Hereafter, we abbreviate this method as LEPC (local-earthquake P-wave coda) SI. The coda waves are the tail part of a signal consisting of multiply scattered waves [27]. Hence, we assume that their directivity is weak [e.g. 28–30], and thus that they illuminate the subsurface beneath the receivers favourably for retrieval of reflections. We apply LEPC SI to data recorded by an exploration-type receiver array called MalARRgue [31] that was located in the Malargüe region (Mendoza, Argentina) (Figure 3.1). Because the west coast of Chile has considerable seismicity due to the Nazca-slab subduction, we choose this region to test LEPC SI.

In the following, we show how to apply LEPC SI using the different retrieval methods (crosscorrelation, crosscoherence, and MDD) for the purpose of crustal-scale reflection imaging.

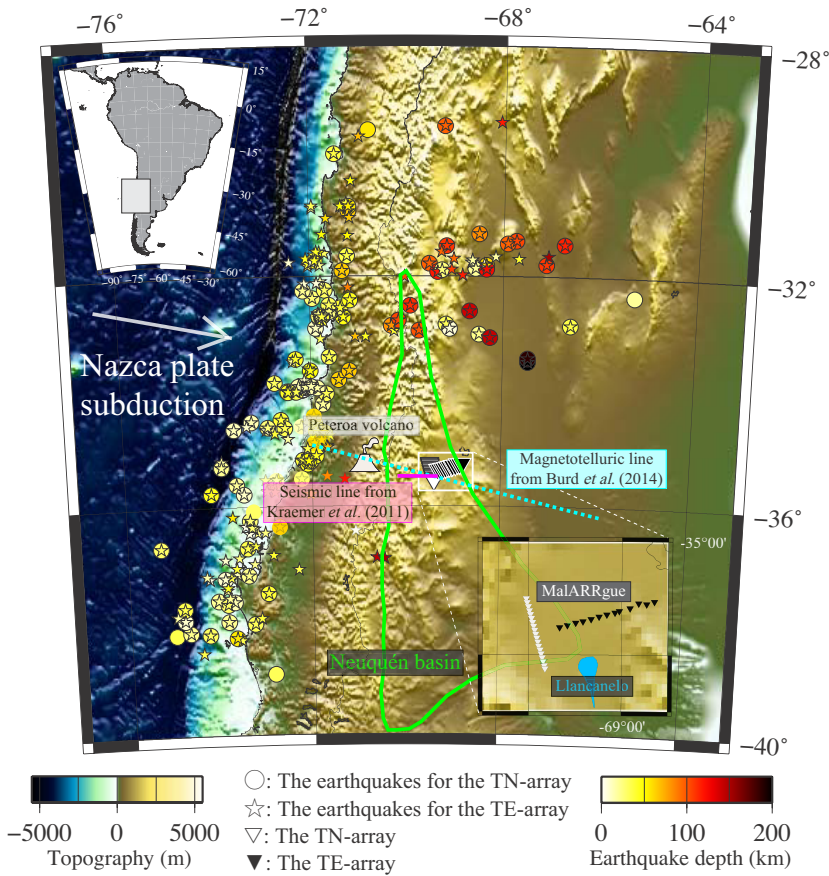


Figure 3.1: Distribution map of the local earthquakes ( $2^\circ \leq$  epicentral distances  $\leq 6^\circ$ ) used in our study. The 115 circles and 210 stars show the locations of the earthquakes recorded by the TN- (the white triangles) and TE-array (black triangles) parts of the MalARRgue array; the earthquakes are color-scaled as a function of their focal depth. The volcano symbol indicates the location of the Peteroa volcano. The green outline indicates an approximated location of the Neuquén basin (derived from [32]). The blue polygon indicates an approximated location of the lake Llanquanelo. The magenta solid and blue dashed lines indicate the location at which active-source seismic and a magnetotelluric sections are obtained by Kraemer *et al.* [33] and Burd *et al.* [34], respectively, which are discussed in Results and Interpretation of this chapter



### 3.1.2. STUDY AREA AND DATA

The Malargüe region is located in the northern part of the Neuquén basin, Argentina. This basin has been producing nearly half of the Argentine hydrocarbons, but has also been providing geothermal power. The Peteroa Volcano, which is an active volcano in the Andes Mountains in the Malargüe region, is situated close to part of the array we use (Figure 3.1). The locations of local earthquakes that occurred in 2012 around the Malargüe region are shown in Figure 3.1 on a topography map [35]. The source locations of the earthquakes are provided by Java version of Windows Extracted from Event Data (JWEED) operated by the Incorporated Research Institutions for Seismology (IRIS). We define local earthquakes as those earthquakes whose epicentral distances are between  $2^\circ$  and  $6^\circ$ . This definition is close to the one introduced by Kayal [36]. For the sake of terminological clarification, regional earthquakes, which we do not use in this study, are the earthquakes whose epicentral distances are larger than  $6^\circ$ . In Figure 3.1, we indicate with triangles the location of the part of the MalARRgue that we use in our study: the T-array, which is an linear receiver array deployed at the surface. The T-array consists of two linear subarrays: the TN-array with 19 stations spaced every 2 km (labelled TN02 to TN20; white triangles in Figure 3.1), oriented in the NNW direction; the TE-array with 13 stations spaced every 4 km (labelled TE01 to TE13; black triangles in Figure 3.1), oriented in the ENE direction. These stations are three-component velocity sensors. The 115 circles and 210 stars indicate the location of the local earthquakes recorded by the TN- and TE-array, respectively, and characterized by sufficient SNR of the P-wave coda. The TE-array recorded a higher number of earthquakes than the TN-array, because the TE-array was operating longer. The coverage of back azimuth of these earthquakes with respect to the T-array is wide (see Figures 3.1 and 3.2). A complete list of the local earthquakes used in this study is shown in Table 3.1.

Table 3.1: Local earthquakes used in this study

Date (month/d/yr)	Time (hr:min:s)	Lat. (°N)	Lon. (°E)	Dep. (km)	$M_b$	Array ID
01/17/12	15:09:02	-30.814	-71.214	75	3.9	TE
01/17/12	23:21:34	-31.605	-71.686	31	5.5	TE
01/18/12	03:17:16	-31.589	-71.789	50	4.7	TE
01/18/12	11:33:03	-31.798	-68.397	10	4.6	TE
01/18/12	11:35:52	-31.665	-68.164	19	5.0	TE
01/19/12	03:58:17	-31.756	-68.657	15	4.6	TE
01/19/12	07:16:20	-31.635	-71.898	38	4.9	TE
01/19/12	08:22:49	-32.193	-71.213	87	3.9	TE
01/20/12	05:26:33	-31.273	-71.736	49	3.4	TE
01/20/12	06:05:41	-31.982	-68.843	117	3.5	TE
01/23/12	16:04:53	-36.455	-73.182	24	5.8	TE
01/23/12	16:29:30	-36.380	-73.267	25	4.0	TE
01/23/12	16:30:55	-36.457	-73.023	25	3.9	TE
01/23/12	17:22:06	-36.344	-73.443	4	5.0	TE
01/23/12	17:53:45	-36.472	-73.365	6	4.4	TE
01/23/12	21:55:15	-36.364	-73.304	28	5.0	TE
01/24/12	01:45:28	-34.525	-71.949	40	4.5	TE
01/24/12	16:08:48	-31.651	-67.078	150	3.7	TE
01/24/12	17:07:49	-31.760	-72.416	9	4.6	TE
01/26/12	02:23:10	-29.325	-68.081	118	3.6	TE
01/26/12	04:57:07	-34.831	-72.498	19	3.9	TE
01/27/12	02:24:10	-34.708	-71.824	17	4.1	TE
01/31/12	13:08:00	-33.817	-72.135	12	4.6	TE
01/31/12	19:40:03	-33.876	-71.997	18	4.0	TE
01/31/12	21:24:05	-32.788	-71.712	39	3.3	TE
02/01/12	02:43:19	-32.678	-71.336	52	4.8	TE
02/01/12	02:43:25	-32.950	-70.256	40	4.7	TE
02/01/12	02:43:27	-33.053	-70.851	44	4.7	TE
02/04/12	10:12:55	-38.551	-74.433	35	4.2	TE
02/05/12	03:42:08	-36.690	-73.243	38	4.7	TE
02/07/12	12:02:11	-37.902	-74.974	18	4.9	TE
02/10/12	02:05:22	-30.791	-71.304	57	4.9	TE
02/10/12	04:07:51	-30.735	-71.222	38	3.8	TE

02/11/12	02:58:17	-37.456	-73.884	20	5.6	TE
02/11/12	08:41:14	-36.851	-72.860	40	4.0	TE
02/14/12	05:58:02	-32.010	-70.034	103	4.5	TE
02/14/12	08:19:27	-34.948	-71.684	52	4.5	TE
02/15/12	07:36:14	-34.665	-72.958	10	4.4	TE
02/15/12	14:08:47	-35.209	-73.926	19	4.7	TE
02/16/12	22:01:46	-37.255	-74.245	5	4.2	TE
02/17/12	08:01:14	-37.208	-74.313	17	4.8	TE
02/17/12	08:01:19	-37.175	-73.646	14	4.8	TE
02/17/12	19:11:23	-37.233	-73.785	35	4.3	TE
02/18/12	02:06:27	-34.547	-72.098	29	4.5	TE
02/18/12	03:50:49	-37.104	-72.316	35	4.0	TE
02/18/12	17:44:48	-32.097	-71.771	18	4.9	TE
02/22/12	15:03:39	-33.089	-71.785	33	4.5	TE
02/22/12	22:38:40	-34.765	-71.809	47	4.0	TE
03/01/12	06:44:27	-38.331	-73.585	35	4.2	TE
03/01/12	18:41:47	-31.572	-69.273	96	4.6	TE
03/03/12	11:01:47	-30.348	-71.129	49	5.5	TE
03/03/12	22:12:55	-35.749	-72.800	13	4.9	TE
03/03/12	22:45:40	-35.731	-72.966	10	4.7	TE
03/03/12	23:41:30	-35.528	-72.726	28	4.6	TE
03/03/12	23:43:04	-35.740	-72.975	10	4.9	TE
03/09/12	00:43:36	-34.730	-72.781	39	4.3	TE
03/12/12	19:37:36	-34.969	-71.664	70	4.9	TE
03/16/12	06:20:12	-36.895	-73.596	27	4.7	TE
03/16/12	23:31:54	-33.606	-72.038	46	4.7	TE
03/17/12	01:36:00	-33.480	-72.372	21	4.0	TE
03/21/12	02:41:00	-35.789	-72.029	67	4.6	TE
03/23/12	09:25:32	-31.691	-69.025	95	4.3	TE
03/24/12	07:28:33	-33.052	-71.063	69	5.0	TE
03/25/12	22:37:06	-35.200	-72.217	41	6.5	TE
03/26/12	02:07:41	-34.994	-72.092	35	4.4	TE
03/27/12	02:46:12	-37.002	-73.275	23	4.5	TE
03/28/12	03:23:39	-35.541	-72.998	16	4.7	TE
03/30/12	07:12:52	-35.196	-72.187	38	4.5	TE/TN
03/31/12	21:52:56	-35.267	-72.089	43	4.4	TE/TN
04/01/12	19:09:57	-31.908	-71.322	65	4.9	TE/TN
04/03/12	02:11:03	-33.847	-72.757	32	5.0	TE/TN
04/06/12	01:30:12	-34.766	-71.608	37	3.7	TE
04/06/12	13:25:05	-38.226	-75.019	35	4.9	TN
04/06/12	17:11:27	-36.926	-73.899	10	4.7	TE
04/06/12	21:04:54	-35.598	-72.834	13	4.1	TE/TN
04/07/12	19:13:29	-37.408	-73.870	44	4.4	TE
04/13/12	06:13:16	-35.210	-72.020	40	4.7	TE/TN
04/15/12	18:58:21	-32.385	-71.940	27	4.4	TE/TN
04/16/12	10:34:14	-36.241	-73.352	27	4.3	TE/TN
04/17/12	03:50:16	-32.625	-71.365	29	6.2	TE/TN
04/17/12	04:03:18	-32.553	-71.366	40	4.9	TE/TN
04/17/12	17:53:57	-33.998	-72.342	11	4.1	TE/TN
04/17/12	23:37:36	-32.617	-71.591	25	3.5	TE/TN
04/19/12	01:14:06	-30.868	-71.188	65	4.7	TE/TN
04/21/12	05:14:37	-36.354	-72.709	63	4.0	TE/TN
04/21/12	22:18:11	-38.224	-74.289	31	4.7	TE/TN
04/27/12	17:58:24	-35.121	-71.901	43	4.7	TE/TN
04/27/12	18:34:38	-34.722	-71.721	43	4.7	TE/TN
04/28/12	20:46:48	-32.653	-71.829	5	4.1	TE
04/30/12	07:39:46	-29.868	-71.460	37	5.6	TE/TN
05/01/12	02:43:34	-29.456	-70.770	57	4.6	TN
05/01/12	20:52:14	-30.813	-71.935	22	4.8	TE
05/05/12	23:06:53	-31.474	-69.173	110	4.3	TE/TN
05/10/12	17:11:52	-37.249	-73.914	10	4.4	TE/TN
05/11/12	19:41:21	-32.901	-71.878	13	4.3	TE/TN
05/12/12	05:27:36	-34.896	-71.864	44	4.0	TE/TN
05/12/12	18:15:09	-34.523	-73.269	15	4.7	TE/TN
05/13/12	12:42:50	-32.740	-71.799	12	4.8	TE/TN
05/16/12	09:02:01	-36.901	-70.623	144	4.3	TE
05/16/12	10:15:36	-35.528	-71.312	118	4.3	TE
05/17/12	02:34:14	-31.777	-69.530	97	4.4	TE/TN
05/17/12	06:50:54	-32.697	-71.816	29	4.6	TE/TN
05/18/12	10:33:12	-31.807	-68.348	60	4.4	TE/TN
05/20/12	03:32:00	-30.782	-71.353	48	3.8	TE
05/21/12	05:15:26	-31.263	-68.507	84	4.3	TE/TN
05/21/12	11:13:33	-30.994	-71.648	59	4.4	TE
05/22/12	06:22:01	-32.244	-71.691	31	4.3	TE/TN
05/24/12	19:18:55	-36.912	-70.467	150	5.1	TE
05/31/12	08:27:17	-34.225	-71.751	20	4.5	TE/TN
06/01/12	18:19:52	-31.718	-68.635	19	4.7	TE
06/02/12	21:36:12	-36.174	-73.725	56	4.1	TE
06/07/12	07:40:54	-31.643	-71.219	36	4.7	TE/TN
06/11/12	09:50:59	-37.072	-73.661	40	4.2	TE
06/15/12	05:43:13	-38.188	-74.702	22	4.7	TE/TN
06/18/12	07:46:23	-36.692	-75.280	30	4.2	TE/TN
06/18/12	08:29:04	-33.009	-68.496	23	5.3	TE/TN
06/21/12	09:24:22	-35.523	-72.223	28	4.5	TE/TN
06/23/12	06:39:32	-34.563	-71.919	47	4.2	TE/TN
06/23/12	18:14:21	-31.580	-71.856	42	4.7	TE
06/25/12	13:38:17	-37.970	-74.821	10	4.6	TE/TN
06/26/12	07:09:27	-35.473	-71.676	84	4.5	TE
06/26/12	17:01:37	-37.758	-74.820	35	4.6	TE/TN
06/27/12	13:06:34	-31.701	-67.692	41	4.5	TE

06/27/12	22:04:25	-32.676	-71.722	20	3.9	TE/TN
06/28/12	10:33:17	-36.085	-73.270	30	4.3	TN
06/28/12	11:49:11	-31.447	-66.754	116	4.6	TE/TN
07/04/12	08:33:05	-38.040	-73.288	33	4.7	TE/TN
07/04/12	22:57:16	-37.631	-74.077	21	4.6	TE/TN
07/05/12	05:53:00	-34.494	-72.638	39	3.9	TE/TN
07/07/12	10:52:15	-32.502	-71.600	33	4.8	TE/TN
07/09/12	01:44:27	-35.213	-72.069	50	4.5	TE/TN
07/09/12	12:56:37	-33.061	-68.263	142	4.6	TE/TN
07/09/12	14:24:37	-37.700	-73.870	30	4.3	TE/TN
07/15/12	08:23:25	-33.483	-67.477	200	4.6	TE/TN
07/17/12	22:03:26	-31.298	-71.210	52	4.0	TE
07/30/12	18:49:45	-35.771	-74.163	44	4.8	TE/TN
08/02/12	15:01:32	-31.862	-68.575	20	4.3	TE/TN
08/04/12	13:11:46	-32.835	-69.175	33	4.3	TE/TN
08/04/12	19:05:39	-31.928	-69.358	119	5.0	TE/TN
08/17/12	20:19:54	-35.613	-73.615	20	4.7	TE/TN
08/23/12	19:03:48	-35.776	-73.462	11	4.8	TE/TN
08/24/12	22:30:01	-33.434	-72.310	42	4.7	TE/TN
08/27/12	01:29:45	-31.386	-67.746	105	4.2	TE/TN
08/27/12	04:17:56	-34.709	-71.762	55	4.0	TE/TN
08/28/12	08:11:25	-32.418	-71.169	44	4.8	TE/TN
08/30/12	08:04:40	-37.199	-73.397	23	5.0	TE/TN
09/04/12	05:30:17	-32.516	-69.916	112	4.5	TE/TN
09/06/12	18:58:03	-36.719	-73.408	35	4.7	TE/TN
09/11/12	06:35:38	-31.875	-68.350	124	5.1	TE/TN
09/11/12	07:24:37	-38.001	-73.860	21	4.6	TE/TN
09/12/12	09:20:58	-32.606	-68.692	139	4.6	TE/TN
09/15/12	00:40:16	-34.638	-72.564	34	4.7	TE/TN
09/15/12	00:50:45	-34.622	-72.923	26	4.5	TE/TN
09/15/12	09:37:18	-32.853	-66.601	36	4.6	TE/TN
09/18/12	03:53:30	-31.893	-69.262	26	4.4	TE/TN
09/20/12	10:07:07	-34.436	-71.951	60	4.5	TE/TN
09/21/12	09:22:26	-32.947	-69.739	101	4.4	TE/TN
09/28/12	03:11:50	-31.430	-67.915	96	4.1	TE/TN
09/28/12	19:21:47	-34.603	-73.369	10	4.3	TE
10/01/12	08:06:29	-30.786	-71.184	56	4.6	TE/TN
10/05/12	08:44:51	-34.899	-71.937	60	4.4	TE/TN
10/06/12	03:18:15	-32.132	-72.107	9	4.6	TE
10/06/12	22:49:38	-32.127	-71.860	7	4.3	TE
10/08/12	13:03:42	-34.654	-73.639	14	4.2	TE/TN
10/09/12	03:30:33	-29.393	-69.211	97	4.8	TE/TN
10/10/12	18:05:02	-34.039	-71.675	33	4.1	TE/TN
10/11/12	02:38:30	-34.000	-72.500	32	4.6	TE/TN
10/11/12	04:38:24	-33.996	-72.442	35	4.7	TE/TN
10/11/12	17:22:10	-32.865	-70.310	82	5.5	TE/TN
10/11/12	21:36:08	-34.011	-72.483	43	4.2	TE/TN
10/14/12	03:37:30	-34.606	-72.209	15	4.5	TE/TN
10/14/12	10:50:17	-35.310	-73.932	21	4.8	TE/TN
10/15/12	21:04:21	-31.814	-71.787	24	5.2	TE
10/18/12	04:38:00	-31.827	-72.034	29	4.5	TE
10/18/12	05:23:14	-34.689	-71.906	43	4.2	TE/TN
10/19/12	05:35:22	-31.793	-72.024	43	3.8	TE
10/19/12	22:48:18	-31.758	-71.950	10	4.6	TE
10/20/12	00:25:48	-32.251	-72.141	22	4.4	TE/TN
10/21/12	11:40:36	-37.658	-73.723	15	4.5	TE/TN
10/24/12	03:46:30	-31.698	-72.069	44	4.7	TE
10/25/12	05:37:58	-32.773	-70.165	105	4.8	TE/TN
10/25/12	19:25:41	-29.568	-70.968	69	4.1	TE
10/27/12	12:33:05	-33.642	-72.006	47	4.4	TE/TN
10/28/12	01:43:00	-33.404	-71.608	34	3.9	TE/TN
11/01/12	23:43:38	-31.794	-67.119	109	4.3	TE/TN
11/02/12	23:42:36	-34.848	-71.789	60	4.5	TE/TN
11/04/12	14:33:06	-31.729	-71.885	43	4.2	TE/TN
11/07/12	15:16:27	-30.780	-71.934	34	4.6	TE
11/07/12	18:37:50	-37.948	-73.141	38	4.4	TE
11/07/12	22:41:33	-37.512	-72.985	39	4.8	TE/TN
11/08/12	06:24:10	-32.710	-71.310	46	4.3	TE/TN
11/08/12	23:57:57	-31.882	-69.070	107	4.6	TE
11/09/12	06:31:44	-33.427	-67.479	187	4.1	TE/TN
11/11/12	05:10:56	-33.962	-72.132	13	4.6	TE/TN
11/11/12	05:46:48	-33.977	-72.183	16	4.8	TE/TN
11/11/12	07:24:21	-33.973	-72.272	38	4.4	TE/TN
11/15/12	20:32:37	-32.666	-71.825	23	4.7	TE
11/15/12	23:41:02	-30.988	-71.171	66	4.2	TE
11/17/12	23:51:39	-37.594	-73.825	21	4.0	TE
11/18/12	13:29:28	-38.286	-73.690	56	4.7	TE/TN
11/19/12	14:08:59	-33.969	-72.150	1	4.2	TE/TN
11/19/12	16:45:50	-33.928	-72.170	11	5.1	TE/TN
11/20/12	16:23:25	-33.921	-72.254	16	5.4	TE/TN
11/21/12	18:16:38	-33.931	-72.100	19	5.1	TE/TN
11/21/12	21:36:23	-33.939	-71.868	18	5.7	TE/TN
11/21/12	22:51:23	-34.012	-72.305	35	4.2	TE/TN
11/21/12	22:52:29	-33.916	-71.994	16	5.2	TE/TN
11/29/12	00:09:39	-32.910	-69.106	8	5.0	TE/TN
11/29/12	20:40:59	-36.426	-71.082	3	4.2	TE
12/02/12	03:29:23	-35.541	-72.766	15	4.3	TE/TN
12/04/12	09:26:14	-32.710	-71.751	38	4.6	TE/TN
12/10/12	15:25:47	-38.932	-72.862	33	4.8	TN
12/16/12	22:46:11	-33.803	-71.408	63	4.7	TE/TN

12/17/12	08:38:25	-32.342	-65.287	20	4.4	TN
12/18/12	00:45:03	-33.645	-71.187	66	3.7	TE/TN

### 3.1.3. LOCAL-EARTHQUAKE P-WAVE CODA SEISMIC INTERFEROMETRY

#### CROSSCORRELATION

In Claerbout [9], virtual reflection traces were retrieved from the autocorrelation of the recorded transmission response in a horizontally layered medium. Later, he conjectured that in 3D inhomogeneous media, one has to use crosscorrelation to retrieve the reflection response between two receivers at the surface. This was proven by Wapenaar [12] for an arbitrary inhomogeneous elastic medium. The author showed that the Green's function  $G_{p,q}^{v,t}(\mathbf{x}_A, \mathbf{x}_B, \omega)$ , representing particle-velocity measurement ( $v$ ) in the  $p$ -direction at a receiver at  $\mathbf{x}_A$  due to a point single-force ( $t$ ) at  $\mathbf{x}_B$  in the  $q$ -direction, can be retrieved from the crosscorrelation of observed particle-velocity measurements  $v_p^{obs}$  and  $v_q^{obs}$  at  $\mathbf{x}_A$  and  $\mathbf{x}_B$ , respectively, from uncorrelated noise sources in the subsurface:

$$2\text{Re}\{G_{p,q}^{v,t}(\mathbf{x}_A, \mathbf{x}_B, \omega)\} S_N(\omega) \approx -\left\langle \left\{ v_p^{obs}(\mathbf{x}_A, \omega) \right\}^* \left\{ v_q^{obs}(\mathbf{x}_B, \omega) \right\} \right\rangle. \quad (3.1)$$

The above equation is written in the frequency domain, indicated by the angular frequency  $\omega$ ; the asterisk denotes complex conjugation;  $\langle \rangle$  indicates averaging over source realizations; and the particle-velocity measurements are in the  $p$ - and  $q$ -directions. The observed data  $v^{obs}$  is representing the superposition of recordings from uncorrelated noise sources distributed along a surface that illuminated the receivers from all directions.  $S_N(\omega)$  denotes the power spectrum of the noise. Due to the source-receiver configuration in this study, we exclude the direct wave, which would not fall inside the stationary-phase region for retrieval of reflections. This happens because the epicentral distances of the earthquakes are relatively long compared to their hypocentral depth. We thus aim to use arrivals characterized by slowness smaller than the ones characterizing the direct waves. Note that the exclusion of the direct waves might give rise to artifacts in the retrieved response. Nevertheless, these artifacts should not pose a problem as long as our main aim is to recover the primary reflections. Moreover, having sufficiently long recordings of coda waves would ensure illumination of the receivers from all directions due to equipartitioning. In such a case, one can exchange the noise recordings in equation 3.1 by recordings of coda waves  $v^c$ . For our application, we define an observed P-wave coda of a local earthquake as

$$v_z^c(\mathbf{x}_A, \omega) = G_z^c(\mathbf{x}_A, \mathbf{x}_S, \omega) E(\mathbf{x}_S, \omega), \quad (3.2)$$

where  $z$  indicates that we are using the vertical component of the recordings and  $E(\mathbf{x}_S, \omega)$  is the Fourier transform of the source time function (STF) of a local earthquake at  $\mathbf{x}_S$  in the subsurface. As P-wave coda, we use the part of the recording after the direct arrival of the P-phase and before the direct arrival of the S-phase.

Because of the limitation on the length of the coda recordings, we cannot expect that the receivers would be illuminated equally well from all directions. Because of this, we would like to repeat the correlation for many local earthquakes with wide distribution of

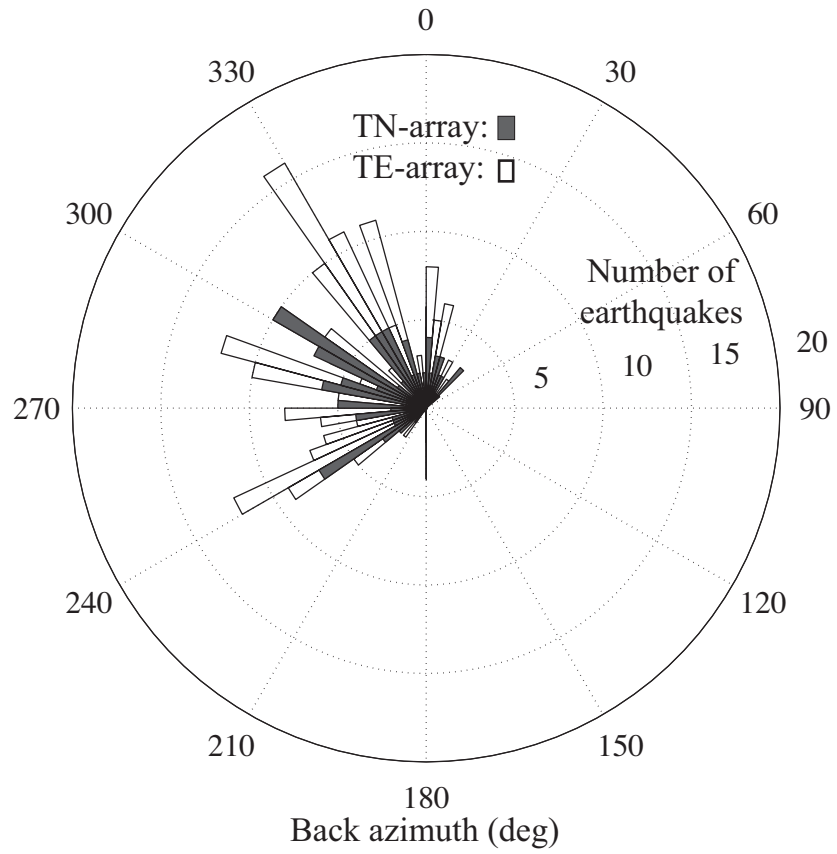


Figure 3.2: Distribution of the back azimuth of the local earthquakes recorded by the TN-array and TE-array.

the back azimuth (see Figures 3.1 and 3.2) and to average the separate correlations. Thus we rewrite equation 3.1 as

$$2\text{Re}\{G_{z,z}^{v,t}(\mathbf{x}_A, \mathbf{x}_B, \omega)\} \bar{S}_E(\omega) \propto - \sum_{S=1}^n [\{v_z^c(\mathbf{x}_A, \omega)\}^* v_z^c(\mathbf{x}_B, \omega)], \quad (3.3)$$

where we have exchanged  $\langle \rangle$  of equation 3.1 by a summation over the independent local earthquakes.  $\bar{S}_E(\omega)$  denotes the average power spectrum of the STF over the earthquakes.

### CROSSCOHERENCE

The crosscoherence method [8] is a technique to normalize the amplitude among different source or receiver pairs. By applying SI by crosscoherence instead of crosscorrelation we expect to retrieve better SNR in terms of the phase in comparison with the crosscorrelation [e.g. 18, 37]. To apply SI by crosscoherence, we rewrite equation 3.3 as

$$2\text{Re}\{G_{z,z}^{v,t}(\mathbf{x}_A, \mathbf{x}_B, \omega)\} \propto \sum_{S=1}^n \frac{\{v_z^c(\mathbf{x}_A, \omega)\}^* v_z^c(\mathbf{x}_B, \omega)}{|v_z^c(\mathbf{x}_A, \omega)| |v_z^c(\mathbf{x}_B, \omega)| + \epsilon}, \quad (3.4)$$

where  $\epsilon$  denotes a stabilization factor (also called a damping factor or a regularization parameter). Since the crosscoherence enhances both the signal and the noise, it is important to have data that is not dominated by noise. Note that in the above equation, the retrieved Green's function is no longer modulated by the average power spectrum of the STF, as the crosscoherence eliminates it.

### MULTIDIMENSIONAL DECONVOLUTION (MDD)

While the aforementioned crosscorrelation and crosscoherence calculate the reflection response trace by trace, MDD is a receiver-array-based SI method that calculates the reflection response (the scattered Green's function in [26]) simultaneously for all observed responses via matrix inversion. Although the application of MDD requires regularly-spaced receivers, a point-spread function (PSF), and a regularization approach for the matrix inversion, this technique theoretically removes the influence of the (variation of the) STF of the sources, takes intrinsic attenuation into account (which is not the case for correlation nor coherence) and compensates for possibly inhomogeneous illumination of the receivers by the coda wavefield.

The PSF is a well-known gauge for imaging quality in optics, such as microscopy. In exploration seismology, the PSF is used to quantify the effect of the source and receiver distribution and of the STF on the imaging results. In analogy with this, van der Neut *et al.* [38, 39] showed that the result from SI by crosscorrelation could actually be seen as the blurring (temporal and spatial convolution) of the desired scattered Green's function with a PSF. This PSF is obtained from the crosscorrelation of recordings at the receivers at the surface as if above the receivers there were a homogeneous half space [e.g. 26]. Nakahara and Haney [40] recently showed that the PSF could also be used for studying earthquake sources. Application of SI by MDD is actually deconvolving the crosscorrelation result by the PSF. To obtain the required wavefield for the retrieval of the correlation result and the PSF, one can apply wavefield decomposition at the Earth's surface [19].

This, though, would require a good velocity model for the near surface, which in areas like Malargüe, characterized by strong lateral inhomogeneity, is not readily available. Because it is not possible to obtain measurements as if the Earth's surface were covered by a homogeneous half space, following Wapenaar *et al.* [26], we use an approximate relation for the application of SI by MDD:

$$\sum_{S=1}^n [\{v_z^c(\mathbf{x}_A, \omega)\}^* v_z^c(\mathbf{x}_B, \omega)] - 2\Gamma(\mathbf{x}_B, \mathbf{x}_A, \omega) \propto \iint_{\partial D_0} G_{z,z}^{scatt,d}(\mathbf{x}_B, \mathbf{x}, \omega) \Gamma(\mathbf{x}, \mathbf{x}_A, \omega) d^2 \mathbf{x}, \quad (3.5)$$

where  $\Gamma$  is the approximated PSF and  $G_{z,z}^{scatt,d}$  is the scattered Green's function due to a dipole source. Figure 3.3 shows a schematic image of the terms in equation 3.5. The integral in equation 3.5 is taken along the receiver positions (Earth's surface  $\partial D_0$ ). A derivation of equation 3.5 is given in Appendix B. Just like Wapenaar *et al.* [26], we look at the recorded wavefield as a part that will be recorded at the receivers in the absence of a free surface and a part due to the presence of the free surface (which is the former after being reflected at the free surface at least once). The  $\Gamma$  in equation 3.5 (see Figures 3.9c and 3.9f later in this paper) can be estimated by extracting time-windowed signals from the crosscorrelation at  $\mathbf{x}_A$  and  $\mathbf{x}_B$  (the right-hand side of equation 3.3) (see Figures 3.9c and 3.9f later in this paper) of the wavefield that would be recorded in the absence of a free surface at the receivers. The signals that make up  $\Gamma$  exhibit a butterfly-shaped window around  $t = 0$  (see Figures 3.9c and 3.9f later in this paper), narrowest when  $\mathbf{x}_A = \mathbf{x}_B$ . We assume that the contribution from the crosscorrelation at  $\mathbf{x}_A$  and  $\mathbf{x}_B$  of the wavefield that would be recorded due to the presence of a free surface at the receivers is sufficiently small to be neglected [26, 38]. Note that the numerical test showed that the approximation can provide the correct scattered Green's function with small inversion artifacts [38]. For notational simplicity, we define the left hand-side of equation 3.5 as

$$C'(\mathbf{x}_B, \mathbf{x}_A, \omega) = \sum_{S=1}^n [\{v_z^c(\mathbf{x}_A, \omega)\}^* v_z^c(\mathbf{x}_B, \omega)] - 2\Gamma(\mathbf{x}_B, \mathbf{x}_A, \omega). \quad (3.6)$$

Substituting equation 3.6 in equation 3.5, we obtain

$$C'(\mathbf{x}_B, \mathbf{x}_A, \omega) \propto \iint_{\partial D_0} G_{z,z}^{scatt,d}(\mathbf{x}_B, \mathbf{x}, \omega) \Gamma(\mathbf{x}, \mathbf{x}_A, \omega) d^2 \mathbf{x}. \quad (3.7)$$

Equation 3.7 can be discretized by fixing the position of  $\mathbf{x}_B$  and varying the receiver position  $\mathbf{x}_A$ :

$$\begin{pmatrix} C'(\mathbf{x}_B, \mathbf{x}_1, \omega) \\ C'(\mathbf{x}_B, \mathbf{x}_2, \omega) \\ \vdots \\ C'(\mathbf{x}_B, \mathbf{x}_m, \omega) \end{pmatrix} \propto \begin{pmatrix} \Gamma(\mathbf{x}_1, \mathbf{x}_1, \omega) & \Gamma(\mathbf{x}_2, \mathbf{x}_1, \omega) & \cdots & \Gamma(\mathbf{x}_m, \mathbf{x}_1, \omega) \\ \Gamma(\mathbf{x}_1, \mathbf{x}_2, \omega) & \Gamma(\mathbf{x}_2, \mathbf{x}_2, \omega) & \cdots & \Gamma(\mathbf{x}_m, \mathbf{x}_2, \omega) \\ \vdots & \vdots & \ddots & \vdots \\ \Gamma(\mathbf{x}_1, \mathbf{x}_m, \omega) & \Gamma(\mathbf{x}_2, \mathbf{x}_m, \omega) & \cdots & \Gamma(\mathbf{x}_m, \mathbf{x}_m, \omega) \end{pmatrix} \begin{pmatrix} G_{z,z}^{scatt,d}(\mathbf{x}_B, \mathbf{x}_1, \omega) \\ G_{z,z}^{scatt,d}(\mathbf{x}_B, \mathbf{x}_2, \omega) \\ \vdots \\ G_{z,z}^{scatt,d}(\mathbf{x}_B, \mathbf{x}_m, \omega) \end{pmatrix}, \quad (3.8)$$

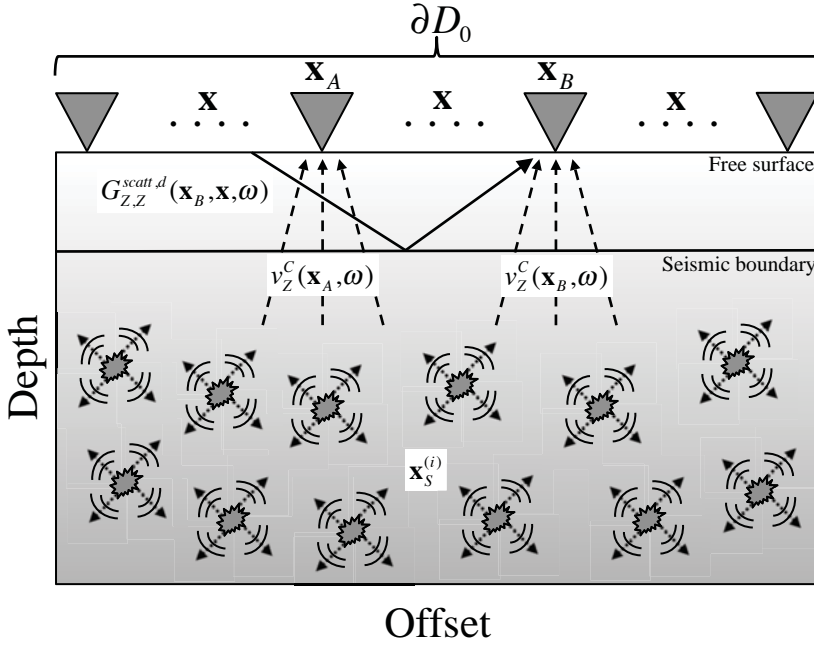


Figure 3.3: Distribution of the back azimuth of the local earthquakes recorded by the TN-array and TE-array.

where we assume that we have  $m$  receivers in total. We can simplify equation 3.8 using matrix-vector notation:

$$\mathbf{c}' \propto \mathbf{\Gamma} \mathbf{g}, \quad (3.9)$$

where  $\mathbf{\Gamma}$  is a  $m \times m$  matrix, respective  $\mathbf{c}'$  and  $\mathbf{g}$  are  $m \times 1$  column vectors showing receiver gathers. Constructing multiple column vectors using equation 3.8 for variable  $\mathbf{x}_B$  and arranging them as columns of a matrix, we obtain:

$$\mathbf{C}' \propto \mathbf{\Gamma} \mathbf{G}, \quad (3.10)$$

where  $\mathbf{C}'$  and  $\mathbf{G}$  are  $m \times m$  monochromatic matrices containing  $C'(\mathbf{x}_m, \mathbf{x}_m, \omega)$  and  $G_{z,z}^{scatt,d}(\mathbf{x}_m, \mathbf{x}_m, \omega)$ , respectively. Estimating the dipole scattered Green's function in equation 3.10 requires matrix inversion:

$$\mathbf{G}' \propto [\mathbf{\Gamma}]^{-g} \mathbf{C}', \quad (3.11)$$

where  $[\mathbf{\Gamma}]^{-g}$  is a generalized inverse of  $\mathbf{\Gamma}$ , and  $\mathbf{G}'$  is an estimate of  $\mathbf{G}$ .

Note that our receiver configuration might not be optimal for MDD studies. The number of receivers we have is relatively small - 19 and 13 for the TN- and TE-array, respectively. Fewer receivers leads to more severely ill-posed solutions in the inversion process. Two approaches to stabilize the MDD in equation 3.11 have been used: a damped least-squares [41]; and a singular-value decomposition (SVD; [42]).



### MDD BY DAMPED LEAST SQUARES

The damped least-square solution is a commonly used approach for MDD studies [e.g. 25, 39, 43]. This scheme can be directly adapted to the generalized inverse matrix in equation 3.11, resulting in

$$\mathbf{G}' \approx [\mathbf{\Gamma}^\dagger \mathbf{\Gamma} + \epsilon \mathbf{I}]^{-1} \mathbf{\Gamma}^\dagger \mathbf{C}', \quad (3.12)$$

where  $\epsilon$  and  $\mathbf{I}$  indicate a stabilization factor and the identity matrix, respectively. The symbol  $\dagger$  denotes the complex conjugate transpose matrix. In practice,  $\mathbf{\Gamma}$  is estimated in the time domain and then transformed to the frequency domain by the Fourier transform. A disadvantage of this scheme is that choosing an appropriate stabilization factor tends to be inevitably subjective because it is difficult to evaluate the data redundancy in a quantitative way.

### MDD BY TRUNCATED SINGULAR-VALUE DECOMPOSITION (SVD)

There are only a few examples of MDD based on the truncated SVD scheme [e.g. 44, 45]. The concept of the truncated SVD scheme is fundamentally close to the principal component analysis [46] in machine learning, which is also called a subspace method or Karhunen-Loève expansion, and the latent semantic analysis [47] in natural language processing. For example, both the truncated SVD scheme and the principal component analysis find the data directions (axes) from the eigenvectors of the covariance matrix using the SVD algorithm via Lagrange multiplier. Here, we briefly introduce the truncated SVD scheme.

Let us define the SVD of  $\mathbf{\Gamma}$  in equation 3.10 as

$$\mathbf{\Gamma} = \mathbf{U} \begin{pmatrix} \Delta_r & \mathbf{0} \\ \mathbf{0} & \mathbf{0} \end{pmatrix} \mathbf{V}^\dagger, \quad (3.13)$$

where  $\mathbf{U}$  is a left-singular matrix (orthonormal-basis matrix),  $\mathbf{V}$  is a right-singular matrix (orthonormal-basis matrix),  $\mathbf{V}^\dagger$  is the adjugate (adjoint) matrix that is the complex conjugate transpose matrix of  $\mathbf{V}$ , and  $\Delta_r$  is an  $r \times r$  diagonal matrix whose elements are the singular values of the monochromatic matrix  $\mathbf{\Gamma}$ , obtained by truncation. We define the dimension  $r$  as the number of significant singular values by specifying a threshold value. Then, we adapt the Moore-Penrose pseudoinverse [48] for equation 3.13:

$$[\mathbf{\Gamma}]^{-g} = \mathbf{V} \begin{pmatrix} \Delta_r^{-1} & \mathbf{0} \\ \mathbf{0} & \mathbf{0} \end{pmatrix} \mathbf{U}^\dagger, \quad (3.14)$$

where  $\mathbf{U}^\dagger$  is the adjugate (adjoint) matrix of  $\mathbf{U}$ . In the following section, we show the MDD results of the damped least-squares scheme and the truncated SVD scheme.

## 3.1.4. DATA PROCESSING

### PREPROCESSING

Our first step in the preprocessing is to remove the instrument response from the recorded data. After that, we compute power spectral densities (PSD) of the local earthquakes to determine a frequency band that exhibits adequate SNR. Examples of PSD of the local

earthquake for the TE-array are shown in Figure 3.4. Analysing the PSDs, we choose the frequency band 1-5 Hz for further seismic processing. We set the high end of the band at 5 Hz due to the presence of irregular noise around 8 Hz (see Figure 3.4), which is masking the signals from weaker earthquakes. The nature of this noise is not clear. The stations are away from continuous anthropogenic sources, so this could be excluded as main contributor. Since this noise is almost continuously seen over the records in MalAR-Rgue, it might be connected to the wave action in the nearby lake Llançanelo (Figure 3.1), but possibly also with deeper activity below the volcanic cones in the vicinity of the array. The noise, which is also continuously seen around 0.3 Hz, likewise to be due to the double-frequency microseisms. In principle, one can use higher frequency (if available) for LEPC SI to obtain images of shallower structures, e.g., at basin scale. For speeding up the computations, after the band-pass filtering, we downsample the data to 0.05 s (Nyquist frequency of 10 Hz) from the original sampling of 0.01 s (Nyquist frequency of 50 Hz).

The useful window length of the coda of the P-wave phase is explained in Figure 3.5 as a function of the epicentral distance. To calculate the times in Figure 3.5, we use the regional velocity model of Fariás *et al.* [49] down to 110 km and ak135 [50] deeper than that. In order to only extract the P-wave coda without the direct wave that usually brings strong directivity in the SI results, we refer to the scaling relation between the moment magnitude,  $M_W$ , and the source duration of the earthquakes [51] assuming that  $M_W$  is proportional to the body-wave magnitude,  $M_b$ , for our magnitude range [52]. Thus, our coda-waves extraction window starts at the time obtained from the summation of the time of the expected P-phase arrival and the expected time length of the STF.

For the local earthquakes ( $2^\circ \leq$  epicentral distances  $\leq 6^\circ$ ), surface waves are expected to arrive almost simultaneously with the S-wave phase onset or later [50]. To make sure that the coda does not contain surface waves related to the earthquake, our coda-wave extraction window terminates a few seconds before the observed S-wave phase onset.

With the above window-length selection criteria, the coda duration is shorter for some earthquakes, but still we have sufficient coda duration (e.g. 15-70 s) for the subsurface imaging. An example of the coda extraction is shown in Figure 3.6. For subsequent seismic processing, we use only the P-wave coda (the blue window) extracted from the vertical component. It is difficult to estimate how much converted S-wave phases are present within the P-wave coda, but they most probably are present. Especially, SV-waves are expected to be present on the vertical component we use. In this study, we assume that the SV-waves are not dominantly recorded for deeper earthquakes (e.g. 50-100 km) due to their small slowness. For shallower earthquakes (e.g. 0-50 km), the SV-waves can be recorded with spatial aliasing due to the larger ray parameter compared to the ray parameter for P-waves. However, the crosscorrelation and summation process should suppress such aliasing effects, emphasizing the reflection responses of the structures. Note that the transverse component in Figure 3.6 is displayed only for the purpose of data comparison with the vertical component.

After extracting the P-wave coda from each selected local earthquake, we interpolate missing traces at certain stations (e.g. due to technical problems in the acquisition) using their two closest neighbouring station records using linear interpolation. For example, if TE10 has a missing trace, we interpolate it only when TE09 and TE11 have non-missing

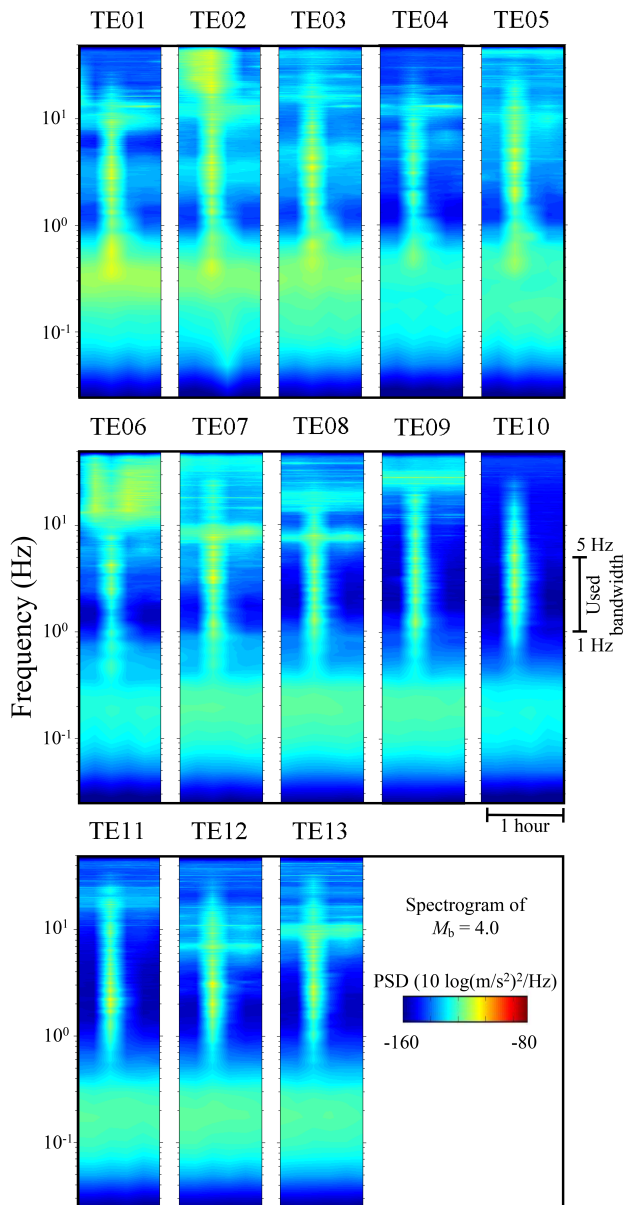


Figure 3.4: Power spectral densities for a local earthquake with  $M_b$  4.0. The power spectral densities are computed for the TE-array.

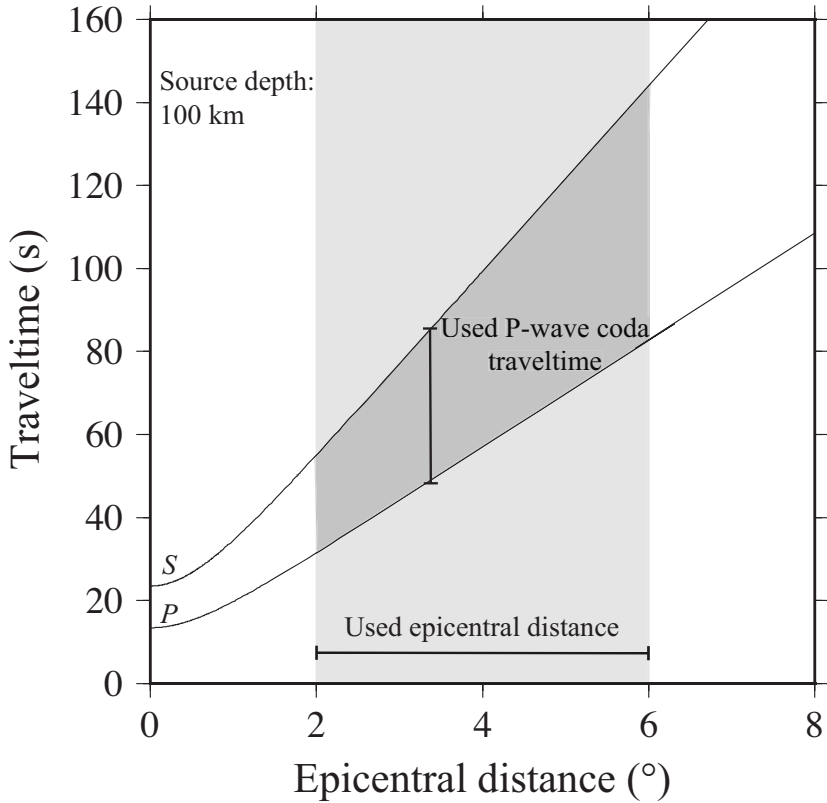


Figure 3.5: Used window length of the P-wave coda as a function of epicentral distance. The traveltime curves are drawn using the regional velocity model from Fariás *et al.* [49] for depths down to 110 km and the ak135 model [50] for greater depths. Light gray rectangular indicates the used epicentral distance, while the dark gray area indicates the the window lengths to be extracted for an earthquake characterized by a source depth of 100 km.

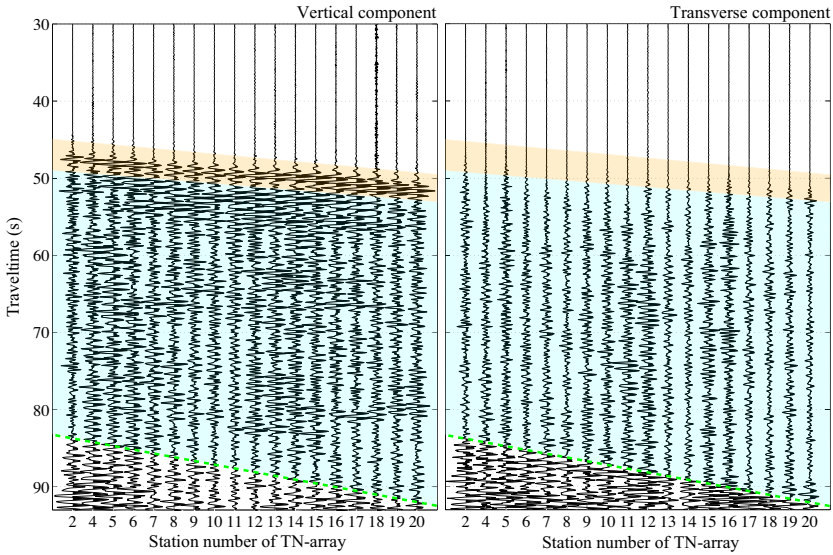


Figure 3.6: An example recording of a local earthquake on the vertical (left panel) and transverse component (right panel) of the stations from the TN-array. The areas highlighted in orange indicate the direct P-wave arrival from the local earthquake, while the green lines indicates the S-wave onset. The area highlighted in light blue indicates the P-wave coda to be extracted.

traces for that time. In Figure 3.7, we show the number of interpolated traces (what we also call events).

### LEPC SI APPLICATIONS

**Crosscorrelation and crosscoherence processing** We apply crosscorrelation to the pre-processed data of the T-array from MalARRgue after applying amplitude normalization per coda-wave window per station. The normalization is used to bring per station the correlation results from each local earthquake to a comparable amplitude and thus to let each correlation have the same weight in the summation over the earthquakes. We test utilization of energy normalization, normalization by the maximum amplitude, and normalization by the maximum amplitude followed by spectral whitening. In Figures 3.8b-d, we show the three respective results obtained from autocorrelation, which represent retrieved zero-offset traces. In Figure 3.8a, we show the retrieved zero-offset trace obtained without any normalization. As can be seen from Figures 3.8a-c, there is no significant difference between the results with and without normalizations, implying that for the earthquakes we choose, the recordings from the different earthquakes have comparable amplitudes in the 1-5 Hz frequency band. Nevertheless, we can notice small differences among the results, so it is better to use normalization before correlation given its numerical robustness. In Figure 3.8e, we show the retrieved zero-offset trace obtained from autocorrelation. In Figure 3.8d, we show for completeness of comparison another correlation result obtained after energy normalization and spectral whitening. The whitening was performed using a running window of 0.025 Hz width. Note that en-

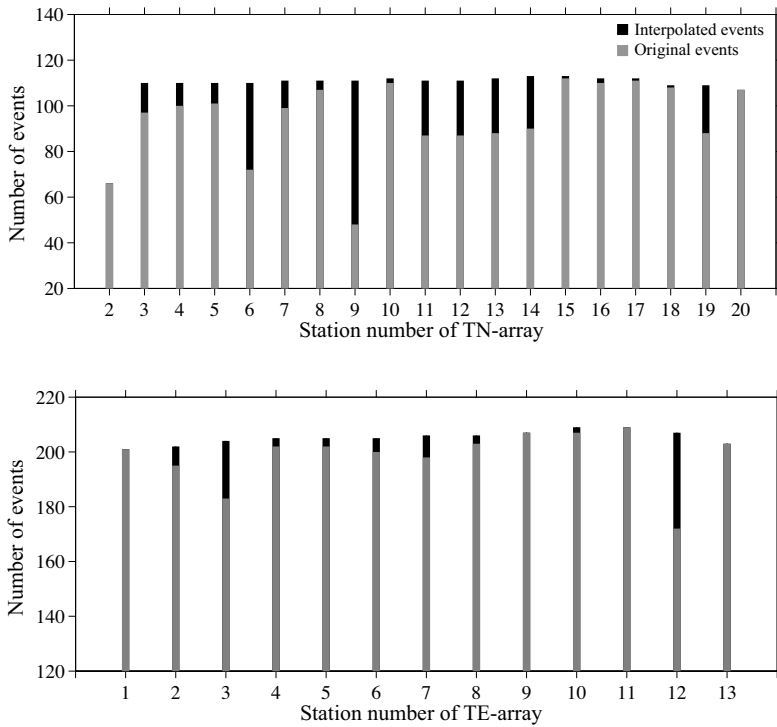


Figure 3.7: Number of original and interpolated events for each of the TN- and TE-array stations.

ergy normalization followed by spectral whitening makes the result retrieved by correlation (Figure 3.8d) close to the one retrieved by coherence (Figure 3.8e). This is because normalization and spectral whitening mathematically approximates coherence. In this study, we use crosscorrelation and crosscoherence. For retrieval using crosscorrelation, we choose to use preprocessing by energy normalization without spectral whitening (as in Figure 3.8b), so that we could see clear differences between the results from crosscorrelation and those from crosscoherence.

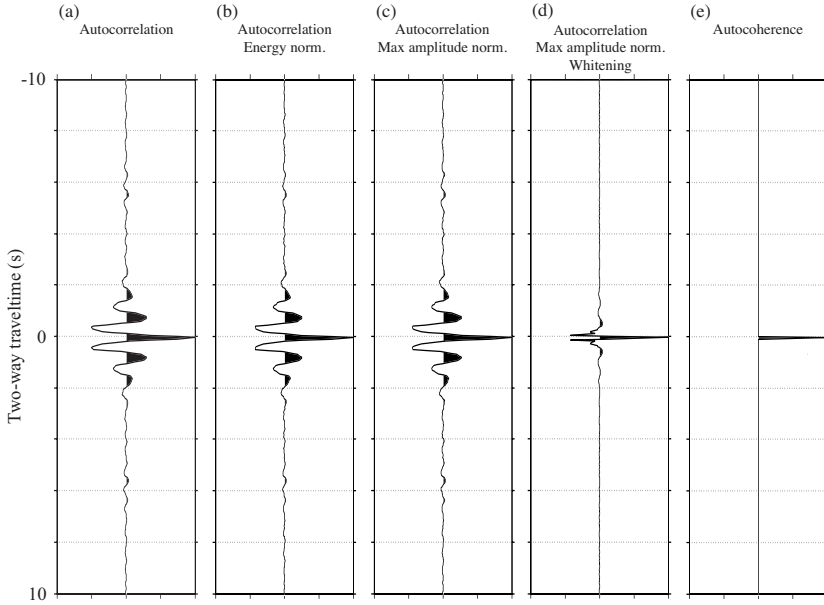


Figure 3.8: Retrieved zero-offset trace at station TE07 of the TE-array obtained using (a) autocorrelation without amplitude normalization, (b) energy normalization before autocorrelation, (c) maximum-amplitude normalization before autocorrelation, (d) maximum-amplitude normalization followed by spectral whitening before autocorrelation, and (e) autocoherece.

Figures 3.9a and 3.9d show retrieved common-source gathers (at positive and negative times) obtained using crosscorrelation for a virtual source at TN11 (the middle station in the TN-array) and TE07 (the middle station in the TE-array), respectively. It can be seen that the common-source gathers exhibit asymmetrically retrieved events with respect to two-way traveltime 0 s, indicating that the coda we use is not illuminating the stations equally from all directions. Even though Mayeda *et al.* [28], Baltay *et al.* [29], and Abercrombie [30] assumed apparent weak to no directivity of the coda, i.e., isotropic energy flux, due to the expected averaging out of radiation pattern of the earthquake, Paul *et al.* [53] and Emoto *et al.* [54] found that the energy flux of the coda is not isotropic. In the case that the coda has no directivity, the causal and acausal parts of the common-source gathers obtained from crosscorrelation would result in a purely symmetric gather. When the coda has directivity, the common-source gather would exhibit asymmetry as shown in Figure 3.9d.

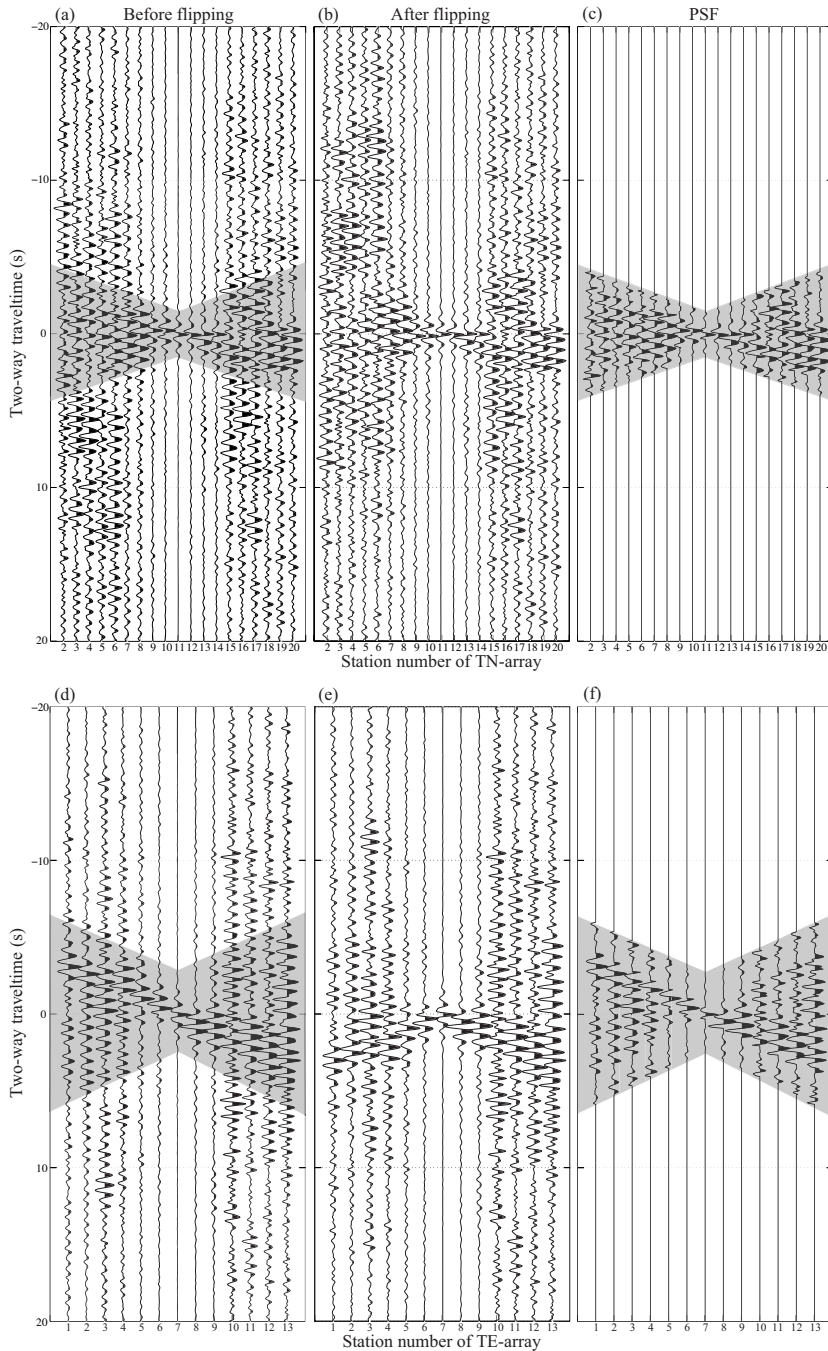


Figure 3.9: Retrieved common-source gather for a virtual source at (a) station TN11 of the TN-array before flipping, (b) after flipping the negative times, (d) station TE07 of the TE-array before flipping, (e) after flipping the negative times. The PSFs of (c) and (f) are extracted from the gray shaded areas in figures (a) and (d), respectively. The results are retrieved using correlation and after summation over the used local earthquakes.



A possible explanation of the directivity in the coda, which is most likely the case with our data as well, is that it is associated with the direct-wave passages [e.g. 54]. Emoto *et al.* [54] discussed that the coda consists of forward scattered waves (early coda), which have directivity, and multiply scattered waves (later coda), which have no directivity.

For the results retrieved from SI by crosscorrelation and crosscoherence, we correct for the asymmetric results (Figures 3.9a and 3.9d) by combining part of the positive and parts of the negative times as follows. To obtain a final retrieved common-source gather, we use the acausal part of the retrieved result for traces to the west of the virtual-source position, reverse this part in time, and concatenate it to the causal part of the retrieved result for traces to the east of the virtual-source position (Figures 3.9b and 3.9e). This processing is strictly valid for horizontally layered medium. In our case, since we rely on secondary scattering, we can still use this processing provided that the scattering results in the illumination of the array mainly from the west of the array and that the structures below the array are not complex.

For the next processing step, we apply a deterministic spiking deconvolution to remove the STF of the retrieved virtual source from each of the retrieved common-source gathers. The deterministic spiking deconvolution is a technique that compress the STF (e.g. known from observation) using the least-squares method. The STF are estimated from the retrieved zero-offset traces at each virtual-source position by extracting a time-window around time 0 s (Figure 3.10). Following the conventional seismic processing, we mute the first breaks and all the events above them from the common-source gathers for the both TN- and TE-array as shown in Figure 3.11. Our estimates of the first breaks are about 3400 m/s (a constant velocity) for both arrays. After that, we re-sort the traces into CMP gathers and apply normal moveout velocity analysis to the data using semblances. In Figure 3.12, two examples of velocity semblance are shown with the regional velocity model by Fariás *et al.* [49] indicated by the dashed magenta lines. There is a good correspondence between the regional model and peaks in the middle part of the semblance. For example, the bright spots in the semblance around 10-11 s (the left panels in Figure 3.12) correspond to the range of the possible Moho velocity in Fariás *et al.* [49]. In this study, though, we use for normal-moveout correction and migration the regional velocity model from Fariás *et al.* [49] because this simplifies the interpretation during the comparison of the current result with our previous result from application of global-phase SI [55]. The global-phase SI is an autocorrelation SI that uses global phases (e.g. PKiKP).

After obtaining stacked sections along both arrays we apply predictive deconvolution to suppress possible multiples from the top basement using the estimated depth of the top of basement beneath MalARRgue [56]. Finally, we apply Kirchhoff post-stack time migration (KTM; [57]) to move dipping structures to their true location in the model. As a final processing step, we apply lateral regularization in the horizontal direction to obtain better imaging in terms of structural interpretation. For the lateral regularization, we use smoothed discretized splines determined by the generalized cross-validation [58]. The stacked sections before and after the mentioned processing (predictive deconvolution, KTM, and lateral regularization) for the TN- and TE-array are shown in Figures 3.13a,b and 3.14a,b, respectively.

The seismic processing of the results retrieved from SI by crosscoherence is the same

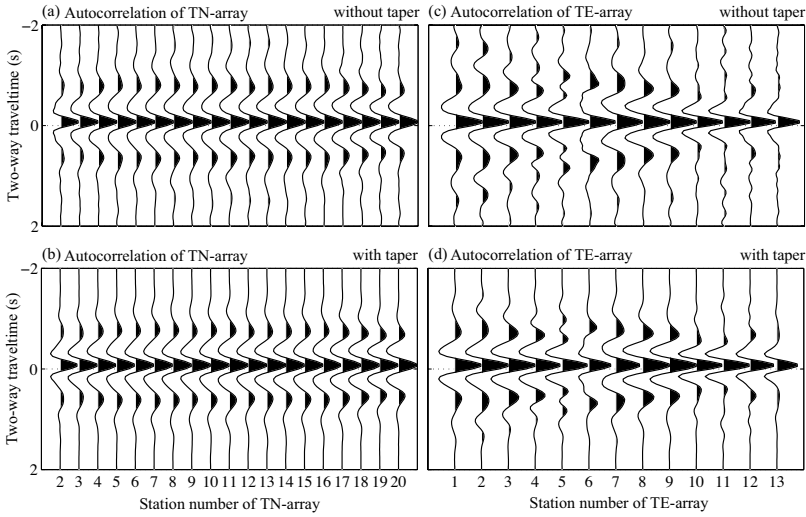


Figure 3.10: Retrieved zero-offset traces using all events from (a) the TN-array (c) the TE-array. (b) and (d) are estimated source time functions from the zero-offset traces in (a) and (c), respectively, after application of time windowing.

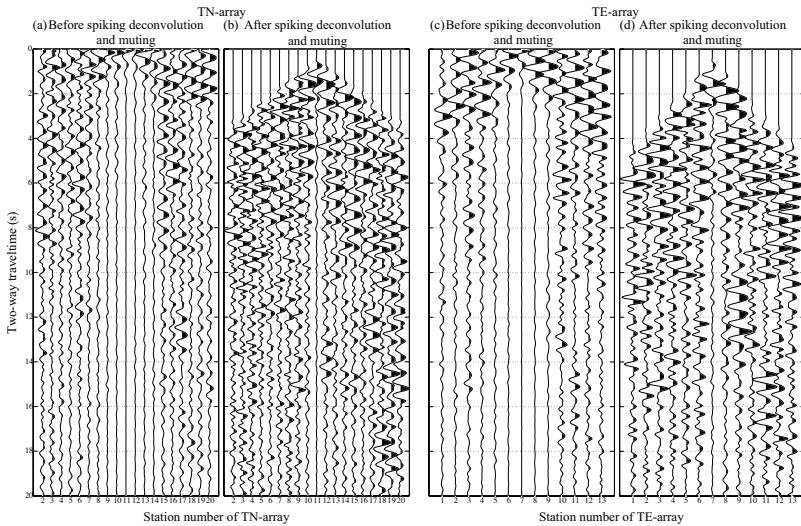


Figure 3.11: A comparison of common-source gather: for station TN11 of the TN-array (a) before spiking deconvolution and muting the first breaks and (b) after spiking deconvolution and muting the first breaks and above; for station TE07 of the TE-array (c) before spiking deconvolution and muting the first breaks and (d) after spiking deconvolution and muting the first breaks and above.

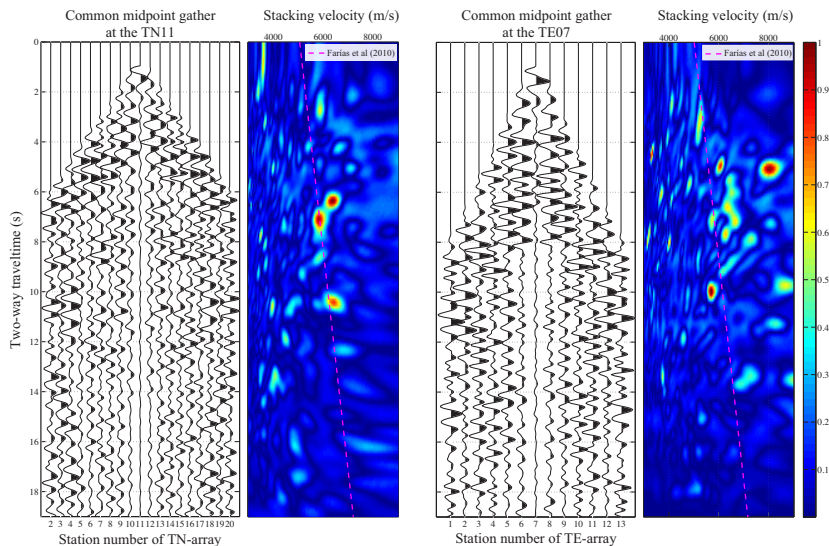


Figure 3.12: Examples of velocity semblance of common midpoint gather for station TN11 of the TN-array (left panels) and station TE07 of the TE-array (right panels) with the regional velocity model of Farias *et al.* [49] denoted by the magenta dashed lines.

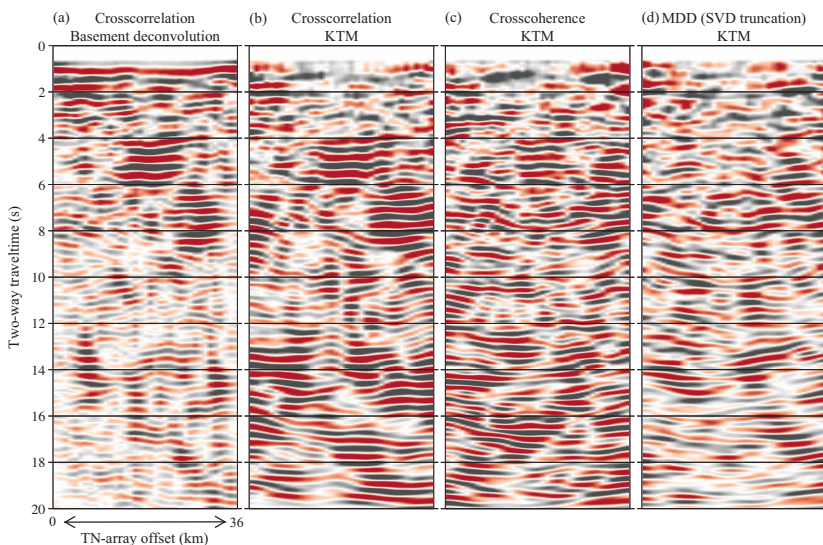


Figure 3.13: A comparison of LEPC SI results for the TN-array using different SI theories: (a) crosscorrelation after basement deconvolution without KTM; (b) same as (a) but with KTM; (c) same as (b) but for crosscoherence; (d) same as (b) but for MDD using the truncated SVD scheme.

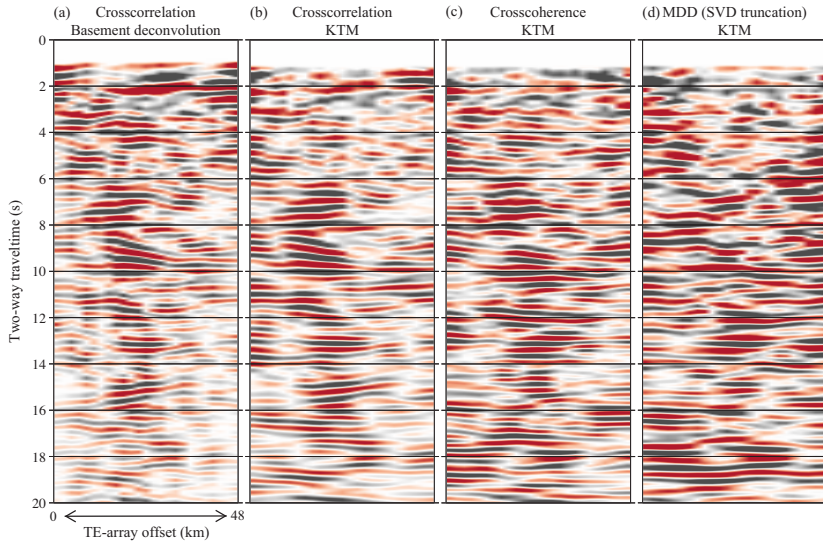


Figure 3.14: Same as Figure 3.13 but for the TE-array.

as for the results retrieved by crosscorrelation, except for the step of applying spiking deconvolution of the STF, which is not needed. The processed stacked section obtained from SI by crosscoherence are displayed in Figures 3.13c and 3.14c. For Figures 3.13c and 3.14c, we select the results obtained using a stabilization factor of 1 % of the maximum in the amplitude spectrum. In our case, we did not see significant differences when using stabilization factors between 1 % and 5 %.

**MDD processing** The data processing for application of SI by MDD differs only in a few steps from the other two LEPC (crosscorrelation and crosscoherence), interferometric applications. Due to the fact that MDD intrinsically deconvolves for the STF of the earthquake sources and compensates for directivity in the illumination, neither spiking deconvolution for the STF of the retrieved virtual source nor selective utilization of parts of the causal and acausal times are needed. Instead, it is necessary to obtain the estimated PSF for solving the inverse problem of the approximated MDD in equation 3.11. In Figures 3.9c and 3.9f, we show two examples of PSFs extracted (cut away with tapered edges) from the retrieved crosscorrelation results in Figures 3.9a and 3.9d, respectively. We extracted the PSF with a butterfly-shaped window around  $t = 0$  and narrowest for  $\mathbf{x}_A = \mathbf{x}_B$ . It aims to include events obtained from the crosscorrelation between waves that are recorded at the surface as direct waves from secondary sources in the subsurface (the scatterers and reflectors). Note that the approximated PSFs are shown after amplitude normalization among the stations for the purpose of displaying only; we do not use amplitude normalization for the actual MDD processing. The time window for the PSF is based on the velocity used for the first-break muting in Figure 3.12.

We apply SI by MDD to the LEPC data using the truncated SVD approach to stabilize

the inversion. We process the two lines separately - we retrieve virtual-source response along the TN-array using the events recorded by and interpolated along the TN-array; we retrieve virtual-source response along the TE-array using the events recorded by and interpolated along the TE-array. As can be seen from Figure 3.7, the number of earthquakes for each station per subarray is different. For example, for the TE-array, the number of interpolated events per station is between 200 and 210. This means that several PSFs for the TE-array contain zeros for the matrix inversion. However, we expect that the illumination compensation for the TE-array from the used 210 events will be affected only to a small degree by the zeros in the PSFs due to the random distribution of the zeros. The same can be said for the TN-array as well, but in its case the number of interpolated events per station is around 115 (except for TN02). After the SVD, we truncate singular values with amplitudes with a threshold value of 10 % of the maximum singular value. The singular values under the threshold are considered negligible to retrieve reflection-data estimates. Figure C-1 is available in Appendix C that shows the singular values we truncate. The discarded singular values would largely contribute to the ill-posedness of equation 3.11. In Figures 3.15a and 3.15b we show the obtained MDD results in the  $f$ - $x$  domain for virtual shots at TN11 and TE07, respectively. We also test application of SI by MDD using the damped least-squares stabilization with a constant stabilization factor for all frequencies, but the results are not as well stabilized as the ones using the truncated SVD scheme (Figure 3.15a).

### 3.1.5. RESULTS AND INTERPRETATION

In Figures 3.16 and 3.17, we show the LEPC SI results for the TN- and TE-array, respectively, obtained by MDD using the truncated SVD; we compare these results to the results obtained by global-phase SI by Nishitsuji *et al.* [55] who used frequency band 0.3-1 Hz. We design the processing parameters for the basement predictive deconvolution based on the estimated two-way traveltime of the basement multiples [56]. For comparison purposes, we use the same processing parameters of KTM for both of the LEPC SI and the global-phase SI results. The reflection imaging exhibits more details than the results from the global-phase SI. The bifurcated Moho and the magma chamber indicated in Figures 3.16 and 3.17 are after Gilbert *et al.* [59]. The gray shades in Figures 3.16 and 3.17 indicate the offset where the CMP fold numbers are less than or equal to 5; we do not interpret the results inside the gray shaded areas as we deem this fold insufficient for imaging. The yellow dashed lines are our structural interpretation where the amplitude and phase discontinuities are seen based on the global-phase SI results. We superimpose those interpreted features over the LEPC SI results because it is difficult to tell which features are the artifacts or not in a decisive way. Although one might like to interpret more structures on the LEPC SI results, we only focus on the major features interpreted by the global-phase SI results. Because we would like to keep the correspondence, no horizon interpretations are given for structures shallower than about 7-seconds two-way traveltime, where the global-phase SI results become unclear (Figures 3.16b and 3.17b). The global-phase SI results (Figures 3.16b and 3.17b) show the limitation in interpreting shallow structures because the subtraction of the average STF for 10 s unavoidably removes some shallow structures. Note that because LEPC SI has retrieved reflections that resulted in imaging structures below the array, we can con-

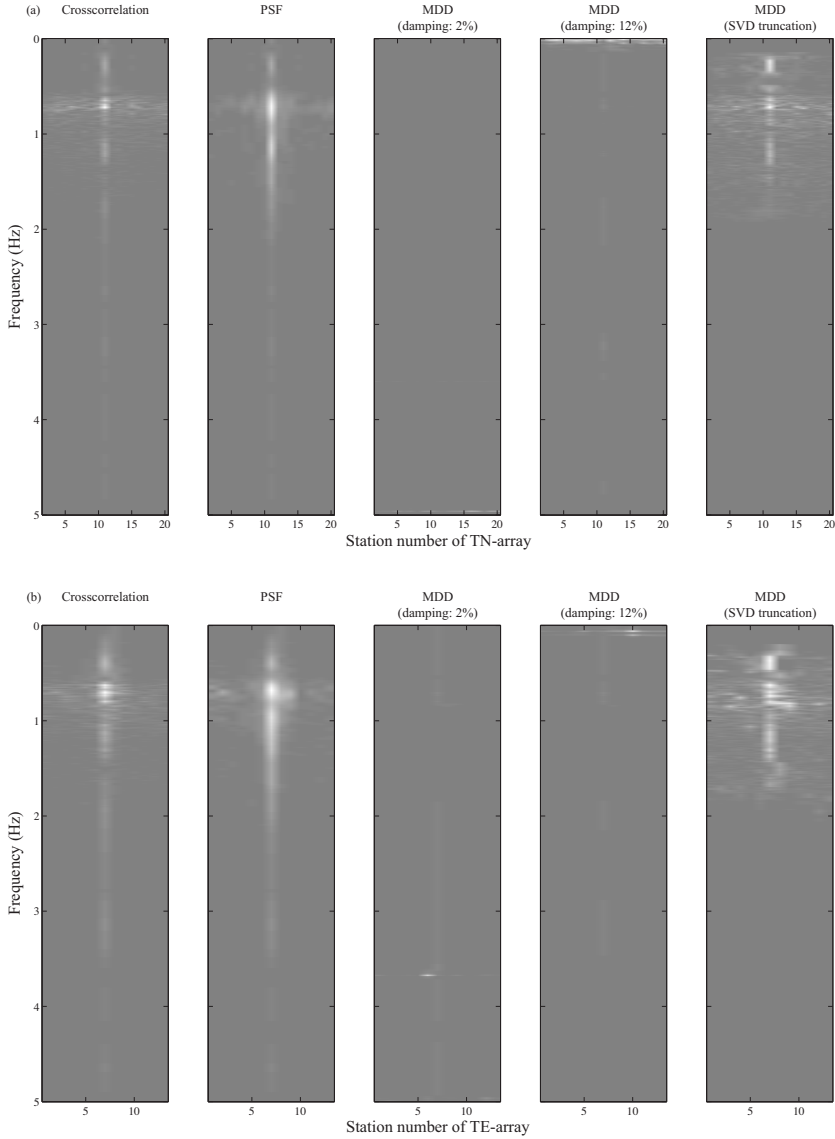


Figure 3.15: Obtained MDD results using the damped least-square and the truncated SVD scheme in the f-x domain for virtual shots at: (a) station TN11; (b) station TE07 in comparison with the crosscorrelation (Figures 3.9a and 3.9d) and the PSF (Figures 3.9c and 3.9f).

clude that there has been sufficient local scattering below the array. This is also expected from the presence of a line of volcanic cones at the surface crossing the TE-array. Local secondary scattering from structures below the array would result in arrivals characterized by small emergence angles at the array; such arrivals will be turned by SI into reflections. As the local earthquakes we use are distanced from the TN- and TE-arrays and the coda window length is limited, if there were little or no local scattering below the array, LEPC SI would not have retrieved reflections. Since all of the LEPC SI results

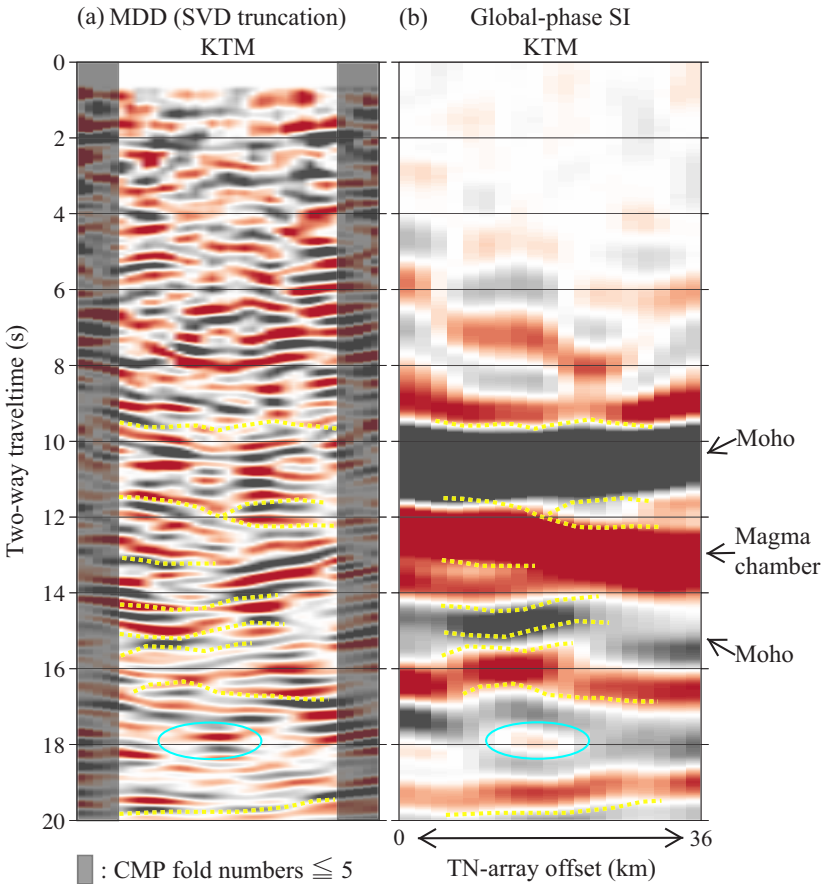


Figure 3.16: Summarized interpretation on the crustal-scale reflection images beneath the TN-array obtained from: (a) LEPC SI (1-5 Hz) with the truncated MDD scheme; (b) global-phase SI (0.3-1 Hz) modified from Nishitsuji *et al.* [55]. The interpretation of the Moho and the magma chamber are after Gilbert *et al.* [59] and Nishitsuji *et al.* [55]. The yellow dashed lines indicate our structural interpretation that can be traced for both the MDD and the global-phase SI results. The gray shades are the offset where the CMP folds are less than equal to 5. The cyan ellipses indicate the amplitude pockets that can be commonly interpretable between the MDD and the global-phase SI results.

(crosscorrelation, crosscoherence, and MDD) appear in general to be similar (see Figures

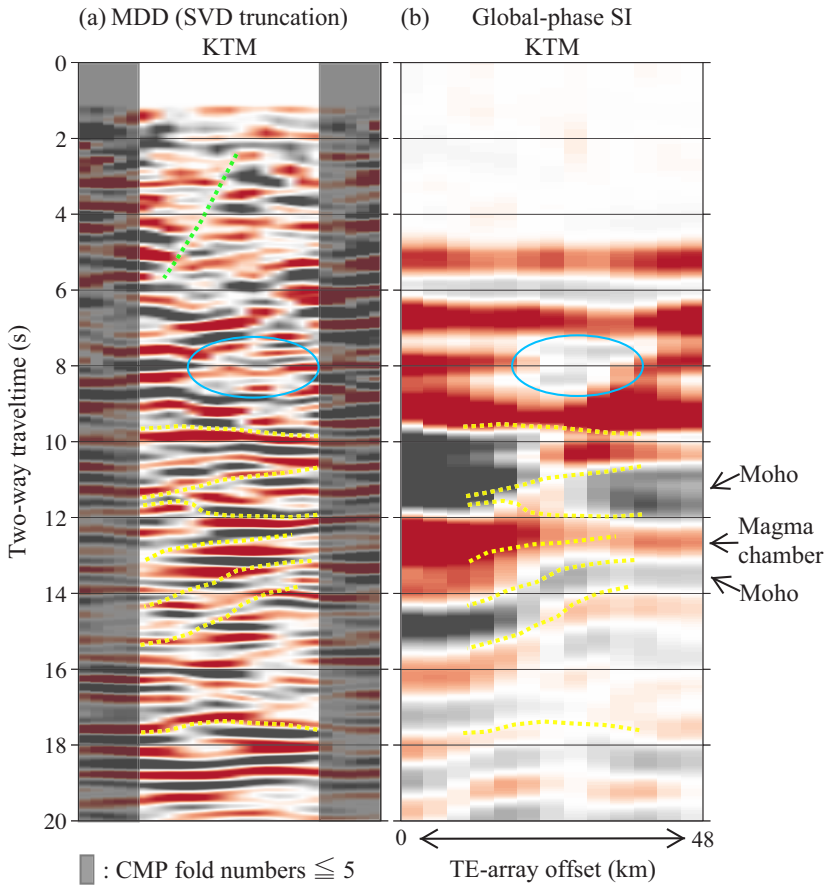


Figure 3.17: Same as Figure 3.16, but for the TE-array. The blue ellipses indicate the dimming imaging parts that can be commonly interpretable between the MDD and the global-phase SI results. The green dashed line indicates our fault interpretation where the major deep thrust fault can be traced.



3.13b-d and 3.14b-d), one might prefer to use for the interpretation of the other LEPC SI results instead of the MDD results. However, if we have a limited number of local earthquakes whose back-azimuth coverage is insufficient with respect to the receiver-array, MDD should in theory work better than the other two methods [19]. This is, because for crosscorrelation and crosscoherence to work, a large number of local earthquakes with sufficiently wide back-azimuth coverage is essential for the effective suppression of the cross-talk [e.g. 21, 27]. On the other hand, assuming a sufficiently good coverage of the local earthquakes is available but the receiver-array is patchy or irregular, both the cross-correlation and crosscoherence would work, whereas MDD would be ill-posed because it requires regularly-spaced receivers. As shown in Figures 3.1 and 3.2, we have good coverage of the local earthquakes recorded at the exploration-type array. This could be the reason why the LEPC SI results in Figures 3.13b-d and 3.14b-d show similar results at our scale of interest. Nevertheless, we decide to select the LEPC SI results based on the MDD by truncated SVD scheme in Figures 3.16 and 3.17 rather than the others because we find that a few structural features showing more continuity in space. For instance, a horizontal coherent feature around 8 s in Figure 3.16 and up-dipping (from west to east direction) structures between 13-15 s in Figure 3.17 are clearer than the images from the other two methods in Figures 3.13 and 3.14. More importantly, the PSFs in Figure 3.15 are smeared in space and time, which means that the crosscorrelation results in Figures 3.13 and 3.14 are biased due to the spatial-temporal blurring effect of the PSF. This is also the reason we select the MDD results in Figures 3.16 and 3.17.

Interpreting results from the magnetotelluric method, Burd *et al.* [34] (the blue dashed line in Figure 3.1) recently suggested the presence of a possible shallow asthenospheric plume (e.g. 0-100 km in depth) nearby the Peteroa volcano. The authors interpreted this shallow plume as possibly connected to the main upwelling plume whose origin would be around the mantle transition zone (410-660 km in depth). Gilbert *et al.* [59] showed the receiver-function imaging at roughly 50 km south of MalARRgue, interpreting a possible bifurcation of the Moho with magma chamber in between (Figure 5 in [59]). The study by Nishitsuji *et al.* [55] using the global-phase SI confirmed such Moho bifurcation beneath the array of the MalARRgue. Summing up the above interpretations, one could expect a dynamic tectonic regime rather than a static one in this Andean region.

As we described earlier, the reflection imaging of the LEPC SI results exhibits more details than the results from the global-phase SI. As shown by Abe *et al.* [60] and Nishitsuji *et al.* [55], the vertical imaging resolution in results retrieved by SI would be at least as high as, but potentially higher, than the ones obtained by the receiver-function method. The difference of the resolution in Figures 3.16 and 3.17 is largely due to the difference in the used frequency band. Nishitsuji *et al.* [55] used global-phase earthquakes with frequency band 0.3-1 Hz, whereas here we use 1-5 Hz for the LEPC SI results. In addition to the correspondence (or similarity) of the structural features (the yellow dashed lines in Figures 3.16 and 3.17) between these two different methods, there is another striking feature - a possible major fault in Figure 3.17a, indicated by the green dashed line, where horizon displacements can be seen. According to the active-seismic reflection profile (the green solidline in Figure 3.1) and nearby exploration well (LPis x-1) given in Kraemer *et al.* [33], deep basement thrust faults, which are reverse faults (see Figure 8a in [33]), are expected to exist in this region as a typical feature of foredeep basins [61]. Such

thrust faults can also be seen in Giambiagi *et al.* [62] and Giambiagi *et al.* [63] in their Figures 7b-c and 2 (e.g. cross-section H), respectively. Because the reverse faults beneath LPis x-1 are thought to be dipping to the west, identifying such faults below the TE-array (Figure 3.17a), but not below the TN-array (Figure 3.16a) is logical. Thus, we interpret the feature indicated by the green dashed line in Figure 3.17a as possibly corresponding to one of those deep thrusts.

The blue ellipses in Figure 3.17 indicate zones where dimmed-amplitude portions can be seen in both the LEPC SI (Figure 3.17a) and global-phase SI results (Figure 3.17b). Since both independent methods use acoustic SI approaches, such dimming features might indicate weaker reflection responses in comparison with the other zones. Referring to the previous studies in this region, such weaker reflectivity might be due to the presence of the shallow asthenospheric plume that has been interpreted by Burd *et al.* [34]. Otherwise, such dimmed amplitudes might be indicative of partial-melting spots that are only locally present.

We also observe that the Moho in the LEPC SI results are not as visually dominant as the ones from the global-phase SI [55] and receiver-function method [59]. This feature could be also found in other high-resolution reflection images by active-seismic sources. For instance, although the reflection results in Singh *et al.* [64] and Calvert and McGearry [65] provided very fine scale of the images (e.g. 50 m in depth after [64]), we find that the Moho in their results is somewhat less prominent than in the image from seismic tomography [e.g. 66] and the receiver-function method [e.g. 59]. This is probably because the Moho discontinuity is rather better sensed with low frequencies (e.g.  $\leq 1$  Hz). The active-source reflection in Singh *et al.* [64] and LEPC SI in this study used 10-30 Hz and 1-5 Hz, respectively. The seismic tomography in Calvert *et al.* [66] and the global-phase SI in Nishitsuji *et al.* [55] used 0.03-0.3 Hz and 0.3-1 Hz, respectively.

Therefore, as long as one's goal is the identification of the Moho, using the lower frequencies would in general be sufficient. Still, LEPC SI can provide useful information at low acquisition cost when finer structural imaging and/or shallower targets are of interest (e.g. basin imaging if one can use higher frequency). For the current imaging resolution, LEPC SI could even assist in deep geothermal exploration (including enhanced geothermal systems) together with magnetotelluric investigations. It is of importance during deep geothermal exploration to estimate the deeply lying conductive feature and the possible fault system between the thermal source (e.g. Moho) and the target basement (up to 10 km). The success of the method depends on the illumination of the receiver array by the coda wavefield. In our case, the results show illumination directivity at the TE-array for the coda-waves part we use. The main advantage of the method is that it turns the passive recordings into reflection recordings, which is not possible without using SI. Note that active-source measurements in the frequency bandwidth we use in this study are not always available. In this case, LEPC SI might complement the low-frequency bandwidth and would be a useful alternative approach.

### 3.1.6. APPENDIX B: APPROXIMATED MULTIDIMENSIONAL DECONVOLUTION

Here, we show the derivation to obtain the approximate expression for seismic interferometry (SI) by MDD - equation 3.5 in the main text. First, we define the following relation

in the frequency domain  $\omega$ :

$$\bar{v}_z(\mathbf{x}_B, \omega) = \bar{v}_z^d(\mathbf{x}_B, \omega) + \bar{v}_z^c(\mathbf{x}_B, \omega), \quad (\text{B-1})$$

where  $\bar{v}_z(\mathbf{x}_B, \omega)$  is the vertical component ( $z$ ) of the particle velocity vector in the absence of a free surface at the receiver  $\mathbf{x}_B$  for a local earthquake in the subsurface,  $\bar{v}_z^d(\mathbf{x}_B, \omega)$  represents only the direct arrival, and  $\bar{v}_z^c(\mathbf{x}_B, \omega)$  represents the coda, i.e., the scattering between inhomogeneities inside the medium. For the situation where there is a free surface at the receiver level, we also define the following relation:

$$v_z(\mathbf{x}_B, \omega) = v_z^d(\mathbf{x}_B, \omega) + v_z^c(\mathbf{x}_B, \omega), \quad (\text{B-2})$$

which is the free-surface counterpart of equation B-1. Note that  $v_z^c(\mathbf{x}_B, \omega)$  is the coda wavefield we actually observe (see the light blue shades in Figure 3.6). Taking into account the fact that  $v_z^d(\mathbf{x}_B, \omega) = 2\bar{v}_z^d(\mathbf{x}_B, \omega)$ , equation B-2 can be rewritten as

$$v_z(\mathbf{x}_B, \omega) = 2\bar{v}_z^d(\mathbf{x}_B, \omega) + v_z^c(\mathbf{x}_B, \omega). \quad (\text{B-3})$$

Using equations B-1 and B-3, we can write for the scattered field

$$v_z^{scatt}(\mathbf{x}_B, \omega) = v_z(\mathbf{x}_B, \omega) - 2\bar{v}_z(\mathbf{x}_B, \omega) = v_z^c(\mathbf{x}_B, \omega) - 2\bar{v}_z^c(\mathbf{x}_B, \omega). \quad (\text{B-4})$$

Here, we recall equation (63) in Wapenaar *et al.* [26]:

$$v_z^{scatt}(\mathbf{x}_B, \omega) = A \iint_{\partial D_0} G_{z,z}^{scatt}(\mathbf{x}_B, \mathbf{x}, \omega) \bar{v}_z(\mathbf{x}, \omega) d^2\mathbf{x}, \quad (\text{B-5})$$

where  $G_{z,z}^{scatt}$  is the scattered Green's function and  $A$  is an amplitude-scaling factor due to the approximation that  $\bar{v}_z(\mathbf{x}, \omega)$  under the integral is proportional to the pressure measurement. The integral in equation B-5 is taken along the receiver positions (Earth's surface  $\partial D_0$ ). Substituting equations B-1 and B-4 into equation B-5, we get

$$v_z^c(\mathbf{x}_B, \omega) - 2\bar{v}_z^c(\mathbf{x}_B, \omega) = A \iint_{\partial D_0} G_{z,z}^{scatt}(\mathbf{x}_B, \mathbf{x}, \omega) \left\{ \bar{v}_z^d(\mathbf{x}, \omega) + \bar{v}_z^c(\mathbf{x}, \omega) \right\} d^2\mathbf{x}. \quad (\text{B-6})$$

Multiplying equation B-6 with  $\bar{v}_z^c(\mathbf{x}_A, \omega)^*$  and summation over the available sources, we get

$$\begin{aligned} & \sum_{S=1}^n \left[ v_z^c(\mathbf{x}_B, \omega) \left\{ \bar{v}_z^c(\mathbf{x}_A, \omega) \right\}^* \right] - 2\Gamma(\mathbf{x}_B, \mathbf{x}_A, \omega) = \\ & A \iint_{\partial D_0} G_{z,z}^{scatt,d}(\mathbf{x}_B, \mathbf{x}, \omega) \left[ \sum_{S=1}^n \left[ \bar{v}_z^d(\mathbf{x}, \omega) \left\{ \bar{v}_z^c(\mathbf{x}_A, \omega) \right\}^* \right] + \Gamma(\mathbf{x}, \mathbf{x}_A, \omega) \right] d^2\mathbf{x}, \end{aligned} \quad (\text{B-7})$$

where  $*$  denotes the complex conjugate and  $\Gamma$  is the point-spread function (PSF; [26]) defined as

$$\Gamma(\mathbf{x}_B, \mathbf{x}_A, \omega) = \sum_{S=1}^n \left[ \bar{v}_z^c(\mathbf{x}_B, \omega) \left\{ \bar{v}_z^c(\mathbf{x}_A, \omega) \right\}^* \right]. \quad (\text{B-8})$$

Equation B-7 can be also written as

$$\sum_{S=1}^n [v_z^c(\mathbf{x}_B, \omega) \{v_z^c(\mathbf{x}_A, \omega)\}^*] - 2\Gamma(\mathbf{x}_B, \mathbf{x}_A, \omega) + \sum_{S=1}^n [v_z^c(\mathbf{x}_B, \omega) \{ \bar{v}_z^c(\mathbf{x}_A, \omega) - v_z^c(\mathbf{x}_A, \omega) \}^*] - \quad (\text{B-9})$$

$$A \iint_{\partial D_0} G_{z,z}^{scatt,d}(\mathbf{x}_B, \mathbf{x}, \omega) \sum_{S=1}^n [ \bar{v}_z^d(\mathbf{x}, \omega) \{ \bar{v}_z^c(\mathbf{x}_A, \omega) \}^* ] d^2\mathbf{x} = A \iint_{\partial D_0} G_{z,z}^{scatt,d}(\mathbf{x}_B, \mathbf{x}, \omega) \Gamma(\mathbf{x}, \mathbf{x}_A, \omega) d^2\mathbf{x}.$$

The third and fourth terms in the left-hand side of equation B-9 retrieve events that are already retrieved by the first term in the left-hand side. Thus, the third and fourth terms can be seen as amplitude corrections to the events retrieved by the first term. If we neglect them to obtain equation 3.5, we will not obtain correct amplitudes in the left-hand side of equation B-9 and we will introduce artifacts. Still, the MDD of the first two terms in the left-hand side by  $\Gamma$  will result in the compensation of the result retrieved from SI by crosscorrelation for inhomogeneous illumination. Furthermore, as  $\Gamma$  cannot be obtained directly, we approximate it by only the dominant arrivals in the result from SI by crosscorrelation (see for examples Figures 3.9c and 3.9f).

### 3.1.7. APPENDIX C: TRUNCATED SINGULAR-VALUE DECOMPOSITION

In Figure C-1, we show the truncated singular values for the TN- and TE-array.

## REFERENCES

- [1] Y. Nishitsuji, S. Minato, B. Boullenger, M. Gomez, K. Wapenaar, and D. Draganov, *Crustal-scale reflection imaging and interpretation by passive seismic interferometry using local earthquakes*, *Interpretation* **4** (2016), 10.1190/INT-2015-0226.1.
- [2] J. W. Granath, R. C. Whittaker, V. Singh, D. E. Bird, and M. G. Dinkelman, *Full crustal seismic imaging in northeast Greenland*, *First Break* **28** (2010).
- [3] J. Zhao, Z. Jin, W. D. Mooney, N. Okaya, S. Wang, X. Gao, L. Tang, S. Pei, H. Liu, and Q. Xu, *Crustal structure of the central Qaidam basin imaged by seismic wide-angle reflection/refraction profiling*, *Tectonophysics* **584** (2013), 10.1016/j.tecto.2012.09.005.
- [4] K. Aki, A. Christofferson, and E. S. Husebye, *Determination of the three-dimensional seismic structure of the lithosphere*, *Journal of Geophysical Research* **82** (1977), 10.1029/JB082i002p00277.
- [5] S. Operto, J. Virieux, J.-X. Dessa, and G. Pascal, *Crustal seismic imaging from multifold ocean bottom seismometer data by frequency domain full waveform tomography: Application to the eastern Nankai trough*, *Journal of Geophysical Research: Solid Earth* **111** (2006), 10.1029/2005JB003835.
- [6] C. A. Langston, *Structure under Mount Rainier, Washington, inferred from teleseismic body waves*, *Journal of Geophysical Research: Solid Earth* **84** (1979), 10.1029/JB084iB09p04749.

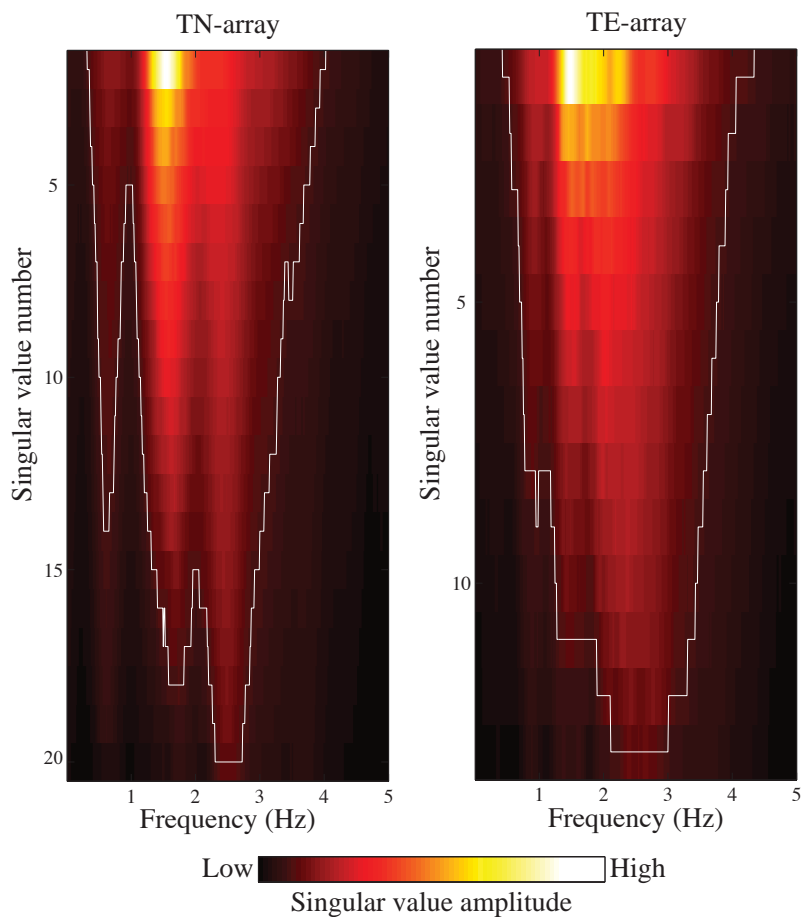


Figure C-1: Truncated singular values for the TN- and TE-array. The white lines show where 10 % of the maximum singular value lie. We truncate the lower amplitude within the white line for MDD.

- [7] I. Doi and H. Kawakata, *High resolution spatial distribution of the velocity discontinuities in and around the swarm region beneath the Wakayama district, southwest Japan*, *Bulletin of the Seismological Society of America* **103** (2013), [10.1785/0120120316](https://doi.org/10.1785/0120120316).
- [8] K. Aki, *Space and time spectra of stationary stochastic waves, with special reference to microtremors*, *Bulletin of the Earthquake Research Institute* **35** (1957).
- [9] J. F. Claerbout, *Synthesis of a layered medium from its acoustic transmission response*, *Geophysics* **33** (1968), [10.1190/1.1439927](https://doi.org/10.1190/1.1439927).
- [10] M. Campillo and A. Paul, *Long-range correlations in the diffuse seismic coda*, *Science* **299** (2003), [10.1126/science.1078551](https://doi.org/10.1126/science.1078551).
- [11] N. M. Shapiro and M. Campillo, *Emergence of broadband Rayleigh waves from correlations of the ambient seismic noise*, *Geophysical Research Letters* **31** (2004), [10.1029/2004GL019491](https://doi.org/10.1029/2004GL019491).
- [12] K. Wapenaar, *Retrieving the elastodynamic Green's function of an arbitrary inhomogeneous medium by cross correlation*, *Physical Review Letters* **93** (2004), [10.1103/PhysRevLett.93.254301](https://doi.org/10.1103/PhysRevLett.93.254301).
- [13] D. Draganov, X. Campman, J. Thorbecke, A. Verdel, and K. Wapenaar, *Reflection images from ambient seismic noise*, *Geophysics* **74** (2009), [10.1190/1.3193529](https://doi.org/10.1190/1.3193529).
- [14] Z. Zhan, S. Ni, D. V. Helmberger, and R. W. Clayton, *Retrieval of Moho-reflected shear wave arrivals from ambient seismic noise*, *Geophysical Journal International* **182** (2010), [10.1111/j.1365-246X.2010.04625.x](https://doi.org/10.1111/j.1365-246X.2010.04625.x).
- [15] T. Ryberg, *Body wave observations from cross-correlations of ambient seismic noise: A case study from the Karoo, RSA*, *Geophysical Research Letters* **38** (2011), [10.1029/2011GL047665](https://doi.org/10.1029/2011GL047665).
- [16] I. Panea, D. Draganov, C. Almagro Vidal, and V. Mocanu, *Retrieval of reflections from ambient noise recorded in the Mizil area, Romania*, *Geophysics* **79** (2014), [10.1190/geo2013-0292.1](https://doi.org/10.1190/geo2013-0292.1).
- [17] C. Almagro Vidal, D. Draganov, J. van der Neut, G. Drijkoningen, and K. Wapenaar, *Retrieval of reflections from ambient noise using illumination diagnosis*, *Geophysical Journal International* **198** (2014), [10.1093/gji/ggu164](https://doi.org/10.1093/gji/ggu164).
- [18] N. Nakata, R. Snieder, T. Tsuji, K. Larner, and T. Matsuoka, *Shear wave imaging from traffic noise using seismic interferometry by cross-coherence*, *Geophysics* **76** (2011), [10.1190/geo2010-0188.1](https://doi.org/10.1190/geo2010-0188.1).
- [19] N. Nakata, R. Snieder, and M. Behm, *Body-wave interferometry using regional earthquakes with multidimensional deconvolution after wavefield decomposition at free surface*, *Geophysical Journal International* **199** (2014), [10.1093/gji/ggu316](https://doi.org/10.1093/gji/ggu316).

- [20] T. L. Duvall, S. M. Jefferies, J. W. Harvey, and M. A. Pomerantz, *Time–distance helioseismology*, *Nature* **362** (1993), [10.1038/362430a0](https://doi.org/10.1038/362430a0).
- [21] R. Snieder, K. Wapenaar, and K. Larner, *Spurious multiples in seismic interferometry of primaries*, *Geophysics* **71** (2006), [10.1190/1.2211507](https://doi.org/10.1190/1.2211507).
- [22] I. Vasconcelos and R. Snieder, *Interferometry by deconvolution: Part 1 — Theory for acoustic waves and numerical examples*, *Geophysics* **73** (2008), [10.1190/1.2904554](https://doi.org/10.1190/1.2904554).
- [23] I. Vasconcelos and R. Snieder, *Interferometry by deconvolution: Part 2 — Theory for elastic waves and application to drill-bit seismic imaging*, *Geophysics* **73** (2008), [10.1190/1.2904985](https://doi.org/10.1190/1.2904985).
- [24] E. Slob, D. Draganov, and K. Wapenaar, *Interferometric electromagnetic Green's functions representations using propagation invariants*, *Geophysical Journal International* **169** (2007), [10.1111/j.1365-246X.2006.03296.x](https://doi.org/10.1111/j.1365-246X.2006.03296.x).
- [25] K. Wapenaar, J. van der Neut, and E. Ruigrok, *Passive seismic interferometry by multidimensional deconvolution*, *Geophysics* **73** (2008), [10.1190/1.2976118](https://doi.org/10.1190/1.2976118).
- [26] K. Wapenaar, J. van der Neut, E. Ruigrok, D. Draganov, J. Hunziker, E. Slob, J. Thorbecke, and R. Snieder, *Seismic interferometry by crosscorrelation and by multidimensional deconvolution: A systematic comparison*, *Geophysical Journal International* **185** (2011), [10.1111/j.1365-246X.2011.05007.x](https://doi.org/10.1111/j.1365-246X.2011.05007.x).
- [27] R. Snieder, *Extracting the Green's function from the correlation of coda waves: A derivation based on stationary phase*, *Physical Review E* **69** (2004), [10.1103/PhysRevE.69.046610](https://doi.org/10.1103/PhysRevE.69.046610).
- [28] K. Mayeda, L. Malagnini, and W. R. Walter, *A new spectral ratio method using narrow band coda envelopes: Evidence for non-self-similarity in the Hector Mine sequence*, *Geophysical Research Letters* **34** (2007), [10.1029/2007GL030041](https://doi.org/10.1029/2007GL030041).
- [29] A. Baltay, G. Prieto, and G. C. Beroza, *Radiated seismic energy from coda measurements and no scaling in apparent stress with seismic moment*, *Journal of Geophysical Research: Solid Earth* **115** (2010), [10.1029/2009JB006736](https://doi.org/10.1029/2009JB006736).
- [30] R. E. Abercrombie, *Comparison of direct and coda wave stress drop measurements for the Wells, Nevada, earthquake sequence*, *Journal of Geophysical Research: Solid Earth* **118** (2013), [10.1029/2012JB009638](https://doi.org/10.1029/2012JB009638).
- [31] E. Ruigrok, D. Draganov, M. Gómez, J. Ruzzante, D. Torres, I. López Pumarega, N. Barbero, A. Ramires, A. R. Castaño Gañan, K. van Wijk, and K. Wapenaar, *Malargüe seismic array: Design and deployment of the temporary array*, *The European Physical Journal Plus* **127** (2012), [10.1140/epjp/i2012-12126-7](https://doi.org/10.1140/epjp/i2012-12126-7).
- [32] J. F. Mescua, L. B. Giambiagi, and V. A. Ramos, *Late Cretaceous Uplift in the Malargüe fold-and-thrust belt (35° S), southern Central Andes of Argentina and Chile*, *Andean Geology* **40** (2013), [10.5027/andgeoV40n1-a05](https://doi.org/10.5027/andgeoV40n1-a05).

- [33] P. Kraemer, J. Silvestro, F. Achilli, and W. Brinkworth, *Kinematics of a hybrid thick-thin-skinned fold and thrust belt recorded in Neogene syntectonic wedge-top basins, southern central Andes between 35° and 36° S, Malargüe, Argentina*, *AAPG Memoir* **94** (2011), [10.1306/13251340M943099](https://doi.org/10.1306/13251340M943099).
- [34] A. I. Burd, J. R. Booker, R. Mackie, A. Favetto, and M. C. Pomposiello, *Three-dimensional electrical conductivity in the mantle beneath the Payun Matru Volcanic Field in the Andean backarc of Argentina near 36.5 S: Evidence for decapitation of a mantle plume by resurgent upper mantle shear during slab steepening*, *Geophysical Journal International* **198** (2014), [10.1093/gji/ggu145](https://doi.org/10.1093/gji/ggu145).
- [35] J. J. Becker, D. T. Sandwell, W. H. F. Smith, J. Braud, B. Binder, J. Depner, D. Fabre, J. Factor, S. Ingalls, S.-H. Kim, R. Ladner, K. Marks, S. Nelson, A. Pharaoh, R. Trimmer, J. Von Rosenberg, G. Wallace, and P. Weatherall, *Global bathymetry and elevation data at 30 arc seconds resolution: SRTM30\_PLUS*, *Marine Geodesy* **32** (2009), [10.1080/01490410903297766](https://doi.org/10.1080/01490410903297766).
- [36] J. R. Kayal, *Microearthquake Seismology and Seismotectonics of South Asia* (Springer, 2008).
- [37] G. A. Prieto, J. F. Lawrence, and G. C. Beroza, *Anelastic Earth structure from the coherency of the ambient seismic field*, *Journal of Geophysical Research: Solid Earth* **114** (2009), [10.1029/2008JB006067](https://doi.org/10.1029/2008JB006067).
- [38] J. van der Neut, E. Ruigrok, D. Draganov, and K. Wapenaar, *Retrieving the Earth's reflection response by multi-dimensional deconvolution of ambient seismic noise*, in *72nd annual EAGE meeting* (2010).
- [39] J. van der Neut, J. Thorbecke, K. Mehta, E. Slob, and K. Wapenaar, *Controlled-source interferometric redatuming by crosscorrelation and multidimensional deconvolution in elastic media*, *Geophysics* **76** (2011), [10.1190/1.3580633](https://doi.org/10.1190/1.3580633).
- [40] H. Nakahara and M. M. Haney, *Point spread functions for earthquake source imaging: An interpretation based on seismic interferometry*, *Geophysical Journal International* **202** (2015), [10.1093/gji/ggv109](https://doi.org/10.1093/gji/ggv109).
- [41] W. Menke, *Geophysical data analysis: Discrete inverse theory* (Academic Press, 1989).
- [42] V. Klema and A. Laub, *The singular value decomposition: Its computation and some applications*, *IEEE Transactions on Automatic Control* **25** (1980), [10.1109/TAC.1980.1102314](https://doi.org/10.1109/TAC.1980.1102314).
- [43] B. Boullenger, J. Hunziker, and D. Draganov, *Reflection-response retrieval with seismic interferometry by multidimensional deconvolution from surface reflection data*, in *EAGE Conference & Exhibition 2015* (2015).
- [44] S. Minato, T. Matsuoka, T. Tsuji, D. Draganov, J. Hunziker, and K. Wapenaar, *Seismic interferometry using multidimensional deconvolution and crosscorrelation for*



- crosswell seismic reflection data without borehole sources*, *Geophysics* **76** (2011), [10.1190/1.3511357](https://doi.org/10.1190/1.3511357).
- [45] S. Minato, T. Matsuoka, and T. Tsuji, *Singular-value decomposition analysis of source illumination in seismic interferometry by multidimensional deconvolution*, *Geophysics* **78** (2013), [10.1190/geo2012-0245.1](https://doi.org/10.1190/geo2012-0245.1).
- [46] K. Pearson, *On lines and planes of closest fit to systems of points in space*, *Philosophical Magazine* **2** (1901), [10.1080/14786440109462720](https://doi.org/10.1080/14786440109462720).
- [47] H. Borko and M. Bernick, *Automatic document classification*, *Journal of the ACM* **10** (1963), [10.1145/321160.321165](https://doi.org/10.1145/321160.321165).
- [48] G. H. Golub and C. F. V. Loan, *Matrix Computations* (The Johns Hopkins University Press, 1957).
- [49] M. Farías, D. Comte, R. Charrier, J. Martinod, C. David, A. Tassara, F. Tapia, and A. Fock, *Crustal-scale structural architecture in central Chile based on seismicity and surface geology: Implications for Andean mountain building*, *Tectonics* **29** (2010), [10.1029/2009TC002480](https://doi.org/10.1029/2009TC002480).
- [50] B. L. N. Kennett, E. R. Engdahl, and R. Buland, *Constraints on seismic velocities in the Earth from traveltimes*, *Geophysical Journal International* **122** (1995), [10.1111/j.1365-246X.1995.tb03540.x](https://doi.org/10.1111/j.1365-246X.1995.tb03540.x).
- [51] H. Kanamori and E. E. Brodsky, *The physics of earthquakes*, *Reports on Progress in Physics* **67** (2004), [10.1088/0034-4885/67/8/R03](https://doi.org/10.1088/0034-4885/67/8/R03).
- [52] G. M. Atkinson and D. M. Boore, *On the  $mN$ ,  $M$  relation for Eastern North American Earthquakes*, *Seismological Research Letters* **58** (1987), [10.1785/gssrl.58.4.119](https://doi.org/10.1785/gssrl.58.4.119).
- [53] A. Paul, M. Campillo, L. Margerin, and E. Larose, *Empirical synthesis of time-asymmetrical Green functions from the correlation of coda waves*, *Journal of Geophysical Research: Solid Earth* **110** (2005), [10.1029/2004JB003521](https://doi.org/10.1029/2004JB003521).
- [54] K. Emoto, M. Campillo, F. Brenguier, X. Briand, and T. Takeda, *Asymmetry of coda cross-correlation function: Dependence of the epicentre location*, *Geophysical Journal International* **201** (2015), [10.1093/gji/ggv081](https://doi.org/10.1093/gji/ggv081).
- [55] Y. Nishitsuji, E. Ruigrok, M. Gomez, K. Wapenaar, and D. Draganov, *Reflection imaging of aseismic zones of the Nazca slab by global-phase seismic interferometry*, *Interpretation* **4** (2016), [10.1190/INT-2015-0225.1](https://doi.org/10.1190/INT-2015-0225.1).
- [56] Y. Nishitsuji, E. Ruigrok, M. Gomez, and D. Draganov, *Global-phase  $H/V$  spectral ratio for delineating the basin in the Malargue region, Argentina*, *Seismological Research Letters* **85** (2014), [10.1785/0220140054](https://doi.org/10.1785/0220140054).
- [57] Ö. Yilmaz, *Seismic data analysis* (Society of Exploration Geophysicists, 1987).

- [58] D. Garcia, *Robust smoothing of gridded data in one and higher dimensions with missing values*, *Computational Statistics & Data Analysis* **54** (2010), [10.1016/j.csda.2009.09.020](https://doi.org/10.1016/j.csda.2009.09.020).
- [59] H. Gilbert, S. Beck, and G. Zandt, *Lithospheric and upper mantle structure of central Chile and Argentina*, *Geophysical Journal International* **165** (2006), [10.1111/j.1365-246X.2006.02867.x](https://doi.org/10.1111/j.1365-246X.2006.02867.x).
- [60] S. Abe, E. Kurashimo, H. Sato, N. Hirata, T. Iwasaki, and T. Kawanaka, *Interferometric seismic imaging of crustal structure using scattered teleseismic waves*, *Geophysical Research Letters* **34** (2007), [10.1029/2007GL030633](https://doi.org/10.1029/2007GL030633).
- [61] P. G. DeCelles and K. A. Giles, *Foreland basin systems*, *Basin Research* **8** (1996), [10.1046/j.1365-2117.1996.01491.x](https://doi.org/10.1046/j.1365-2117.1996.01491.x).
- [62] L. Giambiagi, M. Ghiglione, E. Cristallini, and G. Bottesi, *Kinematic models of basement/cover interaction: Insights from the Malargüe fold and thrust belt, Mendoza, Argentina*, *Journal of Structural Geology* **31** (2009), [10.1016/j.jsg.2009.10.006](https://doi.org/10.1016/j.jsg.2009.10.006).
- [63] L. Giambiagi, J. Mescua, F. Bechis, A. Tassara, and G. Hoke, *Thrust belts of the southern Central Andes: Along-strike variations in shortening, topography, crustal geometry, and denudation*, *Geological Society of America Bulletin* **124** (2012), [10.1130/B30609.1](https://doi.org/10.1130/B30609.1).
- [64] S. C. Singh, A. J. Harding, G. M. Kent, M. C. Sinha, V. Combi, S. Bazin, C. H. Tong, J. W. Pye, P. J. Barton, R. W. Hobbs, R. S. White, and J. A. Orcutt, *Seismic reflection images of the Moho underlying melt sills at the East Pacific Rise*, *Nature* **442** (2006), [10.1038/nature04939](https://doi.org/10.1038/nature04939).
- [65] A. J. Calvert and S. E. McGeary, *Seismic reflection imaging of ultradeep roots beneath the eastern Aleutian island arc*, *Geology* **41** (2013), [10.1130/G33683.1](https://doi.org/10.1130/G33683.1).
- [66] A. J. Calvert, L. A. Preston, and A. M. Farahbod, *Sedimentary underplating at the Cascadia mantle-wedge corner revealed by seismic imaging*, *Nature Geoscience* **4** (2011), [10.1038/ngeo1195](https://doi.org/10.1038/ngeo1195).



# 4

## LITHOSPHERIC-SCALE SEISMIC IMAGING AND CHARACTERIZATION

**Yohei NISHITSUJI, Elmer RUIGROK, Martín GOMEZ,  
Kees WAPENAAR, C. A. ROWE, Jim MORI, Deyan DRAGANOV**

*Don't forget to love yourself.*

Søren Kierkegaard

### **Summary**

*In the first subchapter, we present SI with global phases (GloPSI) for imaging the aseismic and seismic parts of a subducting slab and the mantle above it. GloPSI retrieves reflection responses from coinciding virtual source and receiver at each seismic station to which it is applied. We apply the method to global P-wave phases recorded by an array of short-period stations installed for one year in the Malargüe region, Argentina, located east of the southern part of central Chile. The array consisted of a station distribution to the east of the Peteroa volcano and two linear subarrays to the east of the town of Malargüe. We process the retrieved reflection responses to obtain depth images of the subsurface beneath the array. The images to the east of Malargüe town reveal, with high horizontal and vertical resolution, a bifurcated Moho and a complex-structured upper mantle. On the images, we also interpret the aseismic part of the Nazca slab, which manifests itself as dimmed*

---

The first subchapter has been published in *Interpretation* **4**, 3 (2016) [1].

The second subchapter has been published in *Geophysical Journal International* **196**, 2 (2014) [2].

The third subchapter has been published in *Journal of Geophysical Research: Planets* **121**, 4 (2016) [3].

Note that minor changes have been introduced to make the text consistent with the other chapters of this thesis.

reflectivity due to the relation between the depth of the dipping reflectors and the short array length we use. The aseismic part of the slab appears to be without tears and to be dipping with an angle of  $43^\circ$  to the east. The image beneath Peteroa also shows the Moho. The deeper part of the image shows packages of strong reflectivity with lack of reflectivity between them. These might be interpreted as a deformation in the dipping slab. If so, the interpreted deformation could be in the form of detachment, shearing, necking, or any combination thereof.

In the second subchapter, we estimate source parameters of 216 intermediate-depth (65–150 km) earthquakes ( $M_W$  4.0–7.0) in the Pacific slab beneath Japan along using Hi-net data. We make determinations of static stress drop, radiated energy and radiation efficiency, along with estimates of the whole path attenuation, to study the source scaling as a function of earthquake size and depth. Our results show that there is a small increase in the values of the ratio of radiated energy to seismic moment, as a function of seismic moment, which is due to an associated slight increase of static stress drop with earthquake size. We also estimate the radiation efficiency for these events using the static stress drops and radiated energies. The values of radiation efficiency are slightly lower compared to shallow crustal earthquakes. These results indicate that dissipative energy processes may be relatively more important for intermediate-depth earthquakes.

In the third subchapter, we apply seismic interferometry to P wave codas of deep moonquakes (DMSI) recorded by the Apollo seismic stations to retrieve a reflection image of the Moon's subsurface. With DMSI, we analyze the P wave coda of seven clusters of deep moonquakes whose incoming wavefronts of the direct P wave phases are approximately planar at the stations, and whose ray parameters are sufficiently small. Our DMSI image shows reflections consistent with structures at depths of  $\sim 5$  km to  $\sim 170$  km beneath the Apollo stations on the nearside of the Moon. The image reveals laterally coherent horizontal events with strong amplitudes under all four Apollo stations down to a depth of 50 km, where we observe a laterally coherent horizon characterized by relatively lower amplitudes. Below that horizon, our results are characterized by rather ringing phases with relatively lower amplitude. We interpret the acoustic boundary at 50 km to be the lunar Moho beneath the four Apollo stations with an uncertainty of  $\pm 8$  km due to possible interference from multiple reflections. This depth value is in good agreement with JAXA's SELENE study and is close to the depth in previous travel time studies. The deeper part of the image reveals a laterally heterogeneous picture with very few laterally coherent horizontal events interpretable beneath three of the Apollo stations. These suggest the presence of a strong scattering zone. Our results show that DMSI has the potential to obtain zero-offset reflection images without the need of active sources, such as explosives or other artificial impacts. Our method could be extended to imaging the subsurface below seismic stations on the farside of the Moon if installed by future missions.

## 4.1. ON THE EARTH: GLOBAL-PHASE SEISMIC INTERFEROMETRY

### 4.1.1. INTRODUCTION

It has been shown that at the northern part of Central Chile (30 - 33°S) the Nazca slab is of the flat type [e.g. 4–6]. At that part, the upwelling plume was recently imaged [7]. Still, the slab's geometry in the southern part of central Chile (34 - 37°S) is unclear and it is unknown whether that part of the slab is not torn [e.g. 8, 9].

One of the challenges in imaging the slab in this region by seismological methods relates to the absence of seismicity. Although hypocenter mapping is a useful method for identifying the Wadati-Benioff zone [e.g. 10–12], it cannot be used to image the aseismic region.

The receiver-function method [e.g. 13–15] can be used to image aseismic regions, but so far has not yielded images of the aseismic zone in this region. Yuan *et al.* [16] suggest that the reason for this might be the possible completion of the gabbro-eclogite transformation within the Nazca slab. Gilbert *et al.* [8] suggest large attenuation of S-wave energy in the mantle wedge as another possible reason.

Global tomography [e.g. 17–19] is a tool for investigating global-scale geodynamics and it can be used for imaging aseismic zones. However, the method's resolution ( $\approx 50$  km) poses limitations on estimating the slab's exact location and continuity at local scale, thus leaves a lot of uncertainties.

The reflection method with active sources (explosives, vibroseis, airguns) provides the needed high-resolution imaging capabilities, but its depth penetration is fundamentally limited by the strength of the used sources.

Here, we demonstrate the usefulness of an alternative seismic technique to image the aseismic slab zone with high resolution, namely seismic interferometry (SI) for body-wave retrieval [e.g. 20–24] using global phases (GloPSI) [25]. Global phases are seismic phases that travel through the Earth's core before reaching the surface. They are induced by earthquakes at epicentral distances greater than 120° (global distances). The global phases are extracted from the continuous field recordings and used as contributions from separate transient sources. For the considered configuration, this is closely related to work of Kumar and Bostock [26] and Nowack [27]. For a horizontally layered (1D) acoustic medium, SI retrieves the reflection response of the medium from the autocorrelation of the medium's plane-wave transmission response measured at the surface [20]. GloPSI is a 3D generalization of the mentioned 1D case – it extends the illumination to include a range of ray parameters (horizontal slownesses) allowing retrieval of reflections from 3D structures. At seismic stations, these extra ray parameters would come from recorded global P-wave arrivals, such as the phases PKP, PKiKP, and PKIKP. These arrivals (phases) have ray parameters lower than 0.04 s/km and are characterized in the mantle by nearly planar wavefronts. This makes these phases suitable for SI by autocorrelation. Due to the autocorrelation, GloPSI retrieves pseudo zero-offset reflection arrivals that penetrate deep enough to allow slab imaging with resolution dictated by the frequency bandwidth of the phases, sensor configuration and two-way traveltime difference between consecutive arrivals. GloPSI may further shed light on one of the open questions in the geoscience community of whether small deformations and/or detach-

ments ( $< 25$  km) in the slab are actually present [28]. In the following, we show how to apply GloPSI to field waveform data. First we describe the GloPSI method, then we describe the data we use, phase extraction and preparation, and then we show our results and their interpretation. Our results image the aseismic zone of the slab and possible deformation in the slab.

#### 4.1.2. GLOBAL-PHASE SEISMIC INTERFEROMETRY

##### THEORY

The 1D theory from Claerbout [20] was generalized for a 3D inhomogeneous medium by Wapenaar [24]. Ruigrok and Wapenaar [25] applied the generalization of seismic interferometry for retrieval of body waves from the autocorrelation of global phases recorded at seismic stations in Himalaya and Tibet. They termed this specific application GloPSI.

The GloPSI relation for the retrieval of the zero-offset reflection response  $R(\mathbf{x}_R, \mathbf{x}_R, t)$  for co-located source and receiver at the location of station  $\mathbf{x}_R$  is [25]

$$\sum_{p_{min}}^{p_{max}} \sum_{\theta_{min}}^{\theta_{max}} \{T(\mathbf{x}_R, \mathbf{p}_S, -t) * T(\mathbf{x}_R, \mathbf{p}_S, t) * E_i(-t) * E_i(t)\} \propto \quad (4.1)$$

$$\{\delta(t) - R(\mathbf{x}_R, \mathbf{x}_R, -t) - R(\mathbf{x}_R, \mathbf{x}_R, t)\} * \bar{E}_n(t),$$

where  $T(\mathbf{x}_R, \mathbf{p}_S, t)$  is the transmission response (selected global phase) at the receiver location  $\mathbf{x}_R$  due to an earthquake  $i$ , arriving from direction  $\mathbf{p} = (p, \theta)$  with ray parameter  $p$  and back azimuth  $\theta$ ,  $E_i(t)$  is the source time function of the  $i$ -th earthquake,  $\bar{E}_n(t)$  is the average of the autocorrelations of the different source time functions, and  $*$  denotes convolution. In our case, the absolute value of the ray parameter varies between 0 and 0.04 s/km, while  $\theta$  varies between  $0^\circ$  and  $360^\circ$ . In equation 4.1 the summation is effectively over plane-wave sources, instead of over point sources. A derivation of the SI relation from point sources to plane-wave sources can be found in Ruigrok *et al.* [29]. The zero-offset reflection response retrieved by GloPSI can be used to image the subsurface structures in a way similar to the conventional reflection seismic method with active sources. Note that GloPSI directly produces zero-offset reflection responses of the subsurface, which is one of the conventional goals of the active-source reflection method. With the latter, offset measurements are stacked to obtain pseudo zero-offset traces [30], as direct zero-offset measurements are still commercially impractical. A difference between the zero-offset section retrieved by GloPSI and an active-source pseudo zero-offset section is that the virtual source in the former radiates energy vertically and near-vertically down into the Earth, while in the latter the pseudo zero-offset source radiates in all directions. Because of this, GloPSI will image horizontal to mildly inclined structures directly, while steeply dipping structures will be manifest by a lack of reflections reaching the receivers and can be interpreted by discontinuation of imaged (nearly) horizontal structures. This is similar to the problem in the active-source reflection method, where a steeply dipping structure lying relatively deep compared to the receiver-array length, will not be imaged [e.g. 30].

When the length of the used receiver array is sufficiently long, relative to the depth of the structure of interest, and given a sufficiently wide illumination (in terms of ray parameters and back azimuths), the autocorrelation in the GloPSI relation 4.1 can be

replaced by crosscorrelation, which would permit retrieval of offset reflections as well. This would allow for direct imaging of a broader range of dipping structures.

In Figure 4.1, we show in a schematic way how GloPSI would (or would not) retrieve reflection responses from four different structural settings.

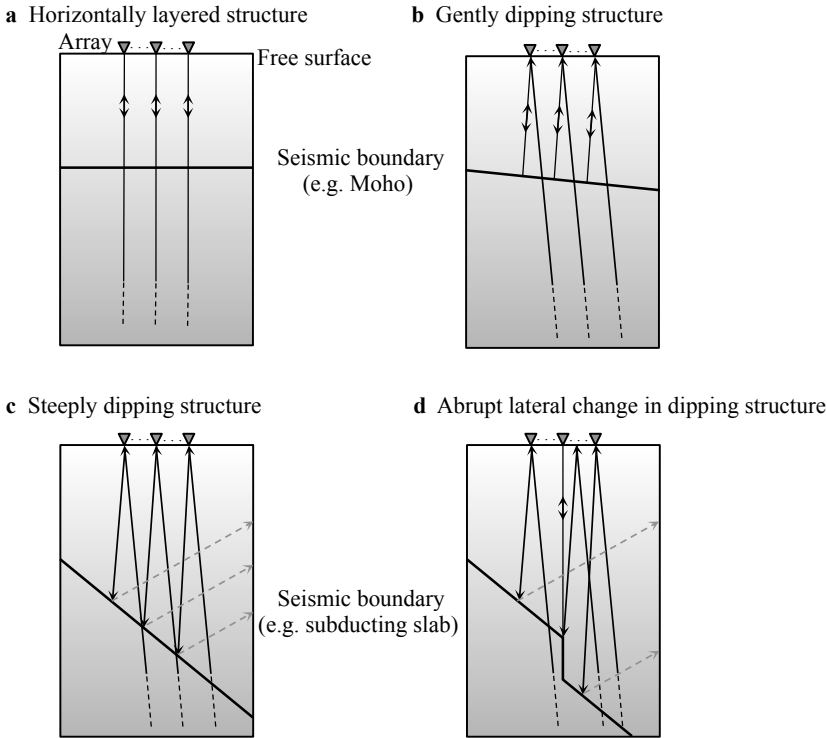


Figure 4.1: A schematic illustration of how GloPSI would or would not retrieve reflection responses for: (a) a horizontally layered structure and vertical transmission responses; (b) a gently dipping structure and nearly vertical transmission responses; (c) as in (b), but for a steeply dipping structure; (d) as in (c), but when an abrupt change (e.g. slab deformation) presents in present in the lateral continuation of the dipping structure. The black lines indicate the transmission response from the global earthquakes, while the gray dashed lines depict the reflection response that will not be recorded at the station due to the configuration. Two-way arrows indicate the reflection response that will be recorded at the station.

#### COMPARISON WITH THE RECEIVER-FUNCTION METHOD

The receiver-function method depends on phase conversions (P-to-S or S-to-P) occurring in transmission. GloPSI with P-wave phases uses reflection information and depends only on the P-wave impedance contrasts, just like the conventional reflection method. Comparisons of imaging results from SI and receiver function have shown that SI provides images with resolution at least as high as the receiver-function image [31]. In cases of structural contrasts that are due to relatively thin layers, SI has the potential to provide higher resolution than the receiver function. For example, suppose there is



a mantle structure 5 km below the Moho, which is illuminated by a P-wave phase with an incidence angle of  $10^\circ$ . The P- and S-wave velocities between the structure and the Moho are 8.1 km/s and 4.5 km/s, respectively, while above the Moho the respective velocities are 5 km/s and 2.5 km/s. The receivers at the surface would record the P-to-S converted waves from the two boundaries with a time difference of 0.49 s – the time difference for the propagation of the P- and S-waves between the mantle structure and the Moho. A virtual zero-offset reflection recording, retrieved from GloPSI, would contain two P-wave reflections from the impedance contrasts at the Moho and the mantle structure arriving with a time difference of 1.23 s. In terms of wavelength, assuming a center frequency for both P- and S-waves of 0.8 Hz, the two arrivals in the recordings used by the receiver-function method would be 0.39 wavelengths apart. In the retrieved recordings from GloPSI, the two P-wave reflections would be 0.99 wavelengths apart, which would allow for higher resolution.

Thus, although until now SI or GloPSI has not been applied for imaging of aseismic slab zones, these methods have the potential to image such zones with temporal (depth) resolution higher than the one that can be achieved using the receiver-function method.

### 4.1.3. DATA

#### STUDY AREA

Figure 4.2 shows the location of intermediate-depth earthquakes that have occurred from August 1906 to July 2014 around the Malargüe region ( $35.5^\circ\text{S}$ ), Argentina. The locations are taken from the U.S. Geological Survey (USGS) earthquake catalog. There could be more earthquakes actually present than we show in Figure 4.2 if they are not in the catalogue. Note that there are no earthquakes deeper than around 200 km. There is also an aseismic spot beneath the Peteroa Volcano. This volcano forms part of the Planchón-Peteroa volcanic complex. We are interested in imaging these aseismic zones, and we achieve this using GloPSI. In Figure 4.2, the station GO05 of the Chilean National Seismic Network and the station C02A of the Talca Seismic Network, which we use later for quality-control purpose, are also plotted.

#### MALARRGUE

We apply GloPSI to data from the MalARRgüe array [25]. The array recorded continuously ambient noise and seismicity during 2012 in the Malargüe region, Argentina, to the east of the southern part of central Chile. The array consisted of a patchy subarray PV and an exploration-style 2D T-shaped subarray T with arms TN and TE pointing north and east, respectively, see Figure 4.3. MalARRgüe used short-period (2-Hz) sensors borrowed from the Program for Array Seismic Studies of the Continental Lithosphere (PASSCAL) managed by Incorporated Research Institutions for Seismology (IRIS). The PV-array consisted of 6 irregularly spaced stations labeled PV01 to PV06; the TN-array formed a line of 19 stations spaced at 2 km and labeled TN02 to TN20, while the TE-array formed a line of 13 stations spaced at 4 km and labeled TE01 to TE13. Figure 4.3 shows the distribution of the global earthquakes we use to extract phases at the PV- and T-array, which phases are then used as input for GloPSI. The T-array lies above the beginning of the Nazca's aseismic zone, where possible slab tearing [9] and/or presence of plume decapitation [32] have been proposed.

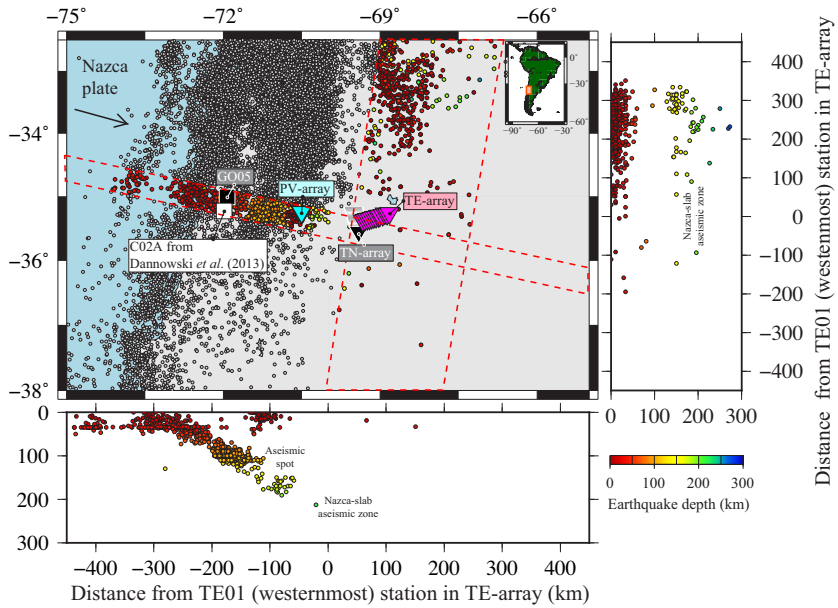


Figure 4.2: Center – Location of the seismic stations used in our study, and hypocenters mapping using earthquakes archived by USGS. Below and right – distribution of the hypocenters in depth within the red dashed-line areas in NWW-SEE and NNE-SSW direction.

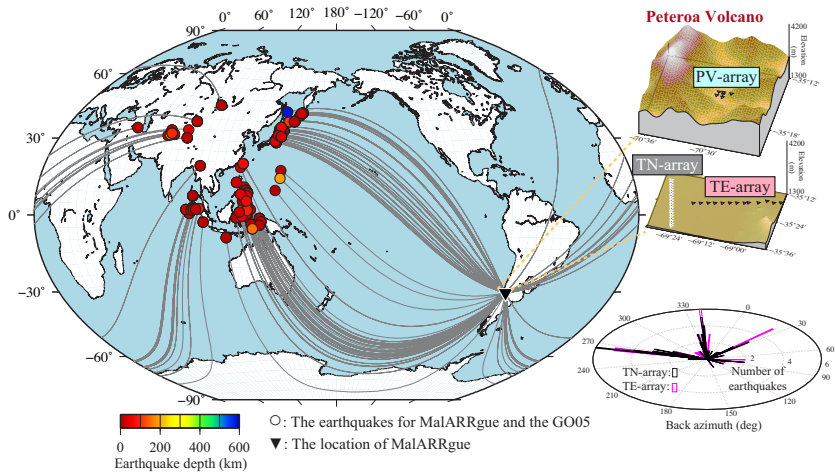


Figure 4.3: Distribution of the global-phase earthquakes used in our study. The circles show the location of the earthquakes used for MalARRgüe and the GO05 station. The location of MalARRgüe is indicated by the black triangle with its topography maps [33] in the insets. The distribution of the back azimuth of the earthquakes for the T-array is shown in the inset.

### SELECTING AND EXTRACTING GLOBAL PHASES

We use the vertical-component recordings of the MalARRgue array for GloPSI. Using Java version of Windows Extracted from Event Data (JWEED) from IRIS and a reference earthquake catalogue from USGS, from the recorded total amount of global earthquakes with  $M_W \geq 5.5$ , we select 66, 72, and 85 earthquakes for the PV-, TN-, and TE-array, respectively (Table 4.4). We use PKP, PKiKP and PKIKP phases (epicentral distances  $\geq 120^\circ$ ), which travel through the mantle and core and arrive at the stations with absolute slowness  $< 0.04$  s/km [34]. We search the phases visually using a window of 900 s, which starts 100 s before the expected arrival of the specific P-wave phase; we also use as guides the phase pickings that are automatically calculated by IRIS. Then, we extract the desired phases from a shorter window, which is at least 200 s long. This window starts before the arrival of the specific P-wave phase and terminates before onset of the first S-wave phase. Figure 4.4 shows an example of the windowing.

4

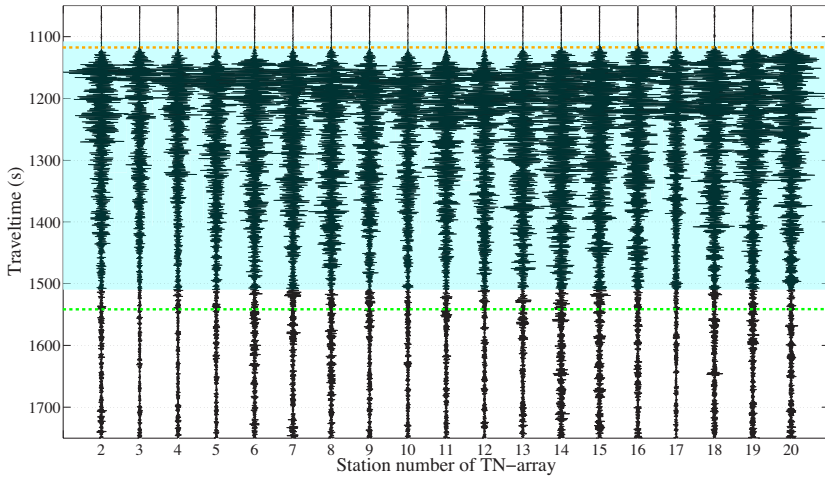


Figure 4.4: An example recording of a global earthquake on the vertical component of the stations from the TN-array. The area highlighted in light blue indicates the used window that contains the global phases. The orange and green lines indicate the P- and S-wave phase onsets by IRIS, respectively.

For quality control, as described below, we also use data from the station GO05 from the Chilean National Seismic Network, which is situated above the seismic zone of the Nazca slab. For GO05, we use 52 earthquakes recorded by the station during the operation of MalARRgue (Table 4.1). The complete list of the used earthquakes for MalARRgue and GO05 is given in Table 4.1.

Table 4.1: Global earthquakes used in this study

Date (month/d/yr)	Time (hr:min:s)	Lat. (°N)	Lon. (°E)	Dep. (km)	$M_W$	Array ID
01/18/12	12:50:21	-0.877	126.829	19	5.7	TE
01/28/12	0:17:11	13.386	124.586	35	5.5	TE
02/04/12	13:09:23	11.872	125.754	12	5.8	PV/TN/TE/GO
02/06/12	3:49:13	9.999	123.206	11	6.7	TE
02/06/12	4:20:00	10.092	123.227	10	5.6	TE

02/06/12	10:10:20	9.885	123.095	9	6.0	PV/TN/TE/GO
02/06/12	11:33:37	9.821	123.080	15	5.9	PV/TN/TE/GO
02/14/12	6:22:01	36.214	141.386	28	5.8	PV/TN/TE/GO
02/26/12	2:35:01	22.661	120.891	28	5.9	TE
02/26/12	6:17:20	51.708	95.991	12	6.6	PV/TN/TE/GO
02/29/12	14:32:48	35.200	141.001	26	5.6	TE
03/08/12	22:50:08	39.383	81.307	38	5.9	TE
03/12/12	6:06:41	36.741	73.152	11	5.7	PV/TN/TE
03/12/12	12:32:46	45.239	147.609	110	5.6	PV/TN/TE
03/14/12	9:08:35	40.887	144.944	12	6.9	PV/TN/TE
03/14/12	10:49:25	40.781	144.761	10	6.1	PV/TN/TE
03/14/12	12:05:05	35.687	140.695	10	6.0	PV/TN/TE
03/16/12	7:58:02	10.037	125.633	18	5.8	PV/TN/TE/GO
03/22/12	0:21:37	3.513	125.859	117	5.6	TE
03/27/12	11:00:45	39.859	142.017	15	6.0	PV/TN/TE/GO
04/01/12	14:04:25	37.116	140.957	48	5.8	PV/TN/TE
04/11/12	8:38:37	2.327	93.063	20	8.6	PV/TN/TE/GO
04/11/12	10:43:11	0.802	92.463	25	8.2	PV/TN/TE/GO
04/13/12	10:10:01	36.988	141.152	11	5.7	PV/TN/TE/GO
04/14/12	15:13:14	49.380	155.651	90	5.6	TE
04/15/12	5:57:40	2.581	90.269	25	6.3	PV/TN/TE/GO
04/20/12	22:19:47	3.256	93.853	25	5.8	TE
04/20/12	22:28:59	3.269	93.821	22	5.8	PV/TN/TE/GO
04/20/12	23:14:31	2.158	93.360	28	5.9	PV/TN/TE/GO
04/21/12	1:16:53	-1.617	134.276	16	6.7	PV/TN/TE/GO
04/23/12	21:21:45	0.374	125.293	48	5.7	TE/GO
04/23/12	22:40:22	48.397	154.739	31	5.7	PV/TN/TE
04/24/12	14:57:10	8.868	93.949	14	5.6	PV/TN/TE/GO
04/25/12	7:42:23	9.011	93.945	9	5.9	PV/TN/TE/GO
04/29/12	8:09:04	2.704	94.509	14	5.7	PV/TN/TE/GO
04/29/12	10:28:52	35.596	140.349	44	5.8	PV/TN/TE/GO
05/12/12	23:28:44	38.612	70.354	10	5.7	PV/TN/TE/GO
05/23/12	15:02:25	41.335	142.082	46	6.0	PV/TN/TE
06/05/12	19:31:34	34.943	141.132	15	6.1	PV/TN/TE
06/09/12	14:23:20	48.851	154.852	49	5.5	TE
06/09/12	21:00:18	24.572	122.248	70	5.9	PV/TN/TE
06/11/12	5:29:12	36.023	69.351	16	5.7	TE
06/14/12	20:17:25	1.293	126.828	61	5.5	TE
06/15/12	1:14:08	5.719	126.354	41	5.7	PV/TN/TE/GO
06/16/12	22:18:47	15.593	119.563	28	5.9	PV/TN/TE/GO
06/17/12	20:32:21	38.919	141.831	36	6.3	PV/TN/TE/GO
06/23/12	4:34:53	3.009	97.896	95	6.1	PV/TN/TE/GO
06/29/12	21:07:34	43.433	84.700	18	6.3	PV/TN/TE/GO
07/08/12	11:33:03	45.497	151.288	20	6.0	PV/TN/TE
07/11/12	2:31:17	45.401	151.424	10	5.7	PV/TN/TE
07/12/12	12:51:59	45.452	151.665	12	5.7	TE
07/12/12	14:00:34	36.527	70.906	198	5.8	PV/TN/TE
07/19/12	7:36:35	37.248	71.375	98	5.6	PV/TN/TE/GO
07/20/12	3:40:12	49.506	155.599	15	5.5	TE
07/20/12	6:10:25	49.407	155.907	19	6.0	PV/TN/TE/GO
07/20/12	6:32:56	49.354	156.132	10	5.9	PV/TN/GO
07/25/12	0:27:45	2.707	96.045	22	6.4	PV/TN/GO
08/11/12	12:23:18	38.329	46.826	11	6.5	TE
08/11/12	12:34:36	38.389	46.745	12	6.4	TE
08/12/12	10:47:06	35.661	82.518	13	6.2	PV/TN/TE/GO
08/14/12	2:59:38	49.800	145.064	583	7.7	PV/TN/TE
08/18/12	9:41:52	-1.315	120.096	10	6.3	PV/TN/TE
08/18/12	15:31:40	2.645	128.697	10	5.8	TE
08/25/12	14:16:17	42.419	142.913	55	5.9	PV/TN/TE/GO
08/26/12	15:05:37	2.190	126.837	91	6.6	PV/TN/TE/GO
08/29/12	19:05:11	38.425	141.814	47	5.5	PV/TN/TE/GO
08/31/12	12:47:33	10.811	126.638	28	7.6	PV/TN/TE/GO
08/31/12	23:37:58	10.388	126.719	40	5.6	PV/TN/TE/GO
09/03/12	6:49:50	6.610	123.875	12	5.9	PV/TN/TE/GO
09/03/12	18:23:05	-10.708	113.931	14	6.3	PV/TN/GO
09/03/12	19:44:22	7.905	125.044	10	5.7	PV/TN/TE/GO
09/08/12	6:54:19	21.527	145.923	5	5.6	TE
09/08/12	10:51:44	-3.177	135.109	21	6.1	PV/TN/GO
09/09/12	5:39:37	49.247	155.750	31	5.9	TE
09/11/12	1:28:19	45.335	151.111	14	5.5	PV/TN/TE/GO
09/11/12	16:36:50	11.838	143.218	8	5.9	TE
09/14/12	4:51:47	-3.319	100.594	19	6.3	PV/TN/GO
10/01/12	22:21:46	39.808	143.099	15	6.0	PV/TN
10/08/12	11:43:31	-4.472	129.129	10	6.2	PV/TN/GO
10/12/12	0:31:28	-4.892	134.030	13	6.6	PV/TN/GO
10/14/12	9:41:59	48.308	154.428	35	5.8	PV/TN
10/16/12	12:41:26	49.618	156.438	81	5.6	PV/TN
10/17/12	4:42:30	4.232	124.520	326	6.0	PV/TN
11/01/12	23:37:18	1.229	122.105	35	5.5	TE
11/02/12	18:17:33	9.219	126.161	37	6.1	TN/TE/GO
11/05/12	4:30:27	37.791	143.610	19	5.6	TN/TE/GO
11/06/12	1:36:22	1.374	122.200	25	5.6	TN/TE/GO
11/06/12	1:42:26	1.357	122.167	35	5.6	TE
11/11/12	1:12:39	23.005	95.885	14	6.8	TN/TE/GO
11/14/12	5:21:42	9.982	122.472	41	5.7	TN/TE/GO
11/16/12	18:12:40	49.280	155.425	29	6.5	TN/TE/GO
11/27/12	7:34:25	17.684	145.763	192	5.5	TE
12/07/12	8:18:23	37.890	143.949	31	7.3	PV/TN/TE/GO
12/09/12	21:45:35	6.703	126.166	63	5.8	PV/TN/TE/GO
12/10/12	16:53:09	-6.533	129.825	155	7.1	PV/TN/GO

12/11/12	6:18:27	0.533	126.231	30	6.0	PV/TN/TE
12/17/12	9:16:31	-0.649	123.807	44	6.1	PV/TN/TE

#### 4.1.4. DATA PROCESSING

##### DATA PROCESSING FOR OBTAINING IMAGES

After deconvolving the recordings with the instrument response, we compute power spectral densities (PSD) of the global-phase earthquakes to help us select a frequency band that provides adequate signal-to-noise ratio (SNR) of the global phases. Figure 4.5 shows an example of the computed PSD for earthquakes of different magnitude higher than 5.5 that occurred at global distances. We select the band 0.3-1.0 Hz using a 5th-order butterworth filter, as in this band all signals of the earthquakes are clearly observed (Figure 4.4). The lower limit of our band is set at 0.3 Hz due to the low-frequency limitations of the used instruments [35], as well as to make sure that the double-frequency microseisms noise is largely excluded.

After selecting the frequency band between 0.3 Hz and 1 Hz, we downsample the data from the original sampling of 0.01 s to 0.25 s with the aim to minimize the volume of data. After that, we normalize each selected and filtered phase with respect to its maximum amplitude. We also apply despiking to trace intervals with very strong (accidental) signal spikes that saturate the trace for some time (the interval duration). For the TN- and TE-array, missing traces at certain stations (e.g. due to despiking) are interpolated using the corresponding records at their neighboring stations (Figure 4.6).

After the above preprocessing, we apply GloPSI to the selected events for each of the subarrays from MalARRgue (Figure 4.7). The retrieved zero-offset reflection trace at each station is dominated in the first few seconds by the average autocorrelation convolved with a delta function,  $\bar{E}_n(t) * \delta(t)$ . To suppress the effect of  $\bar{E}_n(t)$ , for each subarray we extract the effective source time functions  $\bar{E}_n(t)$  from each retrieved zero-offset trace per subarray for a two-way traveltimes from 0 to 10 s, take their mean, and subtract the mean from the individual traces in each subarray (Figure 4.8). This does not cause any changes to signals retrieved later than 10 s, while earlier than 10 s it preserves the differences between a trace and the mean. The effective source time function of 10 s was selected after testing the above procedure for values from 8 s to 13 s with steps of 1 s.

##### PKP TRIPLICATION

We also investigate the effect on our results of the PKP triplication [36] using the T-array. The PKP triplication is expected to arise for earthquakes at epicentral distances from about 135° to 155°. The triplicated arrivals are expected within 10 s from the first PKP arrival [e.g. 37]. Each of the PKP triplications will contribute in the autocorrelation process to the retrieval of the same reflections (for example from the Moho) and thus would result in an increased SNR of the reflections. For each transmission response, the individual PKP triplicated arrivals will also correlate with each other, which will result in the retrieval of artifacts in the result from each transmission response (cross-talk). However, according to the 3D theory of SI for any inhomogeneous medium, i.e., what we use here, such triplication-related artifacts will cancel out after summing over the correlated transmission responses [e.g. 24]. Because of this, Ruigrok and Wapenaar [25]

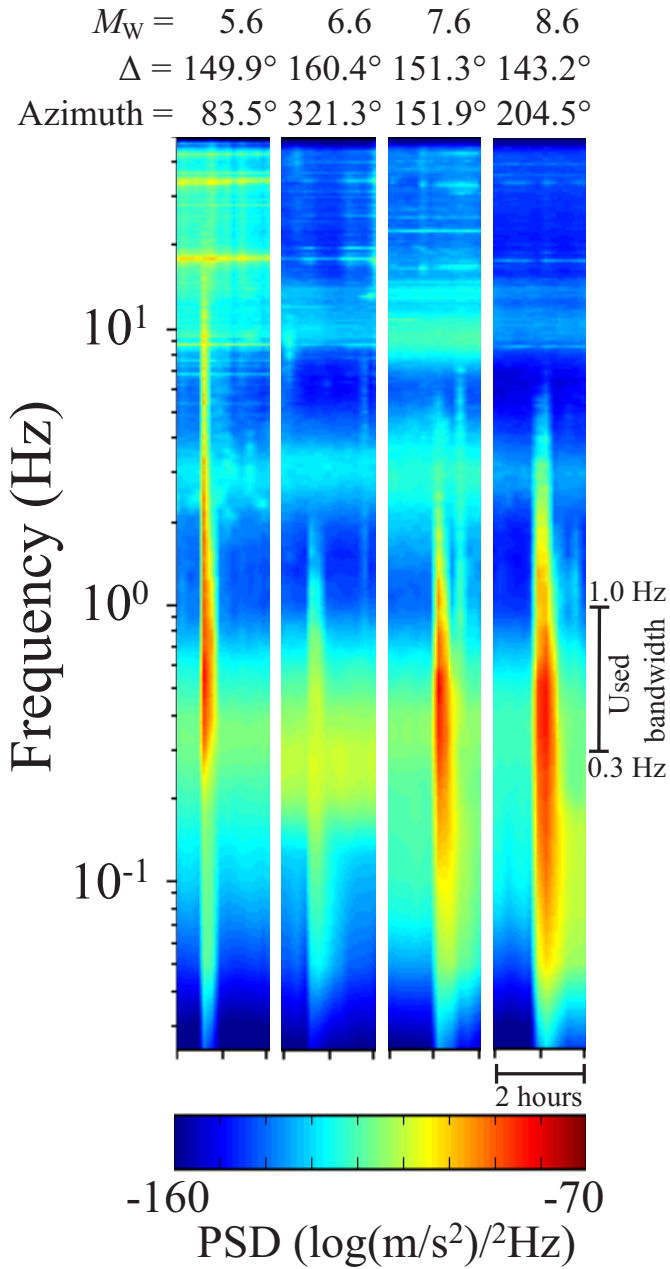


Figure 4.5: The computed power spectral densities for four earthquakes with different magnitudes that occurred at global distances. The densities are computed for station TE01 of the TE-array in MalARRgue.  $\Delta$  indicates the epicentral distances of the global earthquakes.

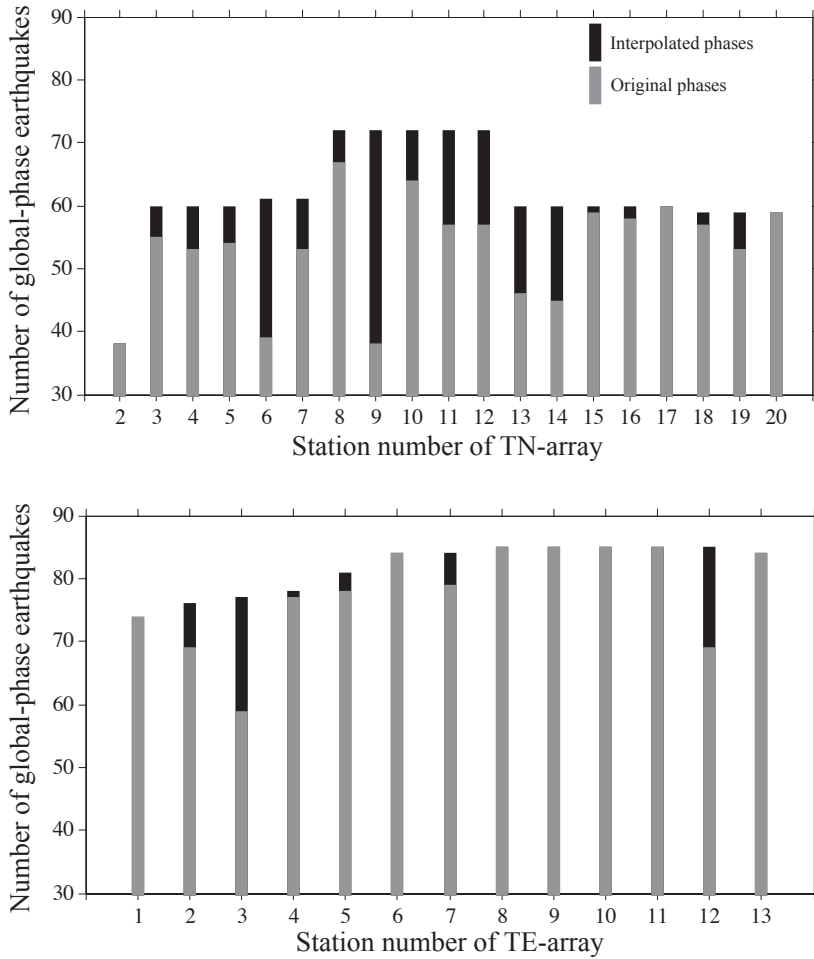


Figure 4.6: Number of original and interpolated global phases for TN- (top) and TE-array (bottom) stations.

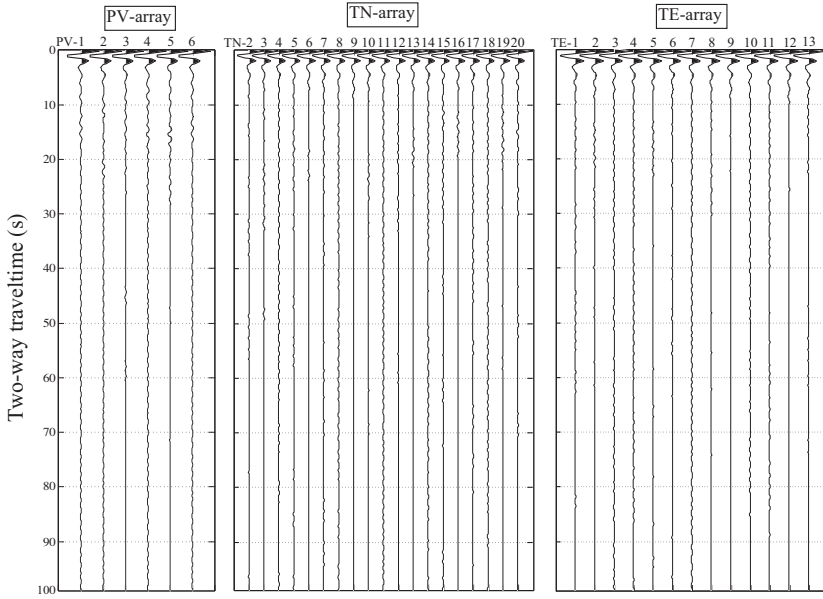


Figure 4.7: GloPSI results retrieved at the MalARRgue stations before seismic processing. The annotations along the horizontal axis show the actual station codes.

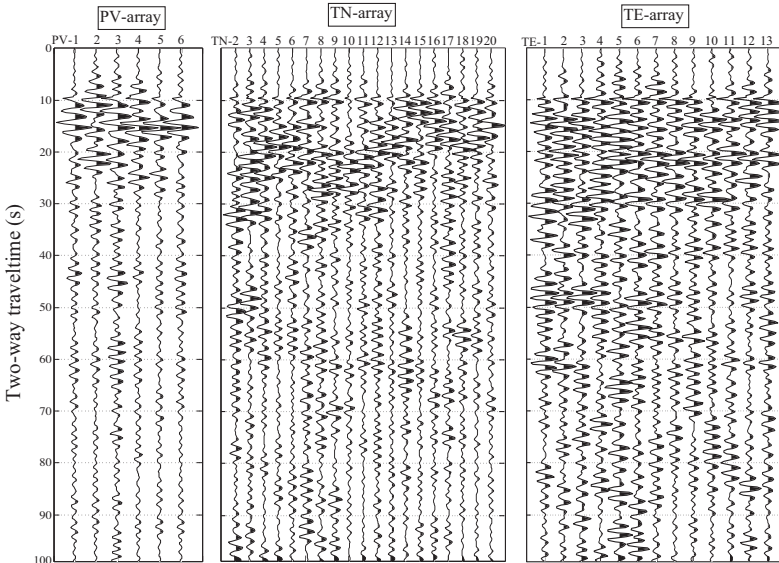


Figure 4.8: The results from Figure 4.7 after subtraction of the mean  $\bar{E}_n(t)$  per subarray



suggested using global phases from a wide range of ray parameters. In the summation process after the autocorrelation, this would cause the different cross-talk artifacts to interact destructively. This happens, as the cross-talk artifacts would be retrieved at different times. On the other hand, correlations of global phases with a wide azimuthal and slowness coverage enhance the physical arrivals; i.e., the SNR of structures like Moho is improved [38]. In our case, the azimuthal coverage and the slowness variation of the earthquakes with epicentral distances  $\geq 120^\circ$  are sufficiently wide (see Figure 4.3), so we did not exclude the earthquakes that would contain PKP triplications. To the contrary, if we exclude the epicentral distances causing PKP triplication, only 13 earthquakes would remain for both arms of the T-array from the original 72 and 85 earthquakes for the TN- and TE-array, respectively. A reduced number of used earthquakes would result in deterioration of the retrieved reflections from deeper structures.

In Figure 4.9, we show a comparison of the obtained images of the subsurface when including and excluding the PKP triplication. When the velocity model of Gilbert *et al.* [8] is used for the depth conversion, the top of the Moho is interpreted at a depth of 35 km, while the possible effect of the PKP triplication should be seen between depths of 35 km and 66 km. The comparison of the results in Figure 4.9 shows that the Moho in the results when earthquakes with triplications are included is well imaged without apparent large-amplitude “ringing” around it due to the PKP triplication. In our context, “large” means the amplitude as large as the one of the first Moho reflection, i.e., the reflection at around 30 km in Figure 4.9. There are some slight differences in the weaker-amplitude events (e.g. positive-amplitude waveforms about 10 km after the Moho reflection), which we attribute to an insufficient integration over the small number of the earthquakes (only 13) when earthquakes with triplications are excluded. Note that the triplication “ringing” should be present also shallower than the Moho, but there it would be suppressed, even when present, by the subtraction of the averaged source time function  $\bar{E}_n(t)$ .

The same reasoning for the suppression of cross-talk due to PKP triplication is also valid for the suppression of source-side reverberations – due to differences in the source depths of the different earthquakes, the cross-talk in the autocorrelation between the transmission and the source-side reverberation would be suppressed when summing over the different earthquakes due to destructively interference [39, 40].

#### PREDICTIVE DECONVOLUTION AND SEISMIC MIGRATION

The bottom of the sedimentary basin (top of basement) often causes relatively strong free-surface multiples [41]. The depth of the Malargüe basin (a sub-basin in the Neuquén basin) below the T-array is known [35]. This allows us to suppress the basement free-surface multiples by applying a predictive-deconvolution filter [30] based on the estimated two-way traveltime of these multiples. Note that such a filter was not used for the PV-array, as it is not above a basin [42]. After interpreting the Moho below each subarray following as guidance the interpretation by Gilbert *et al.* [8], we also apply predictive-deconvolution filter for possible free-surface multiples from the Moho.

As the subsurface structures might not be planar below the subarrays, migration processing would be effective in moving dipping structures to their correct location given an array has a sufficient length. In this study, we apply Kirchhoff post-stack time migration [30] to the GloPSI sections from the TN- and TE-array. Migration is not applied for the PV-array due to its limited aperture; instead, the individual traces are stacked.

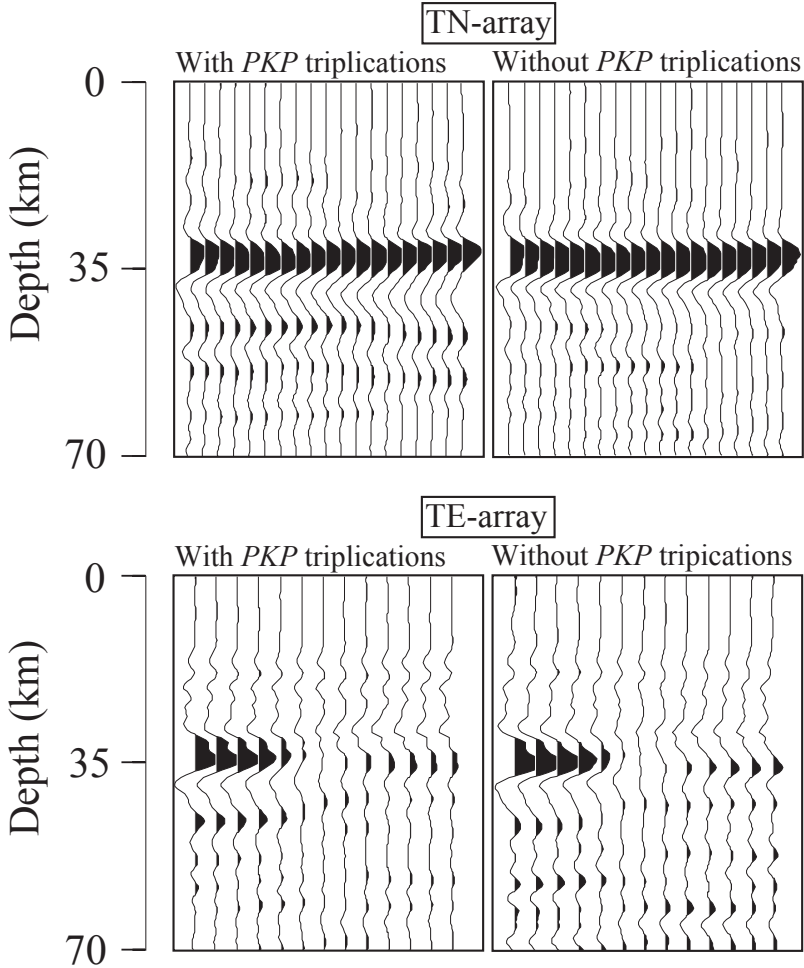


Figure 4.9: A comparison of GloPSI images obtained when including and when excluding global phases with PKP triplications. The number of earthquakes for the TN(TE)-array with and without the PKP triplications are 72 (85) and 13 (13), respectively.

As final processing steps, we apply lateral smoothing along the array to aid the interpretation, using smoothed discretized splines based on the generalized cross-validation [43] (Figure 4.10), and then convert the migrated or stacked traces from time to depth (Figure 4.11). For the depth conversion, we use a regional velocity model down to 70 km depth [8] and the ak135 model [34] deeper than 70 km.

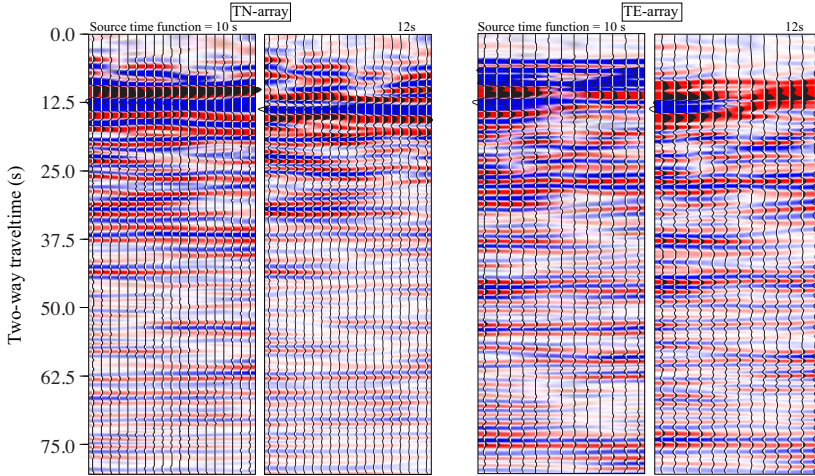


Figure 4.10: GloPSI results for the TN- and TE-array after post-stack time migration with lateral smoothing in the offset orientation when respective source time functions of 10 s and of 12 s are used in the estimation of  $\bar{E}_n(t)$ .

In Figure 4.10, we show a comparison of the obtained images when source time functions of 10 s and 12 s are used in the estimation of  $\bar{E}_n(t)$ . It can be seen that the different values give comparable results, which shows the robustness of the procedure. The only substantial difference between the images in Figure 4.10 is in the interpretation of the top of Moho. When using a two-way traveltme of 12 s, it seems that the Moho is largely removed due to its consistent depth over the subarrays. Although it might be possible to improve the time window by taking into account individual source time functions, we found that the constant time window of 10 s is sufficiently effective as we do not see major differences with the result when using a window of 12 s. According to Kanamori and Brodsky [45], the time window of 10 s covers source time functions for earthquakes smaller or equal to  $M_W$  6.5. Only 8 % of the earthquakes used for the TN array has  $M_W > 6.5$ .

For the GO05 station, we apply the same processing as for the PV-array, except that during the depth conversion we apply the velocity model as used for the C02A station of the Talca Seismic Network in Dannowski *et al.* [44] who utilized the velocity model of Bohm *et al.* [46]. An approximation of  $\bar{E}_n(t)$  is calculated by taking the average of the retrieved results for GO05 and stations GO04 and GO06, which are the N-S neighbors of GO05 in the Chilean National Seismic Network.

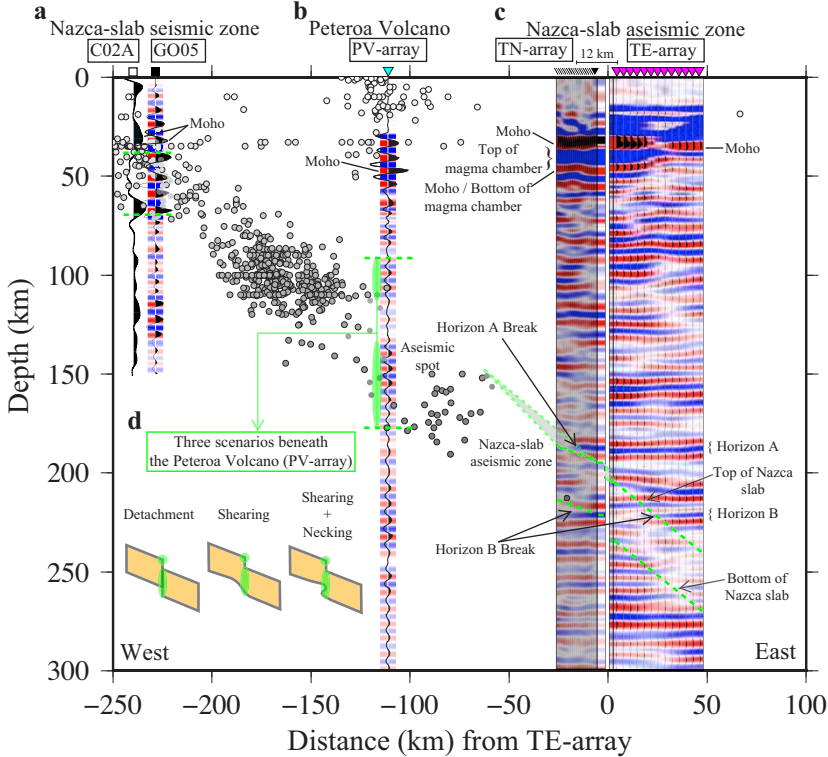


Figure 4.11: Summarized interpretation with seismicity along the NWW-SEE area of GloPSI for MalARRgue and station GO05. (a) GloPSI for GO05 and receiver function for C02A at the Nazca-slab seismic zone. Moho depth is interpreted using receiver function (modified from [44]) at C02A. (b) GloPSI for the PV-array beneath the Peteroa Volcano. (c) GloPSI for the TN- and TE-array at the Nazca-slab aseismic zone. Dashed green lines in the panels indicate where we interpret the Nazca slab and transparent green rectangles indicate possible interval of the interpretation. The transparent green ellipses indicate where we interpret the Nazca-slab deformation, while the transparent gray triangle – the possible connection between the Nazca-slab seismic and aseismic zones in three dimensions. The insets in the bottom left corner illustrate three possible scenarios explaining the retrieved strong reflectivity below the PV-array. Gray circles (some transparent for visibility purposes) indicate earthquake hypocenters.

#### QUALITY CONTROL OF THE RESULTS AT THE SEISMIC ZONE OF THE NAZCA SLAB

For quality-control purpose, we first apply GloPSI to station GO05, which is situated above the seismic zone of the slab. In the processed traces, the peak and trough of the wiggles correspond to depths of P-wave impedance contrasts. We compare the obtained GloPSI zero-offset reflection trace with the receiver-function trace obtained for C02A in Dannowski *et al.* [44], see Figure 4.11a. From the receiver-function results, Dannowski *et al.* [44] estimate the Moho depth at this location at 33 km. GloPSI for GO05 also shows strong amplitude around 33 km (Figure 4.11a). Note that around this depth starts a cluster of hypocenters (Figures 4.2 and 4.11a). Hypocenter clustering delineates the slab, meaning that beneath GO05 the strong positive peaks at depths of about 40 km and 70 km correspond to the slab's top and bottom, respectively (dashed green lines in Figure 4.11a). The correspondence of the imaged reflectivity with the hypocenter clustering, but also with the slab's bottom from the receiver-function trace (second positive peak at C02A trace in Figure 4.11a) confirms the validity of applying GloPSI for slab imaging. Imaging reflectivity that is as strong as the Moho means, that below GO05 the slab is locally (nearly) flat (Figures 4.1a and 4.1b). If the slab were locally inclined, the image would have exhibited lack of reflectivity (Figure 4.1c).

4

#### 4.1.5. RESULTS INTERPRETATION AND DISCUSSION

##### ASEISMIC SPOT BENEATH THE PETEROA VOLCANO (PV-ARRAY)

Similar to the trace for station GO05, beneath the PV-array GloPSI reveals the Moho where the strongest amplitude is seen, that is at a depth of about 45 km (Figure 4.11b). This depth shows good agreement with a recent result of Gravity field and Ocean Circulation Explorer (GOCE) operated by European Space Agency (ESA) [e.g. 47] that shows the Moho depth to be around 45 km in this region. A feature further down in the zero-offset reflection trace from the PV-array is the appearance of reflectivity packages at around 100 km and 150 km depth, where the hypocenters of some intermediate-depth earthquake are present (Figure 4.11b). Another striking feature is the lack of reflectivity for about 15 km around the depth of 125 km. The latter corresponds to an aseismic spot at the Nazca slab. Because of the aseismicity and because GloPSI would not image structures where no impedance contrast exists (after applying predictive-deconvolution filter for possible free-surface multiples from the Moho), the lack of reflectivity might be interpreted as caused by certain amount of melt. If melted substance is indeed present around 125 km depth, then one possible interpretation of the two strong-reflectivity packages at 100 km and 150 km depth would be as reflections from slab deformation, which in turn would be caused by the melted substance. The deformation might be in the form of detachment, shearing, necking, or any combination thereof. We illustrate the three pure deformation scenarios in Figure 4.11d. The present hypocenters indicate vaguely the slab, which is generally characterized as steeply dipping in this zone. The dip would be too steep to retrieve reflections of a dipping interface delineating the slab (Figure 4.1c), but deformations at the slab would give rise to scattered energy. Some of this energy will be in the form of (nearly) vertically scattered fields, which will be recorded at the station (Figure 4.1d). The latter will be turned by GloPSI into zero-offset reflections, and consecutively imaged. If the slab is indeed deformed, depending on its thickness (e.g. the transparent green ellipses in Figure 4.11d), the primary reflection from the top

of the slab on one side of the deformation might interfere with the primary reflection from the bottom of the slab from the other side of the deformation, which would make the interpretation of the exact limits of the slab ambiguous. Because of this, in Figure 4.11b we indicate with dashed green lines only the extent of the possible deformation of the slab. We interpret the bottom of the slab at around 175 km.

Note that if melt is present and forms an impedance contrast with the mantle and/or the slab, GloPSI would retrieve a reflection from this contrast as well unless the melt itself forms a steeply dipping structure [30]. However, if there is no or only weak impedance contrast due to, for example, the gabbro-eclogite transformation of the slab, GloPSI will not retrieve a clear reflection from the melt. Frank *et al.* [48] showed that SI could be applied to S-wave phases as well (e.g. S, SS, ScS, and SKS). S-waves have the advantage that they are more sensitive to melt than P-waves and thus can provide extra information. An implementation of GloPSI to S-wave phases would entail the use of global phases like PKS and SKS. Such implementation to our temporary deployment would be challenging due to the low SNR on the horizontal components and the attenuation of much of the S-wave phases below the sensitivity bandwidth of the instruments.

We do not exclude other possible interpretations for the lack of reflectivity around 125 km. However, our interpretation is a logical consequence of the presence of only a few intermediate-depth earthquakes: the slab here is insufficiently brittle to generate many earthquakes and that might be indicative of a presence of magma with possible slab deformation. Our interpretation is in a good agreement with results from recent geochemical investigations of Jacques *et al.* [49] suggesting that the Planchón-Peteroa complex erupts not only lithospheric magma from the heterogeneous mantle, but also magma from the Nazca slab.

#### ASEISMIC ZONE OF THE NAZCA SLAB BENEATH THE T-ARRAY

The migrated images obtained from the results retrieved from GloPSI beneath the TN- and TE-arrays are shown in Figure 4.11c. With the receiver-function method, Gilbert *et al.* [8] interpreted an apparently bifurcated Moho, with possibly a magma chamber in between, to be present in this region. Our result shows two strong positive peaks, which appears to confirm the observation of Gilbert *et al.* [8]. Based on their interpretation, we label the Moho and the magma chamber in Figure 4.11c where the trough in blue is imaged at a depth of about 40 km. Our GloPSI image shows that the bifurcation is continuous beneath the TN-array, but wedges out to the east beneath the TE-array.

The image of the upper mantle beneath both arms of the T-array reveals a complex structure. This heterogeneous image might correspond to the interpretation of the study of Jacques *et al.* [49]. In their study, the authors indicated that the mantle wedge in this region seems to be characterized, from a point of view of geochemical components, by crustal assimilation or mantle heterogeneity. Note that if non-primary reflections and spurious phases from autocorrelation cross-talk are retrieved, they will contribute to the apparent complexity of the structure. The latter could be caused by source-side reflections (even though we expect such cross-talk to be suppressed by the summation over the different earthquakes), micro-seismic noise, etc.

Below 100 km, we notice a pronounced discontinuity of the imaged reflectors, indicated by the dashed green line in Figure 4.11c. This discontinuity is clearly observed

below the TE-array from the middle of the array (100 km depth) towards the east (150 km depth). Due to the limited aperture of the T-array, deeper steeply dipping structures will not be imaged, but will manifest themselves as lack of reflectivity (Figure 4-43 in [30]). For instance, to record the free-surface multiple of the vertically incident global phase after it is reflected from the Nazca slab characterized by a dip of  $40^\circ$  and depth of 200 km, we need a receiver at the free surface with an offset from the virtual-source position of more than 1000 km (Figure 4.1c). This can also be said in another way: to retrieve zero-offset reflection from a structure with a dip of  $40^\circ$ , we will need to record incoming phases with incidence angle of  $40^\circ$  as well, which is not possible with global phases. Although some reflection discontinuities may be seen shallower than 150 km, it is difficult to interpret them without other geophysical information. Note that a longer seismic array would be required to better interpret the mantle structure. Since there is a possible remnant of an upwelling plume in this region [32], some of these discontinuities might be related to the plume, but they might also be related to a part of the mantle convection or partial melting.

4

Let us look at the deeper part of the GloPSI image, where, based on the extrapolation of the mapped hypocenters, we expect to see the Nazca slab. A dimmed-reflectivity zone (between the dashed green lines) is visible beneath the TN-array dipping from NNW around a depth of 180 km to 200 km to the SSE. This zone causes discontinuity in the strong laterally coherent horizons A and B in Figure 4.11c. Beneath the TE-array, the GloPSI image exhibits a clear dimmed-reflectivity zone (between the dashed green lines) dipping with an angle of  $43^\circ$  to the east and causing discontinuity in horizon B. Note that horizon B is also visible around 62.5 s in Figure 4.10. The dimmed reflectivity might be caused by lack of impedance contrasts. This, though, would not result in discontinuity of the imaged reflectors. As explained above, another reason for the dimmed reflectivity might be the presence of dipping reflectors, which, because of their depth and the relatively short array length, would not be well imaged in the (migrated) section [30]. The presence of such dipping reflectors would be manifested by discontinuity in horizontal reflectors (Figure 4.11c). That is why, we interpret this dipping dimmed-reflectivity zone as the top and bottom of the aseismic zone of the Nazca slab. We see that this part of the interpreted slab is continuous and that the reflectivity does not indicate a possible slab deformation at this latitude ( $35.5^\circ\text{S}$ ). Since there is no seismicity along this part of the slab, the condition of this steeply dipping slab zone might be different from the condition in the shallower zone where seismicity is present. This might support the interpretation of Yuan *et al.* [16] who proposed a completion of the eclogite transformation along this part of the slab.

## 4.2. ON THE EARTH: RADIATION EFFICIENCY OF INTERMEDIATE-DEPTH EARTHQUAKES

### 4.2.1. INTRODUCTION

In this study, we determined source parameters for moderate ( $M_W$  4.0–7.0) intermediate-depth (65–150 km) earthquakes associated with subduction of the Pacific slab under Japan. All these events are considered to be intraplate earthquakes within the slab. Compared to investigations of shallow events, the data are recorded at farther hypocentral distances and are less well studied. We wish to investigate if the scaling of source parameters is dependent on the depth and earthquake size for the shallow and intermediate-depth earthquakes. Some past studies have indicated the possibility that there is a relative increase of the ratio of radiated energy ( $E_R$ ) to moment ( $M_0$ ), as moment increases [e.g. 50–58], while other studies indicate a constant ratio [e.g. 59–68]. Since this scaling is important for understanding the rupture physics [e.g. 61, 69] and for the prediction of strong ground motions, we examine this issue for intermediate-depth earthquakes. Furthermore, we investigated the radiation efficiency, which is expressed by the radiated energy and the fracture energy. Although the fracture energy cannot be measured directly, it can be inferred from estimates of the static stress drop and radiated energy [70]. The radiation efficiency is a measure of the radiated versus dissipative energy during the earthquake. For example, very deep earthquakes, such as the 1994 Bolivia event, have low radiation efficiency [e.g. 71], suggesting the generation of large amounts of thermal energy during the rupture. Estimates of the radiation efficiency for intermediate-depth earthquakes can provide information about the rupture process and may help clarify difference between shallow and deep earthquakes.

### 4.2.2. DATA

Source parameters were determined for 216 intermediate-depth earthquakes from 2002 June 3 to 2010 December 31, recorded by the High Sensitivity Seismograph Network in Japan (Hi-net), which is operated by the National Research Institute for Earth Science and Disaster Prevention (NIED), as shown in Figure 4.12. The waveforms are available through Hi-net on the NIED webpage (last accessed on 2012 September). The data set consisted of all the events in the depth range of 65–150 km during the time period, with magnitudes  $M_W$  4.0–7.0 and recordings on at least eight stations covering a wide range of azimuths with hypocentral distances less than 250 km (Table 4.2). The seismic moments and the focal mechanisms used in this study are available through the Full Range Seismograph Network of Japan (F-net; last accessed on 2012 September) operated by NIED.

Table 4.2: Estimated source parameters in this study

Date (month/d/yr)	Time (hr:min:s)	Lat. (°N)	Lon. (°E)	Dep. (km)	$M_0$ (Nm)	$M_W$	$f_c$ (Hz)	$\Delta\sigma_s$ (Mpa)	$E_R$ (J)	$\eta_R$	$Q_p$	$Q_s$	Strike (°)	Dip (°)	Rake (°)
06/25/02	07:51:24	34.04	140.23	77	1.33E+15	4.0	1.8	0.98	2.38E+09	0.39	1225	1250	196	70	122
07/01/02	15:48:13	40.44	141.61	82	2.35E+15	4.2	2.9	4.67	2.11E+10	1.20	917	569	195	75	72
07/20/02	05:00:20	35.56	140.09	72	2.88E+15	4.2	0.8	1.59	1.26E+09	0.07	1216	1216	7	64	98
07/30/02	01:19:18	40.48	141.24	104	4.54E+15	4.4	2.7	2.28	3.47E+10	0.34	646	621	175	73	54
09/07/02	06:57:23	36.23	139.34	90	1.75E+15	4.1	3.4	3.57	8.28E+10	0.50	624	500	38	54	-54
09/10/02	19:52:20	38.71	141.45	105	1.86E+15	4.1	3.1	9.48	6.05E+10	0.29	734	778	227	54	-65
09/26/02	19:12:51	42.55	142.32	96	3.04E+15	4.3	2.9	6.30	3.83E+10	0.39	654	439	343	78	-13
10/19/02	05:26:49	42.12	142.23	79	2.23E+15	4.2	2.5	4.41	2.61E+10	0.22	613	478	328	63	-46
10/31/02	12:15:44	42.88	142.72	114	4.73E+15	4.4	2.1	3.40	2.64E+10	0.46	563	606	270	77	-108







09/05/09	10:59:35	36.97	140.18	100	3.96E+15	4.3	1.9	4.09	1.69E+11	1.44	1170	860	169	77	61
09/10/09	18:29:19	43.16	146.26	68	1.13E+16	4.6	1.0	1.48	2.75E+10	0.23	660	285	247	85	-102
09/22/09	20:40:44	37.60	141.66	76	7.75E+15	4.5	2.1	8.62	6.55E+10	0.14	555	275	197	58	-115
10/10/09	17:42:48	41.72	142.23	92	4.07E+16	5.0	0.5	0.63	3.79E+10	0.20	820	615	130	78	-52
10/17/09	18:25:55	36.60	140.59	95	1.45E+15	4.0	1.7	0.85	1.16E+10	1.30	785	785	227	55	-114
10/18/09	23:13:03	40.21	141.38	88	3.09E+15	4.3	2.4	5.68	1.24E+10	0.10	730	750	204	70	76
12/18/09	05:41:30	36.33	139.72	78	5.31E+16	5.1	0.7	2.46	1.73E+11	0.18	970	665	252	77	92
12/28/09	09:12:49	43.17	144.64	85	2.91E+16	4.9	1.3	8.7	2.96E+12	1.61	490	520	174	87	73
01/08/10	15:59:41	37.30	140.67	79	1.32E+15	4.0	1.7	0.83	1.19E+10	1.49	380	300	184	83	116
01/21/10	18:49:02	38.08	140.31	123	6.62E+15	4.5	1.1	1.03	6.62E+09	0.13	785	625	201	80	93
02/17/10	04:59:31	34.95	140.09	83	1.26E+16	4.7	1.0	1.48	2.04E+10	0.15	820	660	168	75	54
03/01/10	07:07:47	39.39	140.61	118	4.57E+16	5.0	0.9	4.39	3.68E+11	0.25	925	435	152	74	111
03/08/10	19:48:05	43.75	147.16	90	3.56E+15	4.3	1.0	0.46	1.32E+09	0.11	610	595	73	48	-69
03/13/10	21:46:27	37.61	141.47	78	1.88E+17	5.4	0.8	12.23	1.13E+12	0.07	785	610	204	55	-85
03/16/10	07:30:32	35.67	140.13	68	6.37E+15	4.5	0.9	0.57	1.12E+10	0.43	505	280	209	79	-90
03/27/10	19:54:26	43.74	147.07	86	1.61E+15	4.1	1.3	0.40	1.00E+09	0.21	645	505	233	80	-118
04/04/10	17:35:40	43.26	146.23	80	2.10E+15	4.1	1.4	0.74	2.96E+09	0.26	660	470	251	63	-102
04/26/10	06:22:48	37.99	142.39	76	2.32E+16	4.8	1.2	6.79	2.29E+11	0.20	820	750	236	75	-139
06/04/10	08:25:19	38.44	139.91	149	6.17E+15	4.5	1.0	0.68	5.98E+09	0.20	750	625	172	83	76
07/04/10	15:03:05	35.94	140.30	88	8.52E+15	4.6	1.1	1.48	1.81E+10	0.20	685	660	227	77	-45
08/03/10	07:30:48	36.74	140.31	82	1.70E+16	4.8	1.1	3.30	1.84E+11	0.45	920	840	189	85	94
08/14/10	13:25:08	42.82	142.34	109	2.13E+16	4.8	1.0	2.79	5.23E+10	0.12	470	335	192	83	35
09/27/10	02:55:00	35.70	140.10	68	1.02E+16	4.6	0.9	0.94	2.96E+10	0.42	975	665	197	75	-99
09/28/10	01:13:39	43.50	145.76	99	3.83E+16	5.0	0.8	2.61	4.84E+11	0.67	575	575	136	79	14
10/11/10	23:10:33	41.10	141.30	88	2.67E+15	4.2	1.8	1.98	6.28E+09	0.16	1100	855	309	52	-69
11/13/10	14:17:23	42.59	143.54	69	1.70E+15	4.1	2.4	3.00	7.88E+09	0.21	855	720	132	87	105
11/25/10	05:04:50	38.67	141.14	84	2.22E+15	4.2	4.2	20.17	4.81E+11	1.48	545	510	143	82	23

We analyzed both P waveforms on vertical components and S waveforms on transverse components, which were recorded on 1 Hz seismometers at a sample rate of 100 Hz. The instrument responses were removed using the poles and zeroes information provided by Hi-net. Since Hi-net stations are located in boreholes, we assume that there were generally not strong site responses. All waveforms were visually inspected and data that had high pre-event noise levels were not used in the analyses.

#### 4.2.3. METHOD

For the analyses to determine the source parameters, we used 6.0 s time windows around the P and S waves with 10 per cent tapering and a 0.1 Hz high-pass filter. For the two largest events ( $M_W$  6.8 and 7.0) longer time windows of 15 s were used. Time-series data were converted to the frequency domain using a fast Fourier transform and source parameters were determined using a simple one corner source model of the far-field displacement spectrum with attenuation, described as [51],

$$\Omega(f) = \frac{\Omega_0 e^{-\pi f t_s / Q}}{[1 + (f / f_C)^\gamma]^n}^{1/\gamma}, \quad (4.2)$$

where  $\Omega_0$  is the low frequency amplitude,  $f$  is frequency,  $f_C$  is the corner frequency,  $t_s$  is the traveltime,  $Q$  is the quality factor,  $n$  is the high-frequency fall-off rate and  $\gamma$  is a constant. We assume  $n$  is equal to 2.0 and  $\gamma$  is 1.0, which reduces to a standard Brune [72] model. An example of a waveform and spectrum are shown in Figure 4.13.

For estimates of source parameters, such as radiated energy and corner frequency, appropriate corrections for the attenuation properties are important, especially since hypocentral distances to the recording stations are relatively far. In this study, we assume a frequency-independent, constant whole path  $Q$ . Although a frequency-dependent  $Q$  model may be considered, a frequency-independent attenuation model may be sufficient for these relatively large events that have corner frequencies around 2.0 Hz, since frequency dependence is stronger for the higher frequencies.

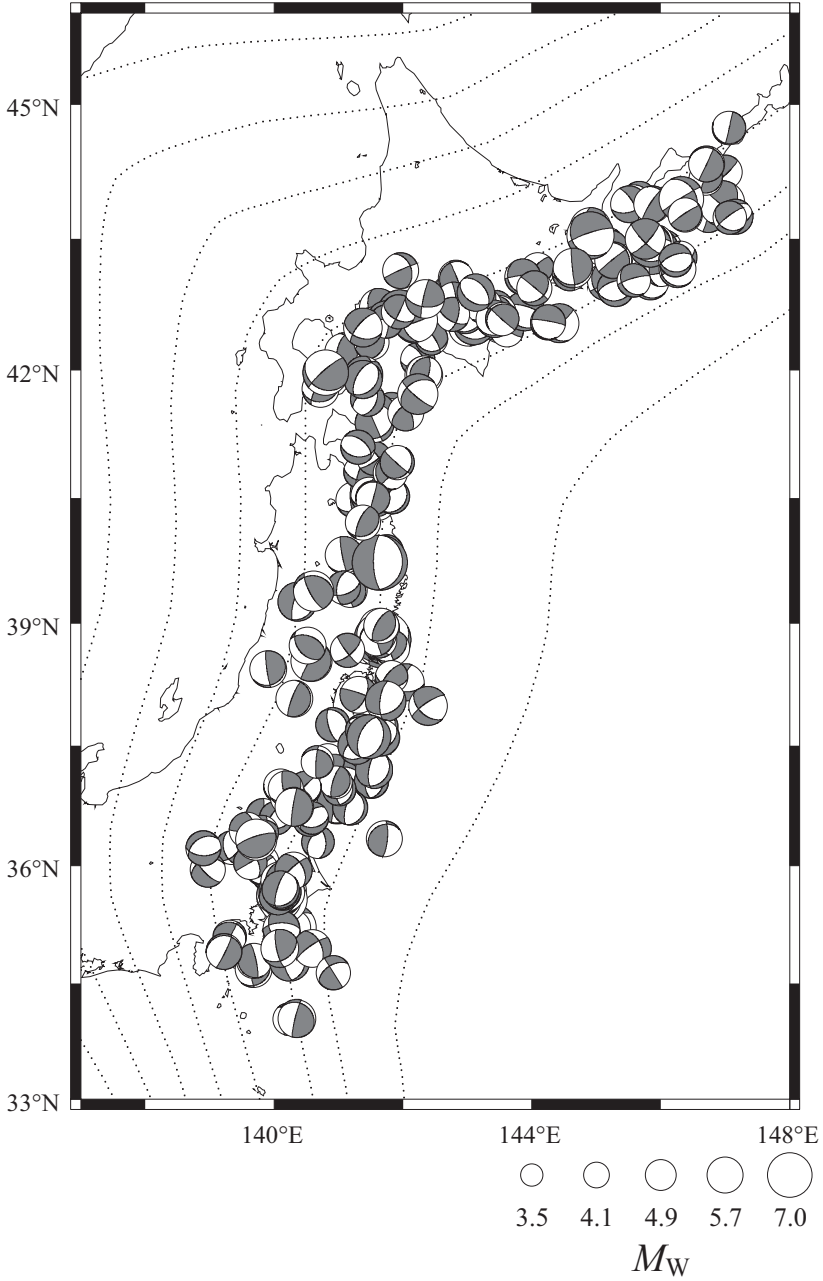


Figure 4.12: Map of the study area and focal mechanisms of the 216 intermediate-depth (65-150 km) earthquakes used in this study provided by NIED,  $M_W$  4.0-7.0. The focal mechanisms shown here are provided by F-net.

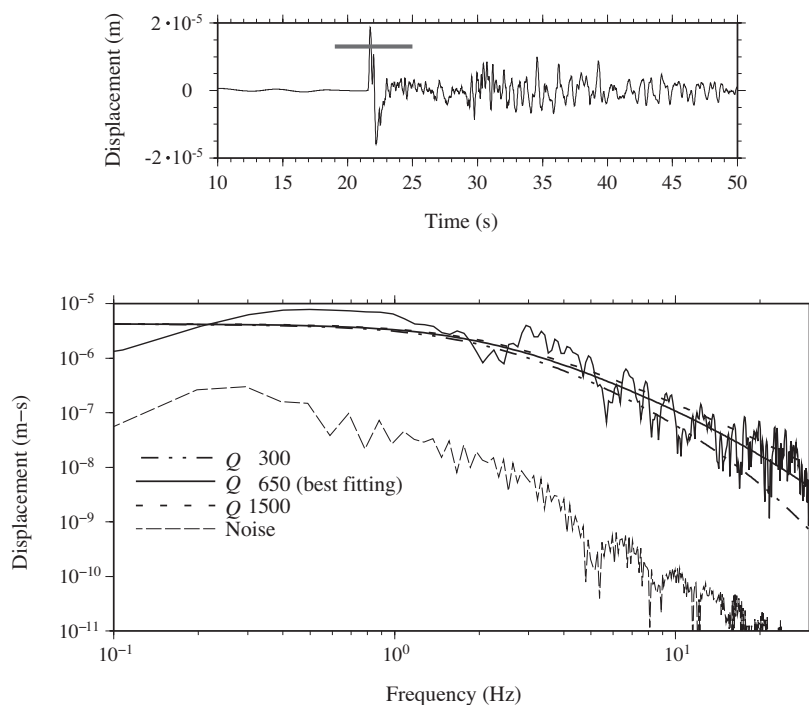


Figure 4.13: Example of spectral fitting of the data. The seismogram shown here is recorded by N. DGDH (station code of Hi-net), with origin time at 18:25:55 on 2009 October 17. The source depth and the epicentral distance are 95 and 0.5 km, respectively. Zero on the time axis is the origin time of this event. The solid bar above the seismogram of the vertical component indicates the time window used. Results assuming difference values of  $Q$ , along with the noise spectrum are shown for comparison.

Using equation 4.2, we estimated the best fitting  $Q$  and the corner frequency for each P and S wave with a grid search. The values of  $Q$  were tested in the range of 10–1500 at intervals of 10. The corner frequencies were tested in the range of 0.1–30 Hz at intervals of 0.1. Since there is a strong trade-off between the corner frequency and  $Q$ , we tried several procedures. For example, fitting the  $Q$  and the corner frequency independently for each event and station pair, gave widely varying estimates of the corner frequency. We found that more stable results were obtained if the corner frequencies were constrained to be the same for the all the P waves and all the S waves, respectively, for each earthquake. This ignores the azimuthal effects of directivity in the source. However, since there is fairly good azimuthal coverage for each earthquake, the results should provide reasonable average values. The  $Q$  and the corner frequency results for each earthquake are given in Table 4.2. The results show that the  $Q_P$  values are about 1.16 times higher than the  $Q_S$  values. The SNR for S waves are generally smaller than those for P waves, and all are larger than 10 for the frequency range of 0.1–30 Hz.

Some past studies reported that the corner frequencies for P waves are higher than those for S waves [e.g. 51, 64, 73, 74]. For circular cracks, Madariaga [74] pointed out that the ratio of corner frequencies for P and S waves are 1.5 times higher when the take-off angles are larger than  $30^\circ$  and this ratio is smaller than 1.0 when the take-off angles are smaller than  $30^\circ$ . Prieto *et al.* [64] argue that the ratio of the corner frequencies for P and S waves is  $1.6 \pm 0.2$  for relatively small observed earthquakes ( $M_L$  1.8–3.4). The ratio of the corner frequencies for P and S waves in this study for intermediate-depth earthquakes with  $M_W$  4.0–7.0 range between 0.5 and 1.6, as listed in Table 4.2, with a somewhat smaller average value of 1.2.

In this study, the static stress drop ( $\Delta\sigma_S$ ) is calculated using the formula of Brune [72] using the circular crack model of Eshelby [75]:

$$\Delta\sigma_S = \frac{7}{16} M_0 / r^3, \quad (4.3)$$

where  $r$  is the crack radius. We estimated the crack radius source model using Madariaga [74]:

$$r = \frac{k\beta_0}{f_c}, \quad (4.4)$$

where  $\beta_0$  is the S-wave velocity with reference to the model of Matsuzawa *et al.* [76] for each depth,  $k$  is 0.21 for S waves and adjusted to be 0.24 for P waves so that the overall averages of the P and S waves give similar values (Figure 4.14). Instead of averaging over the three components, as in Madariaga [74], we used only the vertical component for the P wave and the transverse component for the S wave. Using the seismic moments determined by F-net and the corner frequencies from our results, we obtained the static stress drops for all the events, as listed in Table 4.2. The origin times and the source locations of the earthquakes analyzed in this study are provided by Hi-net. We estimated the radiated energy,  $E_R$ , of S waves for each earthquake following the study of Kanamori *et al.* [50]:

$$E_R(f) = 4\pi h^2 C_f^{-2} \rho_0 \beta_0 \int e^{2(\pi f t_s / Q)} v^2(f) df \cdot \bar{R}^2 / R^2, \quad (4.5)$$

where  $h$  is the hypocentral distances,  $C_f$  is the free-surface amplification factor,  $\rho_0$  is the density for the rupture area,  $v$  is the particle-motion velocity,  $\bar{R}^2$  is the average of the squared radiation pattern over the whole focal sphere and  $R$  is the radiation pattern for this station. The density,  $\rho_0$ , is referred to the model ak135 [34] for each depth of the seismic events. Considering the amplitudes and radiation patterns of the P and S waves for a double-couple source, only about 4 % of the radiated energy is carried in the P wave [77], so we used only S waves for the estimation of the radiated energy for each event. We calculated the radiation pattern,  $R$ , for each station that recorded each event. We used the  $Q_S$  values obtained earlier to correct for the effects of the anelastic attenuation. The integration of the velocity squared quantity was calculated in the frequency domain so that a correction could be made for the attenuation. For the energy estimates, we use the integration of the observed velocity records, so they do not have any source model dependence. The average radiated energy for each event is shown in Table 4.2. The values of the radiated energy have an estimated uncertainty of a factor of about 3.3 mainly due to the uncertainty of the estimates of  $Q_S$  values.

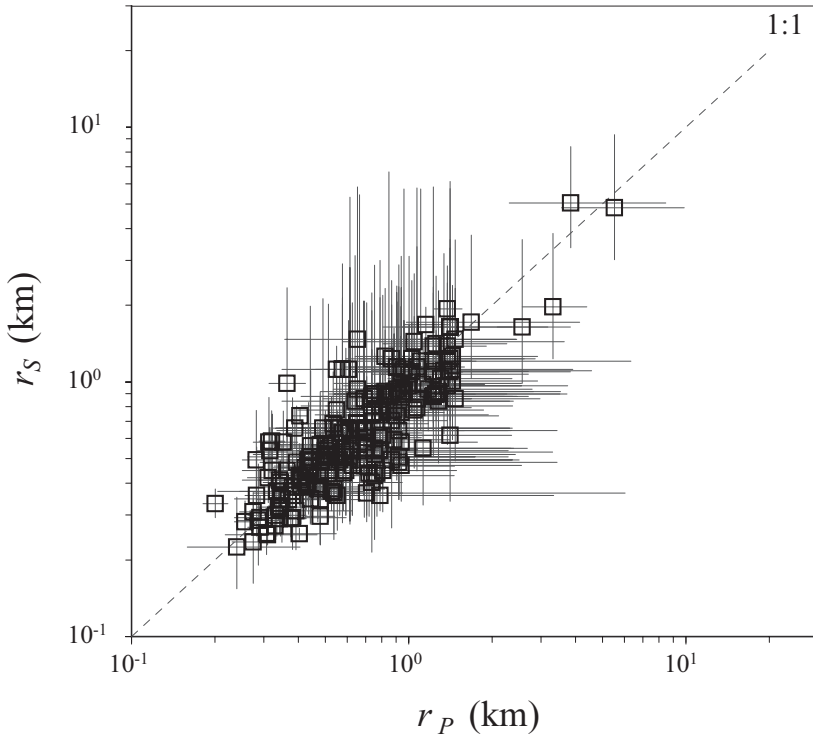


Figure 4.14: The relation of the estimated source radius for P,  $r_P$ , and S waves,  $r_S$ , using Madariaga [74] with a modification of the constant value  $k$  for P waves. The open squares are the average values and the solid lines show the range of the values for earthquakes using at least eight stations.

The radiation efficiency,  $\eta_R$ , is defined as the ratio of the radiated energy,  $E_R$ , to the

sum of radiated energy and fracture energy,  $E_G$  [e.g. 78]:

$$\eta_R = \frac{E_R}{E_R + E_G}. \quad (4.6)$$

This parameter represents the dynamic properties of the rupture. For example, if the radiation efficiency is very small, then the radiated energy is small compared to the fracture energy, and may behave as a slow earthquake or other type of event with a small proportion of radiated energy, such as discussed by Ihmlé [79]. If we assumed a simple slip-weakening model for the rupture process [e.g. 45, 71, 80–83] with Orowan's condition such that the final stress is equal to the dynamic frictional stress [84], then the sum of the radiated energy and the fracture energy can be rewritten as [e.g. 45]

$$E_R + E_G = \frac{\Delta\sigma_S}{2} DS = \frac{\Delta\sigma_S}{2\mu} M_O, \quad (4.7)$$

where  $D$  is the displacement,  $S$  is the rupture area and  $\mu$  is the rigidity. We used a value of 68 GPa for the rigidity,  $\mu$ , in the source region of the intermediate-depth events, calculated from the S-wave velocity with reference to the model of Matsuzawa *et al.* [76] and a value of 30 GPa for shallow earthquakes from Kikuchi and Fukao [85]. From the static stress drop and moment, we can determine the quantity,  $E_R + E_G$  in equation 4.7, and thus the radiation efficiency in equation 4.6. We note that the energy partition of equation 4.7 assumes a linear slip-weakening behavior which is model dependent. This is one of the simplest types of dynamic rupture models, and other types of rupture models could give different interpretations for these data. The values are listed in Table 4.2.

#### 4.2.4. RESULTS

In Figures 4.15a and 4.15b, the estimated corner frequencies,  $f_C$ , and static stress drops,  $\Delta\sigma_S$ , are plotted as a function of seismic moment,  $M_O$ . The values show a large range of stress drops from about 0.5 to 30 MPa. There appears to be a slight dependence on the earthquake size, where the average value of the static stress drops increases with increasing moment as  $M_O^{0.32}$ . The stress drop distribution does not appear to increase simply with moment. Rather, there is a large spread of values for the small events, and for the larger events there appear to be fewer low stress events. However this is hard to evaluate since there are also a greater number of smaller events. The vertical bars in Figure 4.15a show the standard deviation of the values from the multiple stations used for each event. Typically 8-15 stations using both the P and S waves are used for each event. To show the difference in stress drop values obtained using P and S waves, the vertical bars in Figure 4.15b show the range of values for corner frequencies determined by only P waves and only S waves. The corner frequencies determined by only P waves were not systematically higher or lower than for only S waves. Figure 4.16 plots the stress drops as a function of depth and shows no obvious trend.

The estimates of  $t^*$  ( $t_S/Q$ ) and  $Q$  for both the P and S waves are plotted as a function of depth in Figures 4.17a and b. In Figure 4.17b, we can see a range from about 300 to 1000, including the different estimates at each station for one event. The average value of  $Q$  for the P waves is 722 which is slightly higher than 625 for the S waves. There is no strong dependence on the event depth for these estimates of  $t^*$  as a function of depth,



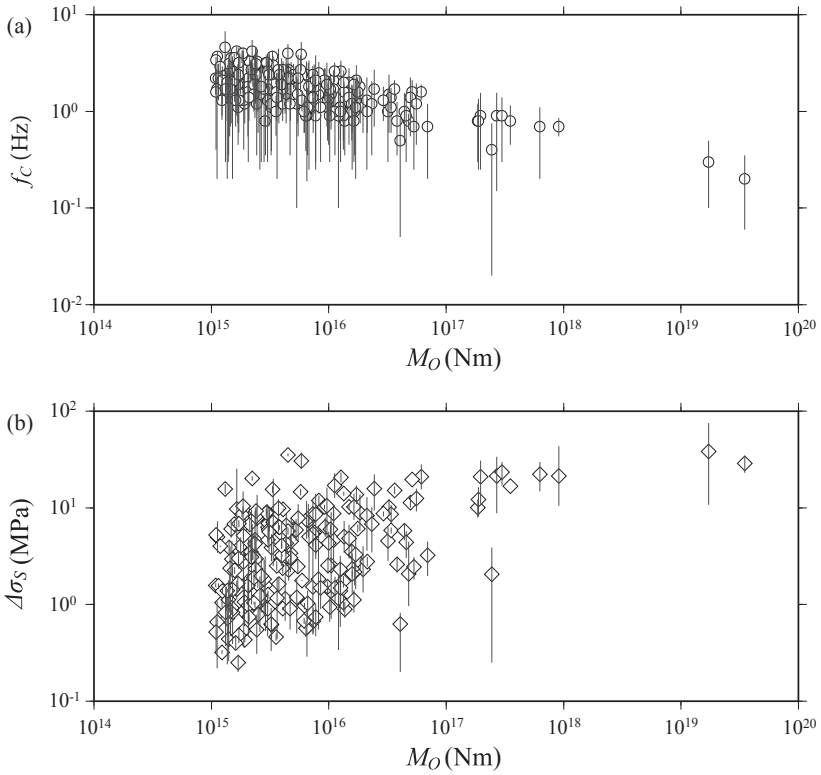


Figure 4.15: (a) Corner frequency as a function of seismic moment. The open circles are the average values and the solid lines show the standard deviations of values from all observations for each event. (b) Static stress drop as a function of seismic moment. The open diamonds are the average values and the solid lines show the range of values derived from using only P and only S waves to determine the corner frequency.

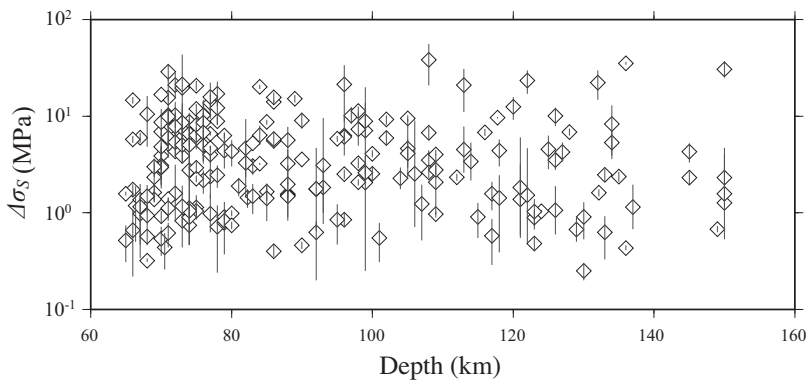


Figure 4.16: Static stress drop as a function of depth. The open diamonds are the average values and the solid lines show the difference of the average values from P and S waves.

suggesting that most of the attenuation occurs in the shallow region which is common to all of the ray paths.

Figure 4.18 shows the values of the radiated energy,  $E_R$ , as a function of moment,  $M_O$ , along with the results from Frohlich [86], which show the radiated energy estimated for earthquakes at depths of 70-150 km. The radiated energy is calculated by integration of squared velocity seismogram using a method that is similar to this study. The diagonal lines show values of constant apparent stress [e.g. 87] which are proportional to  $E_R/M_O$ . The results for the two largest earthquakes ( $M_W$  6.8 and 7.0) show large values because their static stress drops are relatively large. The scaled energy of these two events are slightly high compared with the intermediate-depth events (depths of 70-150 km) of Frohlich [86], however, they are within the general range of this plot.

We plotted the radiation efficiency and their average values in Figures 4.19a and b as a function of moment and event depth, respectively. The values of the radiation efficiency of intermediate-depth events in this study spread over a range from about 0.01-1.0. The results show a large scatter in the estimates of the radiated efficiencies. One reason for the scatter may be due to the model assumption of a  $\omega^{-2}$  fall-off. Spectral data for earthquake data show variations in the high-frequency fall-off which will affect the estimate of the radiation efficiency. For comparison of other depths, we also include the data for shallow events in southern California and Japan (derived from values in [53, 54, 88]). The studies of Izutani and Kanamori [53], Mori [54] and Venkataraman *et al.* [88] use empirical Green's functions to correct for attenuation and site effects. The results from the studies by Kanamori *et al.* [50], Choy and Boatwright [59], Winslow and Ruff [89] and Frohlich [86] use assumed  $Q$  values for the attenuation correction. Following the definition of the energy budget assumed for a simple slip-weakening model, the radiation efficiency should be 1.0 or less, however, some of our values are larger than 1.0. Some possible reasons for such unphysical values for the radiation efficiency can be due to inaccurate estimates of the static stress drop and/or the radiated energy, spatial variations in the levels of stress before the earthquake, and more complicated process of stress release. Considering other mechanisms, such as undershoot rupture [e.g. 74, 90, 91], could produce different results than assuming the simple model which we assume. Also, our estimate of radiation efficiency assumes that the levels of stress before and after the earthquake are the same for all points of the fault. There is likely heterogeneity in the stress levels which could produce the large values of radiation efficiency. There are also fairly large uncertainties in the estimates of radiated energy and static stress drop. Overestimates of the radiated energy and/or underestimates of the static stress drop can give values of efficiency greater than 1.0.

In this data set, we see that the radiation efficiency does not have a strong dependence on earthquake moment. The two largest events ( $M_W$  6.8 and 7.0) in our study have large values of radiated energy but also large static stress drops, so that the radiation efficiency is similar to the rest of the data set within the estimated uncertainty.

One difference we observe between the shallow and intermediate-depth events is a lower value of the radiation efficiency for the earthquakes of this study, compared to shallow crustal earthquakes (Figure 4.19b). Even though there is a large range of the values, the values for the intermediate-depth earthquakes can be seen to be lower than for the shallow earthquakes. The horizontal lines in Figures 4.19a and b show the (lin-

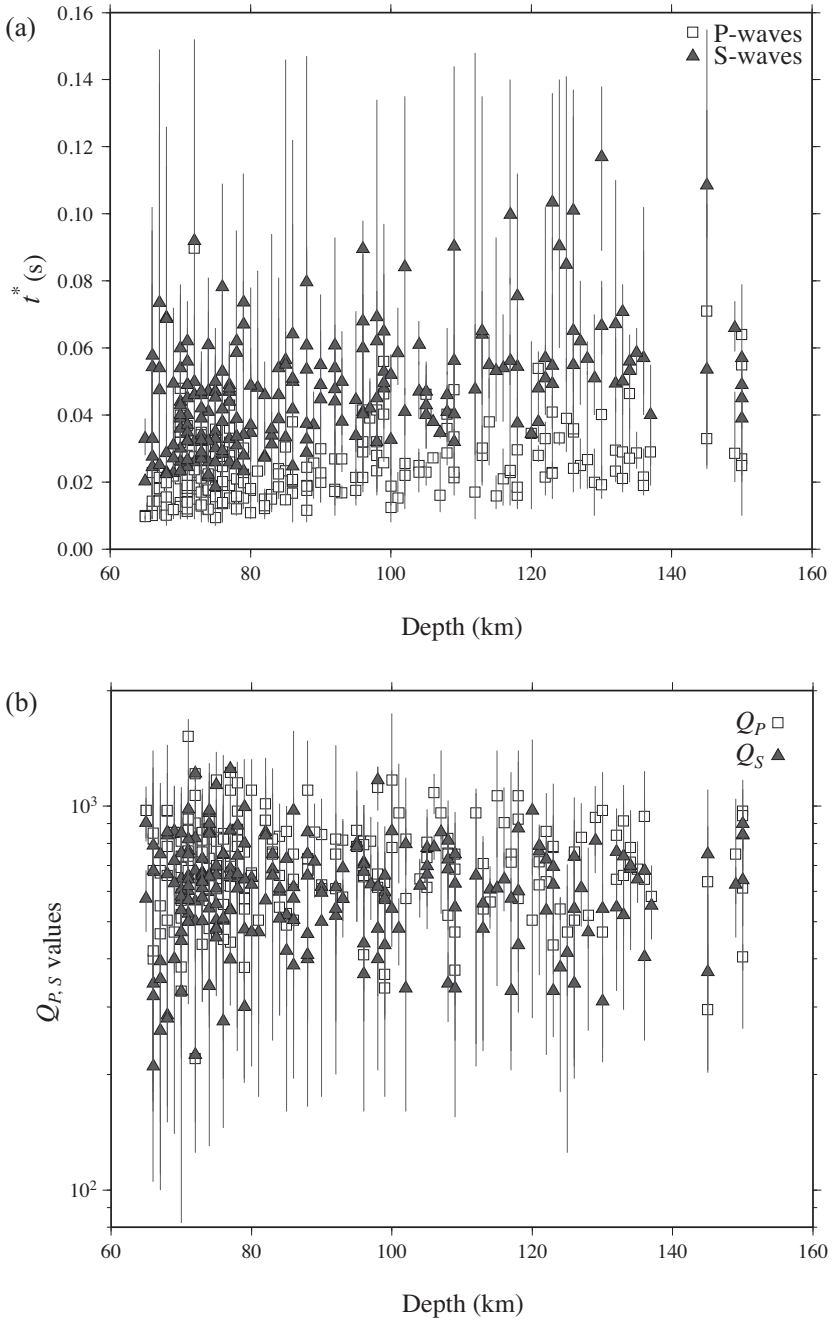


Figure 4.17: (a) Results of the estimated  $t^*$  for P and S waves are shown with open squares and filled triangles, respectively. The solid lines show the standard deviations of the values from multiple stations for each event. (b) Results of the estimated whole path  $Q_P$  and  $Q_S$  values. The open squares and the filled triangles are the average of the values, respectively. The solid lines show the standard deviations of the values from multiple stations for each event.

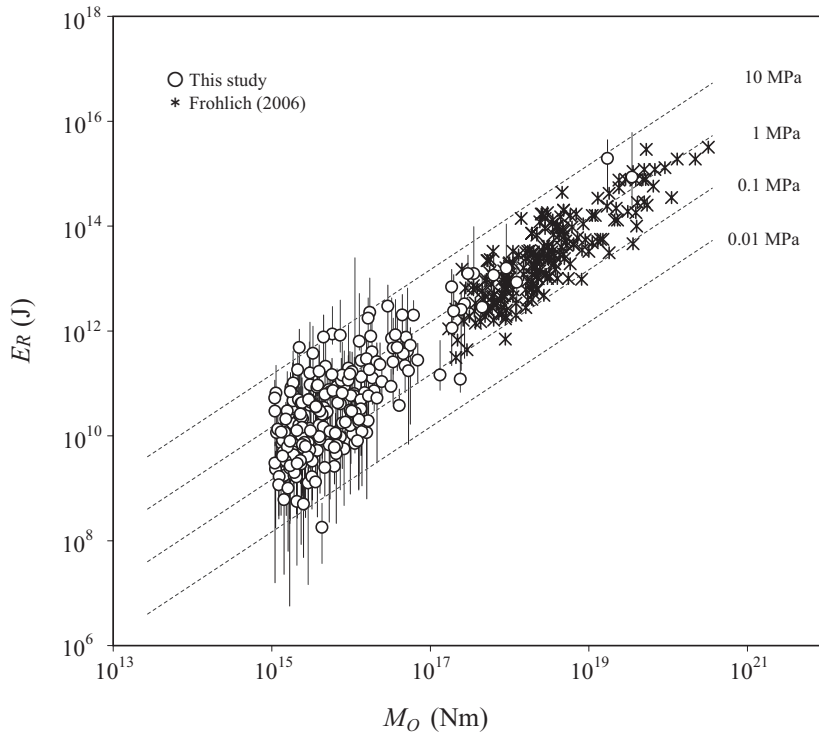


Figure 4.18: Relation between radiated energy and seismic moment for intermediate-depth events at depths of 70-150 km from Frohlich [86] (asterisks) and 65-150 km from this study (filled circles). The diagonal lines show values of apparent stress. The solid lines show the range of the values using the upper and the lower bounds of the estimated  $Q_S$  values in this study.

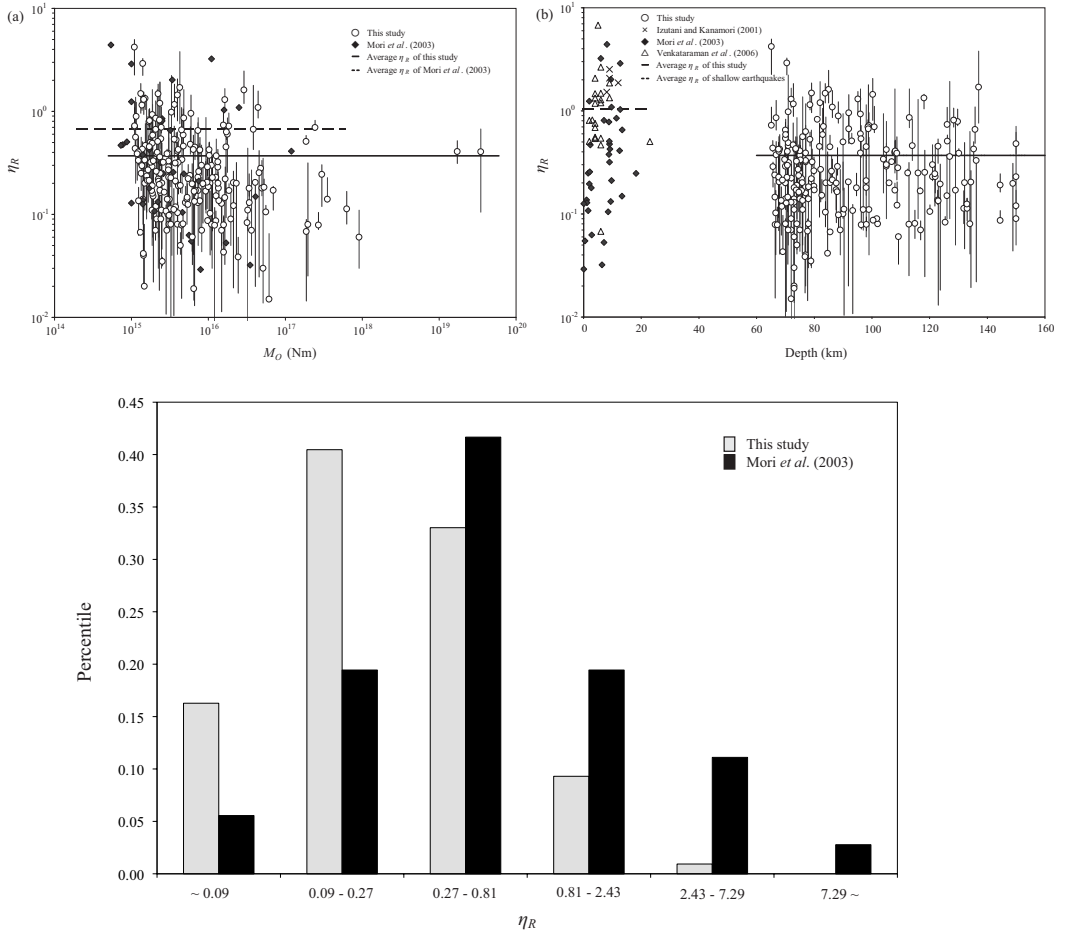


Figure 4.19: Radiation efficiency as a function of seismic moment compared. The filled circles are from this study and the filled diamonds are for shallow events in southern California, derived from Mori [54]. The horizontal dotted and solid lines are the average values for Mori [54] and intermediate-depth events, respectively. The vertical solid lines show the range of the values using the upper and the lower bounds of the estimated radiated energy in this study. (b) Radiation efficiency as a function of depth for this study and shallow events in southern California and Japan, derived from Izutani and Kanamori [53], Mori [54] and Venkataraman *et al.* [88]. The horizontal dotted and solid lines are the average values for the shallow and intermediate-depth events, respectively. The vertical solid lines show the range of the values using the upper and the lower bounds of the estimated radiated energy in this study. (c) Frequency distribution of radiation efficiency of intermediated-depth events from this study (grey) and shallow events from Mori [54] (black). The intermediate-depth events peak for the radiation efficiency in the range of 0.09-0.27, while the shallow events peak in the higher range of 0.27-0.81.

ear) averages of the shallow and intermediate-depth events to help show that there is a difference for the two depth ranges. The frequency distribution of the earthquakes for intermediate-depth and shallow events (derived from [54]) as a function of the radiation efficiency is shown in Figure 4.19c. The peak of the radiation efficiency for the intermediate-depth events is in the range of 0.09-0.27, while the peak for the shallower events is in the higher range of 0.27-0.81. So on average the intermediate-depth earthquakes have lower radiation efficiencies than the shallower events.

#### 4.2.5. DISCUSSION

There is an unresolved issue for shallow earthquakes regarding whether the ratio of radiated energy to seismic moment is constant or increases with moment. Examinations of different data sets give different conclusions. For example, Kanamori *et al.* [50], Abercrombie [51], Mayeda and Walter [52], Izutani and Kanamori [53], Mori [54], Takahashi [57], Mayeda [55], Mayeda *et al.* [56] and Malagnini *et al.* [58] indicate an increase of  $E_R/M_O$ , as a function of moment, which suggests a systematic change in the partition of radiated and dissipative energy distribution with size. On the other hand, Choy and Boatwright [59], McGarr [60], Ide and Beroza [61], Ide *et al.* [62, 63], Prieto *et al.* [64], Yamada *et al.* [65, 66] and Baltay *et al.* [67, 68] argue for a roughly constant value, which support self-similar scaling. Takahashi [57] have analyzed data from events at 32-120 km depth (about 30 km shallower than our data) and Baltay *et al.* [68] analyzed data for shallow and subcrustal earthquakes (intermediate-depth earthquakes were not exclusively studied), however, this issue of scaling has not been extensively studied for intermediate-depth earthquakes.

Combining the results of our study with Frohlich [86] we determine that the dependence of the scaled radiated energy as a function of moment for intermediate-depth earthquakes is  $M_O^{0.08}$ . The data of Frohlich [86] give a value of  $M_O^{0.04}$ . These values are considerably lower than Takahashi [57], which reported a scaling of  $M_O^{0.39-0.44}$  for the moment range from  $10^{11}$  to  $10^{17}$  Nm. One common result of all these studies is that they show a proportional increase of radiated energy as a function of moment.

This slight increase of the  $E_R/M_O$  ratio as a function of moment for the intermediate-depth earthquakes can be seen in Figure 4.18. However, the increase can be associated with the slight increase in static stress drop as a function of moment, which is seen in Figure 4.15b and the radiation efficiency remains constant (Figure 4.19a). If other source parameters are kept constant, larger static stress drops would produce larger amounts of radiated energy. Therefore, the increasing trend of  $E_R/M_O$  in this study does not seem to be indicative of a change in the partition of radiated and dissipative energy, but simply a consequence of larger static stress drops of the larger events.

In Figure 4.16, the static stress drops as a function of depth do not show any obvious trend indicating there is not a strong dependence on source depth for intermediate-depth intraplate earthquakes, which is similar to the results of Chung and Kanamori [92] and Houston and Williams [93]. These results are somewhat different from the study of Iwata and Asano [94] which observes that source areas are smaller, and thus stress drops, are higher for intermediate-depth earthquakes.

Venkataraman and Kanamori [71] studied  $M_W$  6.5 earthquakes and suggested that the static stress drop and the radiation efficiency can be different among different types

of earthquakes, especially deep focus events and tsunami earthquakes show low values of radiation efficiency. The estimate of radiation efficiency is one way of looking at the values of radiated energy with consideration of the static stress drop. If increases in the  $E_R/M_O$  ratio are simply due to increases in static stress drop, the radiated efficiency should stay constant. Our results in Figure 4.19a show that the radiation efficiency appears to be fairly constant as a function of earthquake size for the data set of intermediate-depth events. However, there does seem to be a lower average value of radiation efficiency for the intermediate-depth earthquakes, compared to the shallow crustal earthquakes [53, 54, 88] (Figure 4.16b). Chung and Kanamori [92] also showed that the radiation efficiency decreases for deep events (depths of 110–650 km). Figure 4.20 shows the results for depth dependence of the radiation efficiency obtained in this study compared with the other studies cited earlier for different depth ranges. Changes in the radiation efficiency imply changes in the partition between radiated and dissipative energy, so that a lower radiation efficiency of the intermediate-depth events indicates proportionately larger values of fracture energy, or other types of dissipative energy. Contributions of dissipative energy, perhaps melting or other non-elastic processes, may be occurring during intermediate-depth earthquakes. These effects may have even larger effects for deeper earthquakes (Figure 4.20).

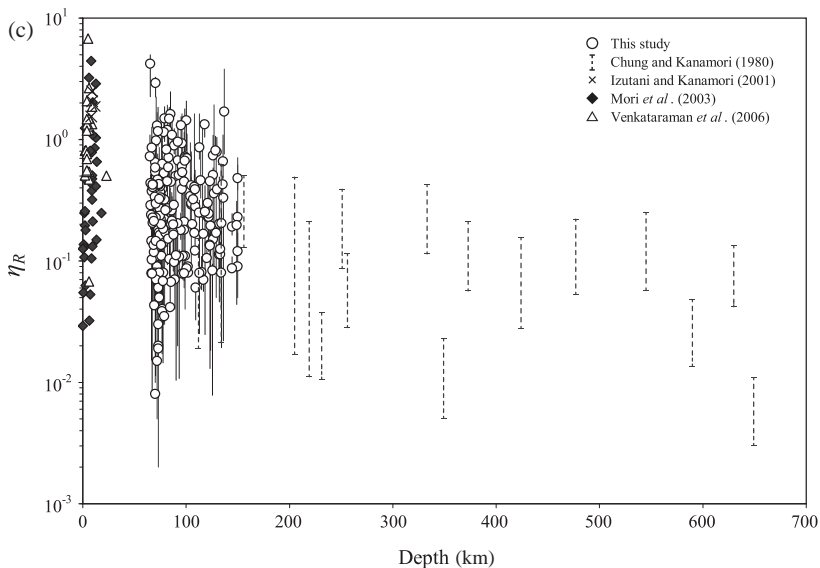


Figure 4.20: Radiation efficiency as a function of depth for this study compared to other results over a greater depth range, including deep events from Chung and Kanamori [92], and shallow events from Izutani and Kanamori [53], Mori [54] and Venkataraman *et al.* [88]. The vertical dotted lines for Chung and Kanamori [92] show the range of the values with an upper bound assuming a complete stress drop.

## 4.3. ON THE MOON: DEEP-MOONQUAKE SEISMIC INTERFEROMETRY

### 4.3.1. INTRODUCTION

During the NASA Apollo missions, seismometers were installed on the Moon which transmitted continuous seismic data to the Earth between July 1969 and September 1977. Early analyses of the data resulted in identification of four types of natural moonquakes: meteoroid impacts [e.g. 95–98], thermal moonquakes [e.g. 98], shallow moonquakes [e.g. 95, 96, 98], and deep moonquakes [e.g. 97–101].

While only 28 shallow moonquakes (hypocenters at depths between 2 km and 220 km; [97]) were detected from the records, 7083 deep moonquakes (hypocenters at depths between 700 km and 1200 km; [102]) have been identified so far. It was also observed that the deep moonquakes appear to occur in spatially limited clusters, rather than being ubiquitously distributed [e.g. 97, 99].

The data from the deep moonquakes have been examined using a variety of seismic methods for the purpose of determining the lunar structure, including travel-time analysis [e.g. 103–106], receiver functions [107], and 3-D tomography [e.g. 108]. Seismic interferometry (SI) using ambient noise has also been employed using these data [109–112]. In these analyses, the authors successfully retrieved higher-frequency Rayleigh waves (Rg) and characterized near-surface shear velocity through the resulting dispersion curves. Heretofore, SI methods have not been employed for retrieval of body-wave information to illuminate lunar structure.

In this study we analyze deep moonquake seismograms. We apply body-wave SI [e.g. 20, 113, 114] via autocorrelation of the first P-wave phase to the P-wave coda. This allows us to retrieve the zero-offset subsurface reflection response from virtual sources co-located with the Apollo stations. For the sake of shorthand notation, we term this technique deep-moonquake seismic interferometry (DMSI). Obtaining virtual reflection responses of the Moon beneath the Apollo stations obviates the need for active seismic sources, such as explosives and artificial impacts recorded by the Apollo instruments.

Our goal is to identify the lunar seismic Moho using the DMSI technique. Knowledge of the crustal thickness is important to the understanding of the evolution of the Moon; it has implications for bulk composition, petrogenesis, and other aspects of lunar evolution. Previous studies using various seismic methods have reported widely varying values of crustal thickness (depth of the Moho). Toksöz *et al.* [115] reported an estimated depth to lunar Moho of 65 km based on P-wave travel times from artificial impact sources (S-IVB booster and LM ascent stage); they later revised this in Toksöz [116], with a mean crustal thickness estimate of 60 km, based on travel-time analysis and comparison to synthetic seismograms. Nakamura [105] found a crustal thickness of 58 km at the Apollo 12/14 sites, whereas Chenet *et al.* [117] and Lognonné *et al.* [118] reported a thinner crust of 30–33 km. On the other hand, Khan *et al.* [119] as well as a JAXA's SELEnological and ENgineering Explorer (SELENE) reported by Ishihara *et al.* [120] suggest values of 45–50 km. In addition, a recent gravity and topography study, Gravity Recovery And Interior Laboratory (GRAIL) operated by NASA, estimated the lunar crustal thickness to be 30–38 km [121].

We are also interested in imaging the upper mantle, where the seismic velocity model



is not well constrained [e.g. 103, 104] or estimated to be roughly constant [e.g. 106]. The reflection imaging using DMSI at these depths might provide some insight not only regarding the internal structure but also the mechanism of the shallow moonquakes, whose hypocentral depth estimates put them in the upper mantle. Researchers seem to have reached a consensus that tidal stress is a primary contributor to the genesis of deep moonquakes [e.g. 122–124]; however the source mechanism is still unclear for shallow moonquakes. It is clear that the crust and upper mantle exhibit a very high quality factor,  $Q$ , (low attenuation) compared to Earth [e.g. 104, 125, 126]. This suggests that a considerable degree of seismic scattering can be anticipated for the source region of the shallow moonquakes. Note that the scattering properties between the shallow crust (e.g. depth of 25 km in [125]) and below the crust would be substantially different. While scattering in the shallow crust is expected to come from the fracturing of the crust by years of impacts, scattering originating below the crust would likely come from compositional heterogeneities rather than mechanical fractures [127].

Our DMSI study may be the first reflection imaging of the shallow Moon using natural sources like moonquakes. With reflections, we mean the energy generated by a source (either active or virtual) at the surface, which propagates into the subsurface, is reflected by impedance contrast at a certain depth, and is recorded at the surface. In the nomenclature of Weber *et al.* [106], we use reflections P $x$ P where  $x$  can be any impedance contrast. In the following, we describe how we apply the method to the deep moonquakes and obtain zero-offset reflection imaging beneath the Apollo stations.

#### 4.3.2. STUDY AREA AND DATA

Figure 4.21 presents a map of the Nearside of the Moon where the Passive Seismic Experiment of the Apollo missions (12, 14, 15, and 16 in the cyan triangles) was carried out. In this study, we analyze 7 clusters of the deep moonquakes whose wavefronts can be approximated as nearly planar when they arrive at the stations (ray parameters are smaller than  $0.36 \text{ s deg}^{-1}$ ). Note that the angle degree we use in this study is for the Moon, whose radius is 1737 km (hence, one degree corresponds to approximately 30 km). Cluster centroids, including their location uncertainties, are also shown in Figure 4.21 (after [128]). The uncertainty bars indicate the range of location scatter within each of the clusters. Numbers in the yellow rectangles indicate the depth with the uncertainties of the centroid of each cluster. In Figure 4.22, we show two extremes, among the clusters we analyzed, for one-way travel-time curves using a recent 1-D velocity model published by Weber *et al.* [106]. The curves are for the largest ( $0.36 \text{ s deg}^{-1}$ ) and smallest ( $0.04 \text{ s deg}^{-1}$ ) ray parameters, characterizing responses from cluster A15 recorded at Apollo station 14 (shown in blue), and responses from cluster A97 recorded at Apollo station 16 (shown in red). The one-way travel times for the P and S phases are extracted from these curves at the respective epicentral distances for A15 and A97 of 14.3 deg and 2.5 deg.

Seismic data of the deep moonquakes were collected using the Moon Seismic Monitor of the Data Archives and Transmission System (DATS), provided by the Center for Science-satellite Operation and Data Archive (C-SODA) at the Institute of Space and Astronautical Science (ISAS) and the Japan Aerospace Exploration Agency (JAXA). We refer to the event catalog of the deep moonquakes, which is summarized by Nakamura *et al.* [97] and also contains additional events identified by Bulow *et al.* [100, 101], to extract

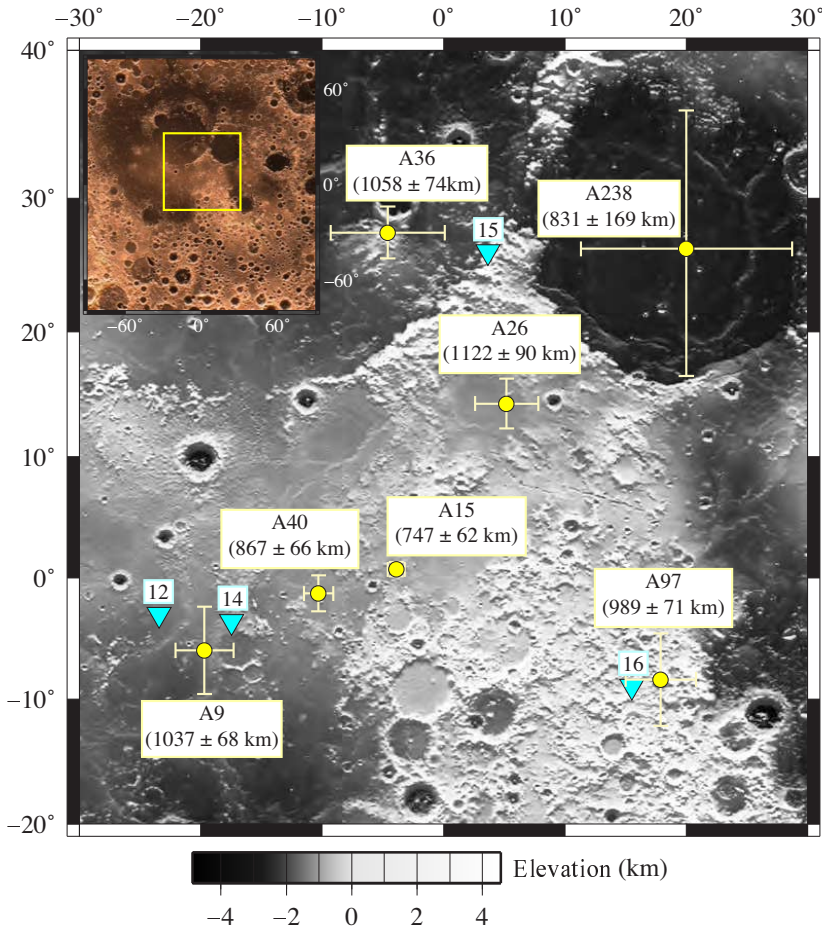


Figure 4.21: Spatial distribution of the seven clusters (labeled with capital A and a number) of deep moonquakes (yellow circles) used in our study. The numbers in the parentheses indicate depths of the clusters. Yellow bars indicate a lateral distribution range of deep moonquakes within the clusters calculated using Nakamura [128]. Cyan triangles identify the locations of the Apollo seismic stations. Topography data, referenced to a moon sphere (radius is 1737 km) whose origin is set to the center of mass, was taken from Araki *et al.* [129].

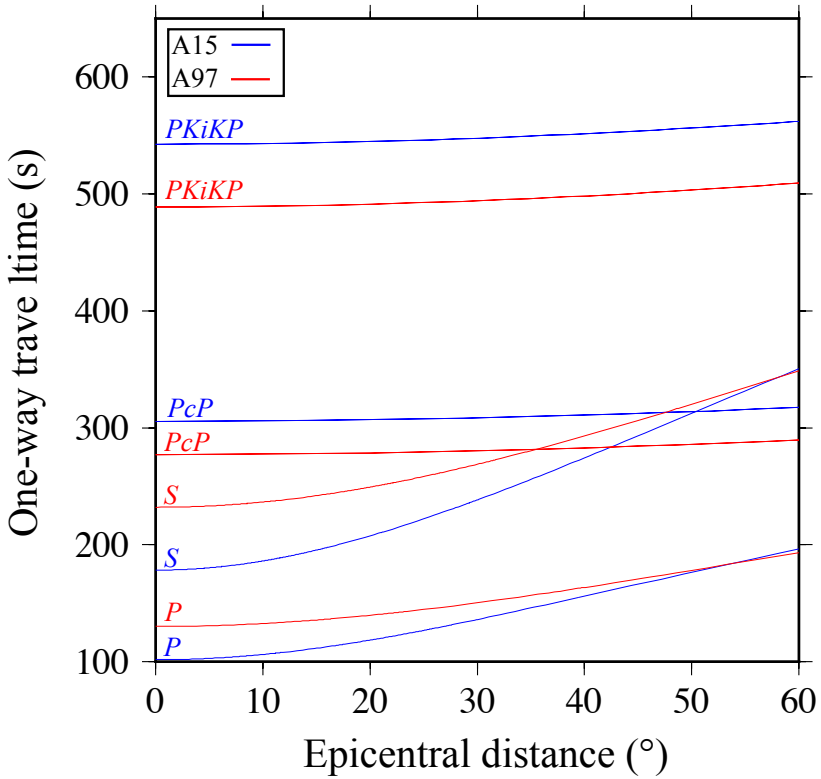


Figure 4.22: Expected one-way travel time of several phases from deep moonquakes as a function of epicentral distance. Blue curves are for cluster A15, whose direct P-wave phase is expected to have the largest ray parameter ( $0.36 \text{ s deg}^{-1}$ ) at the closest receiver (Station 14). A15 is at  $14.3 \text{ deg}$  epicentral distance from Station 14. Red curves are for cluster A97, whose direct P-wave phase will have the smallest ray parameter ( $0.04 \text{ s deg}^{-1}$ ) at the nearest receiver (Station 16). A97 is at  $2.5 \text{ deg}$  epicentral distance from Station 16. The velocity model for both P and S phases is taken from Weber *et al.* [106].

the event hypocenters of the aforementioned clusters. Since it is known that each cluster generally produces repeatable waveforms (deep moonquakes), the event identification was carried out via cross-correlation using a single-event approach [97, 100, 101].

In Table 4.3, we show a summary of the cluster coordinates and the Apollo stations for which each cluster is used. The epicentral distances and the ray parameters were calculated using mean values of the event locations. Note that cluster A40 is not used with station 14, because the number of events selected for DMSI after our quality control (QC) was too low. The complete list of the used deep moonquakes is given in Table 4.4.

Table 4.3: Deep-moonquake clusters used in this study

Cluster ID	Lat. (°N)	Lon. (°E)	Dep. (km)	Before QC No. of events	After QC No. of events	Discarded events %	Apollo station	Epicentral distance (deg)	Ray parameter (s deg <sup>-1</sup> )
A9	-6.0 ± 2.4	-19.7 ± 3.6	1037 ± 68	129	23	82	14	3.2	0.04
A15	0.7 ± 0.7	-3.9 ± 0.6	747 ± 62	50	7	86	14	14.3	0.36
A26	14.3 ± 2.6	5.2 ± 2.0	1122 ± 90	54	27	50	15	11.9	0.12
A36	27.5 ± 4.7	-4.6 ± 1.9	1058 ± 74	43	26	40	15	7.5	0.09
A40	-1.3 ± 1.2	-10.3 ± 1.5	867 ± 66	35	27	23	12	13.3	0.15
A97	-8.4 ± 2.9	17.9 ± 3.8	989 ± 71	45	14	69	16	2.5	0.04
A238	26.3 ± 8.7	20.0 ± 9.8	831 ± 169	36	20	44	15	14.7	0.30

Table 4.4: 144 deep-moonquake clusters used in this study

Cluster ID	Year	Month	Day	Hour	Minute	Apollo station
A9	1971	04	04	13	22	14
A9	1971	04	30	08	40	14
A9	1971	05	27	13	27	14
A9	1971	05	28	20	02	14
A9	1971	06	23	15	07	14
A9	1971	07	20	21	23	14
A9	1971	07	22	09	19	14
A9	1971	08	18	22	31	14
A9	1971	09	15	08	52	14
A9	1971	11	07	16	04	14
A9	1971	12	04	22	32	14
A9	1972	04	19	04	27	14
A9	1972	09	28	17	39	14
A9	1974	06	16	09	38	14
A9	1974	10	03	09	04	14
A9	1974	10	30	11	23	14
A9	1974	12	24	12	00	14
A9	1975	11	15	12	16	14
A9	1976	03	03	03	38	14
A9	1977	01	23	04	38	14
A9	1977	01	24	15	52	14
A9	1977	02	20	20	12	14
A9	1977	04	16	20	02	14
A15	1971	03	24	02	58	14
A15	1972	10	22	18	45	14
A15	1973	05	05	08	59	14
A15	1974	09	12	01	29	14
A15	1974	11	30	18	12	14
A15	1974	12	29	04	43	14
A15	1976	07	05	18	26	14
A26	1971	09	26	02	09	15
A26	1971	09	26	22	02	15
A26	1971	10	24	17	10	15
A26	1971	11	02	16	53	15
A26	1971	11	09	12	41	15
A26	1971	11	16	17	22	15
A26	1971	11	21	01	46	15
A26	1971	11	21	17	57	15
A26	1972	01	11	08	52	15
A26	1972	03	19	04	45	15
A26	1972	04	04	05	05	15
A26	1972	04	29	18	10	15
A26	1972	08	05	12	57	15
A26	1973	02	16	02	27	15
A26	1973	11	09	16	40	15
A26	1974	02	27	16	09	15
A26	1974	10	14	01	36	15
A26	1974	10	23	00	58	15
A26	1975	05	09	02	37	15
A26	1975	05	12	17	02	15
A26	1975	05	24	14	00	15
A26	1975	10	06	06	05	15

A26	1977	03	31	12	17	15
A26	1977	04	01	22	42	15
A26	1977	06	20	14	54	15
A26	1977	07	19	23	07	15
A26	1977	09	09	10	37	15
A36	1971	08	04	03	27	15
A36	1971	09	28	20	32	15
A36	1971	09	30	02	11	15
A36	1971	09	30	18	19	15
A36	1971	11	22	07	53	15
A36	1971	11	24	22	57	15
A36	1971	12	21	18	58	15
A36	1972	01	14	17	09	15
A36	1972	01	17	06	21	15
A36	1972	03	10	05	37	15
A36	1972	03	12	12	49	15
A36	1972	04	06	19	47	15
A36	1972	04	09	11	01	15
A36	1972	05	04	10	40	15
A36	1972	05	07	15	13	15
A36	1972	05	08	16	24	15
A36	1972	05	31	11	28	15
A36	1972	12	29	12	57	15
A36	1973	03	30	12	53	15
A36	1977	03	05	03	13	15
A36	1977	05	01	07	42	15
A36	1977	06	24	01	15	15
A36	1977	07	20	22	50	15
A36	1977	07	20	23	43	15
A36	1977	07	23	07	35	15
A36	1977	09	14	16	23	15
A40	1970	08	13	21	38	12
A40	1972	04	15	16	15	12
A40	1972	06	07	14	13	12
A40	1972	07	05	17	45	12
A40	1972	07	08	06	37	12
A40	1972	08	02	14	16	12
A40	1972	08	29	08	46	12
A40	1972	10	23	21	44	12
A40	1973	01	14	22	29	12
A40	1973	02	11	16	47	12
A40	1973	03	09	18	38	12
A40	1973	04	04	24	00	12
A40	1973	05	02	10	27	12
A40	1973	05	30	10	20	12
A40	1973	06	24	11	45	12
A40	1973	06	27	23	51	12
A40	1973	07	12	06	28	12
A40	1973	07	26	06	45	12
A40	1973	08	22	18	50	12
A40	1973	09	18	10	42	12
A40	1973	12	08	23	08	12
A40	1974	04	25	00	36	12
A40	1974	05	22	08	07	12
A40	1976	06	05	15	35	12
A40	1976	07	01	14	13	12
A40	1976	07	27	21	12	12
A40	1976	09	21	10	26	12
A97	1974	12	11	19	18	16
A97	1975	04	27	00	28	16
A97	1975	05	07	01	05	16
A97	1975	05	24	12	07	16
A97	1975	06	07	17	22	16
A97	1975	06	20	09	27	16
A97	1975	07	04	22	42	16
A97	1975	08	01	07	15	16
A97	1976	03	07	04	43	16
A97	1976	05	01	01	13	16
A97	1977	03	25	04	37	16
A97	1977	04	05	20	32	16
A97	1977	05	19	06	11	16
A97	1977	06	11	12	33	16
A238	1971	08	05	01	28	15
A238	1971	09	01	13	40	15
A238	1971	11	23	14	37	15
A238	1972	03	11	03	15	15
A238	1972	04	08	01	55	15
A238	1972	06	28	13	03	15
A238	1972	07	25	16	26	15
A238	1973	01	04	10	55	15
A238	1973	01	31	16	27	15
A238	1973	02	02	21	00	15
A238	1973	03	02	10	30	15
A238	1973	03	30	00	46	15
A238	1973	03	30	01	06	15
A238	1973	04	26	14	48	15
A238	1973	10	02	16	08	15
A238	1976	09	23	09	59	15
A238	1977	03	06	17	25	15
A238	1977	04	02	19	38	15

A238	1977	07	22	08	05	15
A238	1977	08	18	05	50	15

### 4.3.3. DEEP-MOONQUAKE SEISMIC INTERFEROMETRY

SI is more commonly defined as a method to retrieve new seismic records by correlation with existing records. In the context of seismic exploration, Claerbout [20] showed that the zero-offset (source and receiver locations are co-located) reflection response of a horizontally layered (1-D) medium could be obtained from the autocorrelation of the transmission response measured at that location from noise sources in the subsurface. He termed this technique acoustic daylight imaging. As Yokoi and Margaryan [130] demonstrated, acoustic daylight imaging applied for retrieval of surface waves is related to the spatial autocorrelation method (SPAC). The latter was first introduced by Aki [131], who estimated the subsoil structure from ambient vibration (microtremor) records. Wapenaar [24, 132] generalized Claerbout's acoustic daylight principle to any 3-D inhomogeneous medium and showed that, in the general case, cross-correlation should be used from recordings of transient or noise sources that effectively surround the receivers. This method was then termed SI [133]. Recent work has shown that to remedy some limitations of the correlation method, such as irregular source illumination and intrinsic losses in the medium, SI by multidimensional deconvolution could be used [113].

DMSI, which we use here, is a specific application of SI by correlation for a 3-D medium. Still, it resembles closely the original acoustic daylight imaging. While the acoustic daylight imaging uses ambient noise in a 1-D situation, DMSI uses the P-wave coda of the deep moonquakes in the 3-D approach. DMSI is also closely related to the global-phase seismic interferometry (GloPSI) method, as introduced by Ruigrok and Wapenaar [25], to image the Moho under the Himalayas and Tibet. While GloPSI uses global-phases, however, such as PKP, PKiKP, and PKIKP, DMSI uses the P-wave coda.

To retrieve the zero-offset reflection response from DMSI with the full transmission response, in the general SI-by-correlation relation we use autocorrelation. For an acoustic 3-D medium and transient sources in the subsurface (like moonquakes), the discretized version of the relation in Wapenaar [24] can be written as

$$\sum_k \{T(\mathbf{x}_R, \mathbf{x}_k, -t) * T(\mathbf{x}_R, \mathbf{x}_k, t)\} = \delta(t) - R(\mathbf{x}_R, \mathbf{x}_R, -t) - R(\mathbf{x}_R, \mathbf{x}_R, t), \quad (4.8)$$

where  $T(\mathbf{x}_R, \mathbf{x}_k, t)$  is the transmission response at the receiver location  $\mathbf{x}_R$  from a moonquake at location  $\mathbf{x}_k$ ,  $k$  denotes the  $k$ -th moonquake,  $R(\mathbf{x}_R, \mathbf{x}_R, t)$  is the zero-offset reflection response for co-located source and receiver at location  $\mathbf{x}_R$ ,  $\delta(t)$  is the delta function, and  $*$  denotes convolution.

Equation 4.8 assumes that the receivers are at the Moon's (free) surface, while the sources are distributed along a boundary in the subsurface and are in the far field of the receivers. But this is quite an idealized situation, as moonquakes and earthquakes often occur along specific structures only. Snieder [38] showed that the retrieved reflection energy in the result from SI comes from sources lying inside the stationary-phase zones. For a subsurface, whose structure is composed of horizontal or gently dipping reflectors,

the stationary-phase zone for a zero-offset reflection at location  $\mathbf{x}_R$  is around or close to the vertical below  $\mathbf{x}_R$ . This is because a station co-located with an active source would record only reflection energy that is characterized by vertical or near-vertical incidence.

In a 3-D medium, the stationary-phase zone is a patch. But even such a patch is in general unlikely to be sampled well with moonquakes, as the moonquakes cluster around certain locations (see Figure 4.21). Because of this clustering, applying equation 4.8 directly to clusters that may not be sufficiently close to an Apollo station (e.g. cluster A15 for station 14 and A238 for station 15) might result in an erroneously retrieved zero-offset reflection response because the cluster(s) may be outside the stationary-phase zone. Thus, the strongest contributions to the result, arising from the summation of the autocorrelations of a direct P-wave phase and its free-surface reverberation between the Moon's surface and a subsurface reflector (primary reverberation), would not interfere constructively (stack) optimally. The result would be a reflection at a slightly erroneous time. Due to the source-receiver configuration of this study, we consider the stationary-phase zone for retrieving a zero-offset reflection. The extent of the stationary-phase zone depends on the depth of the reflectors and the depth of the moonquakes [e.g. 134]. Taking an average velocity of 7.7 km/s and center frequency of 0.5 Hz, and a source depth of 800 km, we calculate that the stationary-phase zone for a reflector at a depth of 40 km (e.g. the Moho depth in [106]) will have a radius of 212 km.

This effect can be minimized by targeting the zero-offset plane-wave response as in GloPSI [25]. The authors achieved this by choosing global phases, as these phases will have a planar wavefront at the recording stations and will be arriving nearly vertically. Summation over a sufficient number of ray parameters and azimuths ensures retrieval of the zero-offset (near) vertical-incidence plane-wave response.

Using deep moonquakes close to the Apollo stations would ensure that the recorded transmission responses of P-wave phases are nearly vertical (see Figure 4.22). Due to the clustering of the deep moonquakes, however, it is not possible to average over a sufficient number of ray parameters and azimuths. To remedy this, we select the P-wave coda from direct P-wave phases whose ray parameters are smaller than  $0.36 \text{ (s deg}^{-1}\text{)}$ . The coda from such direct phases would be characterized by even smaller ray parameters and, thus, we can assume that the P-wave coda reverberates nearly vertically between the reflectors in the subsurface and a station at the surface. To describe the use of only coda from the direct P-wave phase, we rewrite equation 4.8 as

$$\sum_k \{T^c(\mathbf{x}_R, \mathbf{x}_k, -t) * T^c(\mathbf{x}_R, \mathbf{x}_k, t) * M_k(-t) * M_k(t)\} \propto \quad (4.9)$$

$$\{\delta(t) - R(\mathbf{x}_R, \mathbf{x}_R, -t) - R(\mathbf{x}_R, \mathbf{x}_R, t)\} * \bar{M}_k(t),$$

where  $T^c(\mathbf{x}_R, \mathbf{x}_k, t)$  is the selected P-wave coda at receiver location  $\mathbf{x}_R$  from a deep moonquake at  $\mathbf{x}_k$  from one cluster,  $M_k(t)$  is the source time function of the  $k$ -th deep moonquake, and  $\bar{M}_k(t)$  is the average of the autocorrelations for the different source time functions of the deep moonquakes in the cluster. A cartoon in Figure 4.23 shows schematically how DMSI with coda, but without the direct P-wave phase, functions. Note that the exclusion of the direct arrival, in our case the P phase, from the DMSI equation 4.8, might result in stronger non-physical arrivals (artifacts) appearing in the retrieved result using

DMSI as in equation 4.9. Such artifacts may be retrieved from the correlation of two primary reverberations (the first free-surface multiples of the direct P-wave phase after bouncing at some impedance contrasts), for example. If the cluster is not situated in the stationary-phase zone, such artifacts will be weakened during the summation over the used cluster moonquakes because of the varying hypocentral depths and locations. The retrieved physical energy will result from correlation of multiply scattered arrivals, which, because of the multiple scattering, is characterized by smaller ray parameters and thus will sum constructively for more (or all) moonquakes in the cluster. Even if the artifacts are strong compared to the retrieved physical energy, the artifacts are normally strongest at the earlier times (close to time 0 s) [e.g. 135], while the later times are less affected. In the following sections, we apply DMSI following equation 4.9.

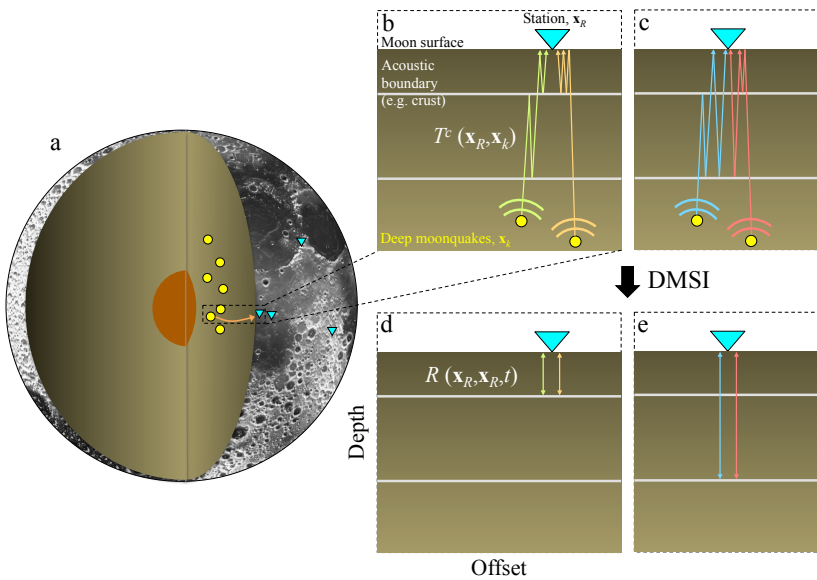


Figure 4.23: Cartoon illustrating how deep-moonquake seismic interferometry (DMSI) works. (a) Deep-moonquake clusters closest to an Apollo station are selected (ray parameter of the direct P-wave phase is smaller than  $0.36 \text{ s deg}^{-1}$ ). Topography data is taken from Araki *et al.* [129]. (b) Schematic ray paths of two types of P-wave coda arrivals: a reverberation between two reflectors and its free-surface reverberation from a shallow reflector (green); a first-order and a second-order free-surface reverberation from the shallow reflector (orange). (c) Schematic ray paths of two other types of P-wave coda arrivals: the reverberation between two reflectors and its free-surface reverberation from a deep reflector (blue); A first-order free-surface reverberation from the shallow reflector and its free-surface reverberation from the deep reflector (red). (d) Retrieved zero-offset plane-wave reflection response beneath the station from the autocorrelation of the green and orange coda arrivals illustrated in b, respectively. Summation over all such coda arrivals would retrieve the zero-offset vertical plane-wave response obtained from DMSI. (e) Same as in d, but using the coda arrivals in c. Note that the horizontal and vertical axes in b-d are not in scale to the actual coordinate.



#### 4.3.4. DATA PROCESSING

We begin by deconvolving the instrument response. For this, we use the instrument information given by Latham *et al.* [136] as well as by Incorporated Research Institutions for Seismology (IRIS) Data Management Center, and we obtain the three-component (two orthogonal horizontal and one vertical) dataset. Following Nakamura [128], we apply a fifth-order Butterworth bandpass filter between 0.2 and 2 Hz to improve the signal-to-noise ratio (SNR) of the deep-moonquake phases. The 2 Hz upper limit is dictated by expected strong scattering due to the megaregolith [137]. Figure 4.24a shows an example of a raw seismogram as recorded by the vertical component of the Apollo 12 station for a deep moonquake from cluster A40. The onset of the P-wave phase is seen at 120 s [97]. In Figure 4.24b we show the seismogram after instrument-response deconvolution, while in Figure 4.24c we show the seismogram (trace) from Figure 4.24b after the band-pass filtering. Note that interpreting an event among several stations is generally known to be difficult as different stations have different SNR. This makes exact arrival-time picking of the direct P-wave phase difficult. Because of this, picking arrival times for both P- and S-phases is commonly done for each station on the resulting trace from stacking individual traces from a cluster [e.g. 100, 101, 128]. A relevant discussion and a few examples can be found in Nakamura [128] (Figures 4.21 and 4.22 in his report). Even if the data is low-bit in appearance (e.g. Figure 4.24a), one can still retrieve desired signals by SI if such signals are repetitive [e.g. 111, 138–140].

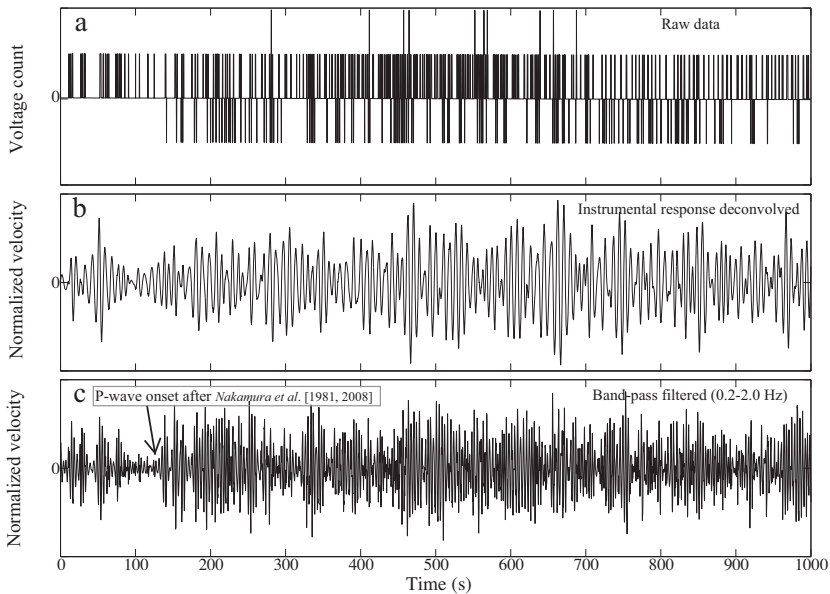


Figure 4.24: (a) Raw data of a deep moonquake from cluster A40 as recorded by the vertical component of Station 12 with origin time at 16:15 on 15 April 1972 [97]. The P-wave onset is expected to be at 120 s. (b) The seismogram after deconvolution of the station's instrument response. (c) The seismogram after applying a bandpass filter (5th-order Butterworth filter) between 0.2 Hz and 2 Hz.

After filtering, we perform a manual QC on each event waveform to decide whether to use it further for DMSI. Spiky and/or amplitude-saturated traces are discarded from further processing. Examples for both used and discarded traces are shown in Figure 4.25. A summary of the number of the event data before and after QC is given in Table 4.3.

Subsequently, we extract the P-wave coda from all vertical-component traces that are selected for further processing. The extraction is done using a time window starting 5 s after the onset of the direct P-wave phase (based on [97]) and finishing before the onset of the direct S-wave phase. Although in DMSI we use only the vertical-component data, as described above, we use also the transverse-component data to aid us in identifying the onset of the direct S-wave phase since S-wave phases are generally clearer on the transverse (Figure 4.25). For the recordings at Apollo stations 12 and 14, we also use the published onset times of the direct S-wave phases provided by Nakamura [105].

As reported in previous studies, the precise arrival times for the direct P-wave phases are sometimes difficult to identify [e.g. 128]. Since we use for DMSI the P-wave-coda as input data, however, precise arrival times are not needed. Needless to say, it would be advantageous to be able to identify the precise onset of the direct P-wave phases so that a longer time window of the P-wave coda could be used. This could permit retrieval of reflections from, and thus imaging of, deeper structures, via DMSI. Due to the uncertainty of the P-wave onset, the length of the P-wave coda tends to be shorter. Because of the onset-time uncertainty, our P-wave-coda extraction windows begin 5 s after the estimated onset of the direct P-wave phase. Note that the maximum two-way travel time we can retrieve (and thus image) via DMSI using the P-wave coda is less than 50 s (Figure 4.22). A further advantage is gained by excluding the P-wave coda after the direct S-wave arrival, to exclude strong surface-wave energy. We assume that the most energetic surface waves begin almost simultaneously with the direct S-wave arrival. Moreover, the frequency bandwidth we use (0.2-2.0 Hz) reduces surface-wave noise which resides largely in the 4-12 Hz band [109]. Surface wave contamination may still exist, but much of it will be random; the stacking process used in DMSI will suppress such noise. At the same time, DMSI enhances the repeatable signals (e.g. reflections). We acknowledge the possibility that DMSI may retrieve scattered surface waves from repeatable scattering due to P-wave conversions arriving ahead of the S-wave. Given this, and other possible concerns (e.g. multiple reflections), we focus our interpretation only on major subsurface features (if present).

After extraction of the P-wave coda from the selected traces, we apply energy normalization (to their respective maxima) to each selected trace. This normalization effectively removes the magnitude differences among moonquakes within a cluster and equalizes the amplitudes. After normalization we apply DMSI.

To retrieve the zero-offset vertical-incidence plane-wave response, one can take two approaches. Following the first technique, all normalized P-wave-coda traces from deep moonquakes pertaining to one cluster are summed together (stacked). This would result in improved SNR also of later arrivals. DMSI is applied to the resulting stacked trace. If the event locations for one cluster are sufficiently close to one another, the stacked trace will be characterized by an improved SNR of the reverberations, providing clear retrieved reflections. The left panels in Figure 4.26a-g show the retrieved zero-offset reflection

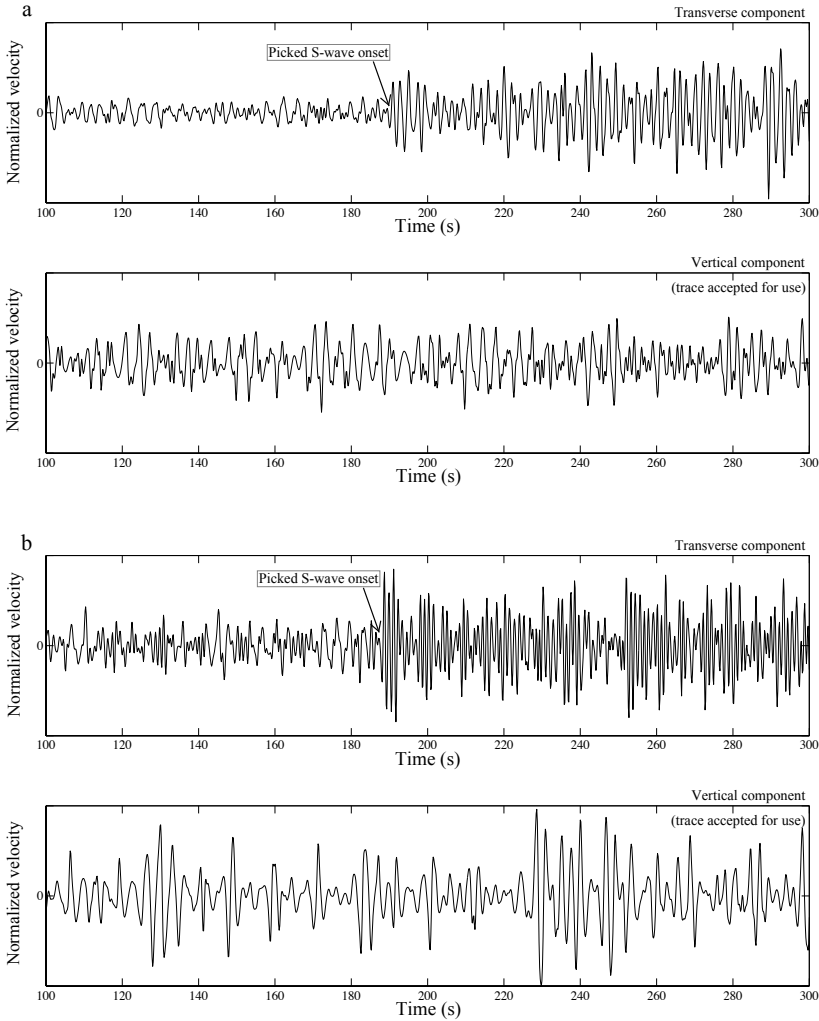


Figure 4.25: Examples of used and discarded seismograms (traces) after applying the data processing of Figure 4. (a) Traces of a deep moonquake at 06:11 on 19 May 1977 from cluster A97 recorded by Station 16. The vertical-component trace is used for further processing. (b) Traces of a deep moonquake from cluster A9 at 22:32 on 4 December 1971, recorded by Station 14. The vertical-component trace is used for further processing. (c) Spiky traces of a deep moonquake from cluster A15 occurring at 14:31 on February 18, 1972 recorded by Station 14. The vertical-component trace is discarded from further processing. (d) Ringing traces of a deep moonquake from cluster A9 recorded at Station 14 from 04:16 on January 29, 1972. The vertical-component trace is discarded from further processing. The origin times are from Nakamura *et al.* [97]. (to be continued)

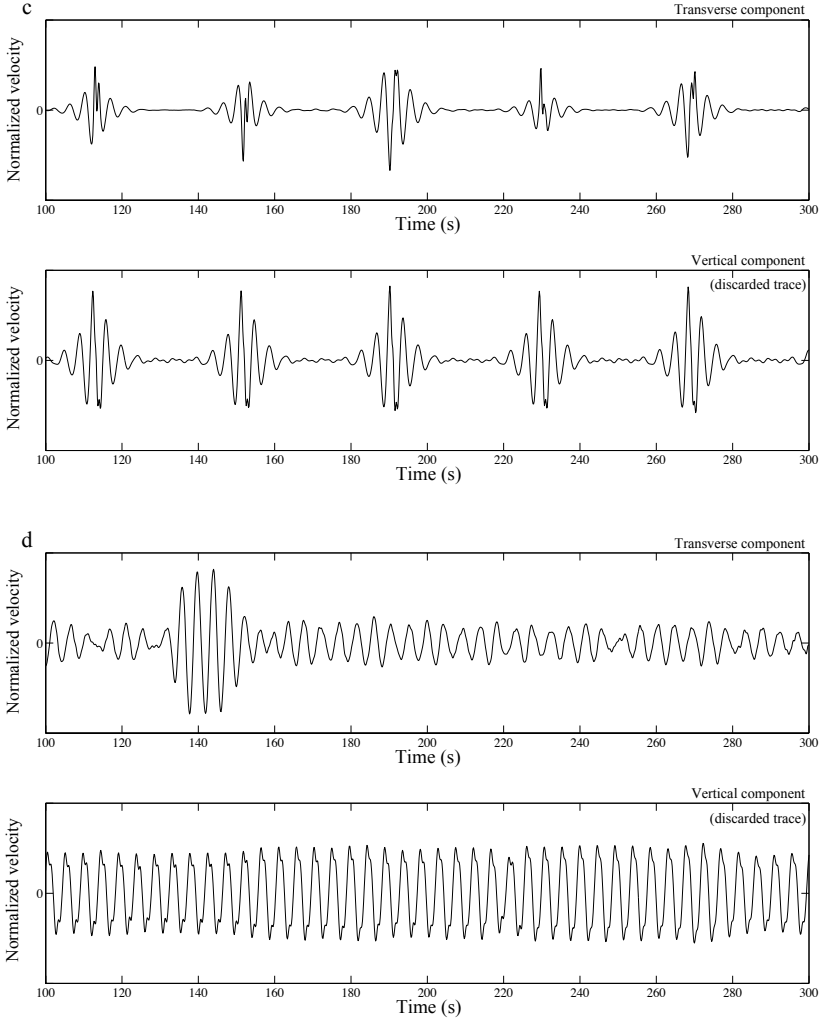


Figure 4.25: (Continued)

trace resulting from the application of DMSI to the stacked trace. This approach will produce meaningful results only when the moonquake hypocenters in a cluster are very close to one another both laterally and in depth. Hence, this approach serves as a test of hypocentral proximity within a cluster.

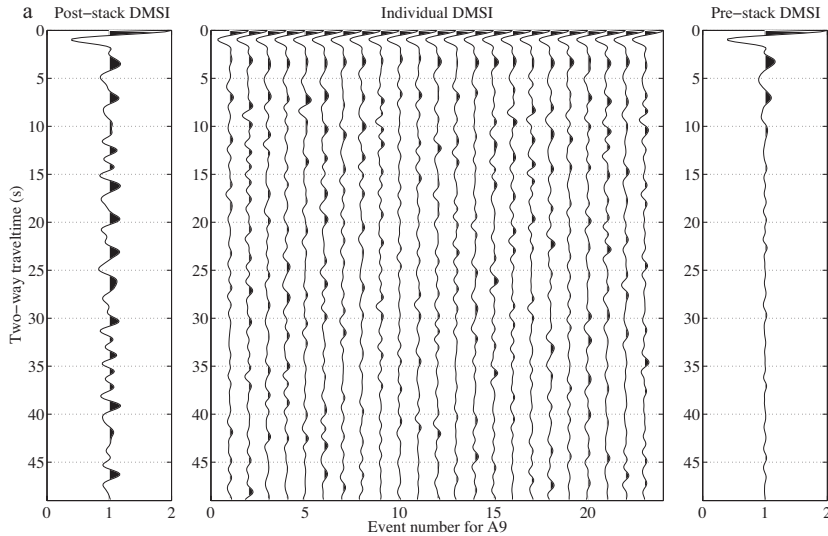


Figure 4.26: Results in two-way travel time retrieved by DMSI for our selected clusters: (a) A9. (b) A15. (c) A26. (d) A36. (e) A40. (f) A97. (g) A238. The left panels represent DMSI results obtained from autocorrelation of the stacked P-wave codas for one cluster. The middle panels show the individual autocorrelations for each selected P-wave coda for one cluster recorded by one station. The right panels show the retrieved DMSI result after stacking the traces in the middle panels. (to be continued)

In the alternative approach, DMSI is applied by autocorrelating each of the normalized P-wave-coda traces from deep moonquakes within one cluster and stacking them. The middle panels in Figure 4.26a-g show the autocorrelation results for all selected traces in each cluster we use, while the right panels in Figures 4.26a-g show the result from stacking the autocorrelated traces from the respective middle panels. If the event locations for one cluster are sufficiently close to one another, the retrieved traces in the left and right panels in Figures 4.26a-g should exhibit the same retrieved reflections, although the right panels may exhibit a lower SNR. The left and right panels, though, show different retrieved results. This means that the event locations for one cluster are not sufficiently near to one another laterally and/or vertically (in depth). The horizontal and depth location uncertainties given in Figure 4.21 (see also Table 4.3) were calculated based on the error ranges in the locations in Nakamura [105], which he attributed to errors in the velocity model.

Because of the location scatter within each cluster, DMSI response applied to a stacked trace is expected to provide poorer results than the stacking of DMSI results applied to individual traces. The difference arises because when the sources are not sufficiently close to one another, the coda from each source in a cluster has different arrival times and their stack will decrease the SNR. When stacking autocorrelated traces, the situation

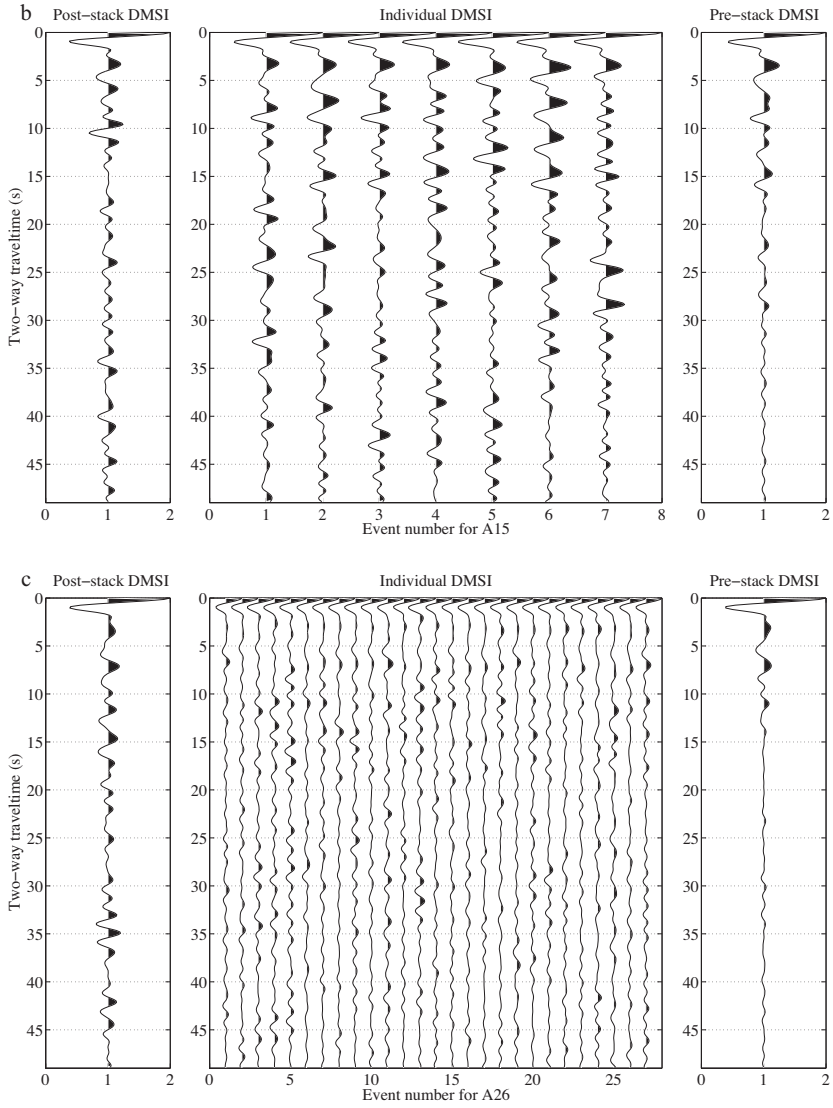


Figure 4.26: Continued (1/3)

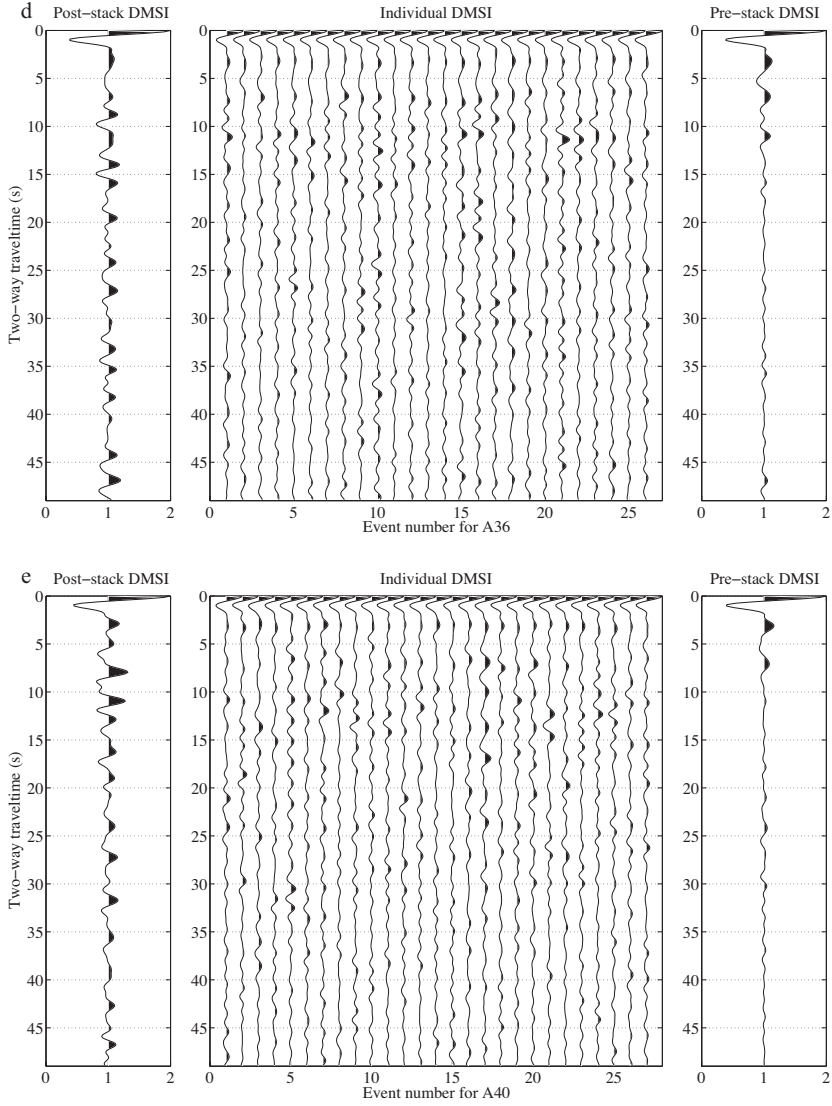


Figure 4.26: Continued (2/3)

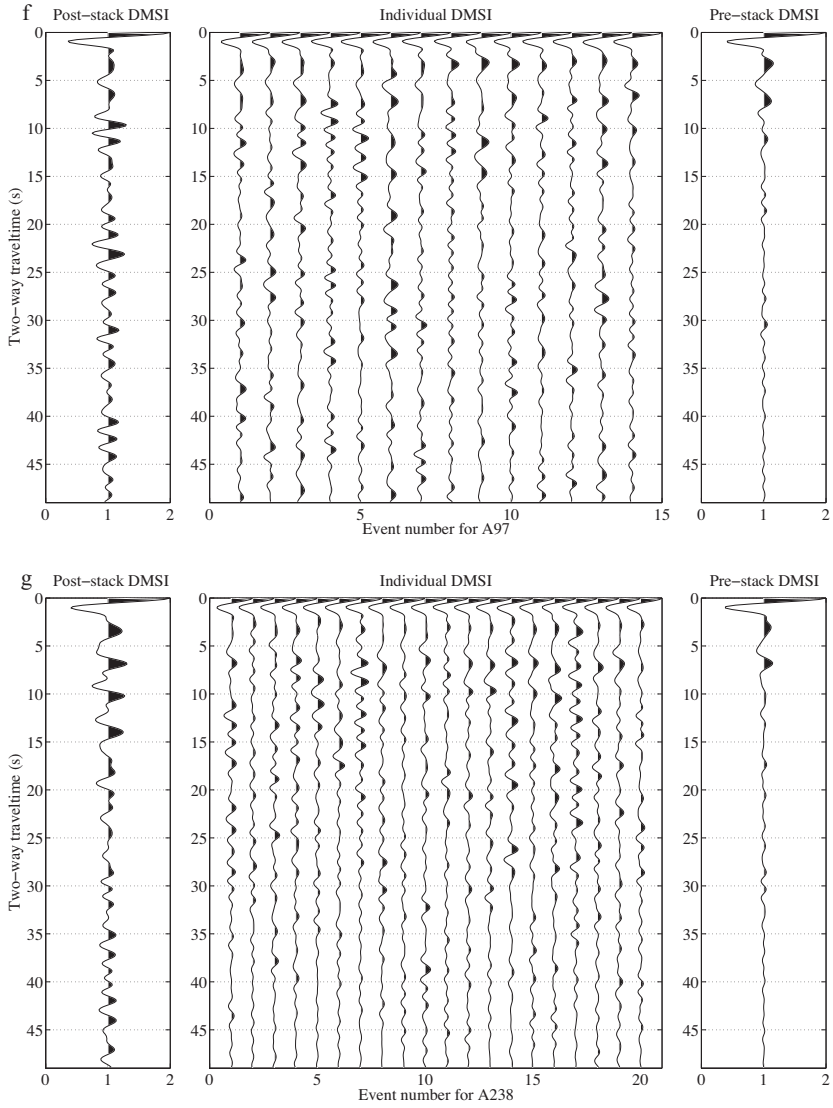


Figure 4.26: Continued (3/3)



is different. Autocorrelating the coda from each source separately accounts for differences in the travel times between a source and the surface, as illustrated in Figure 4.23, thus leaving only the free-surface reverberation (retrieved reflections) in the result. For a sufficient number of events from a cluster, retrieved reflections interfere constructively in the stacking of the autocorrelated traces, so SNR increases. We therefore follow the second path for our full analysis.

After the above processing, from equation 4.9 we retrieved  $-R(\mathbf{x}_R, \mathbf{x}_R, t)$ . We multiply this result by -1 to obtain the reflection response  $R(\mathbf{x}_R, \mathbf{x}_R, t)$ , which is also characterized by a zero-phase wavelet  $\bar{M}_k(t)$ . This means that in forthcoming Figures after 4.27 one can interpret peaks as positive events (filled in black) and troughs as negative events. These peaks and troughs may be blurred by multiples and their interference as demonstrated in the following section. The estimated source time function for a  $M_W$  3.0 earthquake is  $\leq 1$  s [45] and the  $M_W$  and  $M_L$  scales at and below 3.0 are roughly equivalent [141]. Since the magnitudes of our events are estimated to be no greater than  $M_L$  1.3 [142] or 3.0 [143], the first 3 s should sufficiently capture the autocorrelated source time functions. We therefore mute the first 3 s in the correlation result to suppress the autocorrelated source time function (i.e. the first term on the right-hand side of equation 4.9 after convolution). To verify that muting of the first 3 s is sufficient, we compared the suppression using different durations for the autocorrelated source time functions, ranging from 1 s to 4 s with time step of 1 s. The results of the suppressions are shown in Figures 4.27a-d. Any of the three results from 2 s to 4 s can be also used; however, we choose 3 s, as we find this result clearer for interpretation of the shallower part of the retrieved reflection response. If needed, one can also try to remove the source time functions for arrivals later than 3 s. Results would be only improved, however, when individual source time functions are well estimated. In this study, since the magnitude of the deep moonquakes is expected to be rather small [e.g. 142], the retrieved source time function will not be long and thus will not hamper our interpretations of the dominant features (e.g. the Moho).

As a final step, the DMSI results are converted from two-way travel time to depth (Figure 4.28) using the Dix's equation [30] making use of the 1-D velocity model of Weber *et al.* [106]. We include in the model the local thickness (1 km) of the megaregolith whose velocity is estimated to be 1 km/s. Without the low-velocity megaregolith, the estimated depth of the Moho would be a few km deeper than the 50 km of Figure 4.28.

### 4.3.5. NUMERICAL WAVEFIELD MODELING

In order to aid the interpretation of the DMSI results (Figure 4.28), we perform 1D numerical modeling for DMSI using a 2D finite-difference modeling code in acoustic mode [145]. The 1D model we used (Figure 4.29a) is taken from Weber *et al.* [106]. We use it to model transmission responses from subsurface sources at a depth of 50 km clustered laterally within 2 km around the lateral position of the station; with 200 m source spacing. The retrieved reflection at the surface (Figure 4.29c) is obtained by autocorrelating the transmission responses from each source (e.g. in Figure 4.29b for the source vertically below the station) and summing the separate autocorrelations. We use a Ricker wavelet [30] with a center frequency of 0.5 Hz to approximate the DMSI result for cluster A97. Note that the impedance boundary at a depth of 40 km is the Moho in this model. Hav-

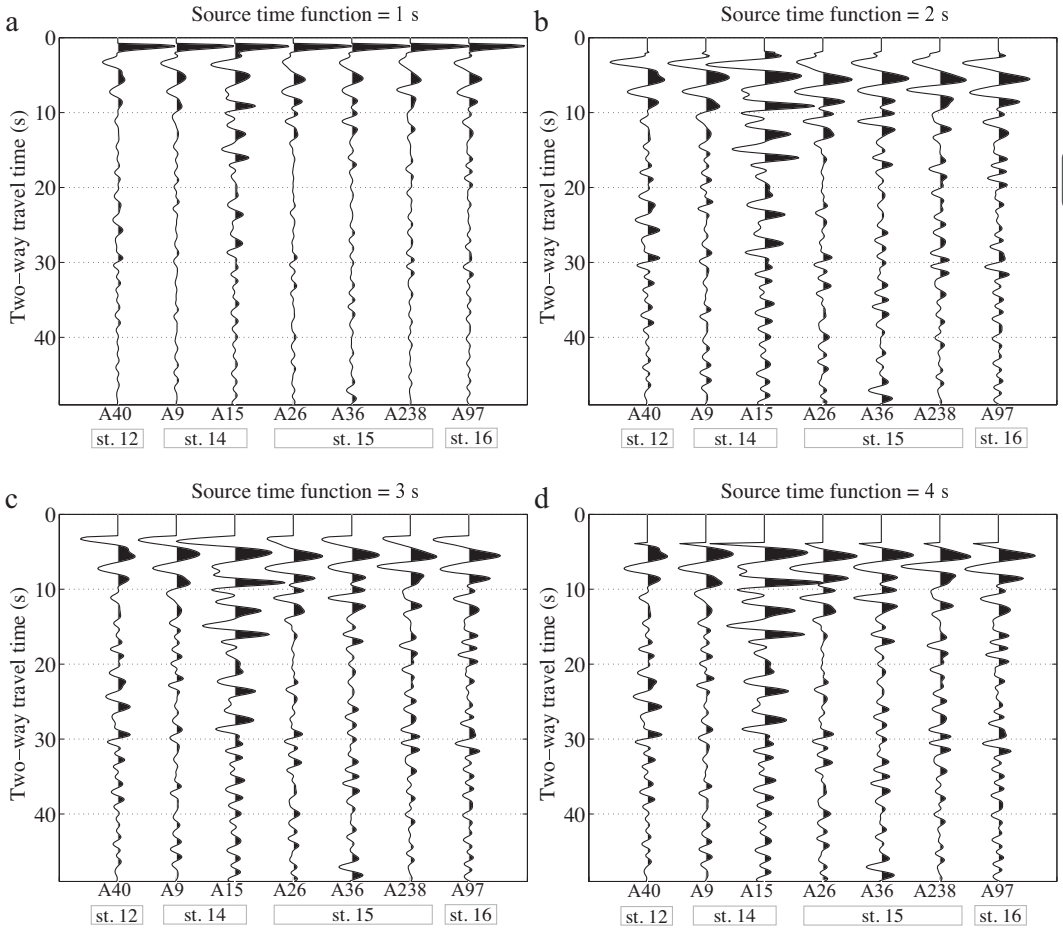


Figure 4.27: A comparison of the retrieved DMSI result (the right panels in Figure 4.26) when the averaged source time function  $\bar{M}_k(t)$  is muted down to (a) 1 s, (b) 2 s, (c) 3 s, and (d) 4 s.

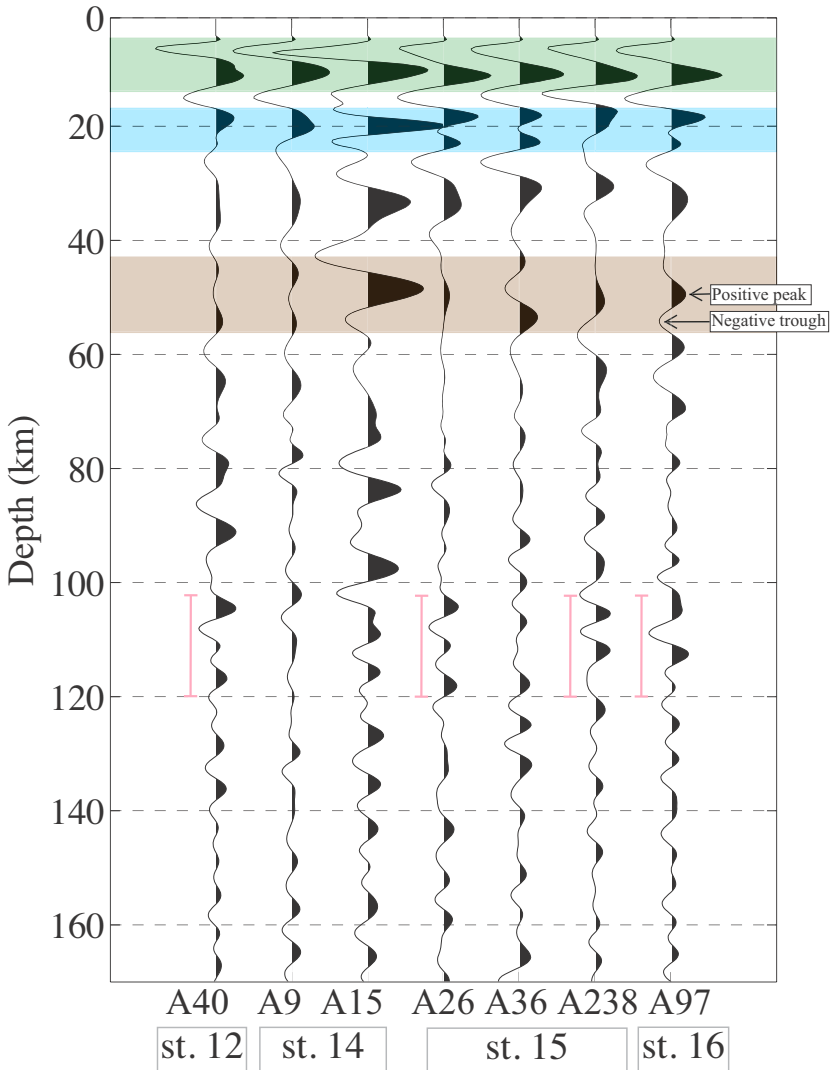


Figure 4.28: Images in depth, with highlighted horizons, obtained from the DMSI results. The transparent green indicates a possible tuned thin-layer reflection from the megaregolith layer (e.g. a depth of 1 km in [144]). The transparent blue rectangle indicates the zone where not only the reflection from the acoustic boundary at ~ 20 km depth, but also two different ghosts: one is the interfered response between the responses from the boundary at ~ 1 km and ~ 20 km; and the other is at ~ 20 km and the Moho, would contribute. The pink bars indicate parts of the upper mantle characterized by laterally coherent horizons under some of the stations. The transparent brown rectangle indicates the zone where we interpret the Moho. Two black arrows indicate the definition of our positive peak and negative trough, respectively.

ing sources at a depth of 50 km and laterally close to the station ensures nearly vertical illumination of the station. As in the previous section, the direct P-wave arrival in the transmission from each source has been muted. The total modeling length of 80 s simulates an average length of the recordings used in the previous section between the direct P- and S-wave phases.

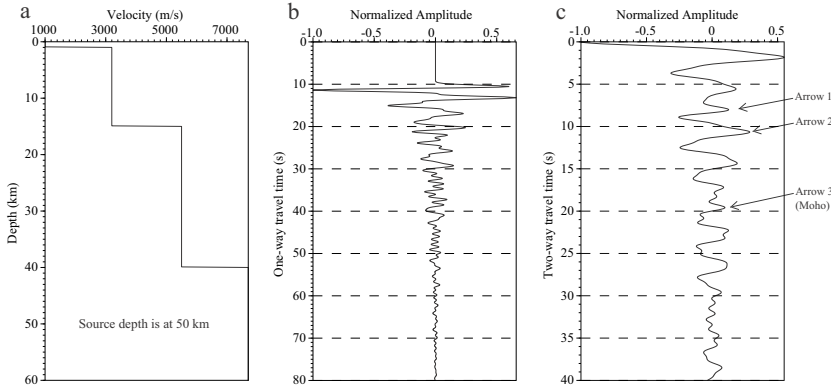


Figure 4.29: (a) The 1-D velocity model of Weber *et al.* [106]. (b) The transmission response from the source radiated from a depth of 50 km and recorded at the surface. (c) The retrieved reflection response obtained by DMSI (autocorrelation) of the coda of the response in Figure 4.29b with three examples of events indicated by: Arrow 1 where an expected arrival time for the ghost caused by interfering responses from a depth of 1 km and 15 km appears at 8.7 s as well as the one from a depth of 15 km and 40 km arrives at 9.1 s; Arrow 2 where an expected arrival time for the reflection from a depth of 15 km appears at 10.7 s; and Arrow 3 where an expected arrival time for the reflection from a depth of 40 km (the modelling Moho) appears at 19.8 s.

For the model in Figure 4.29a, the expected retrieved zero-offset reflections from the three impedance contrasts at 1 km, 15 km, and 40 km should appear at 2 s, 10.75 s (Arrow 2 in Figure 4.29c), and 19.85 s (Arrow 3 in Figure 4.29c). The reflection from the Moho marks a major characteristic difference between earlier and later package of responses. The earlier responses (0-17 s) show relatively higher amplitudes and broad phases, whereas later responses (> 22 s) are characterized by relatively lower amplitudes and ringing phases. We note other arrivals as well. For example, an event is seen with a positive peak at 8 s (Arrow 1 in Figure 4.29c) and a negative peak at 9.1 s. This is an artifact caused by the interference of multiple reflections (multiples) within the shallowest layer of 1 km thickness and the reflection from the impedance contrast at 15 km. Other arrivals not discussed here are combinations between multiples and between multiples and primary reflections. Note that the primary reflection from the low-velocity layer at 1 km cannot be retrieved as a separate reflection, but forms part of the virtual-source time function (tuning effect).

We see based on the modeling results that if low-velocity layers are indeed present beneath our Apollo stations, it would introduce difficulties in distinguishing within the DMSI field results which events arise from which layers. Nevertheless, we are able to identify the Moho via the major characteristic change of waveform for earlier vs later arrivals. If the DMSI results illuminate features similar to those from our numerical mod-

eling, such features are consistent with the impedance boundaries within our velocity model.

#### 4.3.6. RESULTS AND DISCUSSION

Figure 4.28 shows the DMSI traces for our selected clusters, presented on a depth axis rather than time axis. We interpret consistent peaks and troughs as delineating reflectors below the Apollo stations from each of the seven clusters that we used. One of the most striking features is that for all clusters the strongest amplitudes appear laterally coherent at depths of around 5 km and 13 km as a trough and a peak, respectively (the transparent green rectangle in Figure 4.28). Based on the numerical modeling, this may represent a tuned thin-layer reflection from the megaregolith layer (e.g. a depth of 1 km in [144]). By ‘tuned thin-layer reflection’, we mean that the observed waveform arises from interference between two or more reflections at impedance boundaries which are less than one quarter wavelength from one another in depth. The only exception is cluster A15, whose direct P-wave arrivals exhibit the highest ray parameter among the clusters used (see Table 4.3). This cluster is the smallest following QC, hence, we may simply not be benefiting from stacking to the extent that larger clusters provide. The package of relatively strong and laterally coherent amplitudes continues to a depth of 42 km. Deeper than this level, we see relatively lower amplitudes with ringing phases. This characteristic, which is manifested both shallower and deeper than about 50 km, may be viewed as an analogue to the zero-offset trace obtained through synthetic modeling in Figure 4.29c. The Moon’s Moho in that case delineated a boundary between the two distinct zones. We therefore interpret the field results as marking the Moho at about 50 km depth. It is difficult to determine the exact Moho depth, however, because the Moho reflection may be affected by interference from multiples, which depend on the number and depth of unmodeled layers. Uncertainty in our interpretation of the Moho depth is captured by the transparent brown rectangle in Figure 4.28. This rectangle highlights the feature related to the retrieved Moho reflection indicated by Arrow 3 in Figure 4.29c. Thus, we estimate the depth of the Moho as  $50 \pm 8$  km beneath the Apollo stations when relying upon the velocity model in Weber *et al.* [106] for our analysis. The lower boundary of the region containing the Moho (the transparent brown rectangle in Figure 4.28) we set at 58 km because of stronger-amplitude events beneath it (e.g. positive peaks around 60–65 km at A9, A40, and A238). Such events are also present in the synthetic results. Using the events indicated by Arrow 1 and Arrow 2 in Figure 4.29c, the strong positive amplitudes around 20 km in Figure 4.28 (highlighted by the transparent blue rectangle) can be interpreted as a reflection from an impedance contrast at that depth, although we cannot rule out artifacts. The laterally coherent event at around 30–35 km depth may arise from either an impedance boundary or a multiple of the event in the transparent green rectangle in Figure 4.28. In other words, our method supports the presence of layers shallower than the Moho [e.g. 144], but due to the few available stations this cannot be determined unequivocally.

To validate our discussed interpretation for Figure 4.28, we performed a bootstrap test on the cluster A26, which contains the largest number of deep moonquakes (Figure 4.30). In this test, we randomly select 20 of the 27 DMSI traces to produce a stack, and repeat this procedure 30 times. Our interpretation (transparent rectangles) in Fig-

ure 4.30 is superimposed on the bootstrap results in Figure 4.30. The right panel in Figure 4.30 is the mean of the individual bootstrapping realizations (center panel in Figure 4.30). After picking the maximum positive amplitude from the individual bootstrapping realizations for the transparent rectangles, we calculate the 95 % confidence intervals, shown as orange bars in the right panel of Figure 4.30. It turns out, that our interpretation for the transparent rectangles in green and blue has an uncertainty in depth of less than 1 km. For the Moho interpretation (the transparent rectangle in brown), the uncertainty is about  $\pm 8.5$  km from the mean depth of 50 km, supporting our qualitative Moho interpretation of  $50 \text{ km} \pm 8 \text{ km}$ .

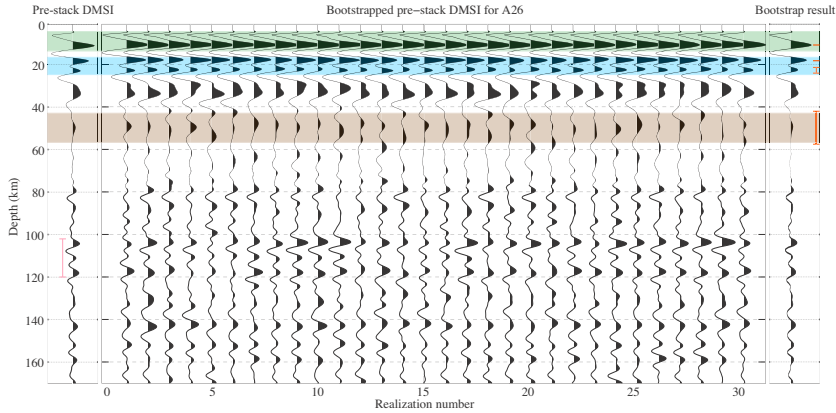


Figure 4.30: The result of a bootstrap test for the A26 cluster. Transparent rectangles follow the interpretation from Figure 4.28. Orange bars in the right panel indicate 95 % confidence interval for the positive peaks in the transparent rectangles.

Looking at regions below the Moho, the image suggests in general a laterally heterogeneous subsurface. This agrees with our synthetic model, which indicates that such a lateral feature arises when no significant velocity layers exist. We do, however, note some coherent features under two or three of the stations and at different depths: a well-correlated trough for stations 12, 15 and 16 at 100-120 km (indicated by the pink bars) for clusters A40, A26, A238 and A97.

A variety of studies using various methods have suggested different depths to the Moho on the Moon, thus Lunar crustal thickness is still unresolved, as well as how much this thickness may vary spatially. Estimates of crustal thickness ranging from 30 to 60 km, arrived at through various analytical methods, are in rough agreement with our 42-58 km estimate, but the wide range of values may be consequential to models for the evolution of the Moon; hence the accurate determination of Lunar crustal thickness is pivotal to developing lunar genesis models.

Our DMSI result (Figure 4.28) provides the first reflection imaging using natural moonquakes. We find relatively higher-amplitude arrivals characterized by lateral coherency at depths of  $\approx 50$  km. This zone is generally characterized by a weak triple peaks/trough feature and is about 10 km thick (the transparent brown rectangle in Figure 4.28). We interpret this characteristic feature at 50 km depth as the reflection from the lunar Moho

beneath our stations with an uncertainty of  $\pm 8$  km. This agrees with the interpretation from Khan *et al.* [119] and Ishihara *et al.* [120] and is close to the results reported by Nakamura [105] and from the deepest level of the Moho as interpreted from the GRAIL data. Our results may be useful to constrain velocity modeling such as Wieczorek *et al.* [121] at the four Apollo stations.

Below 58 km, waveforms exhibit generally incoherent features, suggesting laterally heterogeneous structure. In previous studies, Dainty *et al.* [125], Nakamura *et al.* [126], and Goins *et al.* [104] suggested that the seismic attenuation in the upper mantle is very low ( $Q = 3000\text{--}5000$ ). This is consistent with the very long codas exhibited by moonquakes. The weak suggestion of a consistent horizontal feature in Figure 4.28 at a depth of roughly 100–120 km (the pink bars) combined with the lack of pronounced lateral coherency in the deeper part of our image suggests the presence of a strong scattering zone, consistent with previous studies that yield no clear velocity structure around this depth range [e.g. 104, 116] and the roughly uniform velocity at depth proposed by Weber *et al.* [106].

The average estimated hypocentral depth for the 28 shallow moonquakes is  $\sim 95$  km, (derived from [97]). Depths of the shallow moonquakes near the Apollo stations vary from about 100 km to 129 km that is within the heterogeneous zone observed in our analysis. The lack of observed structure in the source region might point to the assertions that these events do not arise from any lunar tectonic process, but rather may be the result of tidal stresses [e.g. 122–124]. If more stations and/or arrays are deployed, however, one might be able to interpret structures at these depths in the region of the Apollo stations. We therefore cannot exclude the possibility that these events are tectonic in nature [146].

DMSI may also be applied for imaging structures under future seismic deployments on the Farside of the Moon if stations are optimally located with respect to seismicity. It might be feasible to use deep moonquakes from the Nearside, assuming adequate SNR after phase propagation to the Farside. Ray parameters in this case should be sufficiently small at the Farside stations to allow application of the traditional SI using directly transmitted P-wave phases and their reverberations (equation 4.8). DMSI using the Nearside deep moonquakes may likewise be feasible.

## REFERENCES

- [1] Y. Nishitsuji, E. Ruigrok, M. Gomez, K. Wapenaar, and D. Draganov, *Reflection imaging of aseismic zones of the Nazca slab by global-phase seismic interferometry*, *Interpretation* **4** (2016), 10.1190/INT-2015-0225.1.
- [2] Y. Nishitsuji and J. Mori, *Source parameters and radiation efficiency for intermediate-depth earthquakes in Northeast Japan*, *Geophysical Journal International* **196** (2014), 10.1093/gji/ggt458.
- [3] Y. Nishitsuji, C. A. Rowe, K. Wapenaar, and D. Draganov, *Reflection imaging of the Moon's interior using deep-moonquake seismic interferometry*, *Journal of Geophysical Research: Planets* **121** (2016), 10.1002/2015JE004975.
- [4] G. Rosenbaum, D. Giles, M. Saxon, P. G. Betts, R. F. Weinberg, and C. Duboz,

- Subduction of the Nazca Ridge and the Inca Plateau: Insights into the formation of ore deposits in Peru*, *Earth and Planetary Science Letters* **239** (2005), [10.1016/j.epsl.2005.08.003](https://doi.org/10.1016/j.epsl.2005.08.003).
- [5] M. Anderson, P. Alvarado, G. Zandt, and S. Beck, *Geometry and brittle deformation of the subducting Nazca Plate, Central Chile and Argentina*, *Geophysical Journal International* **171** (2007), [10.1111/j.1365-246X.2007.03483.x](https://doi.org/10.1111/j.1365-246X.2007.03483.x).
- [6] C. M. Eakin, M. D. Long, S. L. Beck, L. S. Wagner, H. Tavera, and C. Condori, *Response of the mantle to flat slab evolution: Insights from local S splitting beneath Peru*, *Geophysical Research Letters* **41** (2014), [10.1002/2014GL059943](https://doi.org/10.1002/2014GL059943).
- [7] J. R. Booker, A. Favetto, and M. C. Pomposiello, *Low electrical resistivity associated with plunging of the Nazca flat slab beneath Argentina*, *Nature* **429** (2004), [10.1038/nature02573.1](https://doi.org/10.1038/nature02573.1).
- [8] H. Gilbert, S. Beck, and G. Zandt, *Lithospheric and upper mantle structure of central Chile and Argentina*, *Geophysical Journal International* **165** (2006), [10.1111/j.1365-246X.2006.02867.x](https://doi.org/10.1111/j.1365-246X.2006.02867.x).
- [9] J. D. Pesicek, E. R. Engdahl, C. H. Thurber, H. R. DeShon, and D. Lange, *Mantle subducting slab structure in the region of the 2010 M8.8 Maule earthquake (30-40°S), Chile*, *Geophysical Journal International* **191** (2012), [10.1111/j.1365-246X.2012.05624.x](https://doi.org/10.1111/j.1365-246X.2012.05624.x).
- [10] T. Cahill and B. L. Isacks, *Seismicity and shape of the subducted Nazca Plate*, *Journal of Geophysical Research: Solid Earth* **97** (1992), [10.1029/92JB00493](https://doi.org/10.1029/92JB00493).
- [11] E. M. Syracuse and G. A. Abers, *Systematic biases in subduction zone hypocenters*, *Geophysical Research Letters* **36** (2009), [10.1029/2009GL037487](https://doi.org/10.1029/2009GL037487).
- [12] W. Bloch, J. Kummerow, P. Salazar, P. Wigger, and S. A. Shapiro, *High-resolution image of the North Chilean subduction zone: Seismicity, reflectivity and fluids*, *Geophysical Journal International* **197** (2014), [10.1093/gji/ggu084](https://doi.org/10.1093/gji/ggu084).
- [13] C. A. Langston, *Structure under Mount Rainier, Washington, inferred from teleseismic body waves*, *Journal of Geophysical Research: Solid Earth* **84** (1979), [10.1029/JB084iB09p04749](https://doi.org/10.1029/JB084iB09p04749).
- [14] P. Audet, M. G. Bostock, N. I. Christensen, and S. M. Peacock, *Seismic evidence for overpressured subducted oceanic crust and megathrust fault sealing*, *Nature* **457** (2009), [10.1038/nature07650](https://doi.org/10.1038/nature07650).
- [15] H. Kawakatsu and S. Yoshioka, *Metastable olivine wedge and deep dry cold slab beneath southwest Japan*, *Earth and Planetary Science Letters* **303** (2011), [10.1016/j.epsl.2011.01.008](https://doi.org/10.1016/j.epsl.2011.01.008).
- [16] X. Yuan, S. V. Sobolev, R. Kind, O. Oncken, G. Bock, G. Asch, B. Schurr, F. Graeber, A. Rudloff, W. Hanka, K. Wylegalla, R. Tibi, C. Haberland, A. Rietbrock, P. Giese,



- P. Wigger, P. Röwer, G. Zandt, S. Beck, T. Wallace, M. Pardo, and D. Comte, *Subduction and collision processes in the Central Andes constrained by converted seismic phases*, *Nature* **408** (2000), [10.1038/35050073](https://doi.org/10.1038/35050073).
- [17] K. Aki, A. Christofferson, and E. S. Husebye, *Determination of the three-dimensional seismic structure of the lithosphere*, *Journal of Geophysical Research* **82** (1977), [10.1029/JB082i002p00277](https://doi.org/10.1029/JB082i002p00277).
- [18] A. M. Dziewonski, B. H. Hager, and R. J. O'Connell, *Large-scale heterogeneities in the lower mantle*, *Journal of Geophysical Research* **82** (1977), [10.1029/JB082i002p00239](https://doi.org/10.1029/JB082i002p00239).
- [19] L. Boschi and T. W. Becker, *Vertical coherence in mantle heterogeneity from global seismic data*, *Geophysical Research Letters* **38** (2011), [10.1029/2011GL049281](https://doi.org/10.1029/2011GL049281).
- [20] J. F. Claerbout, *Synthesis of a layered medium from its acoustic transmission response*, *Geophysics* **33** (1968), [10.1190/1.1439927](https://doi.org/10.1190/1.1439927).
- [21] F. Scherbaum, *Seismic imaging of the site response using microearthquake recordings. Part II. Application to the Swabian Jura southwest Germany, Seismic network*, *Bulletin of the Seismological Society of America* **77** (1987).
- [22] F. Scherbaum, *Seismic imaging of the site response using microearthquake recordings. Part I. Method*, *Bulletin of the Seismological Society of America* **77** (1987).
- [23] M. R. Daneshvar, C. S. Clay, and M. K. Savage, *Passive seismic imaging using microearthquakes*, *Geophysics* **60** (1995), [10.1190/1.1443846](https://doi.org/10.1190/1.1443846).
- [24] K. Wapenaar, *Synthesis of an inhomogeneous medium from its acoustic transmission response*, *Geophysics* **68** (2003), [10.1190/1.1620649](https://doi.org/10.1190/1.1620649).
- [25] E. Ruigrok and K. Wapenaar, *Global-phase seismic interferometry unveils P-wave reflectivity below the Himalayas and Tibet*, *Geophysical Research Letters* **39** (2012), [10.1029/2012GL051672](https://doi.org/10.1029/2012GL051672).
- [26] M. R. Kumar and M. G. Bostock, *Transmission to reflection transformation of teleseismic wavefields*, *Journal of Geophysical Research: Solid Earth* **111** (2006), [10.1029/2005JB004104](https://doi.org/10.1029/2005JB004104).
- [27] R. L. Nowack, *Correlation migration using gaussian beams of scattered teleseismic body waves*, *Bulletin of the Seismological Society of America* **96** (2006), [10.1785/0120050036](https://doi.org/10.1785/0120050036).
- [28] M. J. R. Wortel, *Subduction and slab detachment in the Mediterranean-Carpathian region*, *Science* **290** (2000), [10.1126/science.290.5498.1910](https://doi.org/10.1126/science.290.5498.1910).
- [29] E. Ruigrok, X. Campman, D. Draganov, and K. Wapenaar, *High-resolution lithospheric imaging with seismic interferometry*, *Geophysical Journal International* **183** (2010), [10.1111/j.1365-246X.2010.04724.x](https://doi.org/10.1111/j.1365-246X.2010.04724.x).

- [30] Ö. Yilmaz, *Seismic data analysis* (Society of Exploration Geophysicists, 1987).
- [31] S. Abe, E. Kurashimo, H. Sato, N. Hirata, T. Iwasaki, and T. Kawanaka, *Interferometric seismic imaging of crustal structure using scattered teleseismic waves*, *Geophysical Research Letters* **34** (2007), [10.1029/2007GL030633](https://doi.org/10.1029/2007GL030633).
- [32] A. I. Burd, J. R. Booker, R. Mackie, A. Favetto, and M. C. Pomposiello, *Three-dimensional electrical conductivity in the mantle beneath the Payun Matru Volcanic Field in the Andean backarc of Argentina near 36.5 S: Evidence for decapitation of a mantle plume by resurgent upper mantle shear during slab steepening*, *Geophysical Journal International* **198** (2014), [10.1093/gji/ggu145](https://doi.org/10.1093/gji/ggu145).
- [33] J. J. Becker, D. T. Sandwell, W. H. F. Smith, J. Braud, B. Binder, J. Depner, D. Fabre, J. Factor, S. Ingalls, S.-H. Kim, R. Ladner, K. Marks, S. Nelson, A. Pharaoh, R. Trimmer, J. Von Rosenberg, G. Wallace, and P. Weatherall, *Global bathymetry and elevation data at 30 arc seconds resolution: SRTM30\_PLUS*, *Marine Geodesy* **32** (2009), [10.1080/01490410903297766](https://doi.org/10.1080/01490410903297766).
- [34] B. L. N. Kennett, E. R. Engdahl, and R. Buland, *Constraints on seismic velocities in the Earth from traveltimes*, *Geophysical Journal International* **122** (1995), [10.1111/j.1365-246X.1995.tb03540.x](https://doi.org/10.1111/j.1365-246X.1995.tb03540.x).
- [35] Y. Nishitsuji, E. Ruigrok, M. Gomez, and D. Draganov, *Global-phase HIV spectral ratio for delineating the basin in the Malargue region, Argentina*, *Seismological Research Letters* **85** (2014), [10.1785/0220140054](https://doi.org/10.1785/0220140054).
- [36] R. D. Adams and M. J. Randall, *Observed triplication of PKP*, *Nature* **200** (1963), [10.1038/200744a0](https://doi.org/10.1038/200744a0).
- [37] R. Garcia, S. Chevrot, and M. Weber, *Nonlinear waveform and delay time analysis of triplicated core phases*, *Journal of Geophysical Research: Solid Earth* **109** (2004), [10.1029/2003JB002429](https://doi.org/10.1029/2003JB002429).
- [38] R. Snieder, *Extracting the Green's function from the correlation of coda waves: A derivation based on stationary phase*, *Physical Review E* **69** (2004), [10.1103/PhysRevE.69.046610](https://doi.org/10.1103/PhysRevE.69.046610).
- [39] D. Draganov, K. Wapenaar, and J. Thorbecke, *Passive seismic imaging in the presence of white noise sources*, *The Leading Edge* **23** (2004), [10.1190/1.1803498](https://doi.org/10.1190/1.1803498).
- [40] D. Draganov, K. Wapenaar, and J. Thorbecke, *Seismic interferometry: Reconstructing the earth's reflection response*, *Geophysics* **71** (2006), [10.1190/1.2209947](https://doi.org/10.1190/1.2209947).
- [41] R. F. Hansen, *Multiple reflections of seismic energy*, *Geophysics* **13** (1948), [10.1190/1.1437377](https://doi.org/10.1190/1.1437377).
- [42] E. Moscoso, I. Grevemeyer, E. Contreras-Reyes, E. R. Flueh, Y. Dzierma, W. Rabbell, and M. Thorwart, *Revealing the deep structure and rupture plane of the 2010 Maule, Chile earthquake (Mw=8.8) using wide angle seismic data*, *Earth and Planetary Science Letters* **307** (2011), [10.1016/j.epsl.2011.04.025](https://doi.org/10.1016/j.epsl.2011.04.025).

- [43] D. Garcia, *Robust smoothing of gridded data in one and higher dimensions with missing values*, *Computational Statistics & Data Analysis* **54** (2010), [10.1016/j.csda.2009.09.020](https://doi.org/10.1016/j.csda.2009.09.020).
- [44] A. Dannowski, I. Grevemeyer, H. Kraft, I. Arroyo, and M. Thorwart, *Crustal thickness and mantle wedge structure from receiver functions in the Chilean Maule region at 35°S*, *Tectonophysics* **592** (2013), [10.1016/j.tecto.2013.02.015](https://doi.org/10.1016/j.tecto.2013.02.015).
- [45] H. Kanamori and E. E. Brodsky, *The physics of earthquakes*, *Reports on Progress in Physics* **67** (2004), [10.1088/0034-4885/67/8/R03](https://doi.org/10.1088/0034-4885/67/8/R03).
- [46] M. Bohm, S. Lüth, H. Echtler, G. Asch, K. Bataille, C. Bruhn, A. Rietbrock, and P. Wigger, *The Southern Andes between 36° and 40°S latitude: Seismicity and average seismic velocities*, *Tectonophysics* **356** (2002), [10.1016/S0040-1951\(02\)00399-2](https://doi.org/10.1016/S0040-1951(02)00399-2).
- [47] M. Reguzzoni, D. Sampietro, and F. Sanso, *Global Moho from the combination of the CRUST2.0 model and GOCE data*, *Geophysical Journal International* **195** (2013), [10.1093/gji/ggt247](https://doi.org/10.1093/gji/ggt247).
- [48] J. G. Frank, E. N. Ruigrok, and K. Wapenaar, *Shear wave seismic interferometry for lithospheric imaging: Application to southern Mexico*, *Journal of Geophysical Research: Solid Earth* **119** (2014), [10.1002/2013JB010692](https://doi.org/10.1002/2013JB010692).
- [49] G. Jacques, K. Hoernle, J. Gill, F. Hauff, H. Wehrmann, D. Garbe-Schönberg, P. van den Bogaard, I. Bindeman, and L. Lara, *Across-arc geochemical variations in the Southern Volcanic Zone, Chile (34.5–38.0°S): Constraints on mantle wedge and slab input compositions*, *Geochimica et Cosmochimica Acta* **123** (2013), [10.1016/j.gca.2013.05.016](https://doi.org/10.1016/j.gca.2013.05.016).
- [50] H. Kanamori, J. Mori, E. Hauksson, T. H. Heaton, L. Katherine, and L. M. Jones, *Determination of earthquake energy release and ML using TERRAscope*, *Bulletin of the Seismological Society of America* **83** (1993).
- [51] R. E. Abercrombie, *Earthquake source scaling relationships from -1 to 5 ML using seismograms recorded at 2.5-km depth*, *Journal of Geophysical Research: Solid Earth* **100** (1995), [10.1029/95JB02397](https://doi.org/10.1029/95JB02397).
- [52] K. Mayeda and W. R. Walter, *Moment, energy, stress drop, and source spectra of western United States earthquakes from regional coda envelopes*, *Journal of Geophysical Research: Solid Earth* **101** (1996), [10.1029/96JB00112](https://doi.org/10.1029/96JB00112).
- [53] Y. Izutani and H. Kanamori, *Scale-dependence of seismic energy-to-moment ratio for strike-slip earthquakes in Japan*, *Geophysical Research Letters* **28** (2001), [10.1029/2001GL013402](https://doi.org/10.1029/2001GL013402).
- [54] J. Mori, *Stress drops and radiated energies of aftershocks of the 1994 Northridge, California, earthquake*, *Journal of Geophysical Research: Solid Earth* **108** (2003), [10.1029/2001JB000474](https://doi.org/10.1029/2001JB000474).

- [55] K. Mayeda, *Evidence for non-constant energy/moment scaling from coda-derived source spectra*, *Geophysical Research Letters* **32** (2005), 10.1029/2005GL022405.
- [56] K. Mayeda, L. Malagnini, and W. R. Walter, *A new spectral ratio method using narrow band coda envelopes: Evidence for non-self-similarity in the Hector Mine sequence*, *Geophysical Research Letters* **34** (2007), 10.1029/2007GL030041.
- [57] T. Takahashi, *Scale dependence of apparent stress for earthquakes along the subducting Pacific plate in Northeastern Honshu, Japan*, *Bulletin of the Seismological Society of America* **95** (2005), 10.1785/0120040075.
- [58] L. Malagnini, L. Scognamiglio, A. Mercuri, A. Akinci, and K. Mayeda, *Strong evidence for non-similar earthquake source scaling in central Italy*, *Geophysical Research Letters* **35** (2008), 10.1029/2008GL034310.
- [59] G. L. Choy and J. L. Boatwright, *Global patterns of radiated seismic energy and apparent stress*, *Journal of Geophysical Research: Solid Earth* **100** (1995), 10.1029/95JB01969.
- [60] A. McGarr, *On relating apparent stress to the stress causing earthquake fault slip*, *Journal of Geophysical Research: Solid Earth* **104** (1999), 10.1029/1998JB900083.
- [61] S. Ide and G. C. Beroza, *Does apparent stress vary with earthquake size?* *Geophysical Research Letters* **28** (2001), 10.1029/2001GL013106.
- [62] S. Ide, G. C. Beroza, S. G. Prejean, and W. L. Ellsworth, *Apparent break in earthquake scaling due to path and site effects on deep borehole recordings*, *Journal of Geophysical Research: Solid Earth* **108** (2003), 10.1029/2001JB001617.
- [63] S. Ide, M. Matsubara, and K. Obara, *Exploitation of high-sampling Hi-net data to study seismic energy scaling: The aftershocks of the 2000 Western Tottori, Japan, earthquake*, *Earth, Planets and Space* **56** (2004), 10.1186/BF03352533.
- [64] G. A. Prieto, P. M. Shearer, F. L. Vernon, and D. Kilb, *Earthquake source scaling and self-similarity estimation from stacking P and S spectra*, *Journal of Geophysical Research: Solid Earth* **109** (2004), 10.1029/2004JB003084.
- [65] T. Yamada, J. J. Mori, S. Ide, H. Kawakata, Y. Iio, and O. Hiroshi, *Radiation efficiency and apparent stress of small earthquakes in a South African gold mine*, *Journal of Geophysical Research: Solid Earth* **110** (2005), 10.1029/2004JB003221.
- [66] T. Yamada, J. J. Mori, S. Ide, R. E. Abercrombie, H. Kawakata, M. Nakatani, Y. Iio, and H. Ogasawara, *Stress drops and radiated seismic energies of microearthquakes in a South African gold mine*, *Journal of Geophysical Research: Solid Earth* **112** (2007), 10.1029/2006JB004553.
- [67] A. Baltay, G. Prieto, and G. C. Beroza, *Radiated seismic energy from coda measurements and no scaling in apparent stress with seismic moment*, *Journal of Geophysical Research: Solid Earth* **115** (2010), 10.1029/2009JB006736.

- [68] A. Baltay, S. Ide, G. Prieto, and G. Beroza, *Variability in earthquake stress drop and apparent stress*, *Geophysical Research Letters* **38** (2011), [10.1029/2011GL046698](https://doi.org/10.1029/2011GL046698).
- [69] R. E. Abercrombie and J. R. Rice, *Can observations of earthquake scaling constrain slip weakening?* *Geophysical Journal International* **162** (2005), [10.1111/j.1365-246X.2005.02579.x](https://doi.org/10.1111/j.1365-246X.2005.02579.x).
- [70] H. Kanamori and T. H. Heaton, *Microscopic and macroscopic physics of earthquakes*, in *GeoComplexity and Physics of Earthquakes* (American Geophysical Union, 2000).
- [71] A. Venkataraman and H. Kanamori, *Observational constraints on the fracture energy of subduction zone earthquakes*, *Journal of Geophysical Research: Solid Earth* **109** (2004), [10.1029/2003JB002549](https://doi.org/10.1029/2003JB002549).
- [72] J. N. Brune, *Tectonic stress and the spectra of seismic shear waves from earthquakes*, *Journal of Geophysical Research* **75** (1970), [10.1029/JB075i026p04997](https://doi.org/10.1029/JB075i026p04997).
- [73] P. Molnar, B. E. Tucker, and J. N. Brune, *Corner frequencies of P and S waves and models of earthquake sources*, *Bulletin of the Seismological Society of America* **63** (1973).
- [74] R. Madariaga, *Dynamics of an expanding circular fault*, *Bulletin of the Seismological Society of America* **66** (1976).
- [75] J. D. Eshelby, *The determination of the elastic field of an ellipsoidal inclusion, and related problems*, *Proceedings of the Royal Society A: Mathematical, Physical and Engineering Sciences* **241** (1957), [10.1098/rspa.1957.0133](https://doi.org/10.1098/rspa.1957.0133).
- [76] T. Matsuzawa, N. Umino, A. Hasegawa, and A. Takagi, *Upper mantle velocity structure estimated from PS-converted wave beneath the north-eastern Japan Arc*, *Geophysical Journal International* **86** (1986), [10.1111/j.1365-246X.1986.tb00659.x](https://doi.org/10.1111/j.1365-246X.1986.tb00659.x).
- [77] J. Boatwright and J. B. Fletcher, *The partition of radiated energy between P and S waves*, *Bulletin of the Seismological Society of America* **74** (1984).
- [78] M. I. Hussein, *Energy balance for motion along a fault*, *Geophysical Journal International* **49** (1977), [10.1111/j.1365-246X.1977.tb01313.x](https://doi.org/10.1111/j.1365-246X.1977.tb01313.x).
- [79] P. F. Ihmlé, *Monte Carlo slip inversion in the frequency domain: Application to the 1992 Nicaragua Slow Earthquake*, *Geophysical Research Letters* **23** (1996), [10.1029/96GL00872](https://doi.org/10.1029/96GL00872).
- [80] Y. Ida, *Cohesive force across the tip of a longitudinal-shear crack and Griffith's specific surface energy*, *Journal of Geophysical Research* **77** (1972), [10.1029/JB077i020p03796](https://doi.org/10.1029/JB077i020p03796).
- [81] A. C. Palmer and J. R. Rice, *The growth of slip surfaces in the progressive failure of over-consolidated clay*, *Proceedings of the Royal Society A: Mathematical, Physical and Engineering Sciences* **332** (1973), [10.1098/rspa.1973.0040](https://doi.org/10.1098/rspa.1973.0040).

- [82] V. Li, *Mechanics of shear rupture applied to earthquake zones* (Academic Press, 1989).
- [83] H. Kanamori and L. Rivera, *Energy Partitioning During an Earthquake, in Earthquakes: Radiated Energy and the Physics of Faulting* (American Geophysical Union, 2006).
- [84] E. Orowan, *Chapter 12: Mechanism of Seismic Faulting*, in *Memoirs Rock Deformation* (Geological Society of America, 1960).
- [85] M. Kikuchi and Y. Fukao, *Seismic wave energy inferred from long-period body wave inversion*, *Bulletin of the Seismological Society of America* **78** (1988).
- [86] C. Frohlich, *Deep Earthquakes* (Cambridge Univ. Press, 2006).
- [87] M. Wyss and J. N. Brune, *Seismic moment, stress, and source dimensions for earthquakes in the California-Nevada region*, *Journal of Geophysical Research* **73** (1968), [10.1029/JB073i014p04681](https://doi.org/10.1029/JB073i014p04681).
- [88] A. Venkataraman, G. C. Beroza, S. Ide, K. Imanishi, H. Ito, and Y. Iio, *Measurements of spectral similarity for microearthquakes in western Nagano, Japan*, *Journal of Geophysical Research: Solid Earth* **111** (2006), [10.1029/2005JB003834](https://doi.org/10.1029/2005JB003834).
- [89] N. W. Winslow and L. J. Ruff, *A hybrid method for calculating the radiated wave energy of deep earthquakes*, *Physics of the Earth and Planetary Interiors* **115** (1999), [10.1016/S0031-9201\(99\)00077-1](https://doi.org/10.1016/S0031-9201(99)00077-1).
- [90] J. C. Savage and M. D. Wood, *The relationship between apparent stress and stress drop*, *Bulletin of the Seismological Society of America* **61** (1971).
- [91] N. M. Beeler, *On the expected relationships among apparent stress, static stress drop, effective shear fracture energy, and efficiency*, *Bulletin of the Seismological Society of America* **93** (2003), [10.1785/0120020162](https://doi.org/10.1785/0120020162).
- [92] W.-Y. Chung and H. Kanamori, *Variation of seismic source parameters and stress drops within a descending slab and its implications in plate mechanics*, *Physics of the Earth and Planetary Interiors* **23** (1980), [10.1016/0031-9201\(80\)90008-4](https://doi.org/10.1016/0031-9201(80)90008-4).
- [93] H. Houston and Q. Williams, *Fast rise times and the physical mechanism of deep earthquakes*, *Nature* **352** (1991), [10.1038/352520a0](https://doi.org/10.1038/352520a0).
- [94] T. Iwata and K. Asano, *Characterization of the heterogeneous source model of intraslab earthquakes toward strong ground motion prediction*, *Pure and Applied Geophysics* **168** (2011), [10.1007/s00024-010-0128-7](https://doi.org/10.1007/s00024-010-0128-7).
- [95] N. R. Goins, *Lunar seismology: The internal structure of the moon*, Ph.D. thesis, Massachusetts Institute of Technology (1978).

- [96] P. Horvath, G. V. Latham, Y. Nakamura, and H. J. Dorman, *Lunar near-surface shear wave velocities at the Apollo Landing Sites as inferred from spectral amplitude ratios*, *Journal of Geophysical Research: Solid Earth* **85** (1980), [10.1029/JB085iB11p06572](https://doi.org/10.1029/JB085iB11p06572).
- [97] Y. Nakamura, G. V. Latham, H. J. Dorman, and J. E. Harris, *Passive seismic experiment long-period event catalog*, Tech. Rep. (University of Texas Institute for Geophysics, Galveston, 1981).
- [98] Y. Nakamura, G. V. Latham, and H. J. Dorman, *Apollo Lunar Seismic Experiment—Final summary*, *Journal of Geophysical Research: Solid Earth* **87** (1982), [10.1029/JB087iS01p0A117](https://doi.org/10.1029/JB087iS01p0A117).
- [99] W. B. Chapman, B. M. Middlehurst, and A. Frisillo, *Moonquake predetermination and tides*, *Icarus* **21** (1974), [10.1016/0019-1035\(74\)90145-6](https://doi.org/10.1016/0019-1035(74)90145-6).
- [100] R. C. Bulow, C. L. Johnson, and P. M. Shearer, *New events discovered in the Apollo lunar seismic data*, *Journal of Geophysical Research: Planets* **110** (2005), [10.1029/2005JE002414](https://doi.org/10.1029/2005JE002414).
- [101] R. C. Bulow, C. L. Johnson, B. G. Bills, and P. M. Shearer, *Temporal and spatial properties of some deep moonquake clusters*, *Journal of Geophysical Research: Planets* **112** (2007), [10.1029/2006JE002847](https://doi.org/10.1029/2006JE002847).
- [102] A. Khan, A. Pommier, G. Neumann, and K. Mosegaard, *The lunar moho and the internal structure of the Moon: A geophysical perspective*, *Tectonophysics* **609** (2013), [10.1016/j.tecto.2013.02.024](https://doi.org/10.1016/j.tecto.2013.02.024).
- [103] M. N. Toksöz, A. M. Dainty, S. C. Solomon, and K. R. Anderson, *Structure of the Moon*, *Reviews of Geophysics* **12** (1974), [10.1029/RG012i004p00539](https://doi.org/10.1029/RG012i004p00539).
- [104] N. R. Goins, A. M. Dainty, and M. N. Toksöz, *Lunar seismology: The internal structure of the Moon*, *Journal of Geophysical Research: Solid Earth* **86** (1981), [10.1029/JB086iB06p05061](https://doi.org/10.1029/JB086iB06p05061).
- [105] Y. Nakamura, *Seismic velocity structure of the lunar mantle*, *Journal of Geophysical Research: Solid Earth* **88** (1983), [10.1029/JB088iB01p00677](https://doi.org/10.1029/JB088iB01p00677).
- [106] R. C. Weber, P.-Y. Lin, E. J. Garnero, Q. Williams, and P. Lognonne, *Seismic detection of the lunar core*, *Science* **331** (2011), [10.1126/science.1199375](https://doi.org/10.1126/science.1199375).
- [107] L. Vinnik, H. Chenet, J. Gagnepain-Beyneix, and P. Lognonne, *First seismic receiver functions on the Moon*, *Geophysical Research Letters* **28** (2001), [10.1029/2001GL012859](https://doi.org/10.1029/2001GL012859).
- [108] D. Zhao, J. Lei, and L. Liu, *Seismic tomography of the Moon*, *Chinese Science Bulletin* **53** (2008), [10.1007/s11434-008-0484-1](https://doi.org/10.1007/s11434-008-0484-1).
- [109] E. Larose, A. Khan, Y. Nakamura, and M. Campillo, *Lunar subsurface investigated from correlation of seismic noise*, *Geophysical Research Letters* **32** (2005), [10.1029/2005GL023518](https://doi.org/10.1029/2005GL023518).

- [110] T. Tanimoto, M. Eitzel, and T. Yano, *The noise cross-correlation approach for Apollo 17 LSPE data: Diurnal change in seismic parameters in shallow lunar crust*, *Journal of Geophysical Research: Planets* **113** (2008), 10.1029/2007JE003016.
- [111] C. Sens-Schönfelder and E. Larose, *Lunar noise correlation, imaging and monitoring*, *Earthquake Science* **23** (2010), 10.1007/s11589-010-0750-6.
- [112] A. Obermann, T. Planes, E. Larose, C. Sens-Schönfelder, and M. Campillo, *Depth sensitivity of seismic coda waves to velocity perturbations in an elastic heterogeneous medium*, *Geophysical Journal International* **194** (2013), 10.1093/gji/ggt043.
- [113] K. Wapenaar, J. van der Neut, and E. Ruigrok, *Passive seismic interferometry by multidimensional deconvolution*, *Geophysics* **73** (2008), 10.1190/1.2976118.
- [114] G. T. Schuster, *Seismic interferometry* (Cambridge Univ. Press, 2009).
- [115] M. N. Toksöz, F. Press, K. Anderson, A. Dainty, G. Latham, M. Ewing, J. Dorman, D. Lammlein, G. Sutton, F. Duennebier, and Y. Nakamura, *Lunar crust: Structure and composition*, *Science* **176** (1972), 10.1126/science.176.4038.1012.
- [116] M. N. Toksöz, *Geophysical Data and the Interior of the Moon*, *Annual Review of Earth and Planetary Sciences* **2** (1974), 10.1146/annurev.ea.02.050174.001055.
- [117] H. Chenet, P. Lognonne, M. Wieczorek, and H. Mizutani, *Lateral variations of lunar crustal thickness from the Apollo seismic data set*, *Earth and Planetary Science Letters* **243** (2006), 10.1016/j.epsl.2005.12.017.
- [118] P. Lognonné, J. Gagnepain-Beyneix, and H. Chenet, *A new seismic model of the Moon: Implications for structure, thermal evolution and formation of the Moon*, *Earth and Planetary Science Letters* **211** (2003), 10.1016/S0012-821X(03)00172-9.
- [119] A. Khan, K. Mosegaard, and K. L. Rasmussen, *A new seismic velocity model for the Moon from a Monte Carlo inversion of the Apollo lunar seismic data*, *Geophysical Research Letters* **27** (2000), 10.1029/1999GL008452.
- [120] Y. Ishihara, S. Goossens, K. Matsumoto, H. Noda, H. Araki, N. Namiki, H. Hanada, T. Iwata, S. Tazawa, and S. Sasaki, *Crustal thickness of the Moon: Implications for farside basin structures*, *Geophysical Research Letters* **36** (2009), 10.1029/2009GL039708.
- [121] M. A. Wieczorek, G. A. Neumann, F. Nimmo, W. S. Kiefer, G. J. Taylor, H. J. Melosh, R. J. Phillips, S. C. Solomon, J. C. Andrews-Hanna, S. W. Asmar, A. S. Konopliv, F. G. Lemoine, D. E. Smith, M. M. Watkins, J. G. Williams, and M. T. Zuber, *The crust of the moon as seen by GRAIL*, *Science* **339** (2013), 10.1126/science.1231530.
- [122] M. N. Toksöz, N. R. Goins, and C. H. Cheng, *Moonquakes: Mechanisms and relation to tidal stresses*, *Science* **196** (1977), 10.1126/science.196.4293.979.
- [123] C. Frohlich and Y. Nakamura, *The physical mechanisms of deep moonquakes and intermediate-depth earthquakes: How similar and how different?* *Physics of the Earth and Planetary Interiors* **173** (2009), 10.1016/j.pepi.2009.02.004.



- [124] R. C. Weber, B. G. Bills, and C. L. Johnson, *Constraints on deep moonquake focal mechanisms through analyses of tidal stress*, *Journal of Geophysical Research: Planets* **114** (2009), [10.1029/2008JE003286](https://doi.org/10.1029/2008JE003286).
- [125] A. M. Dainty, M. N. Toksöz, K. R. Anderson, P. J. Pines, Y. Nakamura, and G. Latham, *Seismic scattering and shallow structure of the moon in oceanus procellarum*, *The Moon* **9** (1974), [10.1007/BF00565388](https://doi.org/10.1007/BF00565388).
- [126] Y. Nakamura, F. K. Duennebieber, G. V. Latham, and H. J. Dorman, *Structure of the lunar mantle*, *Journal of Geophysical Research* **81** (1976), [10.1029/JB081i026p04818](https://doi.org/10.1029/JB081i026p04818).
- [127] J. Besserer, F. Nimmo, M. A. Wiczeorek, R. C. Weber, W. S. Kiefer, P. J. McGovern, J. C. Andrews-Hanna, D. E. Smith, and M. T. Zuber, *GRAIL gravity constraints on the vertical and lateral density structure of the lunar crust*, *Geophysical Research Letters* **41** (2014), [10.1002/2014GL060240](https://doi.org/10.1002/2014GL060240).
- [128] Y. Nakamura, *Farside deep moonquakes and deep interior of the Moon*, *Journal of Geophysical Research: Planets* **110** (2005), [10.1029/2004JE002332](https://doi.org/10.1029/2004JE002332).
- [129] H. Araki, S. Tazawa, H. Noda, Y. Ishihara, S. Goossens, S. Sasaki, N. Kawano, I. Kamiya, H. Otake, J. Oberst, and C. Shum, *Lunar global shape and polar topography derived from Kaguya-LALT laser altimetry*, *Science* **323** (2009), [10.1126/science.1164146](https://doi.org/10.1126/science.1164146).
- [130] T. Yokoi and S. Margaryan, *Consistency of the spatial autocorrelation method with seismic interferometry and its consequence*, *Geophysical Prospecting* **56** (2008), [10.1111/j.1365-2478.2008.00709.x](https://doi.org/10.1111/j.1365-2478.2008.00709.x).
- [131] K. Aki, *Space and time spectra of stationary stochastic waves, with special reference to microtremors*, *Bulletin of the Earthquake Research Institute* **35** (1957).
- [132] K. Wapenaar, *Retrieving the elastodynamic Green's function of an arbitrary inhomogeneous medium by cross correlation*, *Physical Review Letters* **93** (2004), [10.1103/PhysRevLett.93.254301](https://doi.org/10.1103/PhysRevLett.93.254301).
- [133] G. T. Schuster, J. Yu, J. Sheng, and J. Rickett, *Interferometric/daylight seismic imaging*, *Geophysical Journal International* **157** (2004), [10.1111/j.1365-246X.2004.02251.x](https://doi.org/10.1111/j.1365-246X.2004.02251.x).
- [134] W. P. Kimman and J. Trampert, *Approximations in seismic interferometry and their effects on surface waves*, *Geophysical Journal International* **182** (2010), [10.1111/j.1365-246X.2010.04632.x](https://doi.org/10.1111/j.1365-246X.2010.04632.x).
- [135] D. Draganov, R. Ghose, E. Ruigrok, J. Thorbecke, and K. Wapenaar, *Seismic interferometry, intrinsic losses and Q-estimation*, *Geophysical Prospecting* **58** (2010), [10.1111/j.1365-2478.2009.00828.x](https://doi.org/10.1111/j.1365-2478.2009.00828.x).
- [136] G. Latham, M. Ewing, F. Press, and G. Sutton, *The Apollo passive seismic experiment*, *Science* **165** (1969), [10.1126/science.165.3890.241](https://doi.org/10.1126/science.165.3890.241).

- [137] J.-F. Blanchette-Guertin, C. L. Johnson, and J. F. Lawrence, *Investigation of scattering in lunar seismic coda*, *Journal of Geophysical Research: Planets* **117** (2012), [10.1029/2011JE004042](https://doi.org/10.1029/2011JE004042).
- [138] A. Derode, A. Tourin, and M. Fink, *Ultrasonic pulse compression with one-bit time reversal through multiple scattering*, *Journal of Applied Physics* **85** (1999), [10.1063/1.370136](https://doi.org/10.1063/1.370136).
- [139] G. Montaldo, P. Roux, A. Derode, C. Negreira, and M. Fink, *Ultrasound shock wave generator with one-bit time reversal in a dispersive medium, application to lithotripsy*, *Applied Physics Letters* **80** (2002), [10.1063/1.1446996](https://doi.org/10.1063/1.1446996).
- [140] E. Larose, A. Derode, M. Campillo, and M. Fink, *Imaging from one-bit correlations of wideband diffuse wave fields*, *Journal of Applied Physics* **95** (2004), [10.1063/1.1739529](https://doi.org/10.1063/1.1739529).
- [141] T. C. Hanks and D. M. Boore, *Moment-magnitude relations in theory and practice*, *Journal of Geophysical Research: Solid Earth* **89** (1984), [10.1029/JB089iB07p06229](https://doi.org/10.1029/JB089iB07p06229).
- [142] D. R. Lammlein, *Lunar seismicity and tectonics*, *Physics of the Earth and Planetary Interiors* **14** (1977), [10.1016/0031-9201\(77\)90175-3](https://doi.org/10.1016/0031-9201(77)90175-3).
- [143] T. Minshull and N. Gouly, *The influence of tidal stresses on deep moonquake activity*, *Physics of the Earth and Planetary Interiors* **52** (1988), [10.1016/0031-9201\(88\)90056-8](https://doi.org/10.1016/0031-9201(88)90056-8).
- [144] M. R. Cooper, R. L. Kovach, and J. S. Watkins, *Lunar near-surface structure*, *Reviews of Geophysics* **12** (1974), [10.1029/RG012i003p00291](https://doi.org/10.1029/RG012i003p00291).
- [145] J. W. Thorbecke and D. Draganov, *Finite-difference modeling experiments for seismic interferometry*, *Geophysics* **76** (2011), [10.1190/geo2010-0039.1](https://doi.org/10.1190/geo2010-0039.1).
- [146] J. Oberst, *Unusually high stress drops associated with shallow moonquakes*, *Journal of Geophysical Research: Solid Earth* **92** (1987), [10.1029/JB092iB02p01397](https://doi.org/10.1029/JB092iB02p01397).



# 5

## GENERAL CONCLUSIONS

### 5.1. CONCLUSIONS

In this thesis, we have investigated the potential usage of several passive-seismic methods as cost-effective applications for multiscale subsurface imaging and characterization. The applications were carried out on data from the Earth and Moon. The application of a specific passive-seismic method was dictated by the specific problem and dataset at hand. Among the different methods, we particularly focused on approaches that retrieve reflection arrivals from the application of the seismic interferometry (SI) technique to body-wave recordings. The several passive-seismic methods we used were successful in imaging/characterization/interpretation of targets, ranging from the basin to the lithospheric scale.

In Chapter 2, we developed a method to delineate a basin depth by using the H/V spectral ratio applied to global phases of earthquakes. Using this method, we estimated the depth of a part of the Neuquén basin, Argentina. Our estimates showed a very good agreement with the results from an active-source seismic profile acquired in the past in the area and with the Bouguer gravity anomaly in this region. The method we presented here was not sensitive to the mix of global phases after suppressing source-side resonances and phase cross terms. In this chapter, we also proposed an application to image the subsurface heterogeneities using local earthquakes. In this application, we used Sp-waves and a frequency-dependent quality factor analysis,  $Q_S/Q_P$ , from the local earthquakes. We applied this method to data from one of the exploration and production blocks in Japan where past active-seismic profiles were available. Our interpretation showed a good agreement with the active-seismic profiles for possibly three major geological horizons. The applications in this chapter showed that the basin depth and the subsurface heterogeneities on the basin scale could be imaged/characterized using natural quakes without the need to conduct active-source shooting.

In Chapter 3, we proposed an SI method that uses P-wave coda of local earthquakes for reflection retrievals in order to image crustal-scale subsurface structures. We used field data recorded at a part of the Neuquén basin. The results retrieved using mul-

tidimensional deconvolution with a singular-value decomposition scheme allowed interpretation of the Moho and a major deep basement thrust fault. This suggests that our method has a possible application for crustal-scale imaging without active-source shooting for, e.g., deep geothermal exploration whose reservoirs can be down to a depth of 10 km.

In Chapter 4, we proposed to apply global-phase SI (GloPSI) for imaging the aseismic zones of the Nazca slab beneath the Neuquén basin. For GloPSI, we used global phases, such as PKP, PKiKP, and PKIKP, recorded on the vertical component of the seismic sensors. These phases illuminate the lithosphere below the receivers with small angles of incidence, which illumination suffices for retrieving virtual sources that radiate primarily downwards. Thus, we retrieved virtual zero-offset reflections. We then migrated the retrieved virtual zero-offset reflections to obtain a subsurface reflection image with high resolution ( $< 15$  km in depth). From our results beneath the Peteroa volcano, we interpreted packages of strong reflectivity with lack of reflectivity between them as a deformation in the dipping slab. Just to the east of the town of Malargüe, we further interpreted the aseismic part of the Nazca slab manifested in the image as a dimmed-reflectivity zone, the dimmed reflectivity due to the relation between the depth of the dipping reflectors and the relatively short length of the array we used (MalARRgüe). Based on our interpretation, we found that the aseismic part of the Nazca slab in this region is not tearing. In this chapter, we also applied an SI technique using body waves to data from the Moon. We used deep moonquakes recorded by the Apollo stations to retrieve zero-offset reflection responses beneath each seismic station on the nearside of the Moon. We called this application deep-moonquake seismic interferometry (DMSI). We presented the first pseudo-reflection imaging of the lunar Moho, which we interpreted to reside at around 50 km depth. Our interpretation agreed with JAXA's SELENE result, and with earlier travel-time studies. Our DMSI results also showed lateral inhomogeneity beneath the Moho, suggesting strong scattering within a zone characterized by seismic velocity that exhibits little variation at our resolution scale (0.2-2.0 Hz). The passive-seismic applications in this chapter suggest that lithospheric reflection imaging and characterization could be obtained from the natural quakes, i.e., without need for active-source shooting. This can be said not only for the Earth, but also for other celestial bodies if data with natural quakes are available for them. For instance, reflection imaging of the Mars body using possible marsquakes may be obtained after NASA's Mars InSight mission.

Based on our analysis, results, and interpretations, we propose to utilize the different passive-seismic methods, depending on the target and scale, as given in Table 5.1.

Table 5.1: Comparison of the passive seismic methods categorized by the target scale

		Target scale		
		Basin	Crust	Lithosphere
Passive seismic method	<b>Tomography</b>	E.g., Operto <i>et al.</i> [1]	E.g., Operto <i>et al.</i> [1]	E.g., Aki <i>et al.</i> [2]
	<b>Receiver-function method</b>	E.g., Ruigrok <i>et al.</i> [3]	E.g., Audet <i>et al.</i> [4]	E.g., Gilbert <i>et al.</i> [5]
	<b>H/V spectral ratio</b>	E.g., Ruigrok <i>et al.</i> [3] This thesis, chapter 2 [6]	N/A	N/A
	<b>Sp-wave method</b>	This thesis, chapter 2 [7]	Doi and Kawakata [8]	N/A
	<b>Seismic interferometry</b>	E.g., Draganov <i>et al.</i> [9]	E.g., Abe <i>et al.</i> [10] This thesis, chapter 3 [12]	E.g., Ruigrok and Wapenaar [11] This thesis, chapter 4 [13–15]

## REFERENCES

- [1] S. Operto, J. Virieux, J.-X. Dessa, and G. Pascal, *Crustal seismic imaging from multifold ocean bottom seismometer data by frequency domain full waveform tomography: Application to the eastern Nankai trough*, *Journal of Geophysical Research: Solid Earth* **111** (2006), [10.1029/2005JB003835](https://doi.org/10.1029/2005JB003835).
- [2] K. Aki, A. Christoffersson, and E. S. Husebye, *Determination of the three-dimensional seismic structure of the lithosphere*, *Journal of Geophysical Research* **82** (1977), [10.1029/JB082i002p00277](https://doi.org/10.1029/JB082i002p00277).
- [3] E. Ruigrok, X. Campman, and K. Wapenaar, *Basin delineation with a 40-hour passive seismic record*, *Bulletin of the Seismological Society of America* **102** (2012), [10.1785/0120110242](https://doi.org/10.1785/0120110242).
- [4] P. Audet, M. G. Bostock, N. I. Christensen, and S. M. Peacock, *Seismic evidence for overpressured subducted oceanic crust and megathrust fault sealing*, *Nature* **457** (2009), [10.1038/nature07650](https://doi.org/10.1038/nature07650).
- [5] H. Gilbert, S. Beck, and G. Zandt, *Lithospheric and upper mantle structure of central Chile and Argentina*, *Geophysical Journal International* **165** (2006), [10.1111/j.1365-246X.2006.02867.x](https://doi.org/10.1111/j.1365-246X.2006.02867.x).
- [6] Y. Nishitsuji, E. Ruigrok, M. Gomez, and D. Draganov, *Global-phase H/V spectral ratio for delineating the basin in the Malargue region, Argentina*, *Seismological Research Letters* **85** (2014), [10.1785/0220140054](https://doi.org/10.1785/0220140054).
- [7] Y. Nishitsuji, I. Doi, and D. Draganov, *The potential of imaging subsurface heterogeneities by natural local earthquakes*, *Geophysics* **79** (2014), [10.1190/geo2013-0391.1](https://doi.org/10.1190/geo2013-0391.1).
- [8] I. Doi and H. Kawakata, *High resolution spatial distribution of the velocity discontinuities in and around the swarm region beneath the Wakayama district*,

- southwest Japan*, *Bulletin of the Seismological Society of America* **103** (2013), [10.1785/0120120316](https://doi.org/10.1785/0120120316).
- [9] D. Draganov, X. Campman, J. Thorbecke, A. Verdel, and K. Wapenaar, *Reflection images from ambient seismic noise*, *Geophysics* **74** (2009), [10.1190/1.3193529](https://doi.org/10.1190/1.3193529).
- [10] S. Abe, E. Kurashimo, H. Sato, N. Hirata, T. Iwasaki, and T. Kawanaka, *Interferometric seismic imaging of crustal structure using scattered teleseismic waves*, *Geophysical Research Letters* **34** (2007), [10.1029/2007GL030633](https://doi.org/10.1029/2007GL030633).
- [11] E. Ruigrok and K. Wapenaar, *Global-phase seismic interferometry unveils P-wave reflectivity below the Himalayas and Tibet*, *Geophysical Research Letters* **39** (2012), [10.1029/2012GL051672](https://doi.org/10.1029/2012GL051672).
- [12] Y. Nishitsuji, S. Minato, B. Boullenger, M. Gomez, K. Wapenaar, and D. Draganov, *Crustal-scale reflection imaging and interpretation by passive seismic interferometry using local earthquakes*, *Interpretation* **4** (2016), [10.1190/INT-2015-0226.1](https://doi.org/10.1190/INT-2015-0226.1).
- [13] Y. Nishitsuji, E. Ruigrok, M. Gomez, K. Wapenaar, and D. Draganov, *Reflection imaging of aseismic zones of the Nazca slab by global-phase seismic interferometry*, *Interpretation* **4** (2016), [10.1190/INT-2015-0225.1](https://doi.org/10.1190/INT-2015-0225.1).
- [14] Y. Nishitsuji and J. Mori, *Source parameters and radiation efficiency for intermediate-depth earthquakes in Northeast Japan*, *Geophysical Journal International* **196** (2014), [10.1093/gji/ggt458](https://doi.org/10.1093/gji/ggt458).
- [15] Y. Nishitsuji, C. A. Rowe, K. Wapenaar, and D. Draganov, *Reflection imaging of the Moon's interior using deep-moonquake seismic interferometry*, *Journal of Geophysical Research: Planets* **121** (2016), [10.1002/2015JE004975](https://doi.org/10.1002/2015JE004975).

# ACKNOWLEDGEMENTS

Because I always find values in changing and challenging things, my acknowledgment style is different from conventional ones. Here, I itemize my acknowledgments for readers to save their time:

- **Deyan Draganov**, my daily supervisor and co-promotor, for his extraordinary passionate support. I learned a lot from him, in particular, the theory/practice of seismic interferometry, how to effectively write scientific journal papers, how to effectively present our research at conferences. Above all, what I learned most is that the idea itself can be at least as important as the knowledge. His supervision made me really productive throughout my entire PhD life. It perfectly matched with my deadline-oriented personality. Even when he was in Argentina or when I was in Japan, we communicated with each other over Skype or phone when needed. Furthermore, I also thank him for his understanding about my life/work style connected to my family. Doing a PhD is much broader work than just thesis research.
- **Kees Wapenaar**, my promotor, for his solid and sharp support especially for mathematical derivations as well as his rigorous review of journal drafts. His positive comments always motivated me further to pursue my research on time. I am very grateful for his sincere look at my research problems. When we were discussing, I paid my maximum attention to him. Plato said, "Wise men speak because they have something to say; Fools because they have to say something."
- **Elmer Ruigrok**, my passive-seismic guru, for his hands-on supervision and guidance. Without him, I am sure that I could not consolidate the foundation of passive-seismic methods. Also my deep appreciation goes to his generously allowing me use some of his great MATLAB codes. I learned a lot from him about MATLAB implementations too.
- **Makoto Tuzuki**, director at PGS, who is one of my references. Without him, I could not decide to come to TU Delft. After discussions with him over and over, I decided to commit myself to help improving Japan's sustainability of natural resources.
- **Jan Schoolmeesters**, COO at Spectrum ASA, who is one of my references. I learned from him that company managements could be more profitable if they know both the commercial and technical aspects.
- **James Mori**, my former professor at Kyoto University, who is one of my references.
- **Hiroo Kanamori**, the John E. and Hazel S. Smits professor at CALTECH, who is one of my references.
- **Robert Dean**, advising geophysicist at TGS, who is one of references.



- **Issei Doi**, assistant professor at Kyoto University, who is my former senior colleague.
- **Roy van Hooydonk**, owner of Geomet, who helped my start-ups in TU Delft. Without him, I could not get a washing machine (made in Germany) and a Dutch oven that my wife has heavily used.
- **Shogo Masaya**, PhD candidate at TU Delft, with whom we debated a lot about Japan's sustainability of natural resources. He is one of my two fellows. Johann Wolfgang von Goethe said "Knowing is not enough; we must apply. Wishing is not enough; we must do." We must keep this in mind.
- **Taisuke Imamura**, senior geologist at Sumitomo Corporation, with whom we debated a lot about the future of Japan. He is the other one of my two fellows. Louis Gerstner (ex IBM's CEO), said "Four Kinds Of People: Those who make things happen; Those to whom things happen; Those who watch things happen: Those who don't even know things are happening." You know what we need to be.
- **Boris Boullenger**, PhD candidate at TU Delft, who sat in front of me and helped my start-ups. We talked a lot about France and Japan. Merci beaucoup. We played football, tennis, bordering, beach volleyball, and basketball. We spent about four years as members of Team Deyan Draganov.
- **Abdulrahman Alshuhail**, PhD candidate at TU Delft, who attended almost all of the graduate courses with me. I enjoyed every conversation we had.
- **Tomohide Ishiyama**, senior geophysicist at INPEX, who helped my start-ups and body-pump exercise in Delft.
- **Shohei Minato**, postdoc at TU Delft, who helped MATLAB coding.
- **Asiya Kudarova**, research geophysicist at Shell, who sat next to me in TU Delft.
- **Niels Grobbe**, postdoc at MIT, who sat diagonally to me in TU Delft.
- **Carlos Almagro Vidal** who sat behind me and helped a lot my start-ups in TU Delft.
- **Joeri Brackenhoff**, PhD candidate at TU Delft, who translated summary in this thesis to Dutch.

Next to the people mentioned above, I thank all of my colleagues in TU Delft. In order to avoid misspelling and pages, I dare not explicitly state their names on purpose.

Finally, I am deeply grateful to my family for their physical and mental supports. Thank you so much for deciding to come with me all the way from Japan. Kyo, I am proud of you. You could adapt yourself to the local Dutch elementary school by conquering the different environment. This experience and achievement is not something everyone can easily do. At least, I did not do it when I was at your age. I hope this experience eventually

enriches your spirit. To grow up means to enrich the spirit. Kazuma, I am happy to have you in Delft. I respect that you like the Netherlands more than Japan. When you grow up, you can visit the hospital (which has been destroyed, though) you were born in Delft for a possible nostalgia. I explicitly note here that you made my sleeping hours to be about two-three hours every night for the first two years of my PhD life. It was actually much tougher than my PhD research itself. I know that you were mostly unconscious about that, but you screamed a lot (I mean it) at night. I took your cry as my training opportunities to be a tough guy. Hiromi, you are my dearest. It is beyond my vocabulary to express how much I appreciate and respect you to get along with a life in the Netherlands. It is not because of English. The most toughest moment must be when you gave birth to our Kazuma in Delft. You must be very anxious about it because of the tremendous differences between the Netherlands and Japan. But you did it successfully even without any supports from our parents. I do still remember that you said "Nothing will be more difficult and scary than this experience." right after when Kazuma was brought. Last but not the least, thank you very much for making lunch boxes every week days. Boris flattered me on it.

This research was supported by the Division for Earth and Life Sciences (ALW) with financial aid from the Netherlands Organization for Scientific Research (NWO) with grant no. VIDI 864.11.009.

Delft, 2016  
Yohei Nishitsuji



# CURRICULUM VITÆ

## Yohei NISHITSUJI

24-12-1982      Born in Hokkaido, Japan

### EXPERIENCE SUMMARY

2017–Present      Manager  
Petro Summit E&P Corporation, Technical Department

2013–2017      PhD candidate  
Delft University of Technology, Faculty of Civil Engineering and Geosciences

2009–2013      Coordinator - Geophysicist  
Mitsui Oil Exploration Co., Ltd., Exploration & Production Division

2008–2009      Geophysicist  
Mitsui Oil Exploration Co., Ltd., Exploration & Production Division



# LIST OF PUBLICATIONS

## LEAD-AUTHOR JOURNAL PUBLICATIONS

6. **Y. Nishitsuji**, S. Minato, B. Boullenger, M. Gomez, K. Wapenaar, and D. Draganov, *Crustal-scale reflection imaging and interpretation by passive seismic interferometry using local earthquakes*, *Interpretation* **4**, doi:10.1190/INT-2015-0226.1 (2016).
5. **Y. Nishitsuji**, E. Ruigrok, M. Gomez, K. Wapenaar, and D. Draganov, *Reflection imaging of aseismic zones of the Nazca slab by global-phase seismic interferometry*, *Interpretation* **4**, doi:10.1190/INT-2015-0225.1 (2016).
4. **Y. Nishitsuji**, C. A. Rowe, K. Wapenaar, and D. Draganov, *Reflection imaging of the Moon's interior using deep-moonquake seismic interferometry*, *Journal of Geophysical Research: Planets* **121**, doi:10.1002/2015JE004975 (2016). Editor's Highlight html-link
3. **Y. Nishitsuji**, I. Doi, and D. Draganov, *The potential of imaging subsurface heterogeneities by natural local earthquakes*, *Geophysics* **79**, doi:10.1190/geo2013-0391.1 (2014).
2. **Y. Nishitsuji**, E. Ruigrok, M. Gomez, and D. Draganov, *Global-phase H/V spectral ratio for delineating the basin in the Malargüe region, Argentina*, *Seismological Research Letters* **85**, doi:10.1785/0220140054 (2014).
1. **Y. Nishitsuji**, and J. Mori, *Source parameters and radiation efficiency for intermediate-depth earthquakes in Northeast Japan*, *Geophysical Journal International* **196**, doi:10.1093/gji/ggt458 (2014).

## LEAD-AUTHOR CONFERENCE ABSTRACTS

9. **Y. Nishitsuji**, S. Minato, B. Boullenger, M. Gomez, K. Wapenaar, and D. Draganov, *Cost-effective seismic reflection imaging using seismic interferometry for imaging of enhanced geothermal system: A case study in the Neuquén basin, Argentina*, Abstract WS11 C01 presented at 78th EAGE Conference and Exhibition, Vienna, Austria, May 2016.
8. **Y. Nishitsuji**, C. A. Rowe, K. Wapenaar, and D. Draganov, *Pseudo-reflection imaging of the Lunar Moho beneath the Apollo seismic stations using deep-moonquake seismic interferometry*, Abstract EGU2016-5698 presented at EGU General Assembly, Vienna, Austria, April 2016.
7. **Y. Nishitsuji**, S. Minato, B. Boullenger, M. Gomez, K. Wapenaar, and D. Draganov, *Crustal-scale interferometric imaging in the Malargüe region, Argentina, with P-wave coda and multidimensional deconvolution*, Abstract EGU2016-5798 presented at EGU General Assembly, Vienna, Austria, April 2016.
6. **Y. Nishitsuji**, D. Draganov, E. Ruigrok, M. Gomez, and K. Wapenaar, *Reflection imaging of the Moho and the aseismic Nazca slab in the Malargüe region with global-phase seismic interferometry*, Abstract S34B-03 presented at AGU Fall Meeting, San Francisco, United States, December 2015.

5. **Y. Nishitsuji**, E. Ruigrok, M. Gomez, and D. Draganov, *Mapping a part of Neuquén basin in Argentina by global-phase H/V spectral ratio*, Abstract We P5 08 presented at 77th EAGE Conference and Exhibition, Madrid, Spain, June 2015.
4. **Y. Nishitsuji**, and I. Doi, *A method to estimate heterogeneity through Sp-waves and frequency dependent quality factor Q analyses: A case study in southeastern offshore of Hokkaido, Japan*, Abstract ST E-P1 presented at 82nd SEG Annual Meeting, Las Vegas, United States, November 2012.
3. **Y. Nishitsuji**, and J. Mori, *The estimated dominant frequency during initial 3-10 seconds of P-wave for intermediate-depth earthquakes (depth; 60-150km, Mw; 3.5-7.0)*, Abstract P-41 presented at KAGI21 5th International Symposium, Oita, Japan, September 2007.
2. **Y. Nishitsuji**, and J. Mori, *Radiated energy, static stress drop, seismic moment and radiation efficiency of intermediate-depth earthquakes in the Pacific slab beneath Japan*, Abstract SS001 presented at 24th IUGG General Assembly, Perugia, Italy, July 2007.
1. **Y. Nishitsuji**, and J. Mori, *Radiation efficiency of intermediate-depth earthquakes ( $M_j > 4.0$ ) in the Pacific Slab beneath Japan*, Abstract J2a-08 presented at KAGI21 4th International Symposium, Kyoto, Japan, December 2006.